Papers Presented To The

# Symposium On Planetary Cratering Mechanics

FLAGSTAFF, ARIZONA
13-17 SEPTEMBER 1976

A Lunar Science Institute Topical Conference
Hosted By The
U.S. Geological Survey, Geologic Division
Branch Of Astrogeologic Studies

Universities Space Research Association
**The Lunar Science Institute**
3303 NASA Road 1
Houston, Texas 77058

Papers Presented To The

# SYMPOSIUM ON

# PLANETARY CRATERING MECHANICS

*A LUNAR SCIENCE INSTITUTE TOPICAL CONFERENCE*

*HOSTED BY THE*

*U. S. GEOLOGICAL SURVEY, GEOLOGIC DIVISION*

*BRANCH OF ASTROGEOLOGIC STUDIES*

FLAGSTAFF, ARIZONA

13 - 17 SEPTEMBER 1976

Compiled by

The Lunar Science Institute

3303 NASA Road 1

Houston, Texas 77058

LSI CONTRIBUTION 259

# PREFACE

This volume contains papers which were accepted for publication by the Organizing Committee of the Symposium on Planetary Cratering Mechanics. Papers were solicited which addressed one of the following major topics:

I. Experimental studies

II. Planetary impact cratering

III. Theoretical calculations

IV. Scaling

V. Terrestrial impact cratering

VI. Material properties and shock effects

VII. Ejecta

The Organizing Committee consisted of R. O. Pepin (*Lunar Science Institute*) and D. J. Roddy (*U. S. Geological Survey*), cochairmen, and T. J. Ahrens (*California Insitute of Technology*), H. Cooper (*R & D Associates*), M. R. Dence (*Department of Energy, Mines and Resources*), D. E. Gault (*Ames Research Center*), J. W. Head (*Brown University*), F. Hörz (*Johnson Space Center*), H. Masursky (*U. S. Geological Survey*), M. Settle (*Air Force Geophysics Laboratory and Brown University*), and J. Stockton (*Defense Nuclear Agency*).

Logistic and administrative support for this conference has been provided by P. P. Jones (*Administrative Assistant/Symposia Office, Lunar Science Institute*). This abstract volume has been prepared under the supervision of M. S. Gibson (*Technical Editor, Lunar Science Institute*).

Papers are arranged alphabetically by the name of the first author. An index lists the papers which were submitted to address one of the seven major topics. Additional indices by author and subject are included.

The Lunar Science Institute is operated by the Universities Space Research Association under contract No. NSR 09-051-001 with the National Aeronautics and Space Administration.

# TABLE OF CONTENTS

## INDICES

EQUATIONS OF STATE OF THE MOON*, T. J. Ahrens and R. Jeanloz, Seismological Laboratory, California Institute of Technology, Pasadena, CA 91125, and J. D. O'Keefe, Department of Geophysics and Planetary Physics, University of California, Los Angeles, CA 91103.

Shock wave data for samples of the Moon have two applications in the study of this multiply impacted terrestrial planet: (1) They provide a thermodynamic and rheological framework with which to interpret the extensive shock metamorphism observed in the surface samples and; (2) They provide impact data for numerical hypervelocity flow calculations, which can be used with the available constraints, to model meteorite impacts on the surface. To date, the two types of rock samples for which shock wave data are now available are believed to be representative of the lithologies of two of the major provences on the Moon, the brecciated highlands and the mare basins. Sample 15,418, a gabbroic anorthosite (containing $\sim$26% pyroxene and 74% plagioclase), has been previously studied (Ahrens et al., 1973). This rock behaves uniquely differently than terrestrial samples of similar gross mineralogy. Whereas terrestrial diabases, have dynamic compressive yield properties (Hugoniot elastic limits) which are ill-defined and appear to be very weak, with very low values of the Hugoniot elastic limit, the lunar gabbroic anorthosite is strong and dynamic yielding is well defined. Hugoniot elastic limits are found to increase slightly with final shock pressures but generally vary between $\sim$40 and $\sim$65 kb, comparable with data for single-crystal plagioclase (Ahrens et al., 1969). Our previous cratering calculations, which we now believe apply only to highland sites, have been carried out for projectiles of this same gabbroic anorthosite and metallic iron impacting a gabbroic anorthosite surface. (O'Keefe and Ahrens, 1975; 1976; in preparation.)

New shock wave data for a titaniferous mare basalt (70215) have been obtained at low shock stresses from 74 to 156 kbar. Samples having initial porosities in the range, 1.2 to 1.5%, as determined from high precision bulk measurements and weighing upon immersion in toluene, demonstrate well-defined simple compression behavior below 156 kbar. The raw Hugoniot data can be fit with values of bulk modulus, K, of $\sim$0.9 Mbar with a value of $\partial K/\partial P \simeq 5$, where P is pressure. Above this stress range a very marked series of phase changes apparently occur, in this already dense rock [containing $\sim$58% pyroxene, 18% plagioclase, 13% ilmenite, 6% olivine, and 4% quartz (Dymek et al., 1975)] taking it from a crystal density of 3.38g/cm$^3$ to an assemblage of (undoubtedly high-pressure) phases which appear to have an equivalent zero-pressure density of approximately 5g/cm$^3$! The high-pressure release adiabat data (see Figure) were obtained using the impedance-mismatch buffer technique (Ahrens et al., 1969) by utilizing a Na-Ca glass as the buffer material in a light-gas gun apparatus. The present lack of a measurable Hugoniot elastic limit ($\lesssim$ 5 kbar) constrasts sharply with a pronounced $\sim$20 kbar elastic precursor observed in the Vacaville basalt (Ahrens and Gregson, 1964).

---

*Contribution No. 2796, Division of Geological and Planetary Sciences, California Institute of Technology, Pasadena, CA 91125. Supported under NASA Grant NSG 9019.

EQUATIONS OF STATE OF THE MOON

Ahrens, T. J.

Qualitatively, the new data for 70215 implies that for slow speed impacts ($\lesssim$ 5 km/sec) onto mare surfaces, larger craters will form than for comparable (slow) impacts on highland terranes. However, for high-speed impacts, the shock data indicate the converse will occur, that is, the marked compression of 70215 relative to 15,418, implies markedly smaller craters occur on the highlands for a given population of impactors. The quantitative effect of the marked material strength and compression differences on the evolution of crater-size versus number distributions on different lunar provences needs to be evaluated.

References

Ahrens, T. J., J. D. O'Keefe and R. V. Gibbons, 1973, Proc. Lunar Sci. Conf. (4th), pp 2575-2590.

Ahrens, T. J. and V. G. Gregson, 1964, J. Geophys. Res., 69, pp 4839-4874.

Dymek, R. F., A. L. Albee and A. A. Chodos, 1975, Proc. Lunar Sci. Conf.(6th), pp 49-78.

O'Keefe, J. D. and T. J. Ahrens, 1975, Proc. Lunar Sci. Conf.(6th), pp 2831-2844.

O'Keefe, J. D. and T. J. Ahrens, 1976, Proc. Lunar Sci. Conf.(7th), in press.

EQUATIONS OF STATE OF THE MOON

Ahrens, T. J.

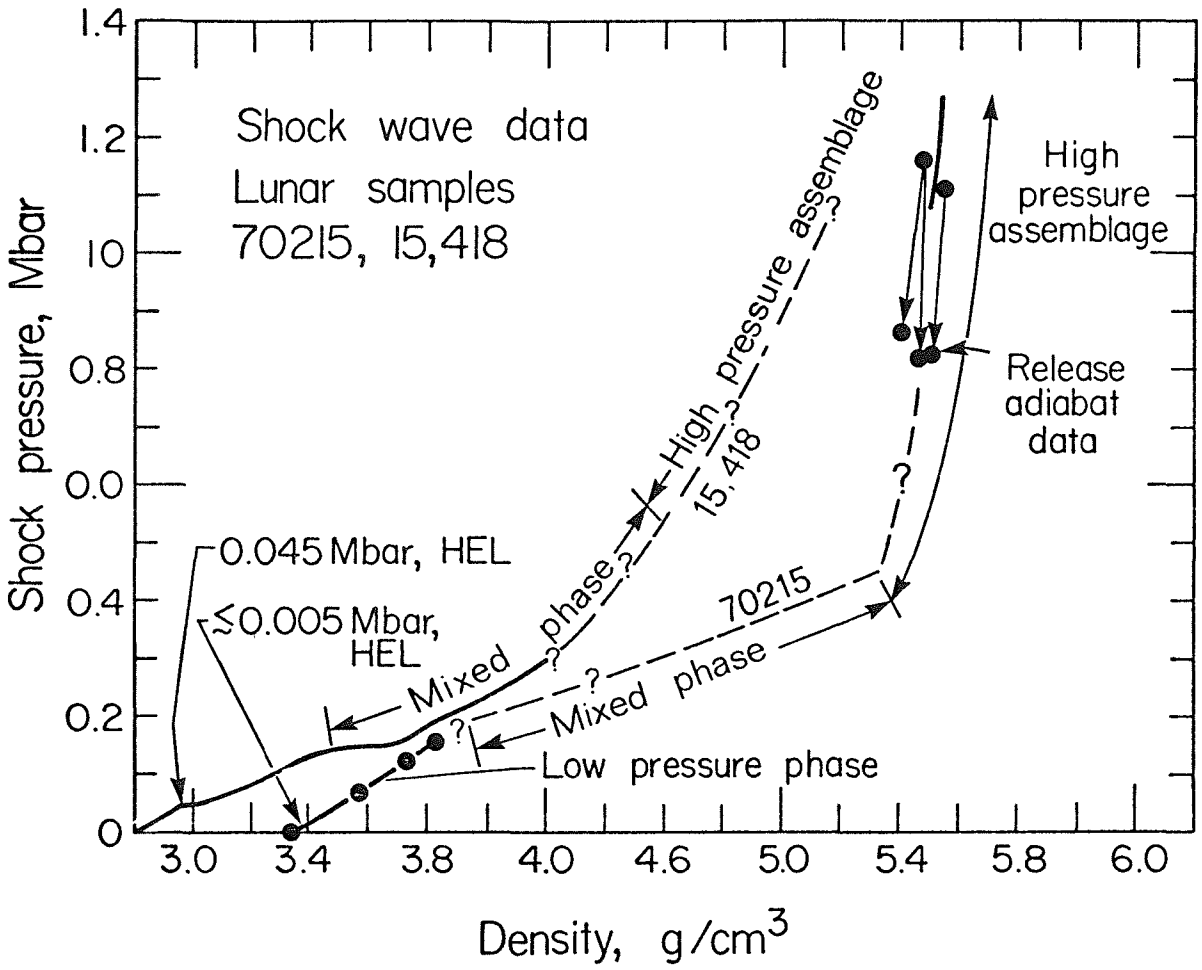

LATE-STAGE EFFECTS IN CRATER AND EJECTA FORMATION. R. T. Allen, Pacifica Technology, P. O. Box 148, Del Mar, California 92014

The late-stages of crater and ejecta formation can be defined for purposes of this presentation as times t such that

$$t > R/C \tag{1}$$

where R is the crater radius and C is the p-wave velocity of the medium. Maxwell[1] has explored both the validity and implications of the assumption that the flow field at these times is consistent with the description for steady, incompressible flow, that is the velocity field satisfies the equation:

$$\nabla \cdot \vec{v} = 0, \tag{2}$$

which leads to the form:

$$\vec{v}\,(R,\theta) = \vec{i}_R \,\alpha\, R^{-Z} + \vec{i}_\theta \,\alpha\, R^{-Z}\,(Z - 2)\,\sin\theta/(1 + \cos\theta) \tag{3}$$

in spherical coordinates. Comparison of Equation (3) with calculated flow fields for several high explosive events as well as for the Johnie Boy and Cactus nuclear tests are favorable. Cratering experiments[2] in Plasticene clay provide further validation of the model. This implies that the effects of source details and the high pressure equation of state are reduced to two parameters: $\alpha$ which is a measure of the coupling of the source energy into ground kinetic energy (and momentum) and Z which is a measure of the geometry of the flow. The model further implies that the final crater volume and shape are some function of these two variables.

This model does not incorporate any additional physical phenomena compared to the detailed numerical calculations discussed in other presentations given at this meeting. The model does allow, however, extrapolation to final crater size and shape with considerable saving in computer time. There are two basic assumptions in the current extrapolation techniques. First, it is assumed that the geometry of the streamlines is constant with time. Second, every mass element is presumed to remain attached to the main body of flow. It is more reasonable to expect (and the detailed calculations indicate) that regions "break away" to coast on paths controlled by gravity, air drag and collision processes. The presumption of constant streamlines is also

open to question. Nevertheless, this model has been quite helpful in predicting the gross features of crater formation and the sensitivity to changes in the strength of the ground and in the gravitational body force.

The vast majority of the codes currently used for the solution of cratering calculations are formulated in finite difference form so that advance of time during a given cycle is limited by the Courant stability condition[3]. Although this criterion can be relaxed by an implicit treatment of time, such a formulation[4] has received only limited application to crater formation studies. At the present time, the final position of mass elements which have fractured and become detached from the main body of flow is estimated by ballistic extrapolation. Several assumptions are implicit in this treatment: (1) air drag is a small correction to the effect of gravity for most of the ejected mass, (2) there is no further communication with the main body at later time and (3) the fracture criterion is sufficiently accurate to provide a good description of the time evolution of material entering ballistic flight.

Finally, a number of mechanisms which may have a significant effect on final crater size and shape remain to be studied in detail. These include two-phase flow effects[5], water washing[6], slumping and elastic rebound[7].

1. Maxwell, D. E., "Cratering Flow and Crater Prediction Methods," Physics International Report TCAM 73-17, September 1973.
2. Seifert, K. and D. Maxwell, "Experimental Report of Cratering, Displacement and Ejecta Processes," Defense Nuclear Agency Report DNA 3382T, August 1974.
3. Courant, Friedricks and Lewy, Math. Ann. 100, 32 (1928).
4. Riney, T. D., and J. E. Welch, "SURGE: A Computer Code for Two-Dimensional Incompressible Flow," Systems, Science and Software Report 3SR-86, March 1969.
5. Allen, R. T., "Crater Formation From High Explosive and Nuclear Surface Bursts," Pacifica Technology Report PT-U75-0030, September 1975.
6. Vortman, L. J., "Craters from Surface Explosions and Scaling Laws," JGR 73, 4621 (1968).
7. Ullrich, G. W., "The Mechanics of Central Peak Formation in Shock Wave Cratering Events," Air Force Weapons Laboratory Report AFWL-TR-75-18, May 1976.

THE LUNAR GRID SYSTEM : Gerard Andlauer, Planet. Invest., Strasbourg , France

Spurr ( 1 ) noted that the rilles and faults of the lunar surface not are distributed at random but define a regular lattice. Fielder ( 2 ) set up the orthographic chart of these features. He found that they can be divided into two families of parallel sets. One is trending SW - NE. The other runs SE - NW. The both plotted together define a roughly orthogonal grid - fig. 1. This fracture lattice is due to strain applied on the lunar surface. Its notable regularity refers to the Piobert Luders effect.

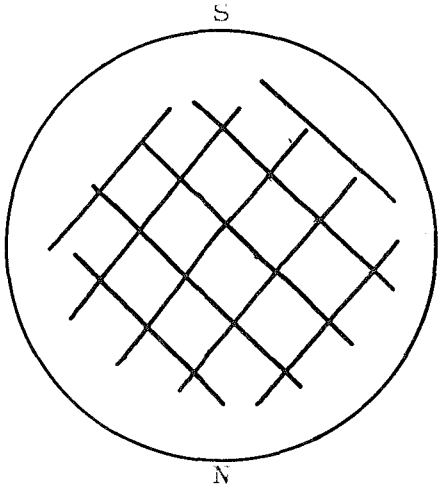


fig. 1 Approximative lattice pattern

A metal or a rock has its own elastic limit. A higher strain applied on it produces a permanent set. This is distributed over the whole surface of the body if it is uninjured. However if it has been before strained over the elastic limit the plastic set will arise along a definite lattice only that coincides with the lunar fracture lattice ( 3 ).

Already Laplace notes ( 4 ) the discrepancy between geometrical and dynamical figure of the Moon. It represents a departure from the hydrostatic equilibrium revealed by the libration around the center of gravity. The result will be a steady strain applied on the lunar surface layers increased by the low temperature and pressure. The lunar crust will be stretched along the orthogonal lattice.

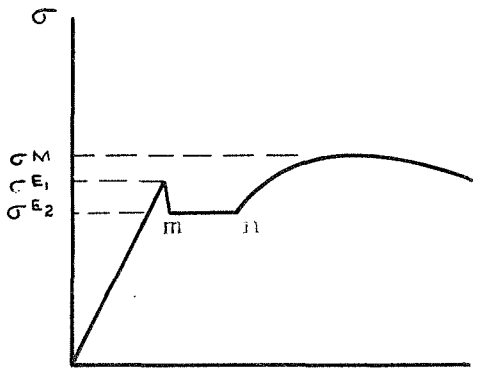


fig. 2 Schematic strain curve. mn represents the Piobert Luders level.

B M Middlehurst has proven ( 5 ) the tectonic instability of the lunar crust along the rille lattice. These areas reveal a notable volcanic and seismic activity at lunar perigee when the tidal effect of the Earth reachs a height.

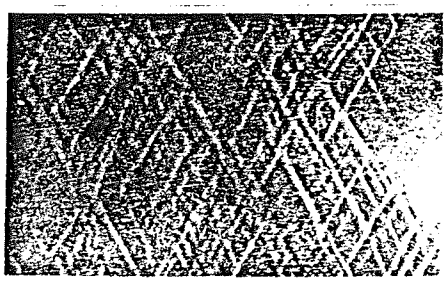

fig. 3 Piobert Luders lattice in a steel plate. The strain axis is horizontal.

# THE LUNAR GRID SYSTEM

Gerard Andlauer

## REFERENCES

1 SPURR J. E., Geology Applied to Selenology, Vol. IV. Concord, N. H., Rumford Press, 1949

2 FIELDER G., "Lunar Lattice Patterns and their time of origin", Pub. A.S.P., 70, 308, 1958
idem, Lunar Geology, Lutterwoth Press, London, 1965

3 SEEGER A., Handbuch der Physik, Band VII, Springer-Verlag, 1958

4 LAPLACE P. S., Traité de mécanique céleste, Oeuvres, Vols; 1 - 5, Paris : Imprimerie royale, 1843-46

5 MIDDLEHURST B. M., "Lunar tidal phenomena and the lunar rille system", The Moon : Symposium n° 47 held at the University of Newcastle upon Tyne, England - 22 - 26 March 1971, p. 450 - 457, D. Reidel Publishing Company, Dordrecht, Hollande, 1972

CHARACTERISTICS OF DEBRIS FROM SMALL-SCALE CRATERING EXPERIMENTS; R. J. Andrews, University of Dayton Research Institute, Dayton, Ohio 45469

Considerable ejecta data have been collected from high-explosive, laboratory-scale cratering experiments. Gram-size lead azide charges have been detonated in Ottawa sand at several near-surface heights of burst. The data derived from these experiments include: the origin of debris particles, the radial distribution of debris, and, some characteristics of the rays formed in the ejecta blanket.

The origin of the ejected material has been obtained by placing tracers in the region of medium to be cratered. Variation of height of burst, in-situ density, moisture content, and layering indicate the origin of particles is a function of all these parameters. However, certain trends exist regardless of the test conditions. The extreme range missiles originate from a region near the surface and centered at approximately 0.5 crater radii. The extent of this region is a function of the above mentioned parameters. These data also indicate that under some conditions large regions of the crater are formed by nonexcavational processes. Figure 1 compares the craters and origin maps for dry dense and dry loose sandbeds. In dry dense sand, the entire cratered region supplies ejecta while in the dry loose sandbed, approximately 40 percent of the crater volume is nonexcavational in nature. The postshot location of tracers within this region indicate a large degree of compaction as the tracers moved down and slightly out during the cratering process.

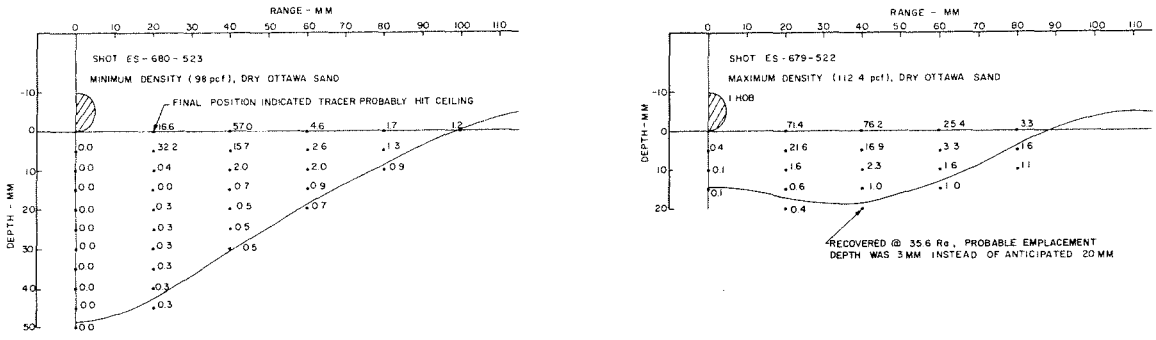


Figure 1. Origin maps for craters formed in dense and loose sand (Note large region in loose sand where tracers were not ejected) Numbers adjacent to points indicate final tracer range in crater radii.

# DEBRIS FROM SMALL-SCALE CRATERING

Andrews, R.J.

High speed photographs of the events indicate that ejecta leaves the cratered region as a thin veil of material. This veil expands outward and while the material is airborne, spires of debris form in the veil and these spires are deposited as rays of ejecta. The spires form between 12 and 50 msec after detonation and are deposited on the preshot surface slightly ahead of the advancing veil of airborne material. The trailing edge of the veil forms the overturned flap of debris near the crater lip.

Debris were collected to determine the distribution of ejecta for various events. A crater volume normalization technique developed by Post (Ref. 1) has been used to scale the radial distribution of ejecta from near-surface events detonated in dry sand. For the heights of burst investigated (Ref. 2) decaying power functions best described the distributions. These functions described the data with a correlation coefficient of >0.99 over a range from the crater lip to 30 crater radii. The distribution for half-buried events is shown in Figure 2.

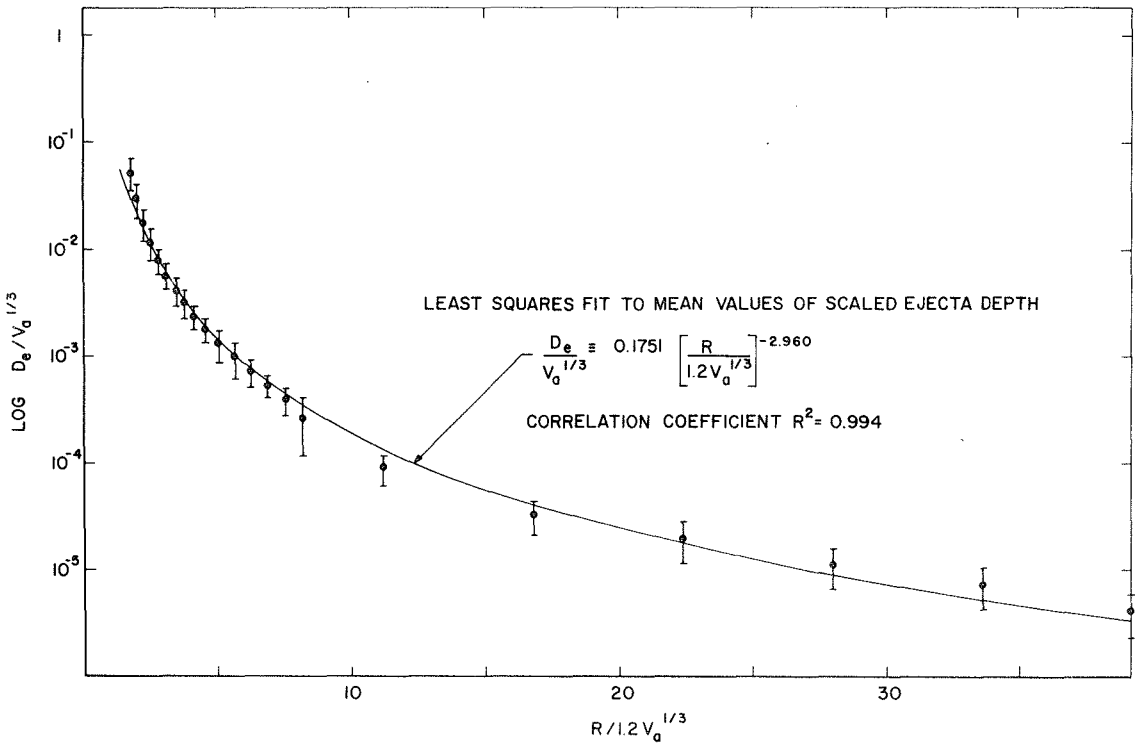


Figure 2. Ejecta Distribution for a half-buried event in dry Ottawa sand.

# DEBRIS FROM SMALL-SCALE CRATERING

Andrews, R. J.

Rayed ejecta deposition patterns which are present around impact and field-scale explosive craters also occur in the laboratory. Several characteristics of rays from near-surface detonations in dry sand are presented. Average ray length increases as the height of burst decreases and also as the depth of burial increases. The maximum number of rays is produced when the charge is near the half-buried configurations. These data are plotted in Figure 3. The Air Vent series of events produced prominent rays near optimum depth of burst (Ref. 3). This depth of burst was not investigated in the laboratory. A limited amount of data also indicated that the presence of a competent lower layer in the medium increases the length of rays but decreases the number of rays produced.

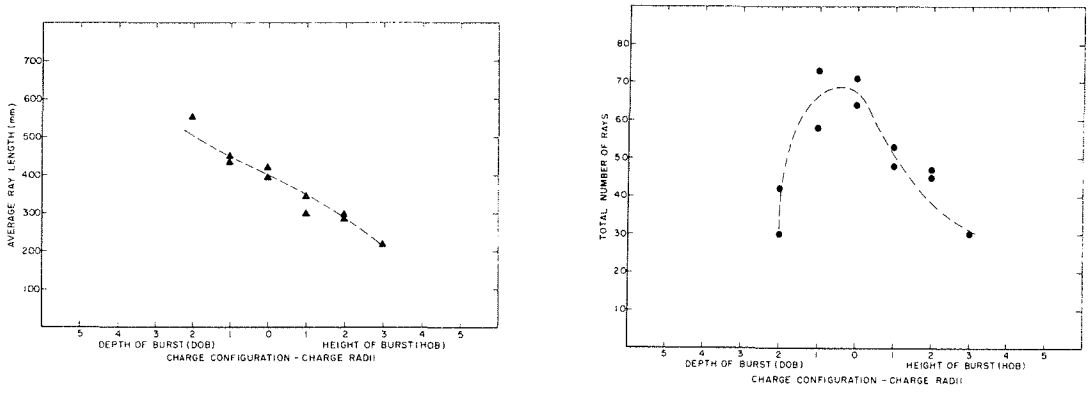


Figure 3. Ray Characteristics as a function of height of burst.

Several observations concerning the mechanisms producing rays have been made during the course of the experiments. Airblast shielding of the preshot surface and ejecta veil significantly reduced the number of rays formed. Also, fireball anomalies appear to correlate with the ray patterns for some events. However, attempts to produce rays at predetermined locations by placing "joints" in the medium were unsuccessful.

References

(1) Post, R. L., Ejecta Distributions from Near-Surface Nuclear and HE Bursts, AFWL-TR-74-51, Air Force Weapons Laboratory, May 1974.

(2) Andrews, R. J., Origin and Distribution of Ejecta From Near-Surface Laboratory-Scale Cratering Experiments, AFWL-TR-74-314, Air Force Weapons Laboratory, April 1975.

(3) Carlson, R. H., Jones G. D., Ejecta Distribution Studies, D2-90575, The Boeing Company, November 1964.

# A STATISTICAL ANALYSIS OF LUNAR CRATER DEPTH/DIAMETER RATIOS

J. C. Anselmo, D. E. Rehfuss, N. K. Kincheloe, D. Michael, S. A. Wolfe
Physics Department, San Diego State University, Ca. 92182

Depth versus diameter studies have been made on Arthur's (1) recently published Orbiter IV crater depths to determine trends in the data. Most of the craters studied are smaller craters with rim diameters between 3 and 20 km but some larger craters are also listed. The 1913 craters considered, located within the earthward sixth of the lunar sphere, were divided into 5 classes according to rim sharpness criteria. The original measurements were made by students at the University of Arizona on standard enlargements supplied by NASA. The depths are reported to be accurate to within 5 to 10% and the diameters to less than 0.5% (2). Four obvious errors in the data were corrected by the helpful assistance of E. A. Whitaker at the University of Arizona (3).

In Table 1 are summarized the calculations on each class and also on the data considered as a whole. The average depths and diameters are listed and the depth (Y) is then considered as a function of diameter (X) to determine curve fits. Four common curves were considered with their correlation coefficients $r^2$. In nearly all cases the power curve fits show the highest correlation coefficients. The plausibility of the fit may be examined in Figure 1 in which the four curves are superimposed on the data for class 1 craters.

In conducting a similar study utilizing other data, Pike (4) found a knee on a depth vs diameter plot at 15 km. Using only Arthur's data, this group found none. An improved correlation coefficient, $r^2 = 0.82$, does exist for a power curve if only data for craters smaller than 15 km is considered, but for craters larger than 15 km a very poor value of 0.03 is obtained. Data reduction was also attempted to determine a preferred knee by removing data less than a distance of 3 fractional standard deviations in two dimensions from the originally determined curves. Again no pronounced knee appeared.

A most unusual feature of the data can be easily seen in Figure 2 which represents a graph of depth vs diameter for all craters. The craters veer away from the ordinate in a most pronounced way. A power curve fit for this boundary was determined by using those points closest to the ordinate, giving depth = $.446\ \text{Diameter}^{.757}$. This curve might be used as an indicator of isotatic adjustment and could no doubt be correlated with the angle of repose for smaller craters.

Arthur's classification system is defined by rim sharpness and the original Arthur catalog (5) warns: "Readers should not expect complete accuracy or consistency in this classification." Although several cratering schemes have been used in planetary science, the smoothly varying values for the regression coefficient B in Table 1 indicate careful and painstaking work by the students at the University of Arizona.

This work was supported by NASA contract No. 07026.

REFERENCES

1. Arthur, D. W. G., Lunar crater depths from Orbiter IV long-focus photographs, Icarus, 23, 116-132, 1974.
2. Arthur, D. W. G., Personal communication, 1976.
3. Whitaker, E. A., Personal communication, 1976.
4. Pike, R. J., Geophys. Res. Lett., 1, 291-294, 1974.
5. Arthur, D. W. G., et al, "The System of Lunar Craters", Communications of the Lunar and Planetary Laboratory Nos. 30, 40, 50, and 70. The University of Arizona, 1963-1966.

Table 1

| | | | | Exponential $Y = Ae^{BX}$ | | | Logarithmic $Y = A + B\ln X$ | | | Linear $Y = A + BX$ | | | Power $Y = AX^{B}$ | | |
|---|---|---|---|---|---|---|---|---|---|---|---|---|---|---|---|
| Class | # | Aver. depth | Aver. diam. | A | B | $r^2$ | A | B | $r^2$ | A | B | $r^2$ | A | B | $r^2$ |
| I | 1078 | 1.16 | 6.94 | .525 | .091 | .59 | -.772 | 1.098 | .78 | .324 | .121 | .71 | .198 | .910 | .80 |
| II | 580 | 1.10 | 9.59 | .570 | .050 | .44 | -.586 | .834 | .64 | .498 | .063 | .54 | .215 | .717 | .60 |
| III | 200 | 1.16 | 14.98 | .625 | .029 | .24 | -.422 | .631 | .35 | .633 | .035 | .27 | .225 | .582 | .37 |
| IV | 49 | 1.11 | 23.30 | .645 | .018 | .22 | -.509 | .535 | .25 | .617 | .021 | .23 | .225 | .490 | .27 |
| V | 6 | .76 | 30.17 | .528 | .009 | .10 | -.032 | .245 | .18 | .629 | .004 | .06 | .163 | .443 | .27 |
| All | 1913 | 1.14 | 9.08 | .661 | .041 | .31 | -.309 | .741 | .52 | .659 | .053 | .36 | .281 | .629 | .52 |

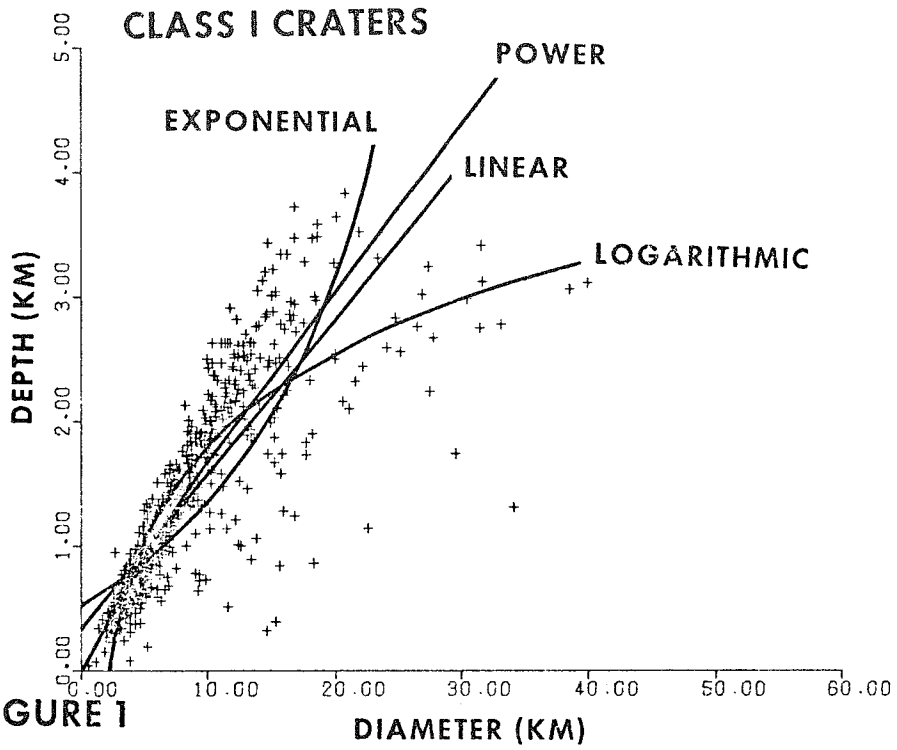


FIGURE 1

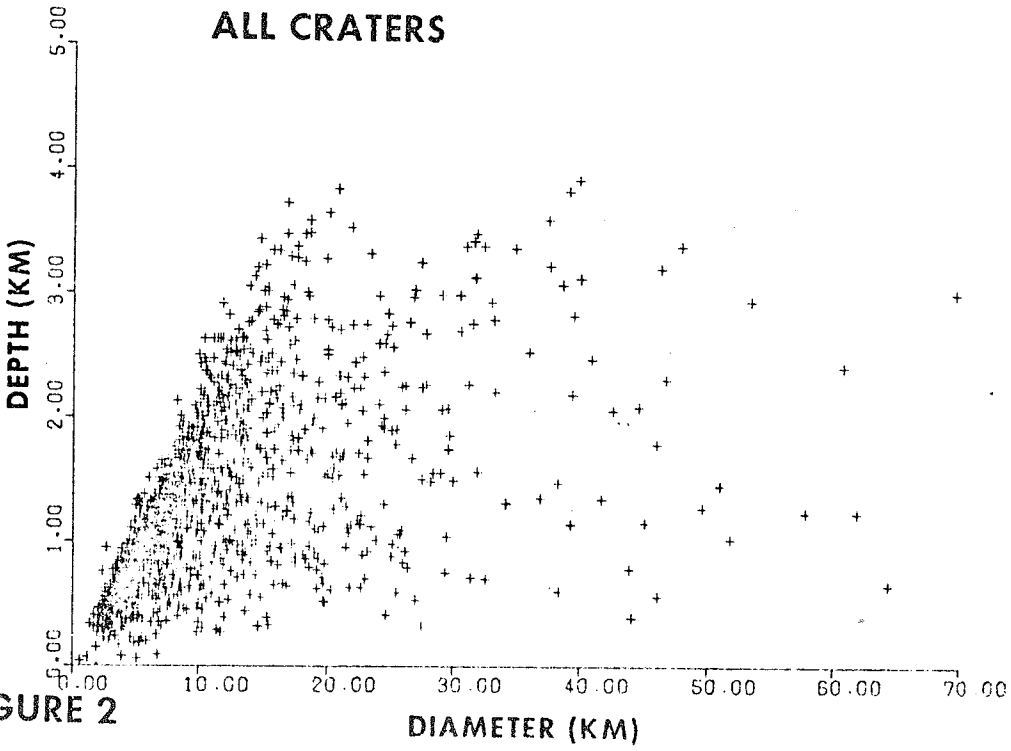


FIGURE 2

NUMERICAL SIMULATION OF SUBSURFACE EXPLOSION CRATERING, Jon B. Bryan, Donald E. Burton, Charles M. Snell, and Jeffrey M. Thomsen, Lawrence Livermore Laboratory, Livermore, CA. 94550.

Two-dimensional computer calculations were performed to model buried high explosive (nitromethane) cratering detonations in saturated Bearpaw clay shale. These calculations were part of a combined theoretical and experimental study of explosive cratering effects called Project DIAMOND ORE. Experimental high-explosive detonations were conducted at Ft. Peck, Montana. This program was later expanded as Project ESSEX with additional experimental cratering being conducted at Ft. Polk, Louisiana. This work was performed in cooperation with the Explosive Excavation Research Laboratory of the U.S. Army Engineer Waterways Experiment Station, under the auspices of the Defense Nuclear Agency, the U.S. Energy Research and Development Administration (formerly the U.S. Atomic Energy Commission), and the Office of the Chief of Engineers.

The calculations consisted of an initial dynamic stress-wave propagation phase using the two-dimensional, Lagrangian, finite difference computer code called TENSOR. The dynamic calculation was followed by a ballistic throwout and slope stability calculation which produced the final crater configuration. The dynamic phase of each calculation was carried to a time representing at least three to four source-to-surface transit intervals. By this time, the kinetic energy transfer from the source to the surrounding medium was essentially complete and a stable velocity field was established in the mound of ejecta material. The velocity field was then used in conjunction with a ballistic throwout code called EJECT to calculate the final crater dimensions.

Calculational results for a 20 ton nitromethane detonation buried at 12.5 m (near optimum cratering depth) agreed with experimentally measured values of peak stress and peak particle velocity, and with observed crater dimensions. Additional calculations were performed for 20 ton nitromethane charges buried at depths of 6 and 17 m with different cratering characteristics. A calculation was also performed for a 10 ton nitromethane charge buried at 12.5 m. The results of this experimentally-verified suite of calculations provide a means of studying the physical mechanisms responsible for crater formation.

Gravitational effects on throwout and crater size were examined by varying the value of the gravitational acceleration "g" used during the ballistic ejecta phase of the calculation. The effects of gravity and overburden were not included in the earlier dynamic phase of the calculation, since these effects are much less important during the early strongly-accelerated motion history. Thus, the results of a single TENSOR dynamic calculation was used to perform many ballistic ejecta calculations for values of "g" ranging from 1.0 to 30.0 $m/s^2$. Included were values for the Moon 1.62 $m/s^2$, Mars 3.73 $m/s^2$, Earth 9.80 $m/s^2$, and Jupiter 26.5 $m/s^2$.

Prepared for U. S. Energy Research and Development Administration
under contract No. W-7405-Eng-48

INFLUENCE OF GRAVITATIONAL FIELDS AND ATMOSPHERIC PRESSURES ON SCALING OF EXPLOSION CRATERS; A. J. Chabai, Sandia Laboratories, Albuquerque, New Mexico 87115

Early examinations of the manner in which crater dimensions scale with explosive energy were generally conducted with small ($< 10^2$ kg) explosive charges. These experiments provided the observation that geometric scaling is obeyed, i.e. that crater dimensions are in proportion to the charge dimension which in turn is proportional to the cube-root of explosive charge energy. Validity of the cube-root rule for these small charge craters suggested that gravity was not influential and consequently that fourth-root scaling was not appropriate. Systematic experiments in a single geologic medium with buried TNT charges having masses from $10^2$ to $10^6$ kg demonstrated conclusively that cube-root scaling is not correct. An empirical scaling relationship, the 1/3.4 rule, was found[1,2,3] to fit the data well. According to this empirical result, linear crater dimensions are proportional to the 1/3.4 power of explosive yield. Lack of similarity among experiments was invoked to account for the empirical scaling exponent.

One quantity postulated[4] to contribute to violation of similarity among experiments was atmospheric pressure. Experiments by Herr[5] and Rodionov[6] revealed that crater dimensions could be significantly altered by varying pressure of the atmosphere above a half space in which explosion craters are produced. In contradiction to this, Johnson[7] et al. found that atmospheric pressure was only weakly influential. An overburden scaling was proposed[4,6] in which linear dimensions are scaled by $(p + \rho gd)^{1/3}/Y^{1/3}$. This rule provided, in effect, a variable exponent which ranged from cube-root for small explosive yields (Y) and shallow burial depths (d) to fourth-root for large yields and burial depths where lithostatic pressures ($\rho gd$) greatly exceeded atmospheric pressure (p). For intermediate yields and depths, the overburden rule scaled data as well as or better than the empirical 1/3.4 scaling rule.

Effects of changing the gravitational field in explosive cratering was dramatically shown by small charge experiments[7,8] in accelerating frames. Large changes in crater dimensions may be produced by simply changing the acceleration of the frame in which experiments are conducted. These results strongly suggest that fourth-root scaling should be the rule employed in modeling prototype experiments. That the fourth-root rule does not properly scale dimensions of large explosive craters is attributed to our inability to conduct experiments with the required similitude. To achieve similarity in experiments, the fourth-root rule imposes severe requirements on medium properties and explosive characteristics.

Violations of similarity in cratering experiments cause larger yields to have smaller cube-root scaled crater dimensions while by fourth-root scaling the larger yields have smaller scaled dimensions. Based on this observation, a scaling intermediate to cube-root and fourth-root was proposed by Saxe and DelMonzo[9] and by Westine.[10] The scaling rule proposed asserts that linear dimensions are scaled by the length dimension $Y^{7/24}/(\rho^{7/24} g^{1/8} c^{1/3})$. The exponent for yield, 7/24, has, within experimental uncertainty, the same value as the empirical value, 1/3.4, established by large yield experiments.

# SCALING OF EXPLOSION CRATERS

Chabai, A. J.

Extensive data analyses by Dillon[11] of craters in several media indicated that 7/24 was the exponent of yield which best fit the data (even though Dillon used 5/16 for the rest of his studies). Crater dimensions from experiments by Johnson[7] et al., under conditions where the gravitational acceleration, g, was simulated to be $0.17g_e$, $0.38g_e$, $1.00g_e$, and $2.50g_e$, ($g_e$ = 9.8 m/s$^2$) were nicely scaled by $g^{1/8}$ as opposed to $g^{1/4}$ demanded by fourth-root scaling. Johnson et al. examined crater diameter as a function of acceleration level for fixed charge burial depth and find that the exponent of g is less than 1/4 and varies from 0.111 to 0.157, the value increasing with increasing depth of burst of the cratering explosive charge. The data of Viktorov and Stepanov from experiments at g = $1g_e$, $25g_e$, $45g_e$ and $66g_e$ are also interpreted by Johnson et al. with the result that the appropriate exponent for g is 0.074 to 0.077.

Scaling a linear dimension from a terrestrial crater to obtain estimates of crater dimensions for lunar or other planetary craters does not result in a large error based on the difference in scaling by $g^{1/4}$ and $g^{1/8}$. However, in laboratory experiments with accelerated frames, differences due to the scaling exponent on g should be readily discernable. The degree of uncertainty in our ability to scale crater dimensions, which is associated with the scaling exponent on g, is unacceptable.

The ad hoc 7/24 rule,[9,10] in which g is scaled by the 1/8 power, cannot be correct as there is no physical basis for this result. Determination of a scaling exponent for g close to 1/8 from the data of Johnson et al. is also not correct. While data are presently not available to settle the question of how the gravitational field is correctly scaled, some small scale experiments of the nature of those already performed[6,7,8] are suggested from which hopefully the question may be resolved.


1. Chabai, A. J., "Crater Scaling Laws for Desert Alluvium," SC-4391 (RR), Sandia Laboratories, 1959.
2. Vaile, R. B., "Pacific Craters and Scaling Laws," J. Geophys. Res. 66, No. 10, 1961.
3. Nordyke, M. D., "An Analysis of Cratering Data from Desert Alluvium," J. Geophys. Res. 67, 1962.
4. Chabai, A. J., "On Scaling Dimensions of Craters Produced by Buried Explosives," J. Geophys. Res. 70, No. 20, 1965.
5. Herr, R. W., "Effects of Atmospheric-Lithostatic Pressure Ratio on Explosive Craters in Dry Soil," NASA Langley Research Center, NASA TR R-366, 1971.
6. Rodionov, V. N., "Methods of Modeling Ejection with Consideration of the Force of Gravity," Lawrence Livermore Laboratory, UCRL-Trans-10476, 1970.
7. Johnson, S. W., et al. "Gravity and Atmospheric Pressure Effects on Crater Formation in Sand," J. Geophys. Res. 74, No. 20, 1969.
8. Viktorov, V. V. and Stepenov, R. D., "Modeling of the Action of an Explosion with Concentrated Charges in Homogeneous Ground," Sandia Laboratories Translation SC-T-392, 1960.

9. Saxe, H. C. and DelManzo, D. D., "A Study of Underground Explosion Cratering Phenomena in Desert Alluvium," Symposium on Engineering with Nuclear Explosives, 1970.
10. Westine, P. S., "Explosive Cratering," J. Terramech. 7, 1970.
11. Dillon, L. A., "The Influence of Soil and Rock Properties on the Dimensions of Explosion-Produced Craters," AFWL-TR-71-144, Air Force Weapons Laboratory, 1972.

PHYSICAL PARAMETERS, EJECTA OVERLAP RELATIONSHIP AND TRANSPORT CHARACTERISTICS, AND THE NATURE OF THE IMPACTING BODY AS CONSTRAINTS FOR THE CRATERING MODEL OF THE RIES. E. C. T. Chao, U. S. Geological Survey, National Center 929, Reston, Va. 22092 (to be presented orally by Jean A. Minkin, U. S. Geological Survey, Reston, Va. 22092).

New data obtained in 1975 and 1976 have helped to clarify and place specific constraints on the cratering model for the shallow multiring basin of the Ries in Southern Germany.

The crater diameter has been determined as about 25 km, and its depth is about 750 m. Hence the depth-to-diameter ratio of the Ries is 1:33. This is very probably the approximate original shape of the crater and not the result of post-cratering readjustment by sliding or kilometers of uplift of the crater floor after the cratering event. Rim subsidence is rare and where present is not more than 30 m. There is no evidence of any melt layer penetrated by the 1206 m hole drilled in 1973 (1), 3.8 km from the geometric center of the crater. Geophysical data also indicate that there is probably no melt layer at the center of the crater and that the possible center uplift due to impact rebound is probably less than 200 m.

The crater or total ejecta volume (without correction for porosity) calculated from the crater diameter and depth is 184 $km^3$. Sedimentary ejecta make up 90-95 percent of this volume and less than 10 percent are ejecta of crystalline rocks and suevite.

Field and laboratory criteria have been established for distinguishing non-ballistically transported ejecta from those transported ballistically. Evidence for the roll-glide mode of non-ballistic transport is as follows:

1. The widespread occurrence of striated surfaces on autochthonous bedrocks showing movement of ejecta on the ground surface radially away from the center of the crater. Such ejecta were transported along the pre-crater topography, with the direction of transport and the thickness of ejecta greatest along and within pre-Ries valleys.

2. Striated surfaces and gouges on different sides of breccia blocks, and between allochthon units, resulting from relative movement under confining pressure of components within the ejecta blanket. Recently mineral-produced high pressure striae and clay polish have been discovered on angular and freshly fractured surfaces of limestones in the ejecta. These are key indications of ejecta transport under confining pressure.

3. Limestone concretions which have been plastically deformed under shock-induced high strain rates -- estimated confining pressures are greater than 30 kb.

Constraints for the cratering model of the Ries

Chao, E. C. T.

4. Incompetent beds such as shale which have flowed plastically, and sedimentary rocks of different stratigraphic horizons which have been rolled as different layers into minor intricate folds.

5. Poorly consolidated autochthonous substrate folded as a result of sustained pressures from the ejecta mass moving over it.

Fallout, fallback and throwout ejecta show none of the characteristics of the roll-glide non-ballistic ejecta. Instead the fallout ejecta reflect an inverted stratigraphic section with no mixing of the type produced by the motion of the roll-glide ejecta.

Two cores drilled in the summer of 1976 at Otting and Itzing, located within 1/2 radius beyond the crater rim, showed that over 80 percent of the ejecta were transported non-ballistically by the roll-glide mode. Ballistically transported sedimentary ejecta were estimated to be only a few percent of the total ejecta volume. Much of the crystalline rock and suevite ejecta were expelled ballistically at moderate to high angles so that they overlie the bulk of the sedimentary ejecta.

Within the crater, studies of the 1973 drill core reveal that high temperature fallback suevite overlies low temperature suevite which directly overlies a compressed zone with abundant shatter cones. The top of the compressed zone represents the intact, unbrecciated and undisplaced bedrock. This is the crater floor because: (a) it is undisturbed and lies directly under the fallback low temperature suevite; (b) shatter cones have low inclination angles of 5-20 degrees, pointing to a center of impact not far above the compressed zone; (c) Fe-Cr-Ni particles and veinlets were discovered at the top of the compressed zone (2); (d) shock features such as intragranular microfractures in quartz and hornblende gradually attenuate in the crystalline rocks downward from depths of 602 m in the 1973 deep drill core, in agreement with the increase in fission ages of the low shocked crystallines (Wagner, oral presentation at the Ries core colloquium in Munich, May 24-25, 1976).

The discovery of Fe-Cr-Ni particles and veinlets in shock-produced microfractures across a wide suite of minerals of the crystalline rocks of the compressed zone gives the first clue that the impacting body of the Ries was a stony meteorite and not an iron meteorite. The lower density of a stony meteorite also favors the production of a shallow crater.

The schematic cratering model developed (3) is consistent with the above data and constraints with emphasis on the importance of non-ballistic transport under confining pressures in the early stage and ballistic transport in the terminal stage of the cratering event.

Constraints for the cratering model of the Ries

Chao, E. C. T.

References

(1) Bauberger, Wilhelm; Mielke, Hubert; Schmeer, Dora; and Stettner, Gerhard, 1974, Petrographische profildarstellung der forschungsbohrung Nördlingen 1973. Geologica Bavarica 72, 33-34.

(2) El Goresy, Ahmed and Chao, E. C. T., 1976, Evidence of the impacting body of the Ries Crater - the discovery of Fe-Cr-Ni veinlets below the crater bottom. Earth Planet. Sci. Lett., in press.

(3) Chao, E. C. T., 1976, The Ries Crater of Southern Germany -- a model for large basins on planetary surfaces. Fortschr. Mineralogie, in press.

EJECTION ENERGY-DIAMETER SCALING LAWS FOR GIANT IMPACTS, S.K. Croft, Dept. Geophysics & Space Physics, Univ. California, Los Angeles, CA 90024.

The total impact energy for large craters is partitioned primarily into energy of ejection and heat. Assuming the fraction of heat to be roughly constant, E-D scaling law may be written:

$$E_{TOT} = A_e \rho g D^B \quad (1)$$

where $\rho$ = density, g = surface gravity, $A_e$ and B are constants. Unfortunately, $A_e$ is uncertain by a factor of $10^5$ (1), resulting in a similar uncertainty in the scaling law. Consequently, an ejection energy model was designed to evaluate the importance of several parameters affecting $A_e$ and B.

The Ejection Model: The initial crater form is assumed to be a spherical segment of radius $R_o$ and central depth $h_s$. The volume is divided into horizontal layers and radial annuli. Each annulus of radius $r_i$ is "lifted" vertically to the surface and "fired" at an elevation angle defined by

$$\theta = 6+84(1-(r_i/R_o)^{\beta})(1-(h/h_i)^{\beta}) \quad (2)$$

to a range ($R_a$) defined by

$$R_a = R_m-(r_i/R_i)^{\alpha}(R_m-R_o)-r_i, \quad (3)$$

where $R_m$ is the outer limit of the ejecta blanket, $R_i$ is the radius of the horizontal layer from which the annulus is derived, and $\alpha$ and $\beta$ are arbitrary parameters. Eq. 3 is essentially a function that maps each layer in the crater onto the ejecta blanket, the center of each to $R_m$ and the edge of each to $R_o$. This mapping reproduces the inverted stratigraphy found in both small experimental (2) and large natural impact craters (3). The kinetic energy of each annulus is found via the ballistic equation using the above values of $\theta$ and $R_a$. The total energy required to a crater of diameter D is found by integrating over all annuli and adding the potential energy required to lift the material to the surface. A scaling law of the form of eq. 1 is determined by a least square fit to the above calculated energies of 11 craters from 50 to 1000 km in diameter. Table I gives the parameters and scaling laws for 10 such calculations. The models and physical meaning of the parameters are discussed below.

TABLE I

| Model # | $h_s$-D | $\theta$ | $\beta$ | $\alpha$ | LogE = A + BlogD | Ratio to STD At | |
|---|---|---|---|---|---|---|---|
| | | | | | | 100 km | 1000 km |
| 1(STD) | PIKEF | $90^o \rightarrow 6^o$ | 0.35 | 0.20 | =21.783+3.835logD | | |
| 2 | " | " | 0.55 | " | =21.592+3.884 " | 1.24 | 1.11 |
| 3 | " | " | 0.15 | " | =22.054+3.760 " | 0.76 | 0.90 |
| 4 | " | $\theta=45^o$ | - | " | =21.179+3.982 " | 2.04 | 1.46 |
| 5 | " | $\theta=6^o$ | - | " | =22.215+3.712 " | 0.65 | 0.86 |
| 6 | " | $90^o \rightarrow 6^o$ | 0.35 | 0.50 | =22.164+3.739 " | 0.65 | 0.81 |
| 7 | " | " | " | 0.50 | =21.415+3.917 " | 1.60 | 1.32 |
| 8 | " | " | " | 0.20 | =21.439+4.031 " | 0.90 | 0.57 |
| 9 | PIKEM | " | " | " | =22.554+3.040 " | 6.59 | 41.11 |
| 10 | BST1 | " | " | " | =22.321+3.289 " | 3.58 | 12.6 |

$R_p$ = 1738 km, $\rho$ = 2.9 g/cm$^3$, g = 162 cm/sec$^2$, $R_m = 11R_o$

SCALING LAW

CROFT, S.K.

Variation in Ejection Angle: Shoemaker (4), in a theoretical calculation, found ejecta to be thrown out at all angles between 90° and 6°. Experimental studies of impacts in sand showed almost all material ejected at ∿45° (2). However, analysis of lunar secondary craters (5) and ejecta "curtains" of larger explosions (6) indicate that, indeed, larger impacts eject material at angles similar to those in Shoemaker's model. The "standard" value of $\beta = 0.35$ approximates Shoemaker's angular distribution, while models 2 and 3 investigate large variations in $\beta$. Models 4 and 5 look at the extreme cases of all material being ejected at 45° (minimum energy) and 6°, respectively. The ratios given in the last column of Table I show that even extreme variations in ejection angle yield at most an uncertainty factor of 2x in the scaling law.

Variation in Ejecta Blanket Shape: The standard value of $\alpha = 0.20$ gives an ejecta blanket roughly equivalent to one described by McGetchin et al's (7) power law with the exponent = -3. With $\alpha = 0.05$, virtually all the ejecta is within one crater radius of the rim, while $\alpha = 0.05$ places about half the ejecta beyond one crater radius. Again, the variation in $A_e$ is seen from Table I to be ≲2x.

Variation in Depth ($h_s$)-Diameter (D) Relations: PIKEF is the extrapolation of Pike's (8) small (≲17 km), fresh crater $h_s$-D relation and represents the probable upper limit to large crater depths. PIKEM is the presently observed $h_s$-D relation of large fresh craters (9), after initial modification and isostatic adjustment, thus representing the lower limit. The ratios of model 1 to model 9 show the $h_s$-D relation to be the dominant factor in $A_e$ by orders of magnitude. A first "best guess" (BST1) of the original $h_s$-D law was found by a least squares fit to 3 points, the best values of the mean ejected volumes of 1) Mare Imbrium and 2) Mare Orientale (10), and 3) the intersection of the Diameter-Volume relations of PIKEF and PIKEM. BST1 was found to be $h_s(\text{km}) = 0.477\ D(\text{km})^{0.532}$.

Variation in Geometry: All models except #8 assumed the spherical surface ballistic equations using the radius ($R_p$) of the moon. Model 8 used the flat surface ($R_p = \infty$) equations. A series of models was run with planetary radii between 1000 and 7000 km. $A_e$ was found to decrease asymptotically towards the flat surface limit, while B increased asymptotically. The limits changed with the $h_s$-D relation used, but the form and magnitude of the variation of $A_e$ and B are approximately independent.

Final Scaling Relation: In the crater diameter range 50 km ≤ D ≤ 1000 km, energy is partitioned into heat (∿30-35%), deformation (10-20%) and ejection (∿50%), using model #10 and relations given in (1). Therefore, the new proposed scaling relation is

$$E_{TOT} \cong 2\rho g \log_{10}^{-1}\left[19.243+\frac{87.43}{R_p^{0.718}}\right] D^{\left[3.518-\frac{59.00}{R_p^{0.742}}\right]} \qquad (4)$$

where E, $\rho$ and g are in cgs units, D and $R_p$ in km. It will be noted from Table I and equation (4) that the power of the scaling law depends strongly on the $h_s$-D relation chosen, and weakly on planetary radius. The usual

SCALING LAW

CROFT, S.K.

1/3.4 (11) scaling for the earth drops naturally out of the model, but this scaling cannot be directly applied to other planets. Also, eq. 4 does not apply to small ($D \lesssim 5$ km) craters where deformation energy becomes important. Finally, based on the variations in Table I, eq. 4 is estimated to be accurate to at least a factor of 10x in the total energy.

References

(1) Gault, D.E., J.E. Guest, J.B. Murray, D. Dzurisin, and M.C. Malin (1975), J.G.R. 80, 2444-2460.
(2) Stöffler, D., D.E. Gault, J. Wedekind, and G. Polkowski (1975), J.G.R. 80, 4062-4077.
(3) Shoemaker, E.M. (1960), Inc. Geol. Cong., XXI SESSION, 18, 418-434.
(4) Shoemaker, E.M. (1962), Interpretation of Lunar Craters, in Zdenek Kopal, ed., Physics and Astronomy of the Moon, 538 pp., Academic, New York.
(5) Oberbeck, V.R. and R.H. Morrison (1974), The Moon 9, 415-455.
(6) Oberbeck, V.R. (1975), Rev. Geophys. Sp. Phys. 13, 337-362.
(7) McGetchin, T.R., M. Settle, and J.W. Head (1973), Earth Plan. Sci. Lett. 20, 226-236.
(8) Pike, R.J. (1974), Geophys. Res. Lett. 1, 291-294.
(9) Pike, R.J. (1972), XXIV I.G.C. 15, 41-47.
(10) Head, J.W., M. Settle, and R.S. Stein (1975), Proc. Lun. Sci. Conf. 6th, 2805-2829.
(11) Nordyke, M.D. (1962), J.G.R. 67, 1965-1974.

MECHANISMS AND MODELS OF CRATERING IN EARTH MEDIA, D. R. Curran, D. A. Shockey and L. Seaman, Stanford Research Institute, Menlo Park, CA., 94025

Introduction The formation of craters and ejecta in geologic materials by impact or explosive detonation can occur by a wide variety of mechanisms. Viscous or plastic flow and compaction are usual mechanisms in soils, brittle fracture and comminution are the principle mechanisms in hard rock, and shear banding and subsequent failure is a primary mechanism in many metals. In any given material cratering probably occurs by the simultaneous operation of a combination of mechanisms. Progress in understanding and modeling these mechanisms is reflected by the success of our attempts to compute cratering behavior. In this paper, we review recent computational modeling work and attempt to assess our present level of understanding for cratering by fracture and comminution.

Fracture behavior in brittle materials like hard rock is strongly dependent on the load duration. This dependence is a result of the fact that fracture is a dynamic process during which inherent flaws in the material are activated, grow, and finally coalesce to cause full separation or fragmentation. For each material there is thus a characteristic time for fracture and comminution that is associated with the fracture kinetics. If the load duration is long compared to this time, the fracture will be, by comparison, instantaneous, and static fracture mechanics concepts will apply. On the other hand, in impact or explosive cratering the load duration is of the same order as the fracture time, and the fracture kinetics must be accurately modeled if the fracture and associated cratering behavior are to be successfully predicted.

During the past several years much work has been done to model the fracture kinetics, i.e., the processes of flaw activation, growth, and coalescence.[1-3] This paper gives a description of the approach used at SRI to measure dynamic fracture properties and to predict damage caused by dynamic loads. Recent results are cited for correlation of predictions and observations of time-dependent fracture and cratering on a laboratory scale for fine-grained polycrystalline quartzite, and on a larger scale in basalt.

Material properties governing dynamic fracture and fragmentation behavior, and rate equations describing the damage mechanisms are deduced from plate impact experiments. Craters in hard rock are produced by the ejection of fragments which form by the activation, growth and coalescence of inherent flaws under an applied dynamic stress. Thus the inherent flaw size distribution of the rock of interest, the activation stress (fracture toughness) and the kinetics of crack growth and coalescence are the important quantities to determine.

# MODELS OF CRATERING

Curran D. R., et al.

We determined the inherent flaw size distribution in a fine grained quartzite rock by counting and measuring flaw profiles on polished sections and using a statistical transformation to convert these surface data to volume data. Flaw activation, growth and coalescence behavior was measured in plate impact experiments. Short, rectangular tensile stress pulses of closely controlled amplitude and duration were produced in plate specimens by accelerating a flyer plate uniformly and simultaneously against the specimen with a gas gun. The stress histories experienced by specimens impacted at different velocities with plates of different thicknesses were either measured or calculated.

Shock loaded specimens were recovered and sectioned to examine the damage. Size distributions of the shock-induced cracks were determined in the manner used to determine the inherent flaw size distribution. Higher amplitude, longer duration pulses were used to cause fragmentation; fragment size distributions were determined by sieve analyses. Correlation of the shock-induced damage with stress histories for a number of specimens resulted in substantiation of the applicability of the crack nucleation and growth NAG laws established previously for other materials, and phenomenological laws for coalescence and fragmentation, FRAG.

Dynamic Fracture Computational Model The SRI NAG/FRAG model for dynamic fracture and fragmentation is written as a constitutive relation subroutine for one and two space dimensional Lagrangian wave propagation codes. Since it is a continuum model, it assigns to each material point a crack size and orientation number distribution, i.e., after each time step the current number of activated flaws per unit volume is computed for each size and orientation increment. Thus, individual flaws or cracks are not handled. Instead, the average flaw and crack behavior is described, much as dislocation dynamics theories treat average dislocation behavior.

When, on the average, the cracks have grown to the point where their stress concentration fields intersect, the NAG model computationally constructs fragments from the intersecting cracks. The results of a computation are thus presented as crack and fragment size distribution functions that can be compared with experimental results.

Fracture and Cratering Experiments, and Comparison with Predictions for Laboratory and Large Scale Experiments Reference 4 describes experiments in which quartzite samples were fractured and fragmented by impacting steel rods and in-contact explosive. Crater dimensions, subcrater fracture damage, and ejecta size, velocity and angle distributions were measured and compared with calculated results. The good agreement we obtained was taken as an indication that the basic physical model of cratering by flaw activation, growth and coalescence is correct for this material, and encouraged us to apply the model to a large scale cratering event.

MODELS OF CRATERING

Curran D. R., et al.

We chose to simulate the Pre-Schooner Delta event,[5] which consisted of 20 tons of liquid nitromethane buried in dry vesicular basalt 14 meters below the surface. The porosity and mechanical properties of the basalt varied strongly with depth; however, the rock was treated as a homogeneous medium with average properties. The inherent flaw size distribution was inferred from the measured block size distributions, and a simple crack growth law was assumed. Comparisons between computed and measured results were made where possible, and again good agreement was obtained.

Summary and Conclusions We conclude from these results that the activation, growth, and coalescence of inherent flaws appear to be the dominant mechanisms for cratering in competent rock. The role of shear cracking or banding as opposed to tensile cracking is not yet understood. However, the agreement obtained here suggests that tensile cracking is more important in competent rock because of the typically low tensile strengths.

For such brittle materials, there appears to be a tendency to produce shallow craters with a large region of subcrater damage. Furthermore, there is a tendency to produce a raised portion in the center of the crater floor. This is not due to "uplift," but to tensile stress wave interactions that produce the maximum fracture activity in a annular region surrounding the impact (or explosive-loading) point.

We conclude in general that computational modeling of such local processes as flaw activity, pore compaction, and plastic flow is a basic requirement for understanding the cratering event.

1. T. W. Barbee, et al., "Dynamic Fracture Criteria for Ductile and Brittle Metals," Journal of Materials, JMLSA, 7, 393-401 (1972).

2. D. A. Shockey, C. F. Petersen, D. R. Curran, and J. T. Rosenberg, "Failure of Rocks Under High Rate Tensile Loads," in New Horizons in Rock Mechanics, Proceedings of the 14th Symposium on Rock Mechanics, H. R. Hardy, Jr., and R. Stefanko, Eds., (American Society of Civil Engineers, New York, 1973).

3. D. A. Shockey, D. R. Curran, L. Seaman, J. T. Rosenberg, and C. F. Petersen, "Fragmentation of Rock Under Dynamic Loads," Int. J. Rock Mech. Sci. Geomech. Abstr., 11, 303-317 (1974).

4. D. A. Shockey, D. R. Curran, M. Austin, and L. Seaman, "Development of a Capability for Predicting Cratering and Fragmentation Behavior in Rock," Final Report for Defense Nuclear Agency, 3730F (May 1975).

5. R. J. Lutton, F. E. Girucky, and R. W. Hunt, "Project Pre-Schooner Geologic and Engineering Properties Investigations," PNE-505F, Nuclear Cratering Group, U.S. Army Engineer Waterways Experiment Station, Vicksburg, Miss. (April 1967).

TERRESTRIAL IMPACT STRUCTURES: PRINCIPAL CHARACTERISTICS AND ENERGY CONSIDERATIONS. M.R. Dence, R.A.F. Grieve and P.B. Robertson, Earth Physics Branch, Department of Energy, Mines and Resources, Ottawa, Canada, K1A 0Y3.

The world census of craters, crater groups and other approximately circular structures which are attributed to hypervelocity impact of extra-terrestrial bodies stands at about 80 (1,2,3). They are so classified on a number of criteria (1), of which the presence of meteoritic fragments or of shock metamorphism of rocks within or around the structure are considered definitive. At least 50 additional structures appear to conform to other, less definitive criteria.

All well-investigated craters up to 3.5 km diameter have simple bowl form (4). Barringer Meteor crater (1.2 km) remains the largest with identified meteorite fragments and the largest simple crater formed in sedimentary rocks. Lonar L. (1.8 km) and Brent (3.5 km) are the largest simple craters in basaltic and granitic rocks respectively. Larger structures are complex (1,4) and have shallower relative dimensions. In general those up to approximately 30 km across have distinct central uplifts (Steinheim, 3.6 km; Deep Bay, 9 km; Gosses Bluff, 24 km); some formed in heterogeneous, layered rocks (Ries, 24 km) and all more than 30 km across are ring structures with alternating topographically high and low features (Clearwater Lake West, 35 km; Charlevoix, 55 km; Manicouagan, 75 km; Popigai, 100 km). The floors of the larger structures are largely covered by thick sheets of impact melted rock (5).

Extensive drilling at Brent Crater has shown it to be a sediment-filled depression underlain by a bowl of breccia 610 m thick. At the base of the breccias is a 35 m thick lens of inclusion-bearing igneous-textured rock with a significant Ni anomaly, interpreted as the limit of penetration of meteorite-contaminated, impact-melted country rock (6). The 2.5 $km^3$ of overlying breccia are considered to have slumped from the crater walls immediately after excavation of the transient cavity. Replacing this material the transient cavity is found to conform closely to a parabola in which $r^2 = 2p^2$ where p = depth of the transient cavity below the original plane, and r is the radius of the transient cavity at the original plane. With the original plane taken as 50 m above nearby heights of land, p is approximately 1.05 km. Immediately below this depth the shock pressures registered are estimated to have been $20 \pm 3$ GPa ($200 \pm 30$ kbar) (7). Taking pressure decay in the overlying excavated rock as approximately $r^{1}/_{3}$ yields a minimum $5 \times 10^{14} cm^3$ of target material (14% of transient cavity volume) as having been above 60 GPa, and hence shock melted. Of this approximately 10% remains within the crater, mainly as glassy fragments (5).

Considering the case of an iron meteorite (density 7.8 g $cm^{-3}$) striking granitic rock (density 2.67 g $cm^{-3}$) at 15 km $s^{-1}$, and taking the values of $1.2 \times 10^{10}$ ergs $g^{-1}$ for internal energy of melting and 23% for the proportion of total kinetic energy portioned into heating target material (8), a kinetic energy of impact is obtained of $6.5 \times 10^{25}$ ergs. This corresponds to a meteorite radius of 120 m, approximately 6% of the radius of the final apparent

crater. This energy is considerably higher than previous estimates (9) and corresponds closely to the crater diameter scaling from the Teapot Ess nuclear explosion crater as kinetic energy $(KE)^{1}/_{4}$ rather than $KE^{1}/_{3}$ or $KE^{1}/_{3.4}$ (10,11).

For larger structures additional complications are introduced by central uplift and downdrop of rim structures. There is considerable variation in structural detail with target rock materials, but the general progression, best exemplified by craters formed in crystalline rocks, appears to conform to the morphologies of lunar and mercurian craters and basins, scaled approximately as gravitational acceleration $(g)^{-1}/_{4}$ (10).

The less rapid attenuation of shock pressures (7) and the greater volumes of impact melt (12) in the larger structures relative to simple craters appear to be in keeping with the fourth root energy scaling relationship. This implies that for terrestrial craters with apparent diameters of approximately 100 km or more the volume of melt generated exceeds the total volume excavated. This transition may correlate with the morphologic change from ring structures with central peaks (Manicouagan) to those in which the central region, although uplifted, remains a depression (Popigai).

References

(1) Dence, M.R. (1972) Proc. 24th Inter. Geol. Congress, Sect. 15, p. 77-89.
(2) Robertson, P.B. and Grieve, R.A.F. (1975) J. Roy. Astron. Soc. Canada, 69, p. 1-21.
(3) Masaitis, V.L. (1974) Meteoritika, 33, p. 64-68.
(4) Dence, M.R. (1968) In "Shock Metamorphism of Natural Materials", French, B.M. and Short, N.M. (eds) p. 169-184. Mono Book Corp., Baltimore.
(5) Dence, M.R. (1971) J. Geophys. Res., 76, p. 5552-5565.
(6) Dence, M.R. and Guy-Bray, J.V. (1972) Guidebook excursion A65, 24th Inter. Geol. Congress.
(7) Robertson, P.B. and Grieve, R.A.F. (1976) this volume.
(8) Gault, D.E. and Heitowit, E.D. (1963) Proc. 6th Hypervelocity Impact Sym., 2, p. 419-456, Cleveland.
(9) Innes, M.J.S. (1961) J. Geophys. Res., 66, p. 2225-2239.
(10) Gault, D.E. et al. (1975) J. Geophys. Res., 80, p. 2444-2460.
(11) O'Keefe, J.D. and Ahrens, T.J. (1975) Proc. Lunar Sci. Conf. 6th, p. 2831-2844.
(12) Grieve, R.A.F. et al. (1976) this volume.

MANICOUAGAN AND POPIGAY STRUCTURES: COMPARATIVE MORPHOLOGY AND SPATIAL DISTRIBUTION OF IMPACT MELT ROCKS. R. J. Floran, NASA Johnson Space Center, Houston, TX 77058

The 65 km-diameter Manicouagan ring-structure of central Quebec (51°30'N, 68°30'W) and the 100 km-diameter Popigay basin of northern Siberia (71°30'N, 111°30'W) are two of the largest well-preserved and least tectonically deformed impact structures on Earth. They are complementary in that each contains ejecta deposits which are no longer present or readily accessible at the other structure and each is exposed at a substantially different level of erosion. Although imperfectly known, the three-dimensional structural-stratigraphic relations at Manicouagan and Popigay can be used to model the formation of multiringed basins on the terrestrial planets.

This paper draws on several recent Russian publications (1-4) which present detailed descriptions of the morphological characteristics and impact deposits of the Popigay basin. These studies represent the first in-depth analysis of a relatively fresh terrestrial impact structure substantially larger than the Ries basin.

Prior to erosion the Triassic-age Manicouagan structure was either a triple-ringed basin, a double-ringed basin or a double-ringed basin transitional to a crater with a central uplift (5). Choosing from among these alternatives depends on whether an outer circumferential depression, ∿150 km in diameter, represents the base of a former ring-structure and whether a massif near the geometric center is a remnant of an uplift that protruded above the basin floor. Assuming similar rock properties and gravitational scaling, Manicouagan should be a structural analog of 400-500 km double-ringed basins on the moon such as the Moscoviense basin (5). A problem in reconstructing the preerosional morphology of Manicouagan is the large uncertainty associated with the radius of the transient cavity rim, estimated at 19±4 km. The probable location of the subsided outer slope of the transient cavity is marked by a 5-10 km wide peripheral trough at a distance of 30-35 km from the center of the structure. Exposures of deformed Lower Paleozoic limestone and shale within the trough suggest that a thin sedimentary veneer, probably less than 100 m thick, overlay the crystalline basement at the time of impact. Their structural position further suggests that downward, inward slumping of the rim took place during the post-cratering modification stage. Moderate to deep erosion at Manicouagan has considerably modified the original basin morphology. A thick surficial layer of ejecta has been stripped away, exposing a 100-200 m thick sheet of clast-laden melt rocks that lie directly on fractured Precambrian basement.

The ambiguities associated with Manicouagan are less severe at Popigay where detailed field mapping combined with geophysical studies reveal a complex basin morphology that is somewhat similar to the Ries basin (1-3; Fig. 1). Responsible for the complexity is the heterogeneity of the target material which consists primarily of Archean crystalline rocks ($\rho$ = 2.8 - 2.9 g/cm$^3$) overlain by northward dipping terriginous and carbonate formations of Proterozoic,Cambrian and Permian age ($\rho$ = 2.2 - 2.7 g/cm$^3$). Minor erosion, sedimentation and tilting in Pliocene-Quaternary time, shortly after the impact, led to uplift and exposure of the SW and W sectors and partial burial of the structure in the NE and E sectors. The basin consists of an inner

Manicouagan and Popigay Structures

R. J. Floran

"crater" in crystalline basement (D = 72 km) and a discontinuous outer "crater" (D = 100 km) confined to the 1 km thick sedimentary cover. The outer crater is characterized by the presence of concentric thrust faults which dip toward the center of the structure at various angles. The multilayered nature of the target is responsible for the disappearance of the outer crater in the north and southwest. Variations in the strength of the substrate have produced concentric craters in the laboratory (6) and have undoubtedly influenced final crater geometry at Popigay.

Within the inner crater lie sinuous and arcuate ridges composed of clast-laden melt rocks (tagamites). These form discontinuous sheets 10's of meters thick overlying fragmental breccias and suevite; they also occur as dikes, necks and irregular bodies within the other impact deposits. The arcuate ridges, which have been termed pseudovolcanic structures because of their resemblance to volcanic flows, are thought to be the surface expression of basement ring-structures (1). Fragmental breccias, suevites and rarely, tagamites form tongues that extend outward into the outer crater. Similar deposits interpreted as impact melts have been described in and around lunar craters (7). Deposits equivalent to tagamite are present at several localities within the Ries basin (8; Hörz, p.c.) but are extremely rare. In contrast, the distribution of suevite and fragmental breccias at Popigay is very similar to that at the Ries (1).

A continuous melt layer is not exposed within the Popigay basin, as at Manicouagan, but is likely to be present at shallow depth. Petrographically, the tagamites resemble melt rocks from the basal melt unit at Manicouagan. Thus within fresh, large impact structures very fine-grained, clast-rich melt rocks overlie a topographically irregular basement at depth and at the surface. Between local elevations of basement or buried ring-structures, thick accumulations of clast-poor melt led to crystallization of coarser-grained, igneous-textured rocks such as the micromonzonite that forms the upper melt unit at Manicouagan (9).

It is interesting to note that the ring-structures within the Popigay basin appear to have approximately $\sqrt{2}$ spacing (Table 1). However, evidence for the existence of the innermost ring is weak, being based entirely on arc-shaped tagamite ridges on the surface. The second ring is well-defined by a circular positive gravity anomaly and discontinuous surface outcroppings of brecciated gneisses (Fig. 1). These data suggest that the second, most prominent ring is the likely location of the transient cavity rim. The inner and outer "craters" are also ring-structures, representing the collapsed margin of the transient cavity in crystalline and sedimentary rocks respectively.

The continuous ejecta deposits at Popigay rarely extend beyond the outer crater rim. Although modified by erosion, this restricted distribution appears to be responsible in large part for the subdued topography of the Popigay basin and burial of ring-structures. As shown by Gault et al. (10),the radial extent of continuous deposits for a given rim diameter decreases systematically in accordance with increases in gravity among the terrestrial planets. Atmospheric drag will further reduce the width of ejecta deposits on Earth. Thus rim and fallback ejecta should be several times thicker at Popigay than at similar-sized lunar craters. Supportive evidence is provided by observations at the Ries basin and Meteor Crater (10) which have narrow ejecta blankets compared

# Manicouagan and Popigay Structures

R. J. Floran

with lunar and Mercurian counterparts. Because of their low surface relief, ancient "multiringed" terrestrial basins may have been relatively featureless, with only slight outward resemblance to lunar basins.

The depth of erosion at Manicouagan precludes a rigorous morphological comparison with Popigay. It is instructive to note, however, that the pre-erosional diameter of the two structures in crystalline basement rocks is nearly identical (Table 1). Although the position of the transient cavity at Manicouagan is uncertain, field mapping has revealed the presence of 50-150 m high basement blocks in two areas 13 and 16 km from the center of the structure which lie at stratigraphic levels normally occupied by the melt sheet. Whether these are analogous to the innermost ring(?) at Popigay or whether they represent local "ripples" formed in the basement is uncertain and can only be resolved by further field studies.

Although morphological comparisons have been made between the eroded Manicouagan structure and relatively fresh lunar basins (11) a more appropriate comparison is possible with the Popigay structure, which at 100 km in diameter, should be a better morphological analog of lunar basins ≥600 km across such as the Orientale basin. In this comparison, the hypothetical innermost ring at Popigay would be analogous to the subdued, 320 km ring at Orientale and the prominent second ring, representing the transient cavity rim, would be equivalent to the Inner Rook Mountains (Table 1). The inner and outer craters at Popigay would thus correspond to the Outer Rook and Cordillera Mountains respectively. If correct, this implies that the Orientale basin has a crater-within-crater morphology in which the outer "crater" is developed primarily in the less dense, surface fragmental layer.

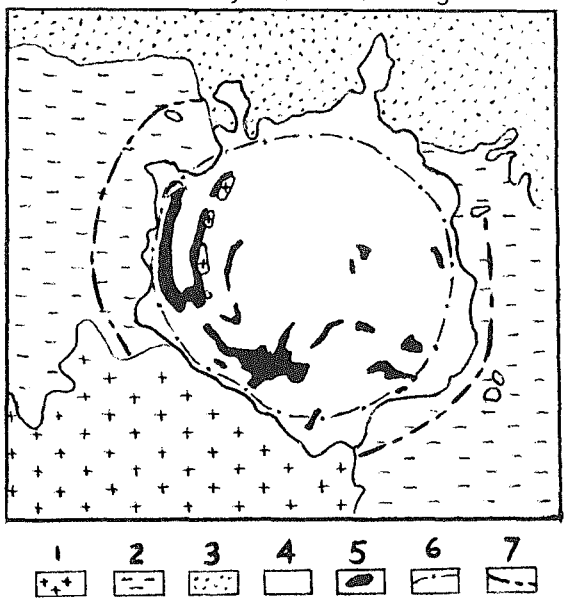


Figure 1: Structure of the Popigay basin (modified from Masaytis et al., 1971).

1. Archean rocks
2. Proterozoic and Cambrian rocks
3. Upper Paleozoic rocks
4. Fragmental breccias and suevites
5. Tagamites
6. Inner crater within Archean rocks
7. Outer crater within Proterozoic and Cambrian rocks

Table 1: Concentric Rings (in km) and Ring-Spacing of Manicouagan, Popigay and Orientale Basins

| Manicouagan | | Popigay | | Orientale | |
|---|---|---|---|---|---|
| | | 327 | } 1.5 | 320 | } 1.5 |
| 30 - 45 | } ~2 | 45 - 52 | } 1.5 | 480 | } 1.3 |
| 75 | } ~2 | 72 | } 1.4 | 620 | } 1.45 |
| 145 - 160 | | 100 | | 900 | |

References:
(1) Masaytis V. L., Mikhaylov M. V. and Selivanovskaya T. V. (1975) "Nauka Press", Moscow, NASA TT F 16,900.
(2) Masaytis V. L., Mikhaylov M. V. and Selivanovskaya T. V. (1972) Meteoritics, 7, 29-46.
(3) Masaytis V. L., Mikhaylov M. V. and Selivanovskaya T. V. (1971) Internat. Geology Rev., 14, 327-331.
(4) Polyakov M. M. and Trukhaiev A. I. (1974) Internat. Geology Rev., 17, 1027-1034.
(5) Floran R. J. and Dence M. R. (1976) Proc. 7th LSC (in press).
(6) Quaide W. L. and Oberbeck V. R. (1968) J. Geophy. Res. 73, 5247-5270.
(7) Howard K. A. and Wilshire H. G. (1975) Jour. Res. U.S.G.S. 3, 237-251.
(8) Dennis J. G. (1971) Jour. Geophys. Res. 76, 5394-5406.
(9) Floran R. J., Simonds C. H., Grieve R. A. F., Phinney W. C., Warner J. L., Rhodes M. J., Jahn B. M. and Dence M. R. (1976) Geophy. Res. Lett. 3, 49-52.
(10) Gault D. E., Guest J. E., Murray J. B., Dzurisin D. and Malin M. C. (1975) Jour. Geophy. Res. 80, 2444-2460.
(11) Floran R. J. (1976) LS VII, 260-262.

# THE FIRST TEKTITE DEPOSITS IN A METEORITIC CRATER (ZHAMANSHIN NORTH ARAL REGION, USSR)

P.V. FLORENSKY

Geological Institute of the USSR Academy of Sciences

The Zhamanshin region (P.V. Florensky, 1975) is surrounded by discountinous rim 10 to 15 km in diameter, composed of loose and brecciated rocks. The central part of the area (5 km in diameter) is filled with loess of unknown thickness (Fig.1)

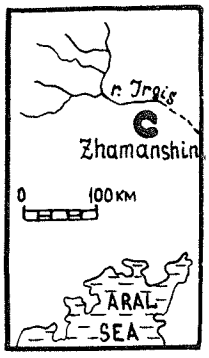


Fig.1
Map of North Aral Region.

With the breccias and directly on the rock glassy scoria-like rocks occur. They are considered to be impectites and bear the name of ZHAMANSHINITES. They are composed of block, up to 1 m in size and form a "flow" or "lake" 3 to 5 m x 10 to 15 m in area and 1 to 2 m thick. The underlying Paleogene greenish clays are red near the contact, with occasional whitish, pumice-like blocks. Near the outcrops of a thick quartz vein some fragments, up to 0,5 m in size, of a very porous and light material were found. The refraction index of 1.460 identifies the material as lechatelierite.

In the south-eastern part of the region drops, balls, "sprays", "braids" etc. of glass were found. Their shape is evidence of the manner of solidification. Their dimensions are from 2 mm to 3 cm. From their

# THE TEKTITES IN A METEORITIC CRATER ZHAMANSHIN, USSR

P.V. FLORENSKY

areal density their nummers in the region can be estimated to be $10^7$ to $10^8$ and the total weight several tens of tons. These objects have composition and structure similar to the known tektites of the Zhamanshin region called IRGIZITES, as they are found in the Irgiz river basin.

In the Zhamanshin region a varieties of rocks are found, transitional in composition and structure from sedimentary and metamorphic to impactites-zhamanshinites, and also to tektites-irgizites. This is evidence that not only zhamanshi-

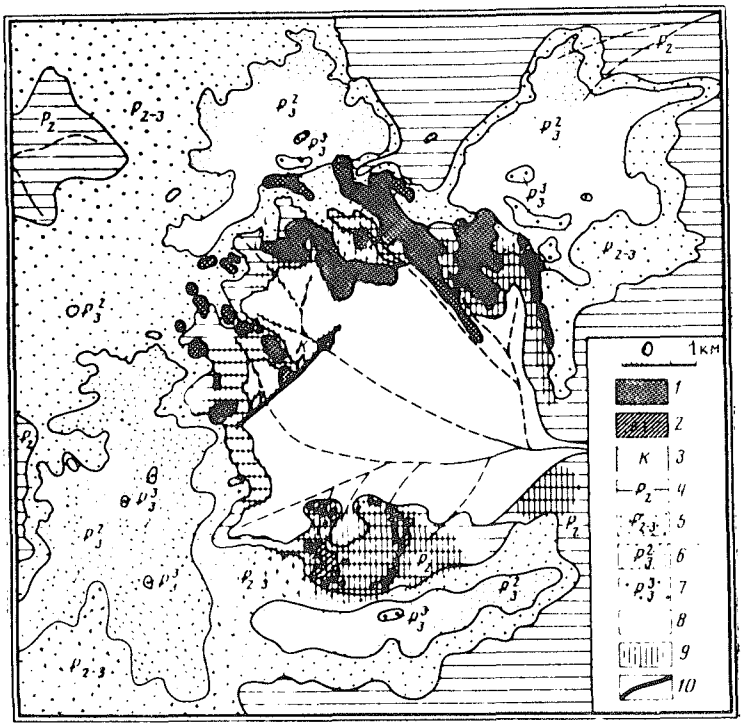


Fig. 2. Geological scheme of the Zhamanshin region. I,2 - allogene breccias containing fragments of several Paleozoic rocks of the basement among loose Meso-Cenozoic rocks; 3 - Cretaceous; 4 - Eocene; 5 - Upper Eocene; 6 - Middle Oligocene; 7 - Upper Oligocene; 8 - Quaternary loesses; 9 - distribution of zhamanshinites and irgizites fragments; IO - faults.

# THE TEKTITES IN A METEORITIC CRATER ZHAMANSHIN, USSR

P.V. FLORENSKY

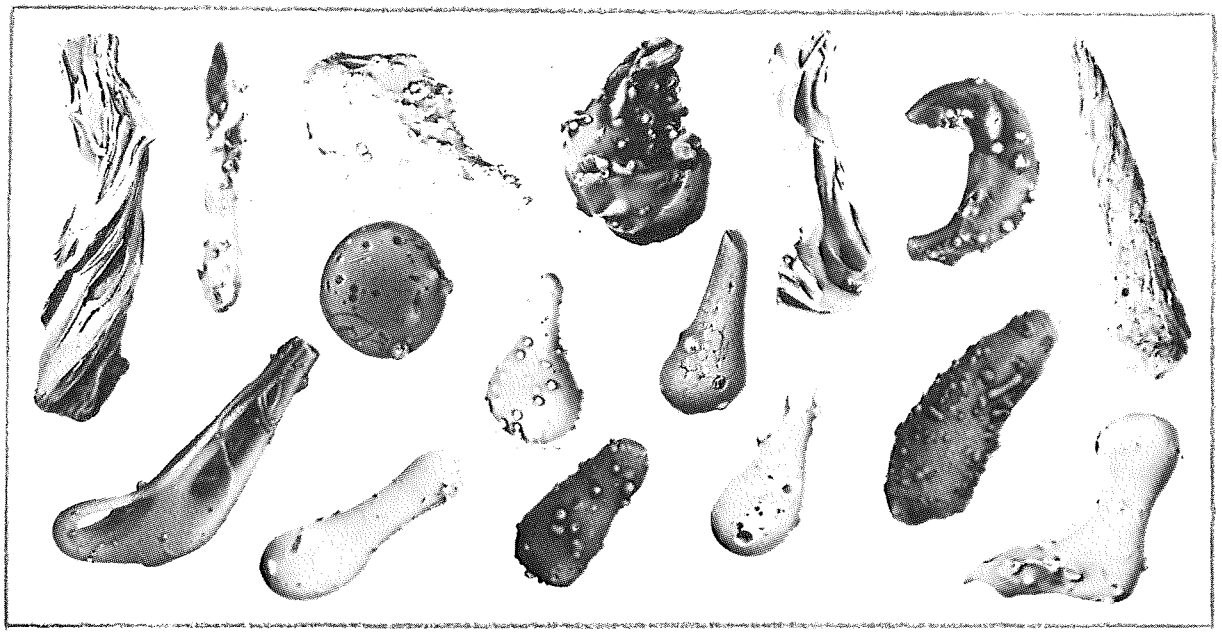

Fig. 3. Tektites-irgizites. Magnification - I,5 to 2.

nites, but also tektites-irgizites were melted during the explosion accompanying the fall of the meteorite. Tektites-irgizites are likely to result from the melting of mostly surface rocks, and their high-temperature degassing produced losses of not only $H_2O$, but also K, Na, as well as compounds that are volatile at high temperatures. Because they solidified in flight, irgizites display the characteristic shape.

To conclusion, the Zhamanshin ring structure contain shock breccias, lechatelierites, impaktites-zhamanshinites and related tektites-irgizites. The co-occurence of these materials shows their common origin during the explosion of the meteorite.

## Bibliography

P. V. Florensky. Meteoritic crater Zhamanshin (North Prearalie) and its tektites and impaktites. Izv. Akad. Nauk SSSR, ser. geolog. No.IO, I975 (in Russian).

SCALING OF CRATERING EXPERIMENTS-AN ANALYTICAL AND HEURISTIC APPROACH TO THE PHENOMENOLOGY, B. K. Germain and L. S. Germain, University of California, Lawrence Livermore Laboratory, Livermore, CA 94550.

During about the last 15 years, a wide variety of scaling criteria for cratering phenomena have been developed and compared with the available experimental data. Most of these criteria attempt to consider the effects of gravity. The approaches vary widely, and some of them indicate agreement with a limited range of experimental data obtained on earth, i.e. gravity has not been significantly varied. Some more recent attempts to obtain experimental results, with different values of gravity and to develop scaling criteria, are currently underway in this country and others.

The approach used in this paper is to start from first principals and to examine the conservation equations of continuum mechanics with rock mechanics added. From these equations, a set of necessary conditions for performing scaled experiments in rock is derived. It is shown that performing scaled experiments in two different materials is virtually impossible because of the scaling restrictions imposed by two equations of state for rock. However, performing dynamically scaled experiments in the same material is possible if: (1) time and distance use the same scaling factor, and (2) the effects of gravity are insignificant. When gravity becomes significant, scaling is no longer directly possible. To illustrate these results, calculational examples are presented.

Work performed under the auspices of the U.S. Energy Research & Development Administration under contract No. W-7405-Eng-48.

Cratering phenomenology can be thought of as consisting of two phases. The first phase consists of the dynamics of the energy source, explosive or impact. In this first phase, the source dynamically imparts its energy to the surrounding rock. During this phase, the effects of gravity are negligible; and as illustrated in this paper, this phase is "scalable" when time and distance use the same scaling factor. Gravity generally remains negligible until a velocity field has been developed in the surrounding rock. The second phase of cratering phenomenology consists of the rock with its already developed velocity field being "thrown out". It is governed by the ballistics equation, and gravity is of primary importance. This second phase of cratering phenomenology is examined heuristically in this paper by examples which use the ballistics equation applied to various cratering situations. Both differences in gravity and the regional extent of the initial velocity field are examined. This heuristic examination of the "throw out" or ballistics phase of cratering illustrates the basic phenomena in crater formation.

The range of a projectile scales inversely with respect to gravity. However, the initial extent of the velocity field is determined in the first phase of the cratering phenomena where gravity is negligible but distance and time are required to have the same scaling factor. Thus, the final distribution of projectiles (i.e. the final crater size) does not scale.

PROJECTILE IMPACT CRATERING OF ROCKS, by W. Goldsmith, M. Kabo, and J. L. Sackman, Coll. of Engineering, Univ. of California, Berkeley 94720

An experimental investigation of the cratering characteristics under normal projectile impact was conducted on two rocks, a hard diorite and a soft green shale, secured from the Wilson Canyon area of the Naval Weapons Center, China Lake, and from an open pit mine at Boron, Cal., respectively. Solid disks of both rocks with diameters of 140 mm and thicknesses ranging from 38 to 226 mm were struck by pneumatically or explosively propelled 6.35-mm diameter spheres traveling at initial velocities between 50 and 2800 m/s; some of the shale specimens were supported at the rear by steel plates to minimize splitting. Another type of diorite sample, specifically designed to measure the energy of elastic waves produced therein by the collision, consisted of a reusable 140-mm diameter core with a central disk sectioned in two halves and subsequently reglued to accommodate three radial strain gages and two tangential gages on the axis of symmetry; this central part was sandwiched between a forward and rearward transmission plate. This entire unit, with a thickness of about 52 mm, was prefaced by replaceable test plates of the same diameter that ranged in thickness from 5.2 to 11.0 mm, and was supported at the rear by a massive aluminum back-up cylinder. An additional group of tests were conducted against the vertical green shale walls of the mine using 20 mm rifled and 40 mm rifled and smooth-bore ammunition at impact speeds of 670 to 970 m/s.

The laboratory tests involved the measurement of the initial and rebound striker velocity, the high-speed photographic observation of the ejecta kinematics, the determination of the size and radial and angular distribution of these fragments from samplings of the retrieved material with the aid of an electronic scanner, and volume and depth measurement of the crater produced. The initial employment of a ballistic pendulum to accommodate the samples was subsequently abandoned when the energy absorbed by this device was found to be a negligible fraction of the initial kinetic energy. The crack patterns produced in the composite diorite speciments were ascertained along the central section with the aid of a dye penetrant. Certain approximations were adopted in order to estimate the magnitude of the new surface area generated by the impact from these data.

In all field tests, the depth and shape of the hole generated in the cliff were measured; the latter consisted of a deep cylindrical stem beyond a much larger diameter shallow surface dish. In some of the tests, the surface area below the cliff was cleared and the debris produced by the shot was collected and analyzed. The partial fragment distribution so obtained was not actually faithfully representative of the initial disintegration process as a significant portion was dislodged from areas other than the crater region and a large percentage of the ejecta was not recovered. The average depth of penetration for the 40 mm rifled projectiles at a speed of 884 and 610 m/s, respectively, were found to be 1.3 and 1.14 m, while that of the 40 mm smooth-bore round at the higher velocity amounted to 1.02 m. The observed erratic behavior of the smooth bore projectiles was expected; similar characteristics for the rifled 40 mm ammunition was attributed to variable surface conditions

and the enhanced possibilities of striking discontinuities in the cliff.

For impact speeds of about 200 m/s, the diorite craters exhibited depths from 1.4 to 2 mm, widths ranging from 6.1 to 14.2 mm, and volumes extending from 82 to 147 mm. The penetration depth and crater volume for all laboratory shale tests are shown as a function of projectile momentum in Fig. 1. The

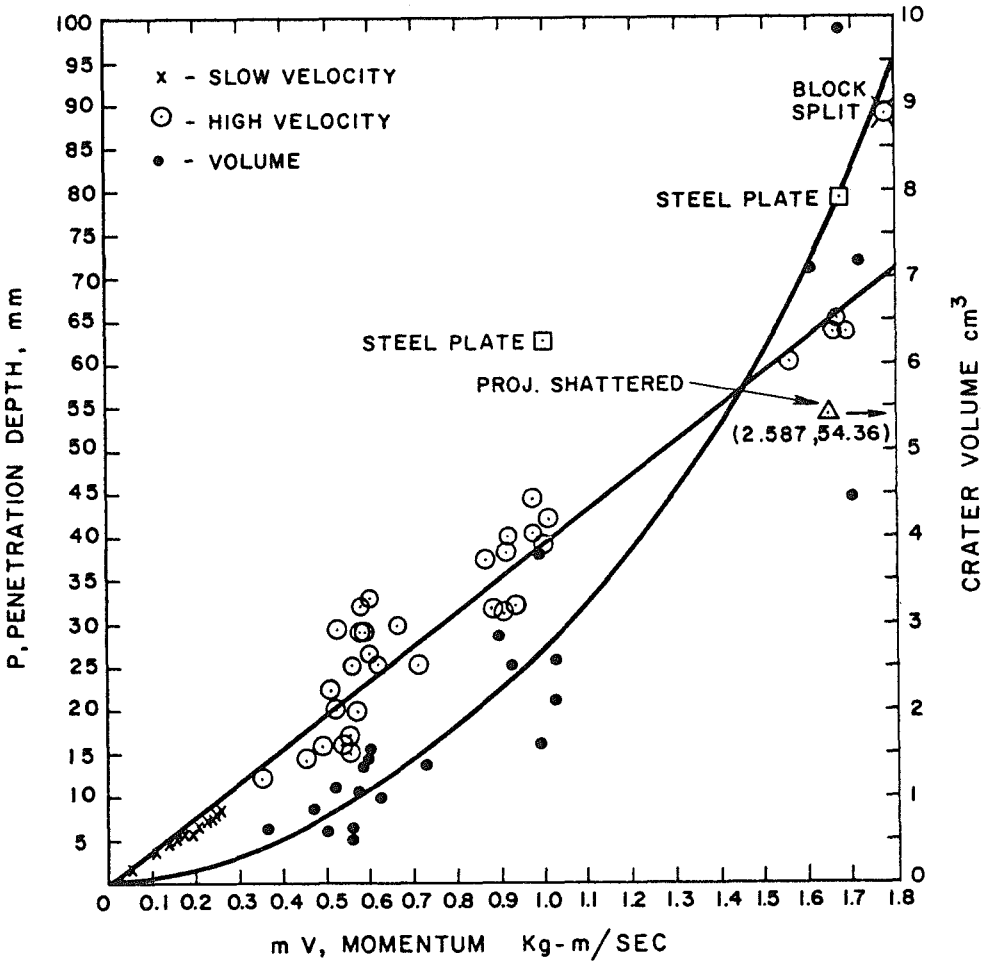


Fig. 1 Penetration Depth and Crater Volume as a Function of Initial Projectile Momentum for all Laboratory Shale Tests

data conforms quite well to the predictions of a simple linearly viscous model, yielding a value of the viscous constant of 25.4 kg/s for a range of impact speeds involving four decades of initial kinetic energy. The diorite ejecta size distribution appeared to follow a logarithmic pattern; higher impact velocities produced smaller mean sizes of the ejecta. The comminution process in the hard rock was substantially completely brittle, while the penetration into shale produced significant plastic deformation and compaction

with insignificant ejecta generation in both laboratory and field tests. The shape of the ejecta cloud was strongly influenced by the hardness of the rock material; for diorite, this was found to be a hollow cone with a kinetic energy about 10 percent of the initial value, while the rodlike emission observed for shale amounted to only 0.1 percent of the initial energy.

The energy of elastic waves in the diorite samples was calculated to be about 10 percent of the original, while the rebound energy of the striker was negligible. No measurable permanent deformation of the projectiles was observed in any of the tests of the present program. By difference, the process of new surface production in this material, generating both ejecta and cracking within the interior of the sample, ranged from 70 to 85 percent of the total input.

The authors would like to express their sincere appreciation to Mr. S. P. Finnegan and others of the Detonation Physics Division, Naval Weapons Center, China Lake, Cal., and to Dr. Danuta Krzyston and Mr. Richard Benson for significant contributions in the conduct of the experiments. The work was sponsored by the Defense Nuclear Agency and the RANN Division of the National Science Foundation.

(1) Goldsmith, W., "Fragmentation Processes in Soft Rock," First Annual Report, Defense Nuclear Agency, Report DNA 3416Z, 1975.

(2) Goldsmith, W., and Sackman, J. L., "Fragmentation Processes in Soft Rock," Final Report, Defense Nuclear Agency, Report DNA 3903F, 1976.

THE GENERATION AND DISTRIBUTION OF IMPACT MELTS:IMPLICATIONS FOR CRATERING PROCESSES, R.A.F. Grieve, M.R. Dence and P.B. Robertson, Earth Physics Branch, Department of Energy, Mines & Resources, Ottawa, K1A 0Y3, CANADA

The principal modes of occurrence of terrestrial impact melts are: as small discrete,glassy bodies in mixed breccia deposits - suevite-type ejecta as at the Ries (1) or within the crater as at Brent (2), and as relatively large coherent, crystalline sheets lining the crater floor such as those at Mistastin, Clearwater and Manicouagan (3). Sizeable quantities of both melt sheet and melt-bearing breccia are observed at some well-preserved structures (3,4).

Within an individual structure, the melt is to a first approximation compositionally homogeneous, with the maximum compositional variation confined to particular individual bodies in the breccias or to the base of the melt sheet (1,4,5). This general property of homogeneity holds even where the target lithologies have highly diverse compositions,e.g. at Manicouagan the silica content of the melt averages $57.3 \pm 2.1$ ($2\sigma$)% compared to a range of 45-75% for the proposed target units (6,7,8). The composition of the melt corresponds to that of the bedrock in a homogeneous target (9) or, in a heterogeneous target, it can be successfully modelled as a mixture of bedrock units (3,5). At large structures, such as Mistastin (present diam. 28km), Manicouagan (75km) and Popigai (100km), the bedrock distribution indicates that some target lithologies were separated by distances of the order of kilometers (4,5,7). Thus the observed composition and homogeneity of the melts require the melting and intimate mixing of large volumes of initially compositionally distinct bedrock units (5,6,8).

A model based on experiment and theory (3,10,11) and consistent with the petro-chemical and field data has been developed for the genesis and subsequent distribution of impact melts in a hypervelocity impact event. Close to the point of impact a relatively small volume of the target is subjected to shock pressures attenuating from several megabars to approximately 600kb and is melted or, in part, vapourized. An acceleration, which is a function of shock pressure, is imparted to this melted volume by the passage of the shock wave giving the melt a particle velocity directed radially away from the point of impact. Thus different portions of the melt, which experience different pressures due to their relative proximity to the point of impact, are accelerated to different initial velocities. It is this differential velocity within the melted volume, as it moves downward into the expanding cavity, that is the principal mechanism for homogenizing the chemical composition. Abnormally low viscosity, resulting from the super-heated nature of the melt (5,6), and minor velocity differences due to variations in the response of individual rock types to a particular shock pressure (12) also contribute to homogenization. During movement melt overwhelms less strongly shocked and therefore slower moving target material, incorporating it as inclusions showing various degrees of

shock metamorphism. The accelerated target materials are deflected outwards and upwards by the interaction of rarefraction waves (13) and some of the melt plus inclusions leaves the expanding cavity to form suevite-type deposits (1). The remainder has insufficient velocity for ejection due to particle velocity attenuation and remains within structure. The bulk of this melt subsequently pools and forms a melt sheet overlying shocked autochthonous rocks of the crater floor (3,5).

Some of the melt ejecta separates from the main body of melt relatively early in the cratering process. In a heterogeneous target such bodies are less completely mixed and may reflect the composition of individual target lithologies (5,14). In the melt sheet divergence from the mean composition is most pronounced in the basal unit. This results from rapid cooling by contact with the relatively cold crater floor, which permits assimilation and partial melting of only the less refractory inclusions (5,8) and leads to compositional variations.

Comparisons between small simple craters (<5km) and larger complex structures suggest that the relative volume and distribution of melt varies with crater size. As simple and complex craters have undergone differing degrees of post-formation modification (3) the data have been normalized to the inferred transient cavity. It has been assumed that all structures initially had a transient cavity with a parabolic cross-section and conforming to the relationship $r^2 = 2p^2$, where r is the radius and p the depth (15). The relevant data and comparisons are given in Table 1. The volume of melt at the simple crater Brent (Table 1) is based on drilling results (13) and is regarded as a realistic estimate of the amount of melt which remained within the transient cavity. Estimates of the melt volumes at the complex structures Mistastin, Clearwater and Manicouagan (Table 1) are derived from the present outcrop distribution of the melt sheet with some allowance for erosion. They are considered to minimum estimates, as no account has been taken of the melt in fall-back breccias, which overlay the melt sheet,as at Popigai (4), but have since been eroded.

Relatively large uncertainties are attached to estimates of the radius of the transient cavity for complex craters because of large structural readjustments (e.g. compare the minimum and maximum estimates given for Manicouagan). Nevertheless Table 1 indicates that complex craters as a group have relatively more melt, normalized to the transient cavity volume, than a simple crater. Therefore, it is believed that a greater proportion of the impact energy in a large event is partitioned into increasing the internal energy of the target and less into excavation processes than in a small impact event. This is consistent with the suggestion that the shock wave attenuates less rapidly relative to the radius of transient cavity as crater size increases(17).

At Brent only 1% of the melt is in the form of a sheet, the bulk is dispersed in the overlying breccias (3). If this relationship for the distribution of melt holds for all sizes of craters then the data in Table 1 suggest that the expected total volume of melt (as a sheet and in breccias) produced at complex craters exceeds that of the transient cavity. It is impossible to increase the volume of the transient cavity sufficiently to overcome this apparent discrepancy. As for example in the case of Manicouagan, the depth and radius of the cavity are constrained by geophysical (18) and shock zoning

data (19). It is concluded, therefore, that a larger percentage of the melt remains in the form of a sheet on the crater floor at complex craters. If 60% of transient cavity volume was raised above its melting point, as suggested by shock wave attenuation data from Charlevoix (transient cavity radius 13km)(20), then at least 10% of the melt produced in the Manicouagan event must remain as a sheet to account for the present distribution of melt.

A possible explanation for the increase in the percentage of melt as a sheet at large structures is that, although the volume of material excavated must scale as some function of the kinetic energy of the impact event, the particle velocity is a function of shock pressure, which is dependent only on impact velocity and the physical properties of the impacting materials (12). The melt moves therefore with the same initial particle velocity irrespective of the size of the event, but in a larger structure the melt moves a smaller radial distance in a given time. It also has further to travel before ejection and is therefore subjected to deceleration forces for a longer period of time. Thus in a large relative to a small crater a greater proportion of shock melted material has insufficient velocity for ejection and remains within the cavity, where it is available to form a relatively larger melt sheet. This conclusion is in keeping with calculations on the distribution of transported target material within the cavity of explosion craters (21) and the earlier general suggestion that excavation processes relative to cavity size are less efficient in large structures.

Table 1: Relative volumes of melt at impact structures of varying size

| | Brent | Mistastin | W. Clearwater | Manicouagan | |
|---|---|---|---|---|---|
| Radius TC,km | 1.5 | 6 | 8.5 | 15(min) | 22(max) |
| Vol.TC, $km^3$ | 3.75 | 240 | 680 | 3750 | 11830 |
| Vol.melt in TC,$km^3$ | $5x10^{-2}$ | 12 | 34 | 80 | 320 |
| Vol.melt/Vol.TC | 0.01 | 0.05 | 0.05 | 0.02 | 0.03 |

TC - Transient cavity; Data from (3,5,8,16) and unpublished work, EPB.

References

(1) Von Engelhardt, W., Geochim. Cosmochim. Acta, 31, 1677-1689, 1967. (2) Dence, M.R., in Shock met. of natural materials, 169-184, 1968. (3) Dence, M.R., J. Geophys. Res., 76, 5552-5565, 1971. (4) Masaitis, W.V. et al.,(NASA Tech. trans. F-16,900), 1975. (5) Grieve, R.A.F., Bull. Geol. Soc. Amer., 86, 1617-1629, 1975. (6) Simonds, C.H. et al., Amer. Min., (in press), 1976. (7) Currie, K.L., Geol. Surv. Canada Bull., 198, 1972. (8) Floran, R.J. et al., Geophys. Res. Lett., 3, 49-52, 1976. (9) Schaal, R. et al., Proc. Conf. on Origin of Mare basalts, LSI, 1975. (10) Gibbons, R.V. et al., Proc. 6th Lunar Sci. Conf., 3143-3171, 1975 (11) O'Keefe, J.D., Ahrens, T.J., Proc. 6th Lunar Sci. Conf., 2831-2844, 1975. (12) McQueen, R.G. et al., J. Geophys. Res., 72, 4999-5036, 1967. (13) Gault, D.E. et al., in Shock met. of natural materials, 87-99, 1968. (14) Stähle, V.,E.P.S.L., 17, 275-293, 1972. (15) Dence, M.R., Meteoritics, 8, 343-344, 1973. (16) Floran, R.J., Dence, M.R., Proc. 7th Lunar Sci. Conf., (in press), 1976. (17) Grieve, R.A.F., Robertson, P.B., Contrib. Min. Pet., (in press), 1976. (18) Sweeney, J.F. (pers. comm.).(19) Murtaugh, J.G., Proc. 24th. Int. Geol. Congr., 15, 133-139, 1972. (20) Robertson, P.B., Bull. Geol. Soc. Amer., 86, 1630-1638, 1975. (21) Hess, W.H., Proc. Geophys. Lab. - Lawrence Rad. Lab. Cratering Symposium, paper 0, 1961.

# WAS THE LUNAR CRATER, GIORDANO BRUNO, FORMED ON JUNE 18, 1178?

Jack B. Hartung, Dept. of Earth and Space Sciences,
State Univ. of New York at Stony Brook, Stony Brook, NY 11794

A spectacular event apparently occurred on the Moon on June 18, 1178.(1,2) The description of the event was included in medieval chronicles written by Gervase of Canterbury. A translation from the original Latin follows.

> "In this year, on the Sunday before the Feast of St. John the Baptist, after sunset when the Moon had first become visible a marvelous phenomenon was witnessed by some five or more men who were sitting there facing the Moon. Now there was a bright new moon, and as usual in that phase its horns were tilted toward the east; and suddenly the upper horn split in two. From the midpoint of this division a flaming torch sprang up, spewing out, over a considerable distance, fire, hot coals, and sparks. Meanwhile the body of the Moon which was below writhed, as it were, in anxiety, and, to put it in the words of those who reported it to me and saw it with their own eyes, the Moon throbbed like a wounded snake. Afterwards it resumed its proper state. This phenomenon was repeated a dozen times or more, the flame assuming various twisting shapes at random and then returning to normal. Then after these transformations the Moon from horn to horn, that is along its whole length, took on a blackish appearance. The present writer was given this report by men who saw it with their own eyes, and are prepared to stake their honor on an oath that they have made no addition or falsification in the above narrative."(2)

I believe this report may be explained by the occurrence of a very large impact on the Moon. The report is sufficiently precise to enable the location and size of the expected crater to be estimated: latitude, $\sim 45^{\circ}$ N.; longitude, $\sim 90^{\circ}$ E.; crater diameter, >10 km. An extraordinary crater, Giordano Bruno, is located at latitude $36^{\circ}$ N. and longitude $103^{\circ}$ E. and is 20 km in diameter. The crater is "the center of a ray system rivaling that of Tycho"(3), although its diameter is only one-fifth as large.

The probability of such a large impact event occurring during recorded history is extremely small; but the existence of an exceptionally fresh bright-rayed crater at a location predicted based on the report alone leads me to conclude the formation of Giordano Bruno did occur on June 18, 1178.

References

1. Newton, R. R. (1972) "Medieval Chronicles and the Rotation of the Earth." Johns Hopkins University Press, Baltimore.
2. Stubbs, W., ed. (1879) "The Historical Works of Gervase of Canterbury, Vol. I." Her Majesty's Stationery Off., London. (Repr. by Kraus Repr. Ltd., 1965.)
3. Whitaker, E. A. (1963) in "The Moon Meteorites and Comets." B. M. Middlehurst and G. P. Kuiper, eds. The Univ. of Chicago Press, Chicago.

IMPACT MELT ON LUNAR CRATER RIMS. B. Ray Hawke and James W. Head. Department of Geological Sciences, Brown University, Providence, RI 02912.

Lavalike deposits that were emplaced in a fluid state occur in and around many lunar craters. Howard and Wilshire[1] have recently presented strong evidence supporting an impact-melt origin for these deposits. They noted that the melt occurs as flow lobes and channels, complexly fractured ponds, and as a hard-rock veneer over irregular surfaces. From a study of 20 fresh craters with lavalike deposits, it was concluded that the distribution of these deposits conformed to asymmetries of other ejecta from the same craters, and that the material was concentrated downrange to distances as great as a crater radius. Numerous possibilities for the mode of emplacement were suggested but the processes controlling the formation and distribution of melt deposits are not well understood. The present study was undertaken to determine the distribution of melt deposits around a large number of lunar craters and investigate the processes responsible. The results should have important implications not only to the understanding of impact cratering events but also for the provenance of the abundant impact melt rocks in the lunar sample collection.

A variety of Lunar Orbiter, Apollo, and Earth-based photography was employed to locate and characterize lunar melt deposits. The criteria used to recognize such deposits were similar to those described by Howard and Wilshire.[1] To date, a total of 55 craters with ponds or flows of lavalike material on their rims have been identified and data were collected concerning their size and location, as well as the morphology of the crater and melt deposits. The directions of the most extensive ejecta and melt deposits, lowest segment of the rim crest, maximum and minimum terrace width, most extensive wall pools, flattest portion of the crater floor, and any pre-existing topographic lows, were determined where possible.

Results and Discussion

Size range - Ponds and flows of probable impact melt have been identified around craters ranging 4 to 300 km in diameter but most of the craters (88%) are less than 100 km. It has been suggested[1] that lavalike flows are generally absent from the rims of craters smaller than 30 km but this survey revealed 18 craters less than 20 km in diameter that have rim ponds and/or flows. This would suggest that the processes acting to emplace these deposits were still operative at crater diameters as small as 4 km.

Morphology of deposits as a function of crater size - Melt around small craters (4 to 10 km) typically occurs as a hard rock veneer which has in places coalesced in local lows to produce small ponds on, or very near, the rim crest. Short flows may also be present and are usually associated with the ponds. Slightly larger craters (10-20 km) are similar but ponds and flows are generally larger and more extensive. Their mean maximum distance from the rim crest is 0.48R (crater radii).

At larger diameters (20-50 km) deposits appear more extensive. Flows often enter and emerge from larger ponds. Ponded material appears to be the dominant mode of rim occurrence at still larger diameters (>50 km). The mean maximum distance of this ponded material from the crater rim is 0.62R and is

Impact Melt on Lunar Crater Rims

Hawke, B. R. and Head, J.W.

generally between 0.5 and 1.0 R as noted by Howard and Wilshire.[1]

Influence of angle of incidence - Various explanations have been offered to account for the asymmetry of melt deposits around impact craters. Howard and Wilshire[1] have noted that when oblique impact is suggested by asymmetry of rays, secondary crater chains, or ejecta blanket, the most extensive melt deposits are often in the inferred downrange direction. It was possible to determine both the direction of most extensive melt deposits and the inferred downrange direction based on crater deposit asymmetry for 39 of the craters in the sample. Of these, only 46% show a strong correlation (direction vectors within 22.5° of each other). Thus, although angle of incidence may be important in many cases, other factors may be important as well.

Influence of pre-event topography - Hawke[2] has recently emphasized the effect of pre-existing topography at the King crater target site in producing a low rim crest segment thus allowing molten material to preferentially eject through the breach. The direction of most extensive melt deposits and the direction of the lowest rim crest segment could be determined with confidence for 42 of the craters under consideration. Of these, 67% show a strong correlation. The direction vectors are separated by 90° or more in only 15% of the cases. It also seems significant that in those instances where melt deposits are found at large distances from the rim crest (greater than ~0.8R) there is usually a major pre-existing topographic low in this direction which was intersected by the growing crater cavity. The largest craters under study (130-300 km) seem to show little correlation between the direction of the most extensive melt deposits and rim height or pre-impact topography but correlate well with the inferred downrange direction for an oblique impact. It seems reasonable that above a certain size (100-130 km), the impact crater would fail to be influenced by topographic variations of the scale generally seen in the lunar highlands.

The results suggest that pre-existing topography and obliquity of impact are both important in producing the observed melt distribution. They may occasionally act in concert to produce the extensive melt deposits such as those north of King crater. In addition, the pre-existing topography may exert some influence over the direction of most extensive ejecta deposits, secondary crater chains, and rays.

Ubiquity of occurrence and the influence of substrate - Howard and Wilshire[1] note that lavalike pools are recognizable on the rims of most fresh craters greater than 40-50 km diameter for which good photography is available. This study has revealed several fresh impact craters of various sizes which seem to lack well-defined melt deposits. A few are located in the highlands (i.e. Crookes, diameter=50 km) but most are developed in the mare. There seems to be a dichotomy between mare and highland craters with regard to exterior melt deposits.

All of the craters with exterior melt deposits investigated in this study are either in the highlands or if located on the mare, penetrate through the basalt and excavate underlying highland material. It would appear from the observations made to date that the extensive deposits of impact melt that are commonly seen around fresh highland craters are largely absent from the rims of craters developed entirely in mare basalt, although melt is observed in the floors of such craters. The reason for this is not clear, but

several explanations appear plausible: 1) Because of the thinness of mare basalts relative to crater depth, the size range of those craters developed exclusively in mare basalt is restricted to rather small craters. Craters of equivalent size in the highlands generally have only small volumes of melt on their rims and these are subject to rapid degradation. 2) Pre-impact mare terrain is generally flat and lacks the relief necessary to effectively concentrate the melt distribution. 3) Less melt may be produced as a result of more energy being partitioned into the comminution of target material. 4) The processes responsible for melt distribution may operate in a different manner in the mare, possibly due to a difference in substrate characteristics.[3] Additional work is planned to investigate these and other possibilities more fully.

References:

1. Howard, K. A. and Wilshire H. G. (1975) Flows of impact melt at lunar craters. Jour. Research U. S. Geol. Survey, 3, p. 237-251.
2. Hawke, B. R. (1976) Ponded material on the north rim of King crater: influence of pre-event topography on the distribution of impact melt. Trans. Amer. Geophys. Union, 57, p. 275.
3. Head, J. W. (1976) The significance of substrate characteristics in determining morphology and morphometry of lunar craters. Proc. Lunar Sci. Conf. 7th, in press.

ORIGIN OF RINGS IN LUNAR MULTI-RINGED BASINS. James W. Head, Department of Geological Sciences, Brown University, Providence, RI 02912.

Lunar basins, large circular depressions with distinctive concentric rings, have been of major importance in the evolution of the surface features and crust of the Moon.[1-5] Although virtually all workers agree that basins are of impact origin, there has been no general agreement on the origin of the specific multiple rings and their relation to features seen in smaller craters.[1] The purpose of this study was to examine the morphology and morphometry of several of the freshest lunar basins (Imbrium, Orientale, Nectaris, Crisium, Humorum) and to compare the characteristics of their three most prominent rings to features seen in smaller impact craters (Fig. 1).

Location of the Crater Rim Equivalent - The first concentric ring to form with increasing crater size is the central peak ring (CPR), so named because of its morphologic similarity to central peaks. Ratios of rim crest diameter /CPR diameter for 12 two-ringed basins between 140-435 km diameter show a range from 2.19 to 1.85 (Fig. 2), generally inversely correlated with size. Therefore, for two-ringed basins, central peak rings are generally relatively closer to the rim crest in larger structures. On the basis of morphologic evidence the central peak ring is interpreted to represent an expansion of the central peaks.

Central peak rings can also be identified in the fresher large basins with more than two rings (Orientale, Imbrium). For the other basins considered here, the position of the central peak ring is believed to be marked by a concentric mare ridge system. Imbrium illustrates both the ridge system and numerous central peak ring segments. Extrapolation of the crater rim crest/CPR data (Fig. 2) to these basins on the basis of the size of their CPR's suggests that the ring representing the crater rim should occur at a position such that crater rim/CPR ratio ranges are about 1.65-1.79 (Fig.2). However, actual basin intermediate ring/CPR ratios are smaller than predicted for crater rims, ranging from 1.29-1.52. Basin outer ring/CPR ratios are larger than predicted for crater rims, ranging from 1.94-2.10 (Fig. 2). The latter values are typical of peak-ring basins in the diameter range 200-350 km. On the basis of morphologic information and the distribution of facies for Orientale in particular[3] the intermediate ring most closely corresponds to the crater rim seen in smaller craters and basins. Assuming proportional growth of CPR's, neither the intermediate ring nor the outer ring correspond exactly to the position of the extrapolated crater rim. However, the intermediate ring represents the same trend, although with smaller ratios. If proportional growth of CPR's occurs, then some process apparently causes the crater rim to form closer to the CPR or for it to be displaced closer to the CPR.

Formation of the Outer Ring - The characteristics and mode of formation of the outer basin ring may be important in interpreting the apparent discrepancy in crater rim/CPR ratios for three-ringed basins. The outer ring generally defines the topograhic basin and, on the basis of the freshest examples

Origin of Rings in Lunar Multi-ringed Basins.

James W. Head

(Orientale, Imbrium), appears to represent an inward dipping fault scarp which forms during the terminal stages of the event by the inward collapse of the rim to form a megaterrace.[3] The region between the outer and intermediate ring is often characterized by a domical facies[1,3,5] which is believed to form from the modification of radial rim ejecta during the formation of the megaterrace.[3] If the intermediate ring most closely corresponds to the initial crater rim, then to what cratering-associated feature does the outer ring correspond? The range of outer ring/intermediate ring ratios for the five three-ringed basins is 1.37-1.50 (Fig. 2). Using the same outer ring dimensions, but plotting them against the intermediate ring position extrapolated from peak-ring basins, yields a range of 1.12-1.22. These ratios lie within the range of the edge of the pronounced rim exterior topography for craters[6,7]. Rim exterior topography is made up of ejecta and structural uplift components, with structural uplift being most important toward the crater rim crest, usually within about 1.50 crater radii from the crater center.[7] On the basis of these comparisons, it is concluded that the outer basin ring forms near the edge of the region of significant structural uplift of the basin rim.

If the outer ring represents failure along the edge of significant structural uplift, what effect might this have on the intermediate ring and its relation to the central peak ring? Several characteristics of the intermediate ring are important in this regard: 1) although the ring and associated facies are morphologically similar to crater rims, the abundant step-like terraces seen in smaller craters are not prominent, 2) the ring is composed locally of straight segments but is regionally crenulated, as if the circumference had undergone shrinkage. These characteristics and the ring ratios suggest the following model for origin of the outer two rings: The cratering event formed two inner rings, a central peak ring and a crater rim, and uplifted the rim, depositing ejecta in the process. In the terminal stages of the event, a large segment of the rim (megaterrace) collapsed, approximately at the edge of intensive structural uplift, and deformed the recently deposited ejecta. Megaterrace formation is in contrast to the modification stage of smaller peak ring basins and craters where a smaller portion of the rim is destroyed by imbricate terrace formation, and rim crest enlargement occurs. Two factors appear to be important in explaining the deviation between extrapolated and actual crater rim/CPR ratios: 1) the terracing that causes up to 20% rim crest diameter enlargement does not seem to be as significant in three-ringed basins, and 2) the formation of the megaterrace and its inward movement compresses and crenulates the crater rim, decreasing its radius. Both of these factors tend to decrease the intermediate ring diameter from the extrapolated values and can easily explain the magnitude of difference observed between actual and extrapolated crater rim/CPR ratios (Fig. 2).

Conclusions - 1) Peak ring basins are characterized by two rings, a CPR and a crater rim crest enlarged by slumping. The CPR corresponds to enlarged central peaks and is not the crater rim crest. 2) In three-ring basins, such as Orientale and Imbrium, the CPR is maintained and the intermediate ring closely corresponds to the crater rim. 3) The outer ring in these basins forms as a fault at the edge of intense structural uplift of the crater rim, forming a wide megaterrace. 4) Crater rim/CPR ratios for three-ringed basins are smal-

Origin of Rings in Lunar Multi-Ringed Basins.

James W. Head

ler than those extrapolated from CPR basins at least in part because of a) the decreased role of crater enlargment by small terrace formation and b) decrease in crater radius caused by megaterrace formation.

References - 1. Howard, K. A. et al. (1974) Rev. Geop. and Space Phys., 12, 309. 2. Hartmann, W. and Wood, C. (1971) Moon, 3, 3. 3. Head, J. W. (1974) Moon, 11, 327. 4. Wood, C. and Head J. (1976) Comparison of impact basins on Mercury, Mars, and the Moon: in press, Proc. 7th Lunar Sci. Conf. 5. Moore, H. J. et al. (1974) Proc. 5th Lunar Sci. Conf., 71. 6. Pike, R. (1976) Lunar Science VII, 700. 7. Settle, M. and Head J. (1976) Radial variation of lunar crater rim topography: sub. to Icarus.

TABLE 1 Basin Ring Dimensions (B-C-D) (KM) Imbrium 670-970-1340; Orientale 480-620-930; Nectaris 400-600-840; Crisium 330-450-670; Humorum 270-410-560.

FIG. 1

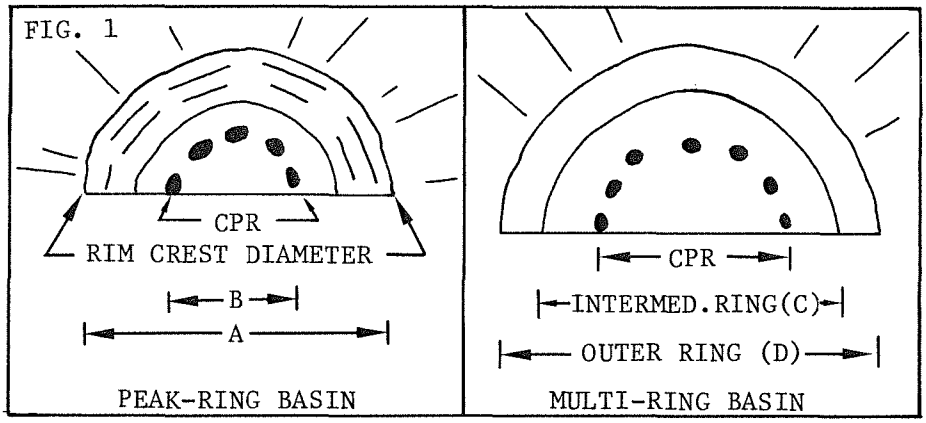


FIG. 2

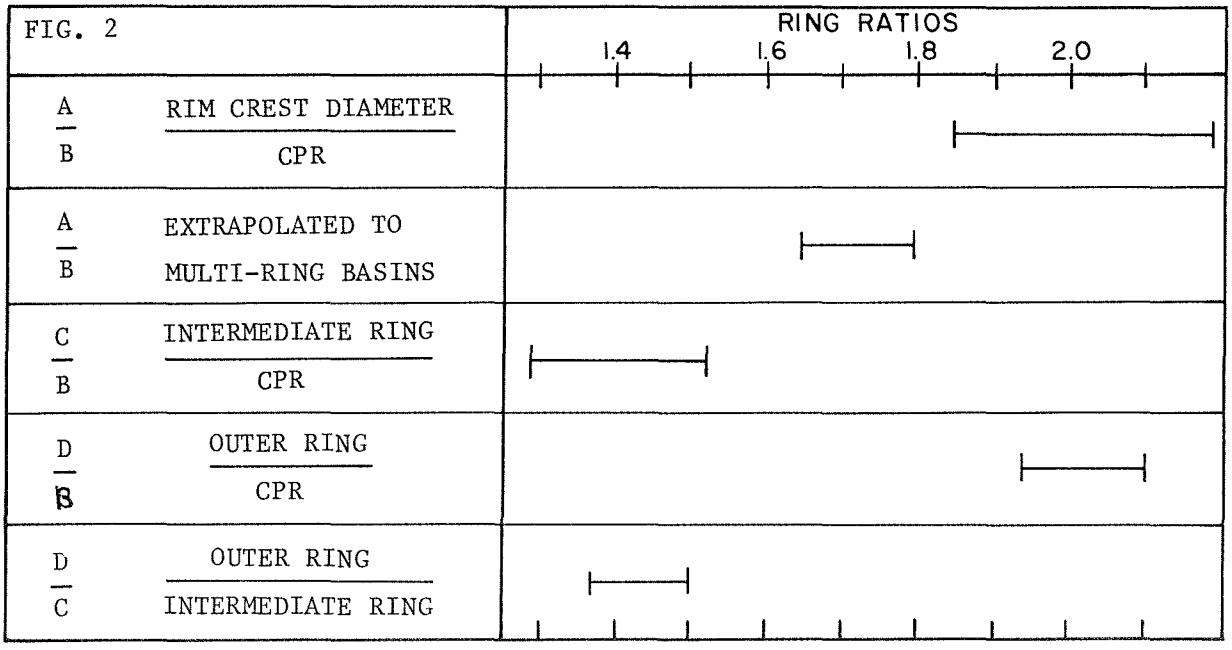

MARS PEDESTAL CRATER ESCARPMENTS: EVIDENCE FOR EJECTA-RELATED EMPLACEMENT, James W. Head and R. Roth, Department of Geological Sciences, Brown University, Providence, Rhode Island 02912.

A distinctive crater morphologic type, termed pedestal crater for the sharply-edged concentric platform surrounding the crater, was described from Mariner 9 imagery.[1] These features have been interpreted to represent erosional remnants of ejecta deposits, where deflation has removed debris surrounding the crater rim, and has left part of the crater rim standing above the adjacent terrain because of the armoring effect of crater ejecta. In this model,[1,2] the scarp at the edge of the pedestal is a receding erosional feature.[1,2] In the present investigation, all Mariner 9 high resolution frames were analyzed for the presence and characteristics of craters that displayed rim deposits of all states of degradation. Analysis of the population of pedestal craters strongly suggests that pedestals form as an integral part of primary ejecta emplacement, rather than as erosional scarps.

Pedestal craters seen on Mariner 9 B-frames range from less than 1 km to about 16 km in diameter. Examination of moderate resolution A-frames shows additional pedestal craters ranging up to 20 km diameter. Craters larger than these diameters lack distinctive pedestals and are characterized by ejecta deposits generally similar to lunar craters. Pedestal craters can be classified into four major types (Fig. 1): Type 1 exhibits a continuous ejecta deposit characterized by radial and hummocky textures in fresh examples and appears the most lunar-like of the pedestal craters; a subtle but noticeable topographic break is seen at the edge of the ejecta deposit; Type 2, concentric pedestal craters, exhibit a distinctive break in relief at the edge of the generally circular concentric pedestal. Two types of pedestal margins are exhibited by these craters, step margin and a rampart margin; Type 3, lobate pedestal craters, are generally similar to Type 2, but their outer margins are extremely sinuous and irregular; Type 4, serrate pedestal craters are characterized by their extremely irregular, but sharp, ray-like boundary, arrayed radially to the crater.

In Fig. 2, pedestal crater types are plotted in relation to crater diameter. Normal concentric pedestal craters are the dominant crater type. Although serrate craters are confined to lower diameters and lobate craters occur at higher diameters, the population is too small for this relationship to be conclusively demonstrated. Pedestal margin diameter normalized to crater diameter is plotted as a function of crater type and diameter in Fig. 2. The majority of pedestal craters lie in the ratio range of 2-3, although craters less than 5 km diameter range to higher ratios. In particular, the serrated craters range between 3 and 5. Pedestal craters appear to be rather evenly distributed in relation to latitude although the normalized pedestal diameter may be generally higher in the high latitudes in the region of the debris mantle.[2,3] The age of pedestal craters is uncertain but the general lack of superposed craters and the rim and rim crest sharpness suggests that they are relatively young.

Normalized pedestal diameters are compared to other characteristics of lunar and martian crater deposits in Fig. 3. The distinctive rim topography

Mars Pedestal Crater Escarpments
James W. Head

associated with lunar craters extends from about 1.3-1.7[4] while the range of the edge of the heavily textured ejecta deposits is 1.8-2.8[5]. The range of the edge of the field of dense satellitic craters extends out to about 4.5[5]. Mars pedestals most closely correspond to the outer portions of lunar ejecta deposits rather than to the prominent rim topography. In relation to the Moon, the higher surface gravitational acceleration on Mars (within 5% of that of Mercury) should produce ejecta deposits that are concentrated closer to the crater rim crest, and satellitic craters should be abundant closer to the rim, as is the case on Mercury.[6] However, Mars pedestal ratios are higher than those for the edge of the continuous crater deposits on Mercury (Fig. 3).

The characteristics of pedestal craters seem inconsistent with a dominantly erosional origin of pedestals. In particular, 1) the symmetric distribution of pedestals around craters requires remarkably even wind direction variations, 2) the rampart nature of some pedestal margins is difficult to explain by processes of eolian-related scarp undercutting and retreat, 3) the lack of visible craters superposed on pedestal craters and their often fresh appearance argues for a relatively young, undegraded state, 4) specific examples of the interaction of pedestal crater margins with each other, and with adjacent topography, argue against an erosional origin, 5) the identification of some preserved secondary crater fields adjacent to the pedestals argues against regional deflation. The characteristics of pedestal craters strongly suggest a model of primary emplacement. In particular, the sheet-like nature of many pedestal rims, and their associated radial lineaments, and the lobate aspect of many margins, and their associated ramparts, are all reminiscent of features associated with primary emplacement of debris flows on Earth[7] and seen on some lunar crater rims.[8, 9] However, these features suggest a mode of emplacement different than the dominantly ballistic mode characteristic of most lunar and mercurian craters. The lack of correspondence of normalized Mars pedestal diameters and normalized continuous ejecta deposit diameters for Mercury, despite similar gravity, is striking (Fig. 3). Together with the morphologic evidence, this strongly suggests that pedestals result from the emplacement of debris flows associated with crater formation. Factors responsible for this distinctive mode of formation may include presence of an atmosphere, presence of groundwater or ice, and grain size differences due to eolian processes, all possibly enhancing fluidization of ejecta. Post-emplacement failure of ejecta which is concentrated near the crater rim due to high martian gravity may also be a factor in pedestal formation.

REFERENCES: [1] McCauley, J. F. (1973) Jour. Geophys. Res. 78, 4123. [2] Arvidson, R. E. et al. (1976) Icarus, 27, 503. [3] Soderblom, L. A. et al. (1973) Jour. Geophys. Res. 78, 4117. [4] Settle, M. and Head, J. (1976) Radial variation of lunar crater rim topography, submitted to Icarus. [5] Head, J. W., unpublished data. [6] Gault, D. E. et al. (1975) Jour. Geophys. Res. 80, 2444. [7] Shreve, R. (1966) Science, 154, 1639. [8] Guest, J. E. and Murray, J. B. (1969) Planet. Space Sci. 17, 121. [9] Head, J. W. (1976) Evidence for the sedimentary origin of Imbrium sculpture and lunar basin radial texture, The Moon, in press.

Mars Pedestal Crater Escarpments

James W. Head

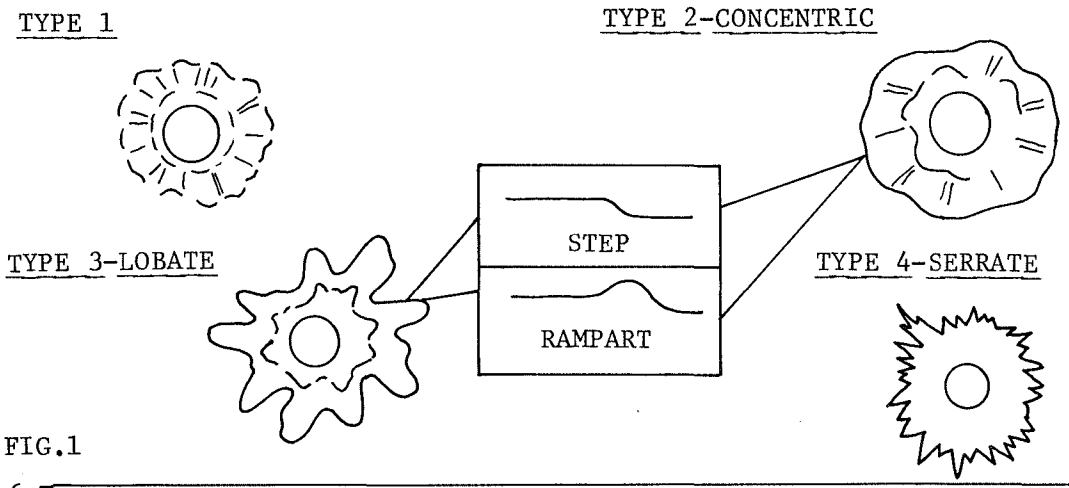


FIG.1

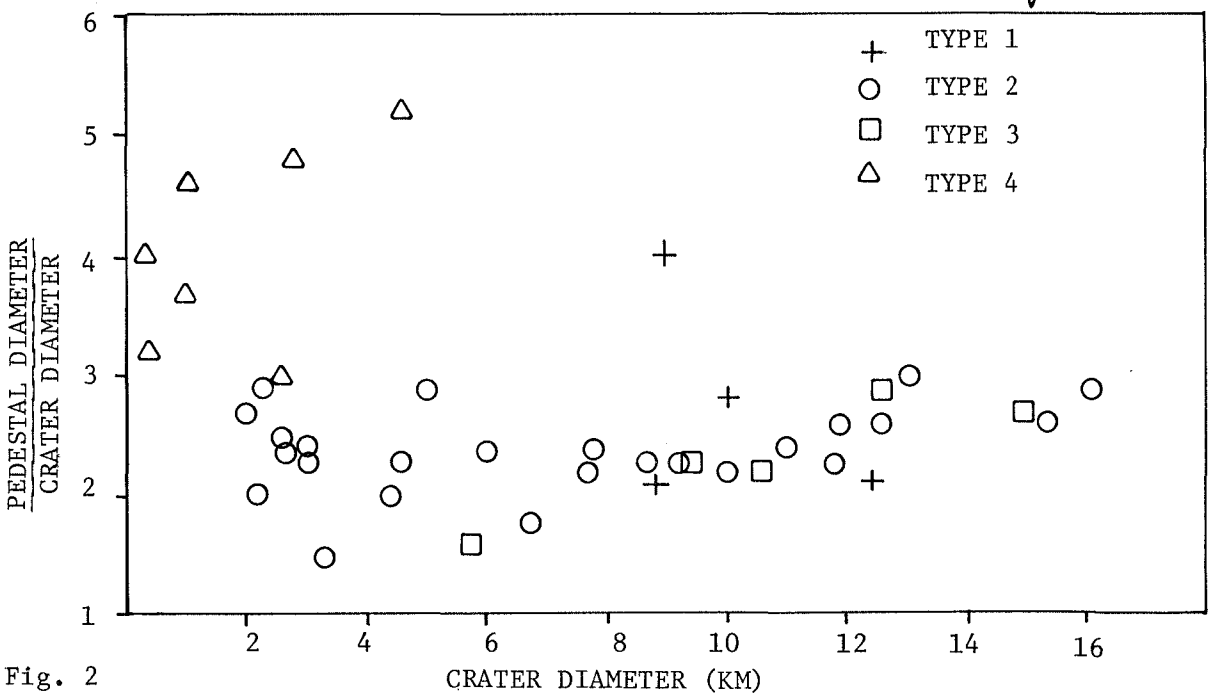


Fig. 2

Fig. 3

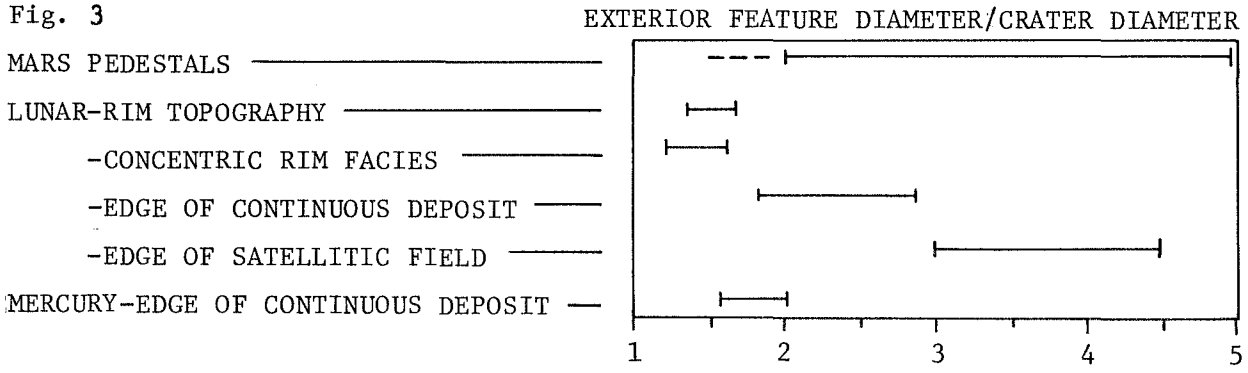

FORMATION OF CONCENTRIC BASIN RINGS; Carroll Ann Hodges and Don E. Wilhelms, U.S. Geological Survey, Menlo Park, Calif., 94025

Speculation about the origin of the multiple concentric rings that characterize lunar impact basins has been widespread. Much controversy has centered on the dimensions of the transient cavity--namely its probable depth and diameter, and the specific basin ring that best approximates the rim crest of this initial cavity of excavation. Most investigators have proposed that one of the inner rings marks this critical rim crest, which either formed in its present position or slumped downward and inward as a "mega-terrace"; rings exterior to this transient cavity thus are fault scarps (1, 2, 3, 4, 5, 6, 7, 8, 9, 10). Instead, we concur with Baldwin (11) and Chao, et al, (12) that it is the outer escarpments surrounding these basins--the Cordilleran at Orientale, the Apennine at Imbrium, and the Altai at Nectaris--that define the transient cavities, enlarged relatively little by slumping, and are thus analogous to the rim crests of craters like Copernicus. We suggest further that the interior concentric rings are produced within the transient cavity immediately after impact by rebound--either as tightly folded anticlines of deep crustal rock or as blocks of resistant rock layers from depth--and therefore are counterparts of central peaks. Our hypothesis is based on photogeologic and seismic data from the Moon and on extrapolation of data from terrestrial impact craters, explosion craters, and laboratory experiments.

On the Moon, there is a gradational sequence in central uplifts from simple central peaks (as in Copernicus) through somewhat annular clusters of peaks (Petavius), peak and ring combinations (Antoniadi) and double ring basins (Schrödinger), culminating in multi-ring structures (Orientale). The conspicuous outer ring in each case marks the inner boundary of lineated ejecta, distinct from the internal blocky ejecta and smooth floor materials. The interior rings are discontinuous rugged peaks.

Most terrestrial impact craters larger than about 2 to 4 km exhibit central uplifts, but at diameters greater than about 20 km, multi-ringed structures form. At Gosses Bluff, Australia (20 km), the interior ring is composed of upturned strata that are relatively resistant to impact excavation as well as to erosion; field evidence suggests that the central depression is due to ejection of weaker rocks in the center of the uplift, derived from 3 km below the present surface (13). At West Clearwater Lake, Quebec (32 km), brecciated basement gneisses formed the central ring (14). In a 500-ton TNT explosion crater (Prairie Flat), concentric rings on the crater floor appeared to be tightly folded anticlines (15). A 100-ton explosion produced concentric morphology in a crater with an upturned bench at a stratigraphic discontinuity (16), duplicating at large scale the concentric craters formed in small-scale laboratory experiments where relatively weak target materials overlie a resistant substrate (17, 18). Similar morphology occurs at the Ries Crater, Germany, where a 24-km-diameter crater in layered strata ($\sim$ 1 km thick) encloses a 10-km crater excavated in the crystalline basement (19, 18).

These terrestrial data suggest that excavation and ejection of material occur across the entire radius from center to outer scarp. Therefore,

assuming the same to be true on the Moon, peak rings bound craters of excavation just as the outer rings do. Surficial slumping may occur along each of these crater walls.

If, as we propose, the interior basin rings are analogous to central peaks, which in effect have become nested crater rims, then the multiple ring configuration may result from uplift of distinct rock layers that were intersected by the impact excavation. These layers may correspond to those defined by the Apollo seismic experiments, which showed major velocity discontinuities at depths of about 20 km and 60 km, marking the transitions between upper and lower crust, and crust and mantle, respectively. In addition, a thin or discontinuous high-velocity layer may exist in the upper mantle (20). Interaction of shock waves with these discontinuities may augment formation of rings (18) but probably does not cause them (21). Accordingly, the semi-regular spacing of rings depends on the depths to these seismic discontinuities at various localities; local heterogeneities would produce variations in spacing and number of rings relative to basin diameter, and a crust thicker on the far side than on the near side may account for the fewer major rings at far-side basins. The multiple structure of rings at Crisium and Humorum, and probably that of Orientale's Rook ring, may be due to splitting by terrace-like slumping.

An approximate depth/diameter ratio of 1/10 for transient basin cavities is consistent with the formation of rings by uplift of the seismically detected layers and with intersection of the mantle at Orientale and Imbrium. Much of the observed mascon (22) in many basins can be accounted for by the instantaneous rebound of dense mantle material, which forms a central plug; inward lateral flow at depth explains the peripheral negative anomalies (6). The present shallow floors of basins are due partly to subsequent isostatic adjustment, as well as to fallback of ejecta and flooding by maria. Slumping increased the apparent diameter of a basin just as it did in Copernican-type craters, but the inner rings did not slump from the outer ring, and they are not correlative stratigraphically. According to this interpretation, the volumes of transient basin cavities and their ejecta may be considerably greater than commonly assumed (3, 4, 8, 10).

References: 1. McCauley, J. F., 1968, Geologic results from the lunar precursor probes: AIAA Jour., v. 6, no. 10, p. 1991-1996.

2. Hartmann, W. K., and Wood, C. A., 1971, Moon: Origin and evolution of multiring basins: The Moon, v. 3, p. 3-78.

3. Short, N. M., and Forman, M. L., 1972, Thickness of impact crater ejecta on the lunar surface: Modern Geology, v. 3, no. 2, p. 69-91.

4. McGetchin, T. R., Settle, M., and Head, J. W., 1973, Radial thickness variation in impact crater ejecta: Implications for lunar basin deposits: Earth and Planetary Sci. Letters, v. 20, no. 2, p. 226-236.

5. Moore, H. J., Hodges, C. A., and Scott, D. H., 1974, Multi-ringed basins --illustrated by Orientale and associated features, in Lunar Sci. Conf., Fifth, Proc.: Geochim. Cosmochim. Acta, Suppl. 5, v. 1, p. 71-100.

Formation of Concentric Basin Rings

Carroll Ann Hodges


6. Howard, K. A., Wilhelms, D. E., and Scott, D. H., 1974, Lunar basin formation and highland stratigraphy: Reviews of Geophysics and Space Physics, v. 12, no. 3, p. 309-327.
7. Dence, M. R., Grieve, R.A.F., and Plant, A. G., 1974, The Imbrium basin and its ejecta (abs.) in Lunar Science V Abstracts: Lunar Science Inst., Houston, Texas, p. 165-167.
8. Head, J. W., 1974, Orientale multi-ringed basin interior and implications for the petrogenesis of lunar highland samples: The Moon, v. 11, p. 327-356.
9. Schultz, P. H., and Gault, D. E., 1975, Seismic effects from major basin formations on the Moon and Mercury: The Moon, v. 12, p. 159-177.
10. Head, J. W., Settle, Mark, Stein, R. S., 1975, Volume of material ejected from major lunar basins and implications for the depth of excavation of lunar samples, in Lunar Sci. Conf., Sixth, Proc.: Geochim. Cosmochim. Acta, Suppl. 6, v. 3, p. 2805-2829.
11. Baldwin, R. B., 1974, On the origin of the mare basins, in Lunar Sci. Conf., Fifth, Proc.: Geochim. Cosmochim. Acta., Suppl. 5, v. 1, p. 1-10.
12. Chao, E. C. T., Hodges, C. A., Boyce, J. M., Soderblom, L. A., 1975,Origin of lunar light plains: U.S. Geol. Survey Jour. Research, v. 3, p. 379-392.
13. Milton, D. J., Barlow, B. C., Brett, Robin, Brown, A. R., Glikson, A. Y., Manwaring, E. A., Moss, F. J., Sedmik, E.C.E., Van Son, J., Young, G. A., 1972, Gosses Bluff impact structure, Australia: Science, v. 175, p. 1199-1207.
14. Dence, M. R., Innes, M.J.S., and Beals, C.S., 1965, On the probable meteorite origin of the Clearwater Lakes, Quebec: Royal Astron. Soc. Canada, Jour., v. 59, no. 1, p. 13-22.
15. Roddy, D. J., 1976, High explosive cratering analogs for central uplift and multiring impact craters, in Proc. Seventh Lunar Science Conf.; Geochim. Cosmochim. Acta, Suppl. 7, in press.
16. Roddy, D. J., 1975, Personal communication.
17. Quaide, W. L., and Oberbeck, V. R., 1968, Thickness determinations of the lunar surface layer from lunar impact craters: Jour. Geophys. Research, v. 73, no. 16, p. 5247-5270.
18. Oberbeck, V. R., 1975, The role of ballistic erosion and sedimentation in lunar stratigraphy: Reviews of Geophysics and Space Physics, v. 13, no. 2, p. 337-362.
19. Englehardt, W. v., 1974, The Ries structure and its impact formations: Fortschr. Miner., v. 52, Beiheft 1, p. 103-109.
20. Toksöz, M. N., Dainty, A. M., Solomon, S. C., Anderson, K. R., 1974, Structure of the Moon: Reviews of Geophysics and Space Physics, v. 12, no. 4, p. 539-567.
21. Ullrich, G. W., 1976, The mechanics of central peak formation in shock wave cratering events: Defense Nuclear Agency, Air Force Weapons Laboratory, Final Report AFWL-TR-75-88, 133 p.
22. Muller, P. M., and Sjogren, W. L., 1968, Mascons: Lunar mass concentrations: Science, v. 161, p. 680-684.

ON THE MECHANICS OF THE SURFACE EXPLOSION, B.A.Ivanov, O.J. Schmidt Institute of Physics of the Earth, USSR Acad. Sci., Moscow, USSR.

Some theoretical and experimental results on the mechanical effects of high explosives (HE) burst near the surface of wet sand and water are presented.

Experiment. Two series of experiment were carried out with wet sand targets. In the first series a 500-kg box with wet sand was used as a target. This box could move vertically with a I-sec period, wich allowed the measurement of the velocity of the target after explosion. The product of the target mass to its velosity gives the value of the rebound impulse (RI). The RIwas measured as a function of depth of burst (DOB, here measured in charge radius $r_0$). For zero DOB RI is 300 $\underline{C}$ g cm/msec, where $\underline{C}$ is is the weight of charge in g of TNT. The RI achives the maximum value I500 $\underline{C}$ at the optimum DOB. For water in the same box the surface burst RI is 4000 $\underline{C}$. The second experimental series dealt with high speed camera records of explosions occuring on the interface of wet sand and thick plexiglass window. Profile pattern of the ground motion were observed, from which it was concluded that the depth of crater bottom $\underline{h}$ increases with time $\underline{t}$ as

$$h \sim t^{0,3} \qquad (I)$$

and the ultimate crater depth is achived during the scaled time aboute I msec/g TNT. This is the end of the first stage of crate formation, at wich the central hemispherical region is formed (fig.I). The center of this hemispherical region situated is above the initial grounde surface. During the second stage of cratering a part of soil around the central region break away and is ejected, forming the "wings" of the crater (fig.I). The ejecta velocities in central region is closely related with the low of crater growth and for (I) is

$$v_e \sim r^{-2.33} \qquad (2)$$

The ejecta velocities on the "wings" decreases as

$$v_e \sim r^{-3} \qquad (3)$$

as was mentioned in [2] . On the boundary between (2) and (3) regions the ejecta velocity is about I0-I5 m/s for wet sand.

Theory. It was suggested on the basis of tese experiments that the behavior of an incompressible fluide subjected to a short impuls of pressure allows a reasonable model for surface burst cratering in soil and in water. The initial velocity fied was calculated using Laplace equation for semispace of incompressibl fluid with halfbured HE charge. On the basis of this calculation we developed a scheme of a simple self-similar flow, which allows to predict the basic effects of cratering such as mass and velocities of ejecta, rebound impuls, etc. The main idea of this

# ON THE MECHANICS OF THE SURFACE EXPLOSION

B.A.Ivanov

scheme is the simplification of the angular and radial velocity fields on the basis of integral mass, impulse and energy conserv ation conitiones, therefore we've called this flow the Jntegrally Balanced Flow (IBF).

Discussion. For an ideal incompressible fluid IBF gives a value of the exponent power N in a self-similar variable $r/t^N$ equal to 0,36-0,38 depending on some initial suggestions. Experimentally we've obsurved for bubble growth in water due to surface burst N=0,37, which is in accordance with N=0,38 [3] in the case of electric explosion of a wire on the water surface. We also verify IBF by calculating RI for water and wet sand. IBF predicted the correct values. Therefore IBF is appearing to be a reasonable basis for the estimate of some cratering effects. In addition we'll demonstrate a close relationship between ejecta motion and crater dimensions in sand. IBF predicts, that a radius of a "neck" of ejecta envelope growthes in time as

$$r_n = (k \cdot t)^{I/4}, \qquad (4)$$

where constant k is connected with ejecta velocity distribution and is proportional to the fraction of the total energy, used for the formation of the crater. Fig.2 illustrstes (4) on the data of previous works [1, 4]. All data scaled to the explosion or impact energy $4{,}2 \times 10^{18}$ erg ( I g TNT ). Fig.3 shows the $k$-$R^3$ relationship ( R is apparent crater radius ) for different impact and explosions events in dry sand. Surface bursts, shallow buried bursts and impacts with high velocity are seemd to be similar in respect to the same relationship between ejecta velocities and final crater dimensions. The low velocity impact generates a less ejecta velocities for a given crater dimension. On the fig.3 the difference between energies, used for the formation of the crater, in the impact events with equal initial kinetic energies, but with different velocities, is apparantly seen: the 7 km/sec impact gives the energy of the crater formation more than 3 times less than the 2 km/sec impact do. The above mentioned facts permit more accurate calculations of the impact and explosion energy distribution and more adequate simulating of impacts with high explosives.

References. 1. Braslau D. J. Geophys. Res., 75, 3987-3999 (1970).
2. Ivanov B.A. (1976) In Lunar Science VII, 411-413.
3. Minin V.F. (1964). Prikladnaya mechanica i technicheskaya physica, No.3, 159 (in Russian).
4. Oberbeck V.R. (1971) J. Geophys. Res., 76, 5732-5749.

# OH THE MECHANICS OF THE SURFACE EXPLOSION

B.A.Ivanov

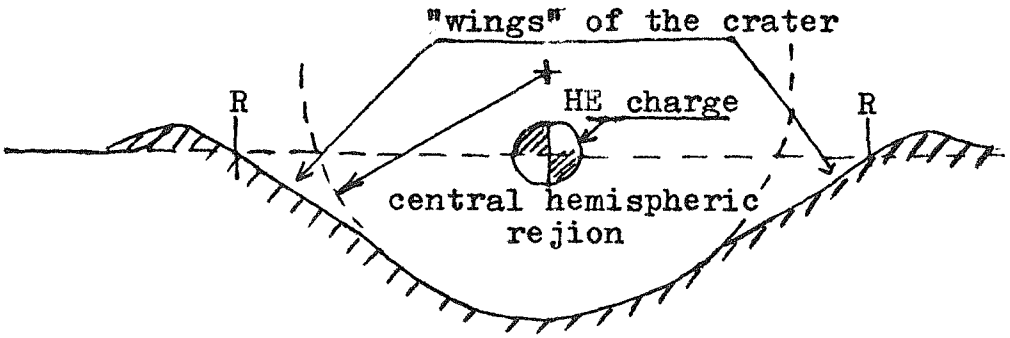


Fig. I. A typical crater profile in wet sand. + is the center of hemisphere.

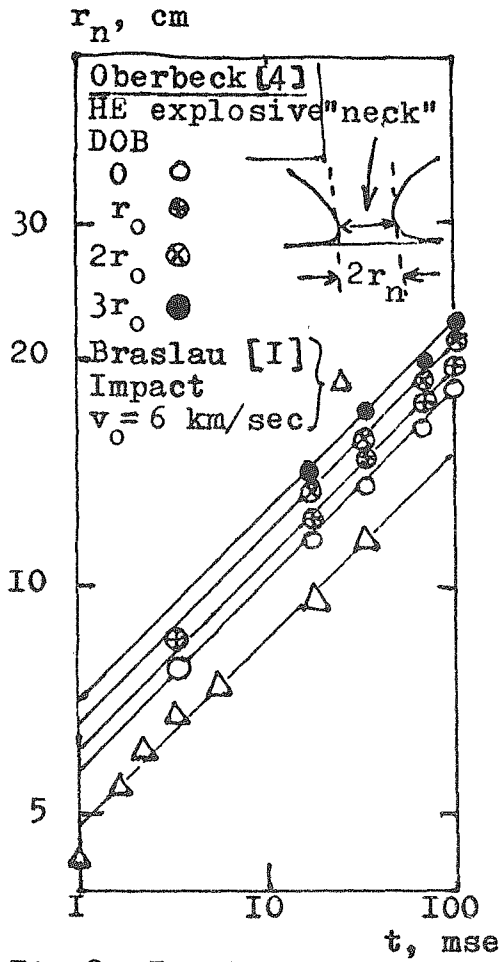


Fig.2. The "neck" radius $r_n$ increasing with time t. Solid lines - $r_n = (k \cdot t)^{I/4}$.

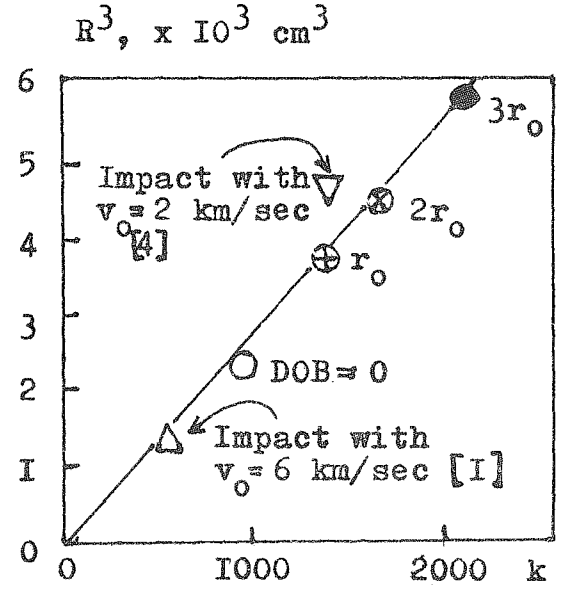


Fig.3. The linear relationship between a characterictic of ejecta velocities $k$ and cube of crater radius $R^3$.

SHOCK WAVE, A POSSIBLE SOURCE OF MAGNETIC FIELDS ?

B.A.Ivanov (O.J.Schmidt Institute of Physics of the Earth), B.A.Okulessky (P.P.Shirshov Insitute of Oceanology) and A.T.Basilevsky (V.I.Vernadsky Institute of Geochemystry and Analytical Chemystry) (all - USSR Academy of Sciences, Moscow, USSR).

Cratering is the most prominent but probably not the most interesting effect of impacts or explosions. Other physical and chemical processes are also induced by shock waves. The results of this processes should be found during the investugation of planets that have the cratered surfaces.

Several effects due to shock wave are well known, such as shock metamorphism, chemical differentiation, etc. One more possible effect due to impact cratering is the transformation of part of the kinetic energy of the projectile to energy of the electro-magnetic field. Shock induced polarization of pieso- and dielectric material could be the mechanism by which this is accomplished. Also the estimates show that the fraction of kinetic energy transformed by this mechanism is rather small, the effect could be sufficient to form some magnetic features of planets that have even a slight planetary magnetic field of their own.

Shock induced polarisation can be considered as an electric current flowing through the shock wave front. This current is capable of causing some magnetic effects on ajacent materiels. When a shock wave is passing through materials containing shock-polarized and ferromagnetic components, the induced electromagnetic field could be fixed by the ferromagnetic components (fig.I). It may also be preceeded or followed by direct shock effects on ferromagnetic components. The local nature of shock-induced polarization (each mineral grane radiates individual e electromagnetic pulses) should cause the random mosaic appearanc of remnant magnetisation in the lunar rock fragments.

The experimental data [I] show that shock compression of polycrystalline samples of rocks induce polarization in the direction, normal to the shock wave front. During the passing of the shock wave, the accompanying electro-magnetic field could change the magnetic state even of parts of the whole rock, which were not undergoued. This mechanism should couse the formation of some magnetic field anomalies near impact craters. The evaluation made show that the magnitude and geometry of the induced magnetic field is in qualitative accordance with some magnetic anomalies revealed by Lunokhod 2 near small craters in Le Monier area (fig.2) [2].

The possible limits of this effect are uncertain. The mechanism suggested is attractive because it gives a possible

# SHOCK WAVE - A POSSIBLE SOURCE OF MAGNETIC FIELD ?

Ivanov B.A. et. al.

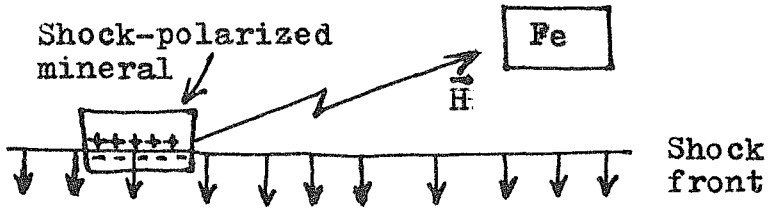


Fig,I.Shocked grain of polarized material creates a magnetic field during shock passing.

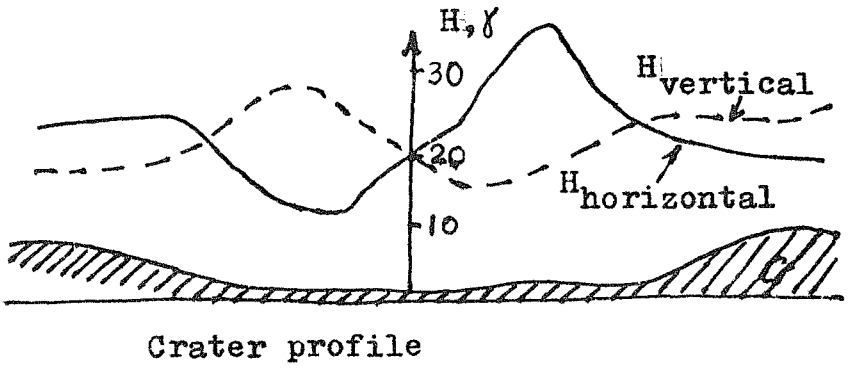


Fig. 2.

a). Obsurved geometry of the magnetic field in the vicinity of the crater (Lunokhod 2 measurements [2])

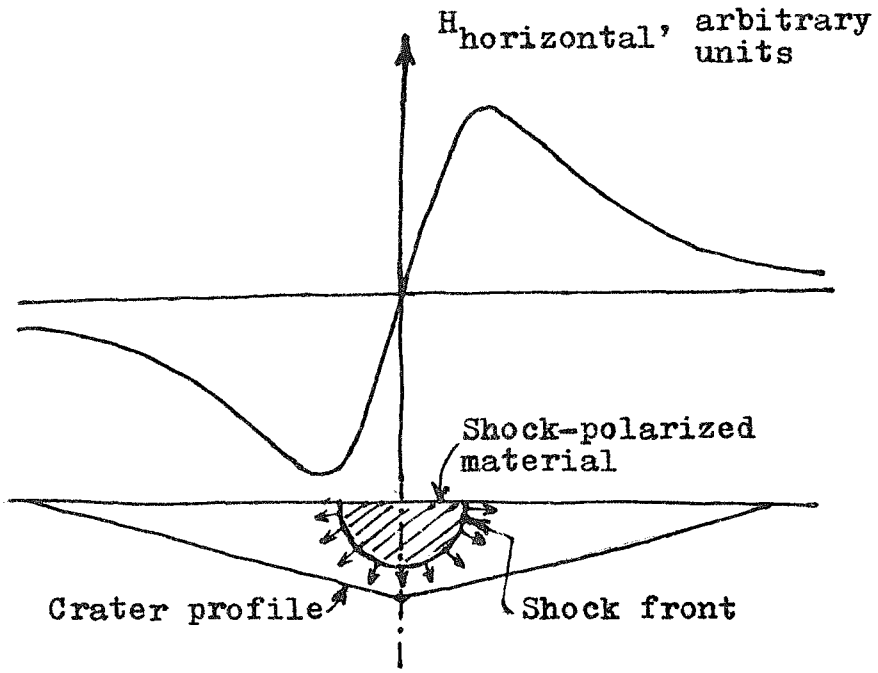


b). Calculated geometry of magnetic field at a moment of time [2] at the level of final crater bottom.

SHOCK WAVE -A POSSIBLE SOURCE OF MAGNETIC FIELD ?

Ivanov B.A. et. al.

explanation of the high values of remnant magnetisation displayed by some lunar samples, without calling for the hypothesis of a strong global magnetism for the Moon in the past epochs.

## References

1. Mineev V.N. et al. (1968) Enstatite and water polarization due to shock waves. Izvestia AN SSSR, Ser. Physics of the Earth, No.4, p.33 (In Russian)

2. Ivanov B.A., Okulessky B.A., Basilevsky A.T. (1976) Impulse magnetic field due to shock-induced polarization in rocks as a possible cause of magnetic field anomalies on the Moon, related to craters. Pisma v Astronomicheskij journal, 2, No. 5, pp. 257-260. (In Russian)

# METEORITIC MATERIAL IN THE ROCHECHOUART CRATER, AND THE PREVALENCE OF IRONS AMONG CRATER-FORMING METEORITES

Marie-Josée Janssens, Jan Hertogen, H. Takahashi, and Edward Anders
Enrico Fermi Institute and Department of Chemistry
University of Chicago, Chicago, Illinois 60637

and

Philippe Lambert
Département Laboratoires, Service Géologique National
Bur. de Recherches Géol. et Minères - BP 6009 - 45018 Orléans Cédex France

Ten samples from the 20 km Rochechouart crater in France (45.49°N, 0.50°E) have been analyzed for 7 siderophile elements (Ir, Os, Re, Au, Pd, Ni, Ge) by radiochemical neutron activation analysis. As shown in Fig. 1, the enrichment of siderophiles correlates with shock effects. It progresses in the order: impact melts > Type D (glassy) breccias > Type C (glass-free) breccias ≈ basement rocks.

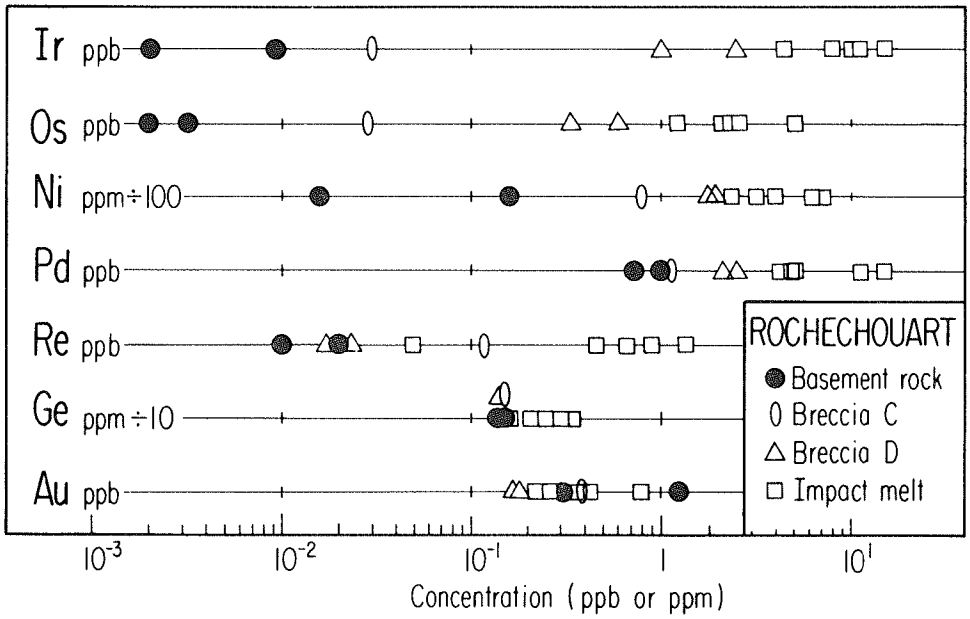


The abundance pattern of the projectile was determined from interelement correlations (Fig. 2). Several samples (open symbols) tended to fall off the correlation lines, presumably due to weathering during their 170 Myr exposure to the (meteorological) elements. The abundance ratios suggest that the Rochechouart meteorite was a IIA iron.

Rochechouart is the 11th terrestrial crater whose meteorite has been identified. All turned out to be irons or stony irons. This prevalence of irons over stones in the crater-forming range stands in contrast with their low abundance (7%) among meteorite falls. Either the size distribution of irons has a smaller slope than that of stones (Hawkins, 1963), or the breakup

ROCHECHOUART CRATER

Janssens M.-J. *et al.*

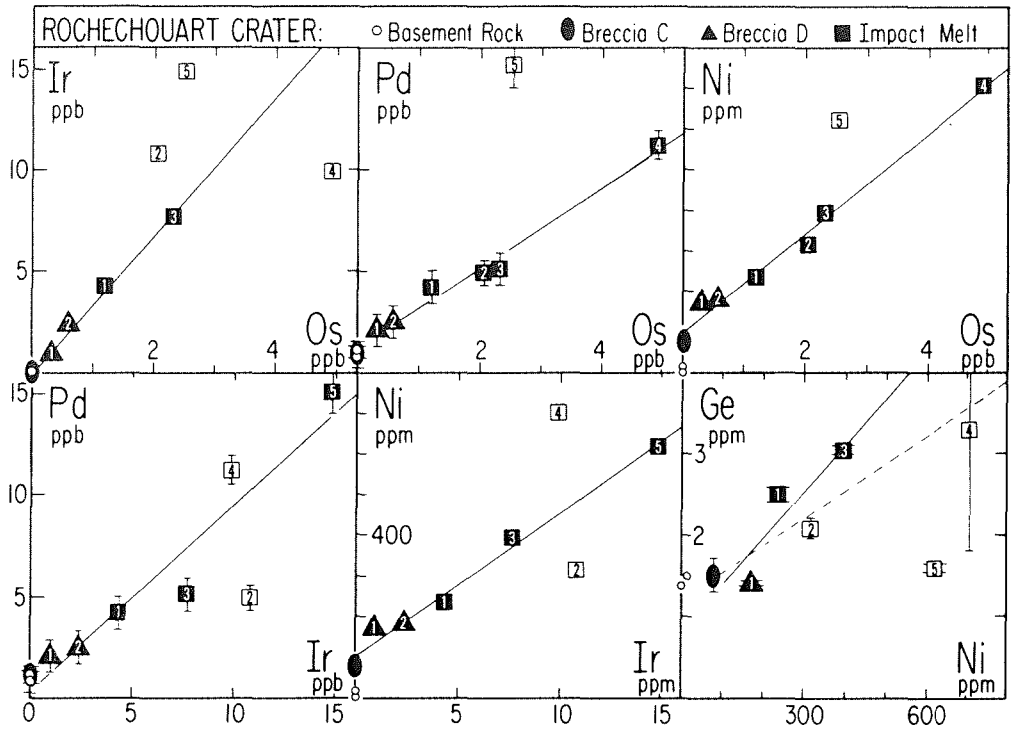


of stones by aerodynamic pressure prevents them from forming craters smaller than 1 km (Öpik, 1961). Because Rochechouart is only the second multi-kilometer crater with an even partially characterized projectile (Mustastin is the other case; Morgan *et al.*, 1975), it is not yet possible to choose between these alternatives.

*References:*

Hawkins G.S. (1963) *Nature* 197, 781.

Morgan J.W., Higuchi H., Ganapathy, and Anders E. (1975) *Proc. Sixth Lunar Sci. Conf.*, Geochim. Cosmochim. Acta, Suppl. 6, 1609-1623.

Öpik E.J. (1961) *Proc. Geophys. Lab. - Lawrence Radiation Lab. Cratering Symp.*, Washington, D.C., March 28-29, 1961, Vol. 2, Paper S, pp.1-28. UCRL Report 6438.

# Numerical Simulation of a Very Large Explosion at the Earth's Surface with Possible Applications to Tektites

Eric M. Jones and Maxwell T. Sandford II
University of California, Los Alamos Scientific Laboratory
Los Alamos, New Mexico 87545

A two-dimensional (cylindrical symmetry) radiation transport/hydrodynamics calculation has been done of a $2.1 \times 10^{25}$ erg explosion at the Earth's surface to show the evolution of the fireball which might be produced by a high velocity impact. An explosion of this energy produces a fireball of size comparable to an atmospheric scale height when the pressure at the impact point has dropped to ambient levels.

For about 60 seconds the low density bubble rises buoyantly but thereafter the bow shock accelerates and reaches 170 km altitude at 120 seconds with particle speeds of 2.5 km/s in the bow shock. The fireball is sucked upward by the bow shock to 115 km altitude at 120 seconds.

Direct shock wave winds exceed 100 m/s for 40 s and reach 26 km from the impact point. Maximum afterwinds (inward surface winds) of 300 m/s occur at 3.5 km range at 40 s. Afterwinds in excess of 100 m/s occur 19 km from the impact point as late as 105 s.

The fan shaped tektite fields downwind of both Reis Crater and Ashanti Crater [1] suggest that tektites, formed during the impact or from rocks carried aloft by the rising fireball, were dropped out of the cloud as it drifted in the prevailing stratospheric winds. We note that at 60 s after the explosion there is 3500 K, $4 \times 10^{-6}$ g/cm$^3$ gas at 40 km altitude moving upward at 1.2 km/s. Seven centimeter radius rock would be held aloft, suspended by drag against gravity.

[1] A. J. Cohen in Tektites, J. A. O'Keefe (Ed.) (Univ. Chicago Press: Chicago), p. 189.

# THE MORPHOLOGY OF EXPLOSION CRATERS WITH CENTRAL UPLIFT STRUCTURES

G.H.S. Jones, Defence Research Board Staff, Ottawa, Canada

The explosion of large charges of TNT on the surface at Suffield, Alberta consistently produced craters with central uplift structures, radial and concentric fracture patterns and the expulsion of fluidised material analogous to secondary vulcanism. Some of these structures have been described (see e.g., refs. 1, 2, 3, 4) but the majority of data are as yet unpublished. This paper discusses the data with special reference to the SNOWBALL crater, produced by the detonation of a 500-ton hemispherical charge on the surface.

Evidence is provided that the role of connate fluids is significant in the production of many features, and may explain the formation of the central uplift. In the specific case of the Suffield craters it is shown that previously unsaturated material was compressed to such an extent that connate water was expelled and entrained particulate matter from levels above the zone of saturation. Hydraulic fracturing by this expelled water explains many of the observed features.

Much of the data obtained in the detailed study of these craters is stratigraphic including the absolute movement of marked elements of the ground at several hundred points within the cratered area. These quantitative data are supplemented by photographic recording of the structures observed during the excavation of the craters. Original data, together with stratigraphic plots and photographs will be made available to delegates at the symposium.

It is shown that while all the available data are consistent the experimental craters show a development hierarchy which results in distinctly different overall visual appearance. Four distinct types may be described as follows:

a. A simple, dome-like central uplift, as demonstrated by several 20-ton craters and the 100-ton DIALPACK 6 tangent sphere explosion.
b. A crater with a central uplift, and some extrusion of fluidised material from the central uplift, forming a single central pseudo-volcanic cone on top of the central uplift. This is illustrated by the 100-ton SUFFIELD 1961 crater.
c. A crater with internal ring structures on the crater floor, with pseudo-volcanic cones superimposed on the ring structures. This stage is illustrated by the PRAIRIE FLAT and DIALPACK craters.
d. A crater with a dominant central uplift, with a depressed rim structure, evident radial and circumferential fissuring both internal and external to the main crater, and pseudo-volcanic cones both internal and external to the main crater. This final stage includes slumping of the crater walls to form internal terracing, and to some extent masking the internal ring structure. This stage is typified by the SNOWBALL crater.

In all observed central uplift craters the ejecta blanket consisted of a coherently overturned, stratigraphically inverted expression of the pre-existing stratigraphy. In the blanket, strata may be traced from the undisturbed position, through a hinge region under the rim, and continuously through the ejecta blanket. In the ejecta the strata, after inversion, suffer radial thinning, but they retain precisely their relative positions even when

the stratum consists of a fine, free flowing sand.

All the craters exhibit circumferential and radial fracturing of the ground surrounding the main crater. In some cases these fractures are accentuated by the injection of fluidised material.

The phenomenon associated with the circumferential fissures internal and external to the main crater is tracable at depth in the form of ring dykes which penetrate the country rock without spreading into sills at the contact with even incompetent strata.

In addition to the ring dykes, there is widespread injection of fluidised material due to hydraulic fracturing.

The material of the central uplift shows signs of tension fracturing, and the injection of fluidised material.

There is evidence of low angle thrust faulting included between the coherently overturned blanket and the undisturbed strata, particularly in the hinge region below the rim.

The ejecta blanket includes fused material deriving from the surface materials, in those cases where the charge was a tangential sphere of explosive.

The floors of the craters are covered by a mantle of fluidised material deriving from locations deep within the structure. In extreme cases, as illustrated by SNOWBALL, regions external to the crater were covered locally by similar beds of ejected fluidised material. These simulate in relative position the magmatic material extruded in the lunar counterparts.

REFERENCES

(1) Diehl, C.H.H. & Jones, G.H.S. "A tracer technique for cratering studies" Jour Geoph Res Vol 70, No. 2, 1965.
(2) Jones, G.H.S. "Prairie Flat Crater and Ejecta Study" DASA Report POR 2115 (1970).
(3) Roddy, D.J., Jones, G.H.S. & Diehl, C.H.H. "Similarities of 100-ton and 500-ton TNT explosions and proposed impact craters". Amer. Geoph. Union. Transactions, Vol 50, No. 4, 1969.
(4) Price, N.J. "Rates of deformation in tectonic processes" Jour of Geol Soc London, Vol 131 (1975).

SINGLE PARTICLE HYPERVELOCITY IMPACT DAMAGE ANALYSIS*, M. E. Kipp, Sandia Laboratories, Albuquerque, New Mexico, 87115.

The normal impact of a spherical particle with a thick plate results in damage to the plate in the form of crater formation and perhaps spallation. To determine the extent of this damage, spheres of low density polyethylene were launched at velocities of $\sim$ 5 km/s against targets of 6061-T6 aluminum. Three different sphere diameters (2.5, 4.0, 10.0 mm) and target thicknesses (7.5, 12.0, 30.0 mm) were used retaining in each case a ratio of sphere diameter to target thickness of 1:3. A diffuse surface interferometer was used to obtain back-surface velocity histories with time resolution on the order of $\pm 5$ ns. This data may be used as a basis for comparison with wavecode calculations, and is a more stringent criterion for code and material model analysis than post-mortem comparisons of crater and spall dimensions (1).

The use of three scaled geometries allows for an experimental evaluation of scaling of crater and spall size. For example, comparing results for the 10 mm and the 2.5 mm sphere cases, the ratio of sphere sizes (and target plates) is 4.0, the ratio of crater widths is 5.0, the ratio of crater depths is 4.5, and the ratio of spall lengths is 8.6. The spall size appears to be in greatest conflict with a geometric scaling relationship.

Two-dimensional Eulerian (CSQ) and Lagrangian (TOODY, with rezoning) wave propagation codes were used to numerically simulate the material behavior in the hypervelocity impact. Both codes solved the 2.5 mm sphere/7.5 mm target problem, with the intent that the results could then be geometrically scaled to the remaining two cases. For example, the crater width in the 10 mm sphere case was 25 mm experimentally, 28 mm from TOODY, and 25 mm from CSQ, the two latter dimensions being scaled from the numerical results.

It has been shown experimentally that in 6061-T6 aluminum, spall formation is dependent upon pulse width (2). Geometric scaling of code solutions is not then expected to predict proper damage levels. Instead, separate solution of each geometry is required. Such an attempt was made using a form of cumulative damage failure model. This model was used in the TOODY solution seen in Figure 1. The slight reloading at 6.3 $\mu$s is a result of the formation of internal damage (spall). The CSQ history, shown in the same figure, employed a simple minimum failure stress criterion. The experimental record in the figure indicates that the damage occurs over a short time interval and that the material models used are providing nearly the proper behavior. Such records are seen as necessary to properly evaluate both the damage and material models that wavecodes employ for hypervelocity impact damage analysis.

---

*This work was supported by the U. S. Energy Research and Development Administration.

# SINGLE PARTICLE HYPERVELOCITY IMPACT DAMAGE ANALYSIS

Kipp, M. E.

1. J. Lipkin and M. E. Kipp, J. Appl. Phys., 47, No. 5, May 1976.
2. F. R. Tuler and B. M. Butcher, Int. J. Frac. Mech., 4, No. 4, 1968.

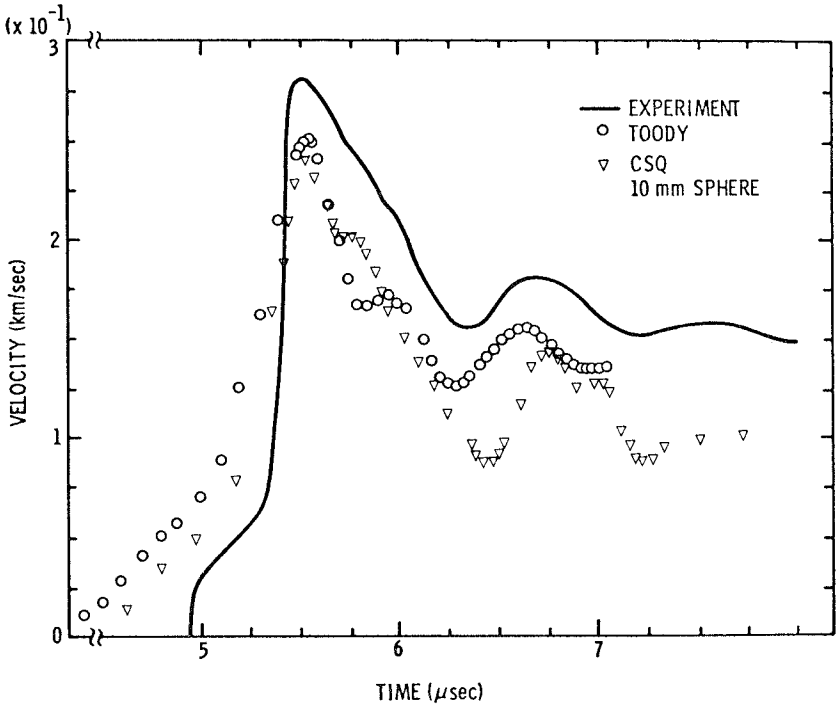


FIGURE 1. COMPARISON OF BACK SURFACE VELOCITY FOR 10mm SPHERE IMPACT

THE METEORITIC CONTAMINATION IN THE ROCHECHOUART CRATER: STATISTICAL GEOCHEMICAL INVESTIGATIONS - P. Lambert, B.R.G.M., B.P. 6009, 45018-Orleans-Cedex - France.

Rochechouart structure (France 45°50'N, 000°16'E) is a deeply eroded impact crater. Only subsists the bottom where are preserved remnants of fall back breccias and melt rocks (fig. 1). Impact occured probably during Middle Jurassic (1). Crater size was between 20-35 km diameter (fig. 1).

Preliminary studies of 50 Rochechouart samples by atomic absorption spectrometry (A.A.S.) indicated a strong Ni enrichment of impact melts with respect to metamorphic and granitic basement rocks (2). 190 new analyses were performed using the same method (fig. 2). The Ni enrichment is confirmed: impact melts (E) have the highest Ni content (some values reaching 600-700 ppm). Their average Ni content is ten times greater than the target one It is five times greater for suevite (D). Polymict breccias C (as "Bunte" breccias from Ries), also show a weak Ni enrichment (factor 2.5). Symphatical variations of Fe and Ni have been observed in Ni rich impact melts (fig. 2), whereas Mg remains constant.

Examination of Mg/Fe ratio of Rochecouart breccias with respect to the one of Rochechouart basement rocks involve that Ni enrichment cannot be due to the contribution from some Ni rich crystalline rocks (as serpentinite) or from any endogenic contamination. The hypothesis of meteoritic origin for Ni is the most convenient as yet suggested by preliminary results (2). Selected samples from each rock type were studied by E. Anders' team for siderophile trace elements. Ni contamination of impact formations was confirmed. The nature of the Rochechouart projectile may be deduced: IIA iron (see this volume (3)). Its composition is supposed to be: Fe: 94.5%, Ni 5.5% from the average of 47 IIA iron meteorites.

Figure 3 gives the distribution of Ni into the whole fall back unit. Ni enrichment is the highest in the centre of the structure, but the distribution is very heterogeneous. There is no regular decrease from the centre to the periphery. The Ni distribution was correlated with the intensity of shock effects into the autochtonous rocks lying just below the crater floor. The Ni distribution is not symmetric. The highest values occur into a band oriented NE-SW.

Selected impact melts (E), suevites (D) showing a significative Ni enrichment were sampled with respect to the glass fraction and clasts from the basement. 140 analyses were performed by A.A.S., but only for Ni recovery (fig. 4). Results clearly indicate that Ni distribution is also very heterogeneous on the scale of one hand sample. Usually Ni is more concentrated in the glass fraction, but clasts always show a higher Ni content in comparison with the autochtonous basement. Sometimes Ni is more abundant in the clast fraction than in the glass (fig. 4). The results imply that meteoritic material was originally located only (or mostly) in the glass fraction. Later Ni moved and was concentrated in basement clasts, reaching breccias without glasses (C).

At this time NiFe spherules, or other metallic particles have never been observed in polished sections from Ni rich breccias. Microprobe analyses of of glasses were performed in order to determine the mineralogical setting of

ROCHECHOUART CR. : STAT. GEOCHEM. INVESTIGATIONS

Lambert P.

Ni and to detect kinds of Ni dispersion and concentration. All Rochechouart glasses from impact melts are recrystallised, essentially in a mixture of K feldspar and quartz (fig. 5). Ni was not detected in these minerals. In most cases Ni is relatively concentrated (about 0.5%) in secondary chlorites filling cavities and bubbles. Sometimes are detected higher Ni contents (1-3%) in secondary limonites (fig. 5). It is noted that limonites have chemical composition very near the projectile one. Exceptionally was found an automorphous bravoite (Ni = 13% Co = 0.7%) (fig. 5) surrounded by limonite The Ni/Co ratio of this bravoite is near 19.5 which is closely the cosmic ratio.

Discussion.

The disymmetric distribution of the Ni enrichment in allochtonous breccias suggests a preferential distribution of the meteoritic material in these breccias. This feature could be explained by an inclined trajectorie of the Rochechouart projectile. It may be supposed that the meteorite was coming from NW or SW.

Actually NiFe spherules were never detected in Rochechouart breccias. The most probable explanation is their entire destruction during 165 Myr by weathering and oxydation. Even in fresh glass (Aouelloul) where spherules are found, the Ni content varies from < 2 to 9% (4) suggesting reactions with glasses. The particular setting of Ni in secondary minerals, in basement clasts and in polymict breccias involve the Ni mobility and the partial or entire destruction of the original meteoritic material. However, this mobility was not too strong as Ni enrichment is only restricted to the fall back breccias (rocks lying under the crater floor show a normal Ni content). Ni in chlorites represents probably the latest stage of Ni "dilution". Limonites are nearer the meteorical material and their origin may be due to the oxidation of NiFe spherules. In the Ni-Co poor milieu as in the granite-gneiss melt of Rochecouart, Ni, Co could have been trapped by sulfurs as bravoite with preservation of the meteorite Ni/Co ratio.

Considering the composition of the Rochechouart meteorite, the Ni content of each breccia type and the basement one, it may be deduced that the contamination by meteoritic material was about 0.2% in impact melt rocks, 0.085 in D breccias and 0.045 in C breccias.

References:

(1) Lambert P. (1974) - La structure d'impact de météorite géante de Rochechouart. Doc. spec., Univ. Paris-Sud, 148 p.

(2) Lambert P. (1975) - Nickel enrichment of impact melt rocks from Rochechouart. Preliminary results and possibility of meteoritic contamination. Meteoritics, vol. 10, n° 4, pp. 433-436.

(3) Janssens M.J., Hertogen J., Takahashi H., Anders E., Lambert P. (1976) - Meteoritic material in the Rochechouart crater. In "Abstracts contributed to the Symposium on Planetary Cratering Mechanics" pp. . The Lunar Science Institue, Houston.

(4) Morgan J.W., Higuchi H., Ganapathy R., Anders E. (1975) - Meteoritic material in four terrestrial meteorite craters - in "Proceeding Sixth Lunar Science Conference".

# ROCHECHOUART CR. : STAT. GEOCHEM. INVESTIGATIONS

Lambert P.

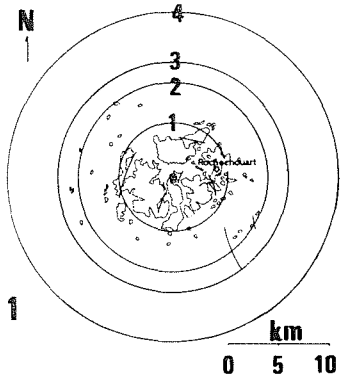


1

| | N | Fe°/₀ | s | Mg°/₀ | s | Ni ppm | s |
|---|---|---|---|---|---|---|---|
| gneiss | 22 | 3.51 | 1.00 | 1.01 | 0.36 | <14 | 8 |
| orthogneiss | 8 | 1.12 | 0.44 | 0.20 | 0.12 | ω 2 | |
| granite | 15 | 0.77 | 0.65 | 0.17 | 0.17 | ω 2 | |
| rock source | | 2.50 | | 0.60 | | ω 9 | |
| breccias C | 43 | 2.70 | 1.12 | 0.70 | 0.32 | 26 | 16 |
| breccias D | 49 | 2.85 | 1.17 | 0.73 | 0.63 | 48 | 34 |
| impact melts E | 50 | 2.54 | 1.25 | 0.41 | 0.34 | 105 | 135 |
| impact melts E (Ni > 30ppm) | 27 | 2.91 | 0.46 | 0.60 | 0.38 | 202 | 169 |

2

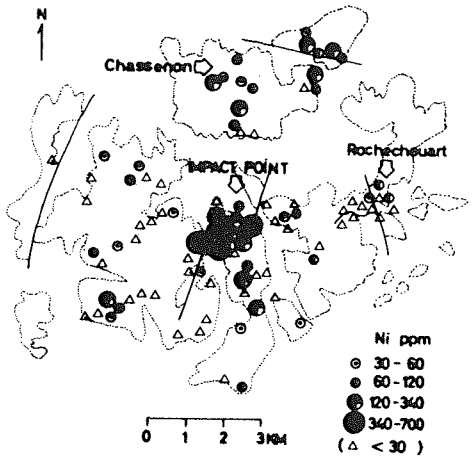


3

| reference | breccias | glass % | glass only N | Ni ppm | s | glass except N | Ni ppm | s |
|---|---|---|---|---|---|---|---|---|
| 4A | D | 30 | 9 | 160 | 38 | 6 | 76 | 58 |
| 101 | D | 30 | 2 | 250 | 140 | 3 | 77 | 64 |
| 377 | D | 10 | 2 | 150 | 90 | 2 | 82 | 4 |
| 919 | D | 10 | 2 | 45 | 14 | 2 | 25 | 7 |
| 948 | D | 5 | 2 | 183 | 25 | 3 | 75 | 30 |
| 950 | D | 15 | 3 | 58 | 25 | 2 | 37 | 4 |
| 9 | E | 60 | 6 | 98 | 50 | 6 | 43 | 50 |
| 203 A | E | 65 | 1 | 260 | | 1 | 210 | |
| 203 E | E | 85 | 4 | 567 | 50 | 1 | 20 | |
| 229 B | E | 50 | 10 | 254 | 143 | 3 | 492 | 114 |
| 447 A | E | 90 | 3 | 480 | 200 | 2 | 180 | 5 |
| 463 B | E | 50 | 2 | 98 | 3 | 3 | 205 | 131 |
| 931 B | E | 40 | 3 | 83 | 6 | 2 | 75 | 14 |
| 932 B | E | 80 | 6 | 276 | 40 | 3 | 218 | 148 |
| 939 A | E | 90 | 4 | 121 | 52 | 1 | 35 | |

4

| | secondary K-feldspar % | c.f. | % | c.f. | secondary chlorite % | c.f. |
|---|---|---|---|---|---|---|
| SiO2 | 63.74 | 2.990 | 65.00 | 3.029 | 42.32 | 8.1298 |
| TiO2 | – | – | – | – | 0.06 | 0.0087 |
| Al2O3 | 18.26 | 1.0090 | 17.49 | 0.9604 | 12.78 | 2.8938 |
| Fe2O3 | | | | | | |
| FeO | 0.21 | 0.0087 | 0.06 | 0.0022 | 10.55 | 1.6950 |
| Cr2O3 | 0.01 | 0.0006 | – | – | – | – |
| MnO | – | – | – | – | 0.23 | 0.0374 |
| MgO | 0.04 | 0.0026 | – | – | 18.68 | 5.3493 |
| CaO | 0.11 | 0.0056 | 0.02 | 0.0012 | 1.08 | 0.2223 |
| Na2O | 0.23 | 0.0210 | 0.11 | 0.0096 | – | – |
| K2O | 15.98 | 0.9564 | 16.60 | 0.9867 | 0.64 | 0.1569 |
| H2O | – | – | – | – | 12.47 | 8.0000 |
| NiO | 0.02 | 0.0008 | – | – | 0.51 | 0.060 |
| TOTAL | 98.59 | 4.9945 | 99.27 | 4.9891 | 99.32 | 26.55 |

| | secondary limonites (crystallochemical formula of goethite) % | c.f. | % | c.f. | % | c.f. |
|---|---|---|---|---|---|---|
| Fe2O3 | 85.95 | 1.9424 | 87.19 | 1.9659 | 89.30 | 1.9813 |
| FeO | | | | | | |
| NiO | 3.44 | 0.0864 | 2.04 | 0.0511 | 1.14 | 0.0281 |
| H2O | 9.97 | 1.0000 | 10.00 | 1.0000 | 10.16 | 1.0000 |
| TOTAL | 99.36 | 3.0288 | 99.23 | 3.0170 | 100.60 | 3.0094 |

| | secondary bravoite % |
|---|---|
| S | 51.05 |
| Fe | 29.90 |
| Co | 0.69 |
| Cu | 0.20 |
| Ni | 13.27 |
| Total | 95.11 |

5

Fig. 1: Extent of Rochechouart breccias:
circle 1: impact melts occurrence
circle 2: minimum crater diameter
circle 3: most probable size
circle 4: maximum crater diameter

Fig. 2: A.A.S. analyses: $\overline{Fe}$, $\overline{Mg}$, $\overline{Ni}$, average contents of rock types from Rochechouart basement and from fall back breccias (breccias C for polymict rocks without glass, D for suevites). s: standard deviation. Rock source is determined from the actual extent of each rock type of the basement, in the estimated area of the crater (circle 2 or 3, fig. 1): gneiss ≃ 50%, granite ≃ 25%, orthogneiss ≃ 25%.

Fig. 3: Ni distribution in fall back breccias of the Rochecouart structure (dashed line: breccias extent, full line: faults).

Fig. 4: A.A.S. analyses - Variation of Ni (in ppm) in the glass fraction and basement clasts of suevites (D) and impact melts (E).

Fig. 5: Microprobe analyses of several phases in the recrystallised impact melt n° 447A - ($\overline{Ni}$ = 480 ppm, $\overline{K}$ = 8.60%) - ($H_2O$ calculated).

SIMPLE Z MODEL OF CRATERING, EJECTION, AND THE OVERTURNED FLAP

D. E. Maxwell, Science Applications, Inc., Oakland, CA 94621

A study of flow fields in the earth following a surface burst revealed surprisingly simple features which provided the basis of the so-called "Z" models of cratering and ejecta. The simplest of these models is described briefly and then applied to unfold the cratering and ejecting lip of a small and large case of energy release. The ejecting lip is followed in detail as it grows, slows, and falls back to the earth as an overturned flap about a hinge. The model results are compared to experimental data and good agreement is obtained.

FINITE TARGET HYPERVELOCITY IMPACT MEASUREMENTS AT MICROSCALE DIMENSIONS - IMPLICATIONS FOR REGOLITH IMPACTS

J.A.M. McDonnell, Space Lab., The Univ. of Kent, Canterbury, Kent, U.K.

1. INTRODUCTION Calculations on the lifetime of a single rock exposed on a planetary surface due to erosion by fine particle hypervelocity abrasion and single impact catastrophic rupture have been well represented[1,2,3,4], as also the turnover rate of a rock assembly (regolith gardening[5]). Hypervelocity impact laboratory measurements used to support these calculations have generally proved acceptable where validation has been possible: centimetre scale rock rupture calculations have shown good agreement with cosmogenic dating[5] for example, but surface grain and microcrater lifetimes have had less opportunity for validation. Rock lifetime calculations generally use light gas gun data at gram scale masses, grain and microcrater calculations electrostatic accelerator data at picogram scale. Restriction of the available impact measurements has generally led to a 'borrowing' of data across these 12 magnitudes of mass and also extrapolation. This paper presents observational features of cratering mechanics at 5μm to 100μm scale, in particular finite target effects, and then considers incorporation into a regolith impact scene.

2. EXPERIMENTAL MEASUREMENTS. *Impact Comminution Distribution*. Data has recently been presented on $10^{-11}$g impacts on a rough lunar rock[6]. An important conclusion of this 'average' comminution distribution is the concentration of mass towards the largest ejecta sizes - most mass is ejected at a frequency of less than unity normalised to 1 impact. Impact ejection of spall is thus considerably enhanced by unusual impact conditions. One concludes that either (1) grain boundary or edge proximity or (2) impact on surface grains or convex features leads to enhanced spallation.

*Finite Target Effects - Single Edge Proximity*. In impacts on a polished lunar sample (14310) Figs.1(a), and 1(b) in proximity to grain boundaries of

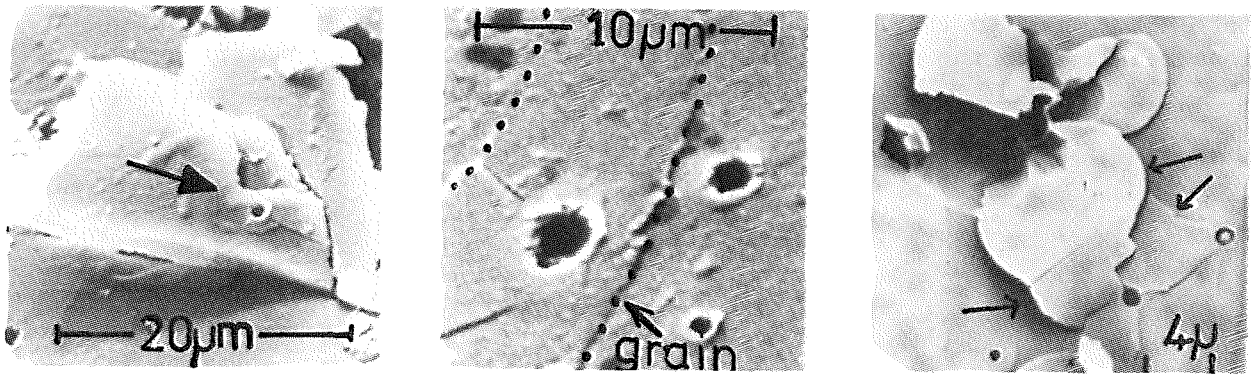


Fig.1 (a) Hypervelocity microsphere impacts ($4Kms^{-1}$-$15Kms^{-1}$) on Apollo 14310 on an elevated chip and (b) near grain boundary. Boundary or edge proximity enhances spall ejection probability. From the chip impact 1(a) a catastrophic rupture limit of ≤4 times the primary crater diameter is suggested. Multiple impacts on quartz 1(c) shows interaction again leading to enhanced ejection of matter but no increase of the area of damage. High surface adhesion characterises impacts at μm dimensions.

# FINITE TARGET IMPACT EFFECTS

McDonnell, J.A.M.

impact sites, shows evidence of stress relief after primary crater formation. With a flat surface little shocked material is ejected. Radial fractures show a maximum extension of ~50% towards grain boundaries; such boundaries generally terminate the strain fractural and enhanced spallation results from an intersection of two or more radial fractures with the boundary to liberate a wedge.

*Finite Target Effects - Catastrophic Grain Rupture*. In Fig.1(a) two impacts are formed on a previously raised chip - essentially free standing. Termination of radial features at the edge is evident without significant mass ejection or destruction of the chip entity. The major fracture on the chip was present before impact. At cm. scale impacts a critical destruction diameter of 10 x the primary crater diameter is accepted[4], but from this micron scale impact a maximum limit of $\lesssim 4$ is inferred.

*Multiple Impact Interaction*. Conditions where previous impacts are within the semi infinite target spall damage area (1(c)) on a quartz sample are seen to lead to an increased uplift (arrowed); again very little extension of the radial fractures results. In the nonlinear interaction of multiple impacts at micron dimensions, experimental evidence points to increased local damage but a non-extension of the area of damage.

*Impact on a Non-Cohesive Small Particle Assembly*. We have no new evidence here but refer to work of Stöffler et al[7] using .3g projectiles at 6Kms$^{-1}$ to 7Kms$^{-1}$ on quartz sand. A displaced mass of 2Kg results, which is now energy scaled to $6.10^4$ times the incident mass at lunar impact velocities.

3. RELATIVE FREQUENCY OF IMPACT CLASSES ON A REGOLITH. Data from photographic analysis of the Apollo 16 site[8] gives exposed rock frequencies at stations 4,5 and 6. An average is taken for diameters >10cm to derive the probability of impact on rocks of these dimensions. From lunar fine analyses[9] the mass content for mass magnitude is derived and by using Rosiwals principle[10] extended to the fractional area exposed. Using the volume content of fines relative to the soil[11] (composing 85%-90%), it may be normalised to an

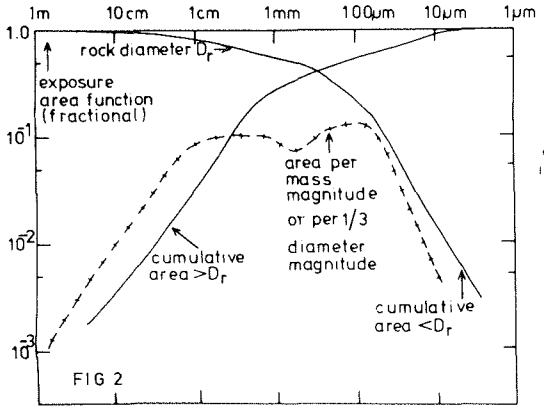


Fig.2 The derived area exposure function of the lunar regolith per magnitude of incident mass from photographic Apollo site data and soil analyses using Rosiwal's principle.

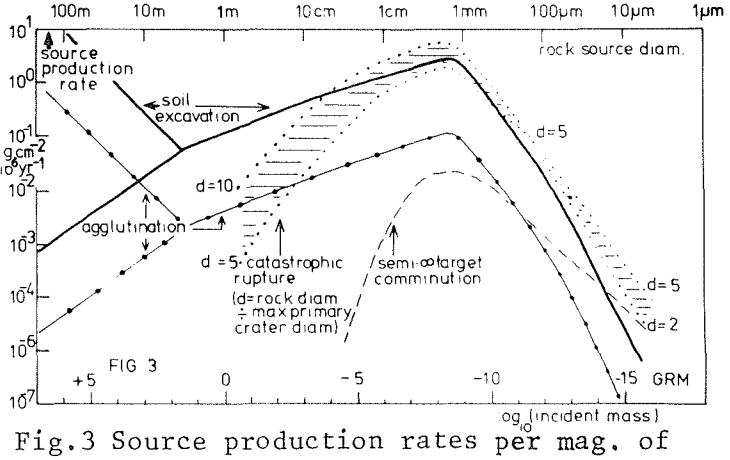


Fig.3 Source production rates per mag. of incident meteorite mass corresponding to the lunar regolith area function(Fig.2). At μm scale the predicted agglutination rate is insufficient to lead to typical soil compositions.

FINITE TARGET IMPACT EFFECTS

McDonnell, J.A.M.

integral of unity for the total exposure area function. An intermediate interval of rock dimensions from 1cm-10cm is analysed from comparison of the Apollo 16 photographic data residue(the fractional rock area beneath the resolution limit)and the trench soil analysis[11], which is more typical of rocks of diameter >1cm. The total derived exposure area friction is shown in Fig.2. From this function the relative number of catastrophic impacts, semi-infinite target impacts and soil displacement impacts is calculated using meteorite fluxes corresponding to Gault's "best estimate" and McCrosky's Prairie Network data[5]. Fig.3 summarises results showing the source functions expected. Catastrophic rupture source production dominates over semi-infinite target cratering but the two approach at dimensions <10μm. Excavation and agglutination exceed all impact comminution at 1m target dimensions but at <10cm catastrophic rock destruction exceeds agglutination and is comparable to excavation. Agreement with existing gardening calculations[5] is good at large(>mm)dimensions. At smaller dimensions implications gain more interest. Comminution appears to be the major source and yet in lunar soils 100μm grain size components comprise only some 50% fresh chips. Agglutinates and glass are in good proportion, so where is the source? We have two possibilities,(a) that microscale agglutinates and glass are formed from large impacts(>10m) where the excavation rate is abundantly high according to McCrosky's flux but not according to Gault's or (b) that the agglutination limit of 4% of displaced mass from Stöfflers work increases very markedly at microscale dimensions. Experimental evidence is clearly needed, but present evidence on the decrease of catastrophic rupture limit with decreasing dimensions does seem to be required if the calculations are to agree with soil content analyses.

ACKNOWLEDGEMENTS: To the Science Research Council(U.K.) for financial support, to R.C.Jennison for laboratory facilities, to W.C.Carey for the data in Fig. 1(c) and Miss D. Paine for manuscript preparation.

REFERENCES: (1) D.E.Gault(1969).Trans.Am.Geophys.Union 50,p219. (2) J.A.M. McDonnell & D.G. Ashworth(1972).Space Res.XII,p333-347. (3) F. Hörz, E. Schneider & R.E. Hill(1974).Proc.5th Lunar Sci.Conf.3,p2397-2412. (4) F.Hörz, E.Schneider, D.E.Gault, J.B.Hartung, D.E.Brownless(1975).The Moon 13,p235. (5) D.E. Gault, F. Hörz, D.E. Brownlee & J.B. Hartung(1974).Proc.5th Lunar Sci.Conf.3,p2365. (6) J.A.M. McDonnell & R.P. Flavill(1976).Proc.7th Lunar Sci.Conf.3,(in press). (7) D. Stoffler, D.E. Gault, J. Wedekind & G.Polkowski (1975).J.Geophys.Res.80,p4062-4077. (8) W.R. Muehlberger et al(1972).Apollo 16 PSR§6. (9) J.C. Bulter, G.M. Greene & E.A. King(1973).Proc.4th Lunar Sci.Conf. 1,p267. (10) A. Rosiwal(1898).p147-175,Vienna. (11) Apollo 14 PE Team(1971), Apollo 14 PSR§5.

CRATER MODIFICATION BY GRAVITY: A MECHANICAL ANALYSIS OF SLUMPING.
H.J.Melosh, Division of Geological and Planetary Sciences, Caltech, Pasadena, California 91125.

The morphology of fresh craters on the moon shows a regular dependence on the crater's size(1). Thus, small fresh craters tend to be bowl-shaped, while slump terraces and central peaks begin to appear in the 10-30 km. size range. Craters larger than 200km. acquire multiple mountain rings. In the intermediate size range, the appearance of slumps on the walls and central peaks coincides with a marked kink in the depth/diameter curve, slumped craters tending to be shallower than bowl-shaped craters(2). This phenomenon has long been attributed to gravity induced mass movements which fill the impact crater shortly after its formation(3). This hypothesis is further supported by studies of fresh craters on Mercury(4) which exhibit the same features at smaller sizes than the corresponding lunar craters, in accordance with Mercury's two times larger surface gravity.

The present study was undertaken to evaluate the effect of gravity in the modification of fresh craters more fully. Impact craters are mechanically quite stable. A crater with a depth/diameter ratio $\lambda$=1/6 (which is typical for small, fresh craters) has an average internal slope of only 18°. Thus, even if the crater were produced in a cohesionless powder, we would not expect major slumping to occur unless the angle of internal friction of the powder were less than this. In fact, most dry rock powders have angles of internal friction in the 35°-45° range(5).

This argument still allows a small amount of slumping near the crater rim where slopes may locally exceed 35°, but it does not allow us to explain the observed large scale slump features. We thus conclude that the observed slumping requires more than gravity: it also requires a reduction in the internal friction of the material the crater formed in.

Given this reduction in internal friction, the inherent shear strength of the target rock must also be overcome. An estimate of this shear strength can be obtained by dividing the weight of the material excavated from the crater ($\frac{\pi}{8} \rho g \lambda D^3$ for a crater of diameter D with a parabolic profile) by the area of a hemisphere ($\pi D^2/2$) enclosing the crater. The result, $\sigma = \rho g D \lambda / 4$ implies that the shear strength of lunar rock must be less than 60 bars to allow the collapse of a 30 km. diameter crater (with initial $\lambda$=1/6).

These requirements show that if gravity induces major modifications of fresh craters, then the target rock must have very unusual properties at the time of the impact. Both the cohesion and the internal friction of the rock must be reduced to very low values. There are several approaches to this situation:

(a) We can deny that gravity makes important modifications to craters, explaining the observed kink in the depth/diameter curve in some other way. This approach is advocated by some authors.

(b) Slumping may accompany the rarefaction wave as it passes through the target. This would eliminate the overburden (thus reducing the apparent internal friction), and perhaps

MECHANICAL ANALYSIS OF SLUMPING

H. J. Melosh

shattering of the rock would reduce its shear strength as well.

(c) Heating of the target rock might reduce both internal friction and shear strength (but it is not clear that enough of a reduction can be obtained under reasonable conditions).

(d) The effective internal friction and shear strength may not be the same over geologic time as they are in the laboratory. If this is the case the crater will collapse slowly, over millions of years.

In all cases except (a) we can learn more about both the nature of crater collapse and the material properties required for it by considering a simplified model. We ask what is the manner of collapse under gravity of a parabolic hole (diameter D, depth $\lambda D$) in a material with zero internal friction and shear strength c. One may argue that if (b) is the correct situation, the stress fields will be far more complex than those of our model. Our philosophy in this case is to see how far the static collapse model can go toward explaning the observed features, without invoking the complexites of dynamic stress fields. We shall see that the static collapse model does yield some insight into how craters actually collapse.

The model described above is a problem in perfect plasticity, for which standard numerical techniques exist for plane-strain (6). These techniques were modified for axial symmetry (7). The method assumes that failure has occured (shear stresses equal c) inside the crater basin. This assumption, along with the stress equations of equlibrium, allows the slipline field to be integrated outward from the crater basin. Failure along a particular slipline is judged by whether or not the normal stress at the surface required to produce failure is tensional (failed) or compressional (not failed). If extra normal stress is required to keep the line at failure, then failure has not occured and the computaion is halted. The initial assumption that failure has occured in the crater is thus justified in an a posteriori fashion. An example of the slipline field generated by such a computation is shown in Figure I. The solid lines are sliplines that have failed, whereas the dotted lines would fail only if an extra overburden were applied at the surface (depth=0). In this case the slope of the crater wall has failed. Velocity vectors parallel the sliplines which run from the crater's interior to the surface. This sort of failure resembles the classic Swedish-circle slump of clay embankments familiar to Civil Engineers (6).

A suite of models of this form has been computed in order to determine the conditions under which failure takes place and the nature of the failure when it occurs. All of these models are characterized by a combined gravity-strength-size parameter $\gamma = \rho g D/c$, and the crater depth/diameter ratio $\lambda$. Notable results at the time of writing are:

(a) There are two types of failure: Slope failure (Fig. I), where

a section of the wall slides into the crater, and base failure where the upper lip again slides down, but the floor of the crater is uplifted as a more or less rigid plug. In base failure the lowest slipline intersects the axis r=0. Base failure occurs at larger $\gamma$ and smaller $\lambda$ than slope failure.

(b) In all cases the crater is only slightly enlarged by the collapse, the sliplines converging at a radius only 20-30% larger than the original crater.

Work is in progress at the present time to map out regions of the various types of failure in ($\gamma$, $\lambda$) space, and also to consider the effect of a small amount of internal friction.

REFERENCES

(1) K.A.Howard, Proc.LSC V, vol.1 pp67-79(1974). (2) R.J.Pike, Geophys. Res. Lett. 1, 291(1974). (3) W.L.Quaide, D.E.Gault, R.A.Schmidt, Ann.N.Y.Acad.Sci. 123, 563(1965). (4) D.E.Gault et al., J.G.R., in press. (5) Carson and Kirkby, Hillslope Form and Process, Cambridge U. Press, 1972. (6) R.F.Scott, Principles of Soil Mechanics, Addison-Wesley, Mass., 1963. (7) H.J.Melosh, to be published

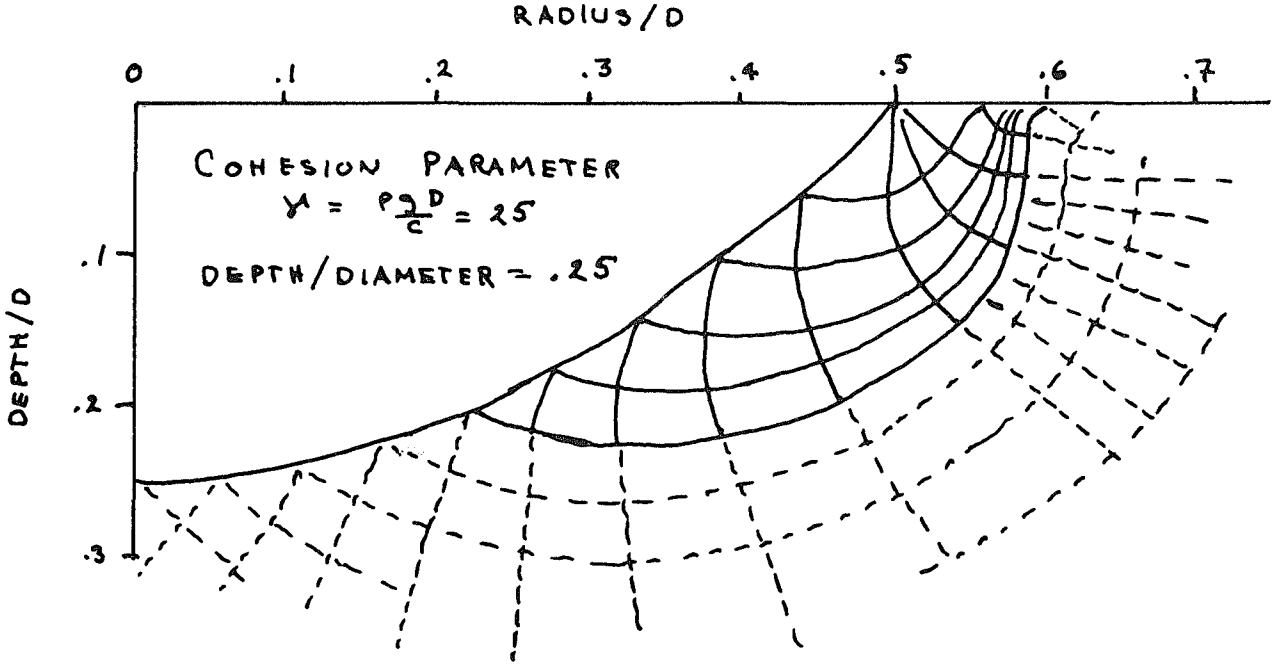


FIGURE I SLOPE FAILURE

EJECTA DYNAMICS OF HIGH-SPEED IMPACT CRATERS; R. H. Morrison, LFE Corp., Richmond, CA 94804; and V. R. Oberbeck, NASA-Ames Research Center, Moffett Field, CA 94035

The ejecta dynamics of high-speed impact craters is of special importance to studies in planetology concerned with regolith dynamics and with interpretation of the origin of deposits and formations surrounding large craters and basins. To investigate this phenomena, high-speed impact experiments were conducted into particulate targets. Such targets are analogues for the lunar regolith, and impact experiments into these targets provide a reasonable basis for understanding ejecta transport from large cratering events. Results are presented in this paper for impacts into quartz sand targets of two different grain sizes and at two different impact velocities: 1.5 km/sec and 5.6 km/sec. The results are applied to nuclear explosion cratering, and they are used to support a previously published theoretical model for transport and emplacement of ejecta from large lunar impact craters and basins. The results are then used to relate the locations of ejecta masses before excavation to their locations in the ejecta plume and crater deposits. Finally, a model is developed for explaining the inverted stratigraphy observed in the rims and deposits of impact craters.

The experiments were conducted in the Ames Vertical Gun Ballistic Range. Plastic cylinders (0.43 g mass) were fired into the targets in a direction normal to the surface. The targets were located in a large chamber evacuated to pressures less than 1 mm Hg of air. A high-speed movie camera having a framing rate of 7000 frames per second recorded the ejecta plumes of the impact craters. The plumes were dissected by a plate placed vertically across the target pan near the final crater rim with a knife edge slit in the middle of the plate that permitted only a portion of the plume to pass through (1). For the experiments with coarse-grained sand, this setup was sufficient to allow determination of the particle trajectories. However, to determine the particle trajectories for the fine-grained sand, it was necessary to dissect the plumes even further by placing wires horizontally across the slit. In this case, the boundaries at the leading edge of the ejecta sheet of the ejecta masses that passed through the slit and between the wires were traced to infer the particle trajectories.

Results show that material is ejected from a high-speed impact crater into ballistic trajectories and that it assumes the shape of a relatively thin conical sheet which expands radially from the crater rim. Although angle of ejection varies only slightly as the cratering event proceeds, ejection velocity decreases significantly. Material near the impact point is ejected early at high velocity and is found high in the ejecta sheet and at large radial range in the crater deposits, whereas material near the crater rim is ejected late with low velocity and is found low in the sheet and just outside the rim. All ejecta impact at the base of the sheet from ballistic trajectories at progressively higher velocities as the sheet expands from the crater rim. However, at any given radius, ejecta impact for only a very short time. At a certain distance, the impact velocities of the ejecta become sufficient to cause significant ricochet of ejecta from the surface and kicking up of surface material. This produces a debris surge that has a lower speed

and a much lower angle than the ejecta sheet and that follows the sheet across the target surface. Thus, crater deposits are produced first at the rim and then at greater range.

The laboratory impact cratering experiments simulate much of the phenomena associated with certain nuclear explosion craters. The ejecta plumes for the impact craters resemble that of Teapot Ess, a nuclear explosion crater produced by a burst equivalent to 1.2 kilotons of TNT at a scaled depth of burst of 0.20 $m/(kg)^{1/3}$ in desert alluvium. This scaled depth of burst is in the range of those which have been found to simulate impact (2). Moreover, the laboratory debris surges are analogous to the base surge observed for this event, except for the fact that material in the base surge was carried along the surface in an aerosol cloud. Therefore, the ejecta dynamics of impact craters and explosion craters with certain scaled depths of burst may not vary significantly for craters differing in size over several orders of magnitude (2).

Propagation of the ejecta sheet for the laboratory craters also compares with that calculated by Oberbeck (2) for ejecta of the lunar crater Copernicus. Although the ejection angles for Copernicus ejecta vary and are much smaller than for the laboratory craters, the essential characteristics of the ejecta plumes are the same. Moreover, the debris surges observed experimentally verify the existence of the debris surge hypothesized for the Copernicus crater event. Therefore, the experiments support the theoretical model of Oberbeck (2) for transport and emplacement of ejecta from large lunar craters and basins.

The experimental results were used to develop a schematic model for ejection, ballistic transport, and emplacement of material originally in spherical segment shells within the crater cavity. According to the model, material from the spherical segment shell nearest the impact point is shocked to the highest pressures, exits the target nearest the impact point at the highest velocity, and therefore is found at positions highest in the ejecta curtain and at greatest range in the deposits on the target surface. Conversely, material from a shell at greater radius is shocked to lower pressures, exits the target farther from the impact point at lower velocity, and is found at lower positions in the ejecta curtain and at distances nearer the final crater rim. Only for a shell very near the impact point is all of the material in the shell ejected. For a shell farther from the impact point, some of the material in the shell is not ejected but is trapped in the crater, even though the material may have been shocked sufficiently to have become molten after release from the induced pressures. The model is therefore compatible with the experimental results of Stöffler et al. (3), who found large amounts of shocked and melted material in the crater, but found that of the material ejected, the percentage of shocked material in the ejecta increased with increasing distance from the crater rim.

The experimental results were also used, together with the above model, to derive a schematic model that explains the development of the inverted stratigraphy observed for natural meteorite craters, such as Meteor Crater (4), and

EJECTA DYNAMICS

Morrison, R. H. et al.

laboratory impact craters (5). Inverted strata are explained as being the natural consequence of ejection and ballistic transport of material from the different strata in an orderly sequence. This results from a systematic decrease in particle velocity behind the radially decaying shock wave, produced by the impact, and from a systematic release of the shock pressures across particles in the target and turning of particles by the radial rarefaction waves in the flow of material behind the shock wave.

References

(1) Morrison R. H. and Oberbeck V. R. (1975) EOS: Trans. of Am. Geophys. Union 56, 1015.
(2) Oberbeck V. R. (1975) Rev. of Geophys. and Space Physics 13, 337-362.
(3) Stöffler D., Gault D. E., Wedekind J., and Polkowski G. (1975) J. Geophys. Res. 80, 4062-4077.
(4) Shoemaker E. M. (1963) In The Solar Systems, 4, The Moon, Meteorites, and Comets.
(5) Quaide W. L. and Oberbeck V. R. (1968) J. Geophys. Res. 73, 5247-5270.

STRATAL EMPLACEMENT IN LUNAR CORES J. Stewart Nagle, Northrop Services Inc., Johnson Space Center, Houston, Texas 77058

Observations: In the Apollo 16 and 17 drill strings, and in drive tubes 60010/60009, there are only two thick units with very coarse grain size, framework texture, low track abundance, and a stratigraphic succession ranging upward from low-grade soil breccias through medium-grade melt breccias to partially shocked crystallines to fresh crystallines. These strata occur in the base of 60009 and in 70007-70009, and occupy approximately 1/5 of the soil column examined to date. All other strata in the cores are much thinner, sparser in rock fragments, show no internal succession of rock types, and are relatively high in track counts.

Approximately 1/3 of the total section in 60010/60009 and in the Apollo 16 drill string show internal inhomogeneity in the form of marbling of light and dark colored material. Marbling appears as interfingering domains of soil, from 0.1 to 4 cm in diameter; it occupies the entire unit and appears to be the result of crushed clasts of friable soil. Marbled strata range from 1.5 to 6 cm. thick, and tend to contain a variety of rock types through the entire unit. Marbled strata are moderately to poorly sorted, and are medium to fine-grained; most glass fragments in such units are fractured and not in position of origin.

The remainder of the section - approximately half of the cores - is massive and relatively structureless. If soil clasts occur in such strata, as in units 8 and 10 of 60009 and 1 of 60010, the clasts tend to be equant and rounded, and are widely dispersed in a uniform matrix. The clasts do not interfinger, as in the marbled units. Some massive strata, as the upper 3 to 6 cm of all the core sections, are fine-grained, relatively well sorted, and rich in fresh glass and agglutinates. However, most massive strata - a quantity comprising approximately 1/3 of the core section examined to date- are medium to coarse-grained, moderately poorly sorted, and show several distinctive common properties including concentrations of splash glass and droplets only at the base of the strata and sparse, rounded soil clasts that do not interfinger. Such massive units are comparable to the marbled units in thickness and composition of lithified rock fragments.

Interpretations The thick massive units with compositional succession, fresh crystallines, low tracks and exposure indications are interpreted as ejecta from major, bedrock-penetrating craters. Relative uncommonness of such units suggests that relatively little bedrock is being introduced into the regolith at present or during the history of the cores.

Two known mechanisms could account for the marbled strata: cratering and mass wastage. Because of the prevalence of craters on the lunar surface and distance from major mass wastage sources at the Apollo 16 and 17 sampling sites, it is relatively probable that cratering generated the marbled strata. Relative textural maturity and homogeneity of strata, and general lack of fresh material suggest that the marbled strata are redistributed and mixed regolith.

# STRATAL EMPLACEMENT IN LUNAR CORES

Nagle, J. S.

A number of hypotheses could account for the massive strata: cratering, mass wastage of homogeneous material, continuous soil accretion, or gardening and surface reworking. Massive, 1-6 cm. units with glass at the base are believed to have formed by cratering. The glass was formed in situ as it is horizontally aligned, and margins of glassy agglutinates are not fractured. Generation of such glass requires high impact velocities associated with primaries. The mechanism which produced the glass - the small primaries - would also have to generate the strata which includes the glass. Because the strata are thin, it is inferred that most of the generating impacts were relatively small.

It is herein hypothesized that the consistent differences between marbled and massive strata is related to the mode of origin. Evidence cited above suggests that the massive strata originated by small primaries. If cratering is the principal mechanism that is likely to produce marbled strata, then it is proposed that the marbled strata were generated by less energetic secondaries. Further study is needed to test this hypothesis: experimentation in the form of correlating strata type with energy of impact, and further examination of lunar cores to determine if marbled strata can contain much splash glass at the base.

The mature soil at the top of all core sections could be reworked or continuously accreted; at present it is not possible to distinguish between the two mechanisms.

CRATERING PHENOMENA AND ENERGY DISSIPATION IN THE CM-SIZE RANGE.

K. Nagel, G. Neukum, H. Fechtig, Max-Planck-Institut für Kernphysik, Heidelberg, Germany.

Simulated craters are of interest in understanding the origin, velocity, mass, density, and chemical composition of the interplanetary dust particles. Furthermore they give information about erosion of surfaces.

Previous experiments were made with a dust accelerator which accelerated particles in the mass range $10^{-10}$ to $10^{-16}$ g to projectile velocity up to 60 km/sec. The projectile materials were Fe, Al, C, glass and Au impinging on all possible target materials.

We report here on experiments using a light gas gun shooting mm-sized projectiles on different targets. Present experiments show that :

1) glass-lined pits can be produced for which the target size is important
2) heat of fusion of the target materials seems to be an essential parameter in the crater-forming process
3) craters in the diameter range from µm to cm have similar shapes, although the energy dissipation into the target material is more effective for the larger projectiles.

I DATA ON MORPHOLOGY AND GEOMETRY

The experimental conditions are projectile velocities $v \geq 4$ km/sec, projectile diameters 1.5 to 2.0 mm, projectile materials iron and steel. Two different target sizes have been used, 10 and 20 cm in diameter. On the larger targets the ratio of spall diameter to pit diameter is lower than on smaller targets. Pits on smaller targets are often rejected. Target size apparently plays an important role in crater-forming process. A small basalt target diameter and a higher threshold projectile velocity for pits in basalt targets may explain why Moore et al. (1963) did not detect any pits.

Metal targets show larger crater diameters compared to glass-lined pits on glass targets under the same experimental conditions. Craters in metals, with the exception of W, display no spallation zone.

The described simulation experiments confirm known projectile dependencies (e.g. Bloch et al., 1971), as already observed in µm-sized craters.

II MELTING AND VAPORIZATION

Crater simulation results with mm-projectiles show that glass-lined pits in glass targets are observed at projectile velocities, $v \geq 4$ km/sec. This means that the energy imparted to the target during the shock process is sufficient to produce a glass melt. In experiments having lower impact velocities there are pieces of melted glass among the ejected material, but the energy is insufficient to produce a glass-lined pit.

Experiments on different metal targets, Al, Ni, Cu, W, Au, Pb, and stainless steel with projectile velocities 4 to 5 km/sec and projectile diameter 2.5 mm yield a correlation between crater diameter and heat of fusion of the target materials.

CRATERING PHENOMENA AND ENERGY DISSIPATION IN THE CM-SIZE RANGE

K. Nagel et al.

In polished cross-sections of glass-lined pits, metallic inclusions have been detected. Qualitatively these inclusions have chemical compositions very similar to the projectiles; however, quantitatively, specific differencies were observed. The inclusions are depleted in Mn and Cr, and enriched in Fe and Ni. The explanation is based on the fact that an enrichment in Cr has been found in the crater glass surrounding the metallic inclusions. The solution of metals in glass depends on oxygen fugacity. The univariant curves of Ni-NiO, Fe-'FeO', $Cr-Cr_2O_3$ and Mn-MnO given by Sato (1971) and Lindsley (1962) explain the described results very well.

III COMPARISON OF EXPERIMENTAL DATA

Comparison of craters produced by mm-sized projectiles with craters produced by µm-sized projectiles show some similarities:

a) the ratio of crater diameter D to projectile diameter d depends on projectile velocity v, $D/d \sim v$

b) the ratio of crater diameter D to crater depth T is related to the projectile density g, $D/T \sim g^{\alpha}$, $\alpha$ depends on target material.

c) the variation of D/d for different targets under the same experimental conditions is correlated with heat of fusion of the target materials.

On the other hand, absolute values of D/d are larger for craters produced by mm-sized projectiles compared to craters produced by µm-sized projectiles.

Quantitative measurements of projectile residues in laboratory produced craters revealed that in µm-craters there are more residues than in cm-craters (Neukum, 1969; Nagel, 1975). These results suggest that the amount of energy dissipated into target material has changed in going from µm- to cm-craters. In figure 1 the crater diameter D is displayed as a function of the kinetic energy $E_{kin}$ of the projectile for simulated craters. The figure shows that the spall diameter of µm- and cm-sized craters is related to the rim diameter of m-sized craters (Moore, 1971).

There remains an interesting question: Is the relation between D/T and g, detected in the µm- to cm-crater size range, also valid in diameter range from m- to km-craters. Fresh-looking craters on the moon in this range have values of D/T = 4 to 10 (Arthur, 1974). The uncertainty of the measurements is greater than $\pm$ 20%. As a result, it is difficult to decide whether the relation between D/T and g is the same for the small and larger craters.

REFERENCES

H. J. Moore et al. (1963), Journal of GEophys. Res., Vol. 76

M. R. Bloch et al. (1971), Proc. II Lunar Sci. Conf., 3, 2639-2652

M. Sato (1971), Research Techniques for High Pressure and High Temperature, 42-99

D. H. Lindsley (1962), Annual Report of the Director of the Geophysical Laboratory, 60-66

G. Neukum (1969), Diplomarbeit, Universität Heidelberg

K. Nagel (1975), Ph.D. Thesis, Universität Heidelberg

CRATERING PHENOMENA AND ENERGY DISSIPATION IN THE CM-SIZE RANGE

K. Nagel et al.

H. J. Moore (1971), Journal of Geophys. Res., Vol. 76
D. W. G. Arthur (1974), Icarus 23, 116-133.

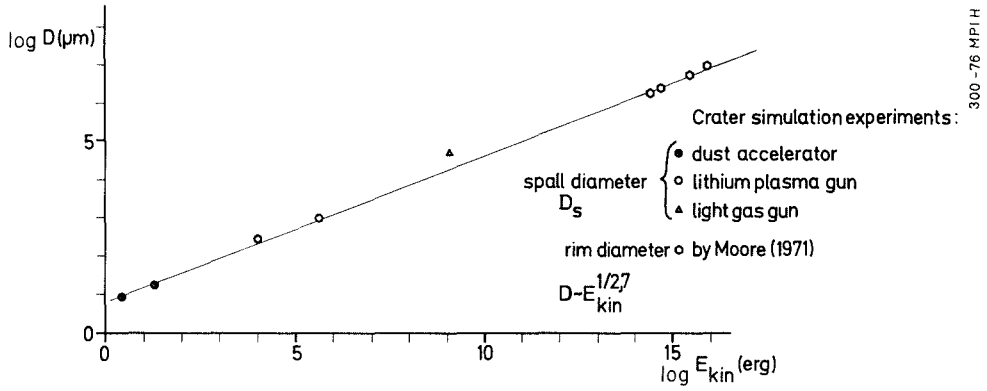


Fig. 1

$\log D \sim \log E_{kin}^{1/2,7}$

THE VREDEFORT STRUCTURE : A REVIEW OF RECENT STUDIES ON ITS CONSTITUTION AND ORIGIN - Prof. L O Nicolaysen, Bernard Price Institute of Geophysical Research, University of the Witwatersrand, Johannesburg.

The Vredefort structure is a large near-circular uplift which occurs 100 km south of Johannesburg. It is not a complete ring, but extends over an arc of ∿280°, thereby closing the NW end of a ∿100 km long elongated domical structure.

The outer 'collar' consists of a 15 km-thick section of layered strata which form near-circular outcrops around the 'core' of basement granite. W.F. Slawson showed that the outer basement also has a quasi-ringed character: old horizontal geochemical zones in the basement have been upturned (together with the collar strata). He claimed that a radial traverse through the basement effectively takes one down a near-vertical profile through ∿15 km of granitic crust. Intensive and multidisciplinary research on the Vredefort basement has been undertaken during the past four years. Most of these studies tend to support Slawson's claim.

Radial traverses, directed from the outer collar to the centre of the basement, expose a sequence of unusual deformations and textures. These include brittle deformations which simulate folds, cataclasis in thin sections, emplacement of pseudotachylite veins, lamellar structures in quartz and shatter cones. N.C.Gay and his associates have studied some of these features over a wide range of scales; he has new evidence that shatter cones formed in episode (s?) of cataclysmic violence.

The pioneers who mapped Vredefort geology 50 years ago demonstrated unusual and massive uplift. However, both the vertical extent and character of the uplift are more striking than these pioneers realised. Structural analysis of a model near-circular uplift - where a large part of the earths crust is turned up sharply in tabular units - yields mechanical adjustment or "accommodation" problems which become increasingly severe towards the centre. Large scale central cratering at Vredefort should therefore be carefully considered: it relieves the "accommodation" problem at shallow levels in the crust, and it is consistent with the violence of the shatter cone event (s?).

The exposures in the centre of the Vredefort basement now take on an added interest. Their nature and textures may reveal details of the processes and accommodations at the deepest levels during a large terrestrial cratering event. The petrography and geophysics of this central region is summarised, and the evidence relating to an impact or internal origin of the Vredefort structure is presented and evaluated.

# THE VREDEFORT STRUCTURE

Nicolaysen L.O.

The impact theory has some grave deficiencies. (1) It calls for a remarkable coincidence: the hypothetical meteorite must have struck into a centre of an igneous and metamorphic 'hot spot', where highly localised hornfelses and unusual alkalic igneous rocks already existed. (2) The lower density of the basement (2,65 tonnes/$m^3$) compared to the overlying strata (2,82 tonnes/$m^3$) shows the gravitational instability could have provided a potent agency for diapiric uplift of the basement. (3) The Vredefort structure is not a complete ring and it has some significant relation to an elongate NW-SE directed domical structure.

Can the long controversy on the origin of this structure be terminated soon, by some decisive scientific experiment? Chetty et al. have reported on their exceptionally detailed geophysical studies of the central zone, where a uniform denser rock of "intermediate" composition ascends to within ∿100 metres of the surface. They made two alternative suggestions concerning this denser, hidden rock:

(i) it is largely constituted of lower crust and forms an ∿8 km wide core of an immense diapir; this core is penetrated by a few intrusive bodies.

(ii) it is an igneous rock which has some striking role in the unusual structural history of Vredefort.

Chetty et al. proposed a modest programme of further seismic work, and diamond drilling, to probe the central zone. Their proposed experiment would provide important new evidence about processes at the deepest levels, during a large terrestrial cratering event. It may also yield decisive information relating to the origin of the Vredefort structure.

SIMULATION OF IMPACT CRATERS WITH HIGH EXPLOSIVES; V. R. Oberbeck, NASA-Ames Research Center, Moffett Field, CA 94035

Present estimates of the energy of formation of natural meteorite craters are derived from studies of high explosion craters. However, the size of explosion craters depends on both the depth of burst of the explosive and the chemical or nuclear energy of formation of the crater. Early studies of Baldwin (1963) concluded that impact craters could be simulated by shallow depth-of-burst high explosion craters because the chemical energy of the explosive is transferred to the target by a shock wave as it is for an impact crater. Shoemaker (1960) concluded on the basis of structural similarities between shallow depth-of-burst explosion craters and meteor crater that shallow depth-of-burst explosion craters are analogs for impact craters.

In this paper we test the hypothesis that a shallow depth-of-burst explosion crater of a given chemical energy and detonation pressure produces the same effect as the impact of a projectile having equivalent kinetic energy and producing equivalent impact pressure. Three effects of impact or explosion were assessed to find the depth-of-burst explosion that simulated impact. Crater size and shape were measured, the growth of the ejecta plume was monitored, and deformation beneath the craters was studied.

These effects were recorded for impact craters produced by aluminum projectiles impacting quartz sand targets at a velocity of 2.0 km/sec and a kinetic energy of $8.7 \times 10^9$ ergs, producing an impact pressure of 83 kb and for explosion craters produced by detonation of PETN explosives placed at various depths of burst, the detonation of which produced a shock wave pressure of 83 kb and chemical energy of $8.7 \times 10^9$ ergs.

The results show that only at a depth of burst of 6.3 mm do explosions produce exactly the same size and shape craters, ejecta plume growth, and subsurface deformation as was observed for the impact craters. The study therefore confirms that effects of impact of Al projectiles in quartz sand targets may be simulated by detonation of high explosives at this depth of burst.

Explosion craters formed in layered targets by charges placed at the surface also have structures which are similar to impact craters produced in layered targets. This suggests that our results, limited to consideration of only a few variables, may remain valid when impact craters formed under different conditions are simulated by suitable explosion craters.

References

Baldwin R. B. (1963) The Measure of the Moon. Univ. of Chicago Press, 488 p.

Shoemaker E. M. (1960) Penetration Mechanics of High Velocity Meteorites Illustrated by Meteor Crater Arizona. 21st Int. Geol. Congr., Copenhagen.

DEFORMATION AT THE DECATURVILLE IMPACT STRUCTURE, MISSOURI T. W. Offield and H. A. Pohn, U.S. Geological Survey, Denver, CO 80225

Detailed mapping of the Decaturville structure in central Missouri has provided new insight into the complex deformation sequence that follows impact cratering in a well-layered sedimentary sequence. The structure is characterized by intense deformation in a circular area 5.5 km across; a 550-m-thick rock sequence was disturbed. A concentric normal fault bounds the structure, which consists of a central uplift and surrounding structural depression. The formation capping the uplift is 300 m above its normal stratigraphic position, but isolated blocks at the center have been lifted as much as 540 m. Drill data at the center show that the capping unit overlies a jumble of blocks from formations occupying the bottom 240 m of the disturbed sequence. Quartz in the mixed breccia surrounding these blocks has planar features, indicating shock pressures of at least 35 kb and of possibly as much as 60-100 kb. Shatter cones occur at the center of the structure, and monolithologic breccias (formed by successive dilation and crushing of individual beds without mixing of adjacent beds) are common throughout. Shock effects in the center of the structure decrease in intensity downward; basement rocks that were 540 m deep when the structure formed were broken and excavated during cratering but do not contain shock metamorphic features. The depth of penetration is uncertain but was not deeper than about 360 m in the disturbed section.

Convoluted strata in the uplift have strike lengths 25-30 percent longer than the perimeters on which they lie, indicating that inward movement and crowding of beds accompanied the upward movement. The inward movement involved folding and thrusting; it was succeeded by adjustments on steep faults that involved both upward and downward displacements of as much as 150 m. The depressed zone around the uplift is characterized by thrusts inward and outward relative to the center, and by steep faults that formed both before and after the thrusting took place. The change from general uplift to structural depression occurs about 2,700 m from the center of the structure.

Blocks of units normally 188-550 m deep lie on the youngest formation in the ring depression and are interpreted as crater ejecta--or fallback--indicating that original ground surface is present in parts of the depression. Poststructure erosion in the area is estimated at no more than 47 m. Because such a small amount of erosion could not have destroyed a crater estimated to be 3,300 m in diameter and 550 m deep, we believe the crater was destroyed by the immediate inward movement of beds to form the central uplift. This movement was a response that followed passage of the shock wave, and it produced the ring fault and struc-

tural depression as necessary concomitants to the development of central uplift (volumes of the uplift and depression are virtually equal). As the crater closed, material spalling from the walls was trapped to form the megabreccia mass at the center of the structure. This explanation may apply to other astroblemes where erosion is not thought to be great but where a central peak is present without a topographic crater.

Figure 1 - Schematic cross section showing inferred time sequence of movements during the cratering event. (The entire sequence probably occurred within minutes.) A. Transient cavity -- ejecta blocks present in the structure are still airborne. B. Beginning of structural adjustments -- ring fault forms; formations collide and fracture at center of structure. C. Numerous faults form in response to differential centripetal movement; folding becomes more intense toward the central breccia column, giving rise to steep faults as seen at the sulfide pit where a large block has been raised. D. Beds glide over the breccia column as seen in present-day configuration. Formations represented in the cross section are as follows: Ordovician: Ojc, Jefferson City Dolomite; Or, Roubidoux Dolomite; Og, Gasconade Dolomite; Ogg, Gunter Sandstone Member of Gasconade Dolomite. Cambrian: Ꞓe, Eminence Dolomite; Ꞓp, Potosi Dolomite; Ꞓdd, Derby and Doe Run Dolomites; Ꞓd, Davis Formation; Ꞓb, Bonneterre Dolomite; Ꞓl, Lamotte Sandstone. Precambrian: pꞒ, schists and pegmatites.

DEFORMATION AT THE DECATURVILLE IMPACT STRUCTURE, MO.

Offield, T. W. et al.

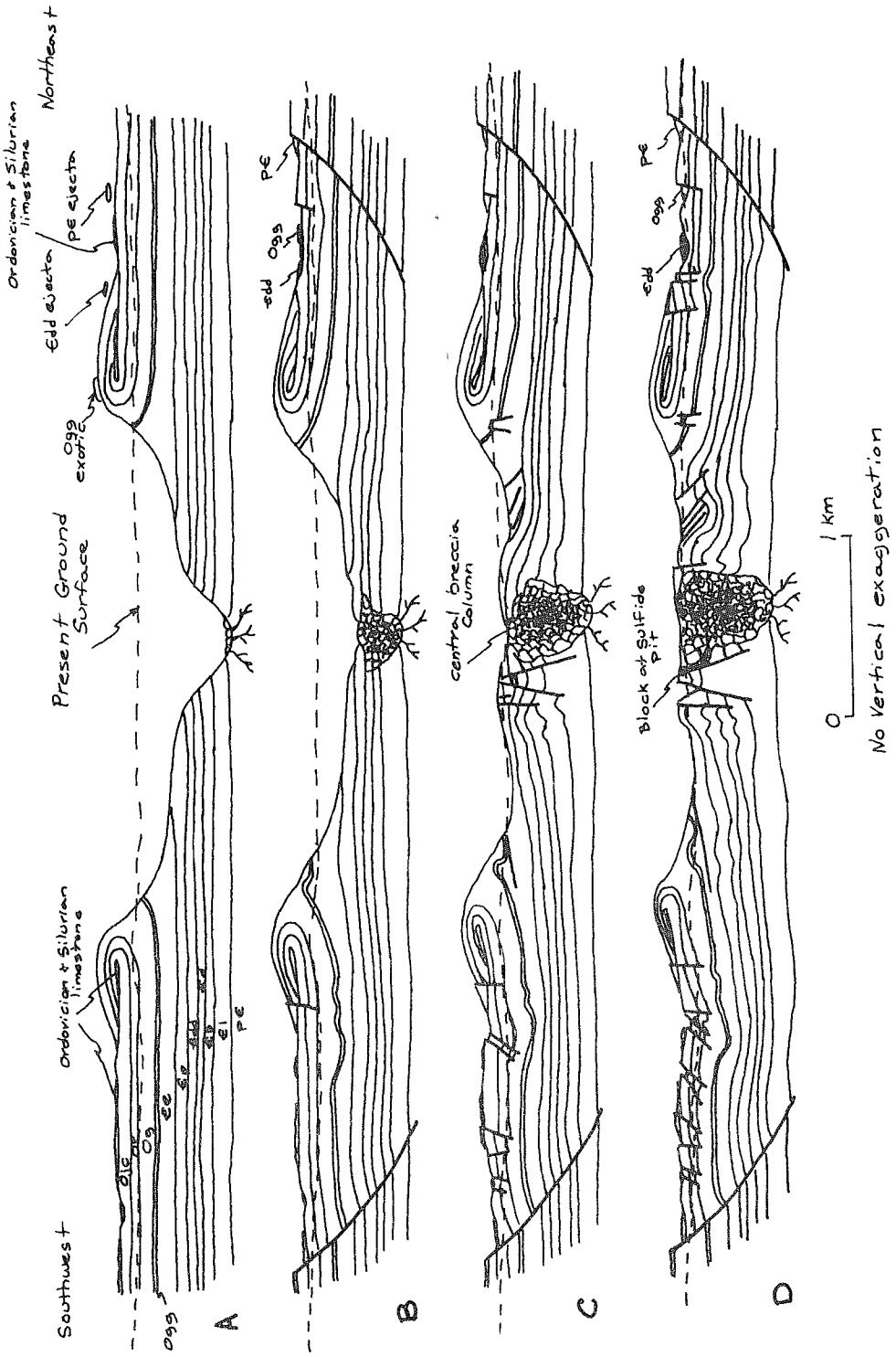


Figure 1

PARTITIONING OF ENERGY FROM IMPACT CRATERING ON PLANETARY SURFACES, J. D. O'Keefe, Dept. of Geophysics and Planetary Physics, University of California, Los Angeles, Los Angeles, CA 90024 and T. J. Ahrens, Seismological Laboratory, California Institute of Technology, Pasadena, CA 91125.

The partitioning of energy and the decay of shock pressure resulting from hypervelocity impacts of an iron object with a gabbroic anorthosite half-space are reported for interactions at 5 and 15 km/sec. The eulerian finite-difference numerical techniques and equations of state previously described (O'Keefe and Ahrens, 1975, 1976) are utilized to prescribe the impact flows, in a situation which recent shock wave data (Ahrens, et al. 1976) indicates can represent a surface with strength properties like the crust of the Moon in a highland province. Gross energy partitions are represented in Table 1, which correspond to late times at which the theoretically calculated flow has decayed so that the stresses are in the elastic regime. Our results demonstrate that in both cases a dominate fraction of the initial projectile energy resides within the internal energy of the ejecta. In both cases, most of the energy is delivered to lunar crustal (ejecta) material. However, the slower, 5 km/sec, impact is less efficient in this process and hence, more energy remains in the meteorite.

We have examined the decay of the peak shock pressure directly beneath the impact point for the two flows summarized in Table 1 and for the case of an anorthosite sphere, impacting an anorthosite half-space. All three flows demonstrate two regimes of pressure decay, not previously recognized. At distances from the impact point comparable to the radius (3-5 radii) of the meteorite, the shock decay is less rapid than previously inferred (Gault and Heitowit 1963). For the 5 km/sec impact the peak pressure decays as $\log_{10}P = -0.23\log_{10}R-0.40$, close-in, whereas for the 15 km/sec impacts, decays of $\log_{10}P = -0.29\log_{10}R+0.47$ and $\log_{10}P = -0.29\log_{10}R+0.47$ and $\log_{10}P = -0.29\log_{10}R+0.29$ are obtained for iron and anorthosite impactors, respectively. At greater distances, the shock pressure from iron impactors, at 5 and 15 km/sec decay as $R^{-1.7}$ and as $R^{-2.5}$, respectively. The crater radii for impacts with energies of $5.11 \times 10^{14}$ and $4.59 \times 10^{15}$ ergs, for 5-cm radius objects, are respectively, 266 and 521 cm. These scale with energy as $E^{0.308}$, the latter relations is comparable to that inferred from comparison with the Ranger and Apollo SIVB craters on the Moon.

Table 1

ENERGY PARTITIONING FOR 5 AND 15 km/sec

IMPACTS OF IRON OBJECTS ONTO GABBROIC ANORTHOSITE

| | Kinetic Energy | | Internal Energy | | Total | |
|---|---|---|---|---|---|---|
| | 5 km/sec | 15 km/sec | 5 km/sec | 15 km/sec | 5 km/sec | 15 km/sec |
| Gabbroic Anorthosite | 4.9 | 6.9 | 77.3 | 86.1 | 82.2 | 93.0 |
| | (3.7)* | (5.8)* | (65.0)* | (66.8)* | | |
| Iron Object | 0.16 | 0.0205 | 17.3 | 6.7 | 17.4 | 6.7 |
| | (0.03)* | (0.0062)* | (11.7)* | (2.4)* | | |

*Ejecta

# PARTITIONING OF ENERGY FROM IMPACT CRATERING

O'Keefe, J. D. et al.

References:

(1) Ahrens, T. J., R. Jeanloz and J. D. O'Keefe (1976) Abstract this volume.
(2) Gault, D. E. and E. Heitowit (1963) Proc. 6th Hypervelocity Impact Symposium, v. 2, 419-456.
(3) O'Keefe, J. D. and T. J. Ahrens (1975) Proc. Lunar Sci. Conf. 6th, 2831-2844.
(4) O'Keefe, J. D. and T. J. Ahrens (1976) Proc. Lunar Sci. Conf. 7th, in press.

# SELECTIVE EVAPORATION IN TARGET ROCKS AFTER METEORITIC IMPACT

Parfenova O.V., Chair of Petrography, Geological Faculty, Moscow State University
Yakovlev O.I., V.I. Vernadsky Institute of Geochemistry and Analytical Chemistry, Moscow, U.S.S.R.

Circular impact structures are widespread on the Earth, as well as on all "small" planets of the solar system. The formation of high-temperature melt accompanied by selective evaporation represents a physical peculiarity of the impact-explosive process. We believe that selective evaporation is the most important process which causes chemical alteration of impact products during impact metamorphism.

In the experimental studies of selective evaporation of silicate melts it was found that this process depends on several physical and chemical factors: temperature, total and partial pressure of gases, initial composition of melts and their acid-base properties (1,2). A comparison between chemical alteration of crater rocks and of experimental products indicates the existence of distinct similarities. This circumstance is the foundation for the explanation of some petrochemical features of the impact-explosive process.

The composition of target rocks and glass impactites of several craters were considered and compared: the craters are the following: Brent, West Clearwater, East Clearwater, Carswell, Manicougan (Canada), Lonar Lake (India), Monturaqui (Chile), Henbury (Australia), Ries Crater (West Germany), Popigay (USSR). The following relationships were found.

1) The percentage content of $K_2O$ commonly increases from target rocks to glass impact rocks, while the percentage content of $Na_2O$ decreases (Fig. 1), thus causing an increase in the ratio of $K_2O/Na_2O$. Fig. 2 illustrates the variation of $K_2O/Na_2O$ in crater rocks and in experimental products. Also in this case it is seen that this ratio increases as the result of impact melting. This phenomenon may be explained by the effects of selective evaporation of alkalies from intermediate and acid melts. As the activity of $K_2O$ is lower than that of $Na_2O$, more intensive removal of $Na_2O$ in the vapor phase follows.

2) The ratio $K_2O/Na_2O$ in glass impact rocks depends on the acid-base properties of country rocks (or target rocks). Fig. 3 illustrates this relationship. The acidity is calculated with the method of Marakushev A.A. (3). The lower ends of the vertical segments indicate the initial ratio $K_2O/Na_2O$

SELECTIVE EVAPORATION IN TARGET ROCKS . .

Parfenova O.V. and Yakovlev O.I.

(in target rock) and the upper ends the final ratio (in glass impact rocks). In general the highest values of $K_2O/Na_2O$ correspond to targets with the highest acidity. This relationship also exists in experimental results. It may be explained as follows. The fugacity of $K_2O$ decreases with increasing acidity of the melt, while the fugacity of $Na_2O$ is higher in all cases.

3) The fugacity of $SiO_2$ in intermediate and especially acid melts is rather high. This may explain the decrease of $SiO_2$ content in some glass impact rocks relative to the target rocks as well as in balance calculations. The $SiO_2$ fugacity in ultraacid melts may even be higher than the fugacity of $K_2O$. Chemical data of impact materials allow the deduction of the relative sequence of the fugacities in acid melts: Na > Si > Al(?) > (Ca,K, Ti, Mg). The components in parentheses have uncertain locations. The beginning of this sequence coincides with that obtained by Walter (4).

These relationships of compositional variations from target rocks to glass impact rocks, particularly the increase in the ratio $K_2O/Na_2O$, are important petrochemical criteria of impact-explosive craters.

The support of C.P. Florensky is gratefully acknowledged.

References

1) Яковлев О.И. и др. (1972), ДАН СССР, т.206, № 4.
2) Яковлев О.И. и др. (1973), Вестник МГУ, серия геология, № 5.
3) Маракушев А.А. (1976), Бюллетень МОИП, № 1.
4) Walter L.S. and Gultronich G.T. (1967), Solar Energy, V.11, p.p. 163-169.

SELECTIVE EVAPORATION IN TARGET ROCKS . . .

Parfenova O.V. and Yakovlev O.I

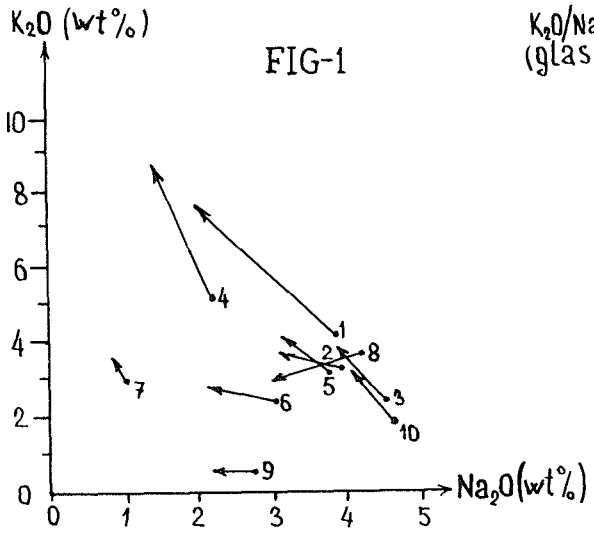


FIG-1

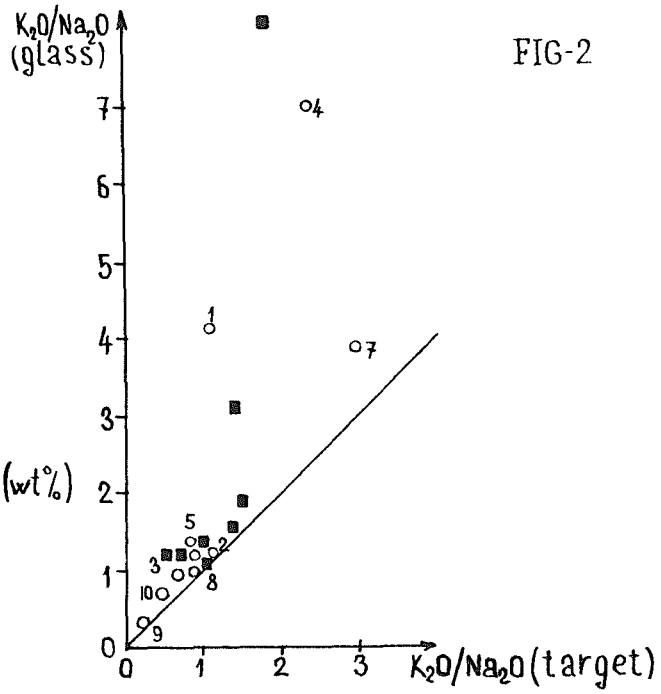


FIG-2

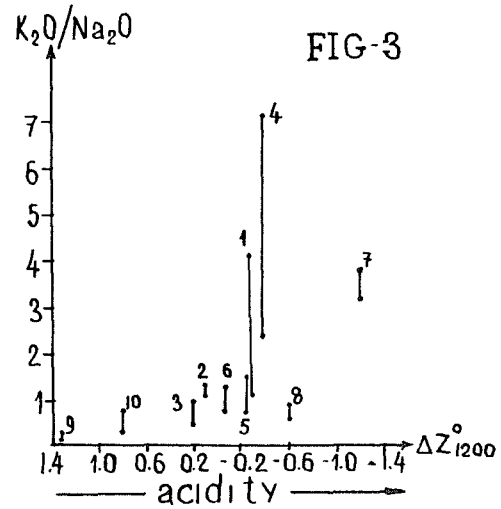


FIG-3

Fig. 1. Variations of $Na_2O$ and $K_2O$ contents from target (the beginning of the vector) to glass impact rocks (the end of the vector).

Fig. 2. Variations of the ratio $K_2O/Na_2O$ in crater rocks and experimentally produced glasses.

■ Experimental data

● Craters

Fig. 3. Relationship of $K_2O/Na_2O$ versus the acidity factor of the target rocks.

DYNAMICAL IMPLICATIONS OF THE PETROLOGY AND DISTRIBUTION OF IMPACT PRODUCED ROCKS. W. C. Phinney, Johnson Space Center, Houston, TX 77058 and C. H. Simonds, The Lunar Science Institute, Houston, TX 77058.

Petrologic studies of lunar highlands samples, intensive investigation of the melt sheet at the Manicouagan structure and review of other terrestrial crater studies allow limits to be placed on: 1) trajectories of impact fused material; 2) mechanical and thermal interactions of melt with less shocked debris; 3) total thermal energy of large cratering events; and 4) depth of penetration of large cratering events. Many of our interpretations are based on a thermal model for breccia lithification describing ejecta as a two component mixture of superheated melt and relatively cool mineral and rock fragments of minerals and rocks[1][2][3]. Studies of interaction of melt with $SiO_2$[4] and $ZrO_2$[5] clasts as well as digestion of clasts by melt[3] suggest melt temperatures of 1600-1800°C or more, whereas the lack of shock features in most fragmental material suggests an upper limit of about 200°C for shock heating. Material with intermediate levels of shock, hence intermediate post-shock temperatures, is observed in nature but are neglected in this simplified model. Mixing of clasts and melt occur in all possible proportions. Petrographic texture of ejecta is in large part a function of the relative proportion of the two components and the resulting temperature to which the mixtures equilibrate, approximate limits are: clastic breccias < 25% melt, suevites 25-50% melt, clast-laden crystalline rocks 50-70% melt and clast-free igneous-looking rocks > 75% melt.

Trajectories of Melt: Because melt forms at high shock pressures occurring largely within a small fraction of the volume excavated and because melt can be identified petrographically, the melt component in ejecta may be used to define motions during cratering. At Manicouagan (65 km diameter, high grade metamorphic target with < 50 m of covering limestone) a partially eroded sheet of melt originally > 230 m thick lies directly on basement near the edge of the inferred 40 km transient cavity[6] and an additional 12 km out over crystalline basement which slumped down > 2 km into the excavation. Suevites, fragmental breccias and microcrystalline rocks form rare discontinuous pods < 5 m thick at the base of the sheet. Within the sheet the preserved clast content decreases upward. All overlying fragmental debris has been eroded off. At West Clearwater Lake (38 km diameter, crystalline target with < 50 m limestone) fragmental breccias line the floor of the structure with overlying melt preserved only on a ring of islands about 25 km in diameter, with a maximum preserved thickness of only 130 m[7]. At Popagai (80 km diameter, crystalline target with 1.2 km sedimentary cover) the basal units have not been sampled, but there are extensive outcroppings of suevites and fragmental breccias within the crater and extending beyond the prominent ring structures[8]. Fragment-laden melt rocks occur as sheets directly on shocked gneisses that form two uplifted rings with diameters of 30 and 45 km and as tongues which flow outward and are locally within or on top of fragmental breccias and suevites. The Ries crater (25 km diameter, 500 m of sediments overlying granitic basement) has the least eroded ejecta of the larger terrestrial structures. Fragmental breccias occur both within the structure and extend > 25 km beyond the topographic rim, however suevites do not occur more than

12 km from the rim[9]. No sheet of melt has been sampled either on the surface or by drilling. In the Boltysh structure (25 km diameter, crystalline target with little sedimentary cover at time of impact) the base of the interior of the crater has clastic breccias and suevites which are interbedded with and overlain by over 200 m of fine grained melt rock[10]. At Brent (3 km diameter, sedimentary target) melt occurs at the base of the excavation overlying shocked and fractured basement. The melt is covered by over 500 m of fragmental breccias[11].

The distributions of impactites in all craters except possibly the Ries indicate that the hottest melt rich portions of the debris is deposited in the basal and lowest portions within the craters and as tongues that extend only a small distance outward from the crater rim. The direct contact of melt with basement at Manicouagan, Brent and with suevites and other relatively melt rich breccias at Boltysh and West Clearwater structures indicates that the melt must move downward and outward displacing colder fragmental debris. If melt rich rocks occur beneath the fragmental breccias at the two large but little eroded structures Popagai and Ries as they do at Brent then some general cratering mechanism must be found to essentially turn the debris within the crater inside out. One potential mechanism would be to have the melt driven directly downward while fragmental debris is lifted upward before settling down on top of the hot debris. For the debris outside the craters, that with the lowest melt content occurs at the uppermost units at Popagai but not at the Ries, although at the latter debris once overlying the suevites may have been eroded off. Nearly melt free ejecta lies beneath the suevites at the Ries and beneath the suevites and tongues of melt-rock at Popagai. Engelhardt's (1971)[9] interpretation, supported by Stöffler's (1975)[12] experiments, of the relationships of suevite and clastic breccias at the Ries requires that highly shocked and melted materials (suevites) be ejected ballistically at higher angles than the less shocked material that remained closer to the ground and were deposited first. It should be noted that these trajectories seem contrary to those suggested to explain the distributions within the craters.

Turbulent Flow: The limited compositional range and even distribution of clastic debris in melt rocks indicate extensive and extremely rapid mixing of target materials over distances of tens of km at Manicouagan. The estimated 600 $km^3$ of melt at Manicouagan contains 57.3 $\pm$ 2.1% (2 $\sigma$) $SiO_2$ while the targets range from 49-72%. At Popagai the melt contains 63.1 $\pm$ 2.44% $SiO_2$ while the target has a broad composition range. The heterogeneities in the targets range in scale from cm to km and to smooth out the heterogeneities, material initially separated by nearly 10 km must be mixed into every 1 gm sample analyzed. Mineral debris at Manicouagan, and lunar and other terrestrial impact melts, are so evenly mixed into the melt that no 1 $mm^2$ of a thin section is free of clasts. Most of the preserved clasts lack features suggestive of shock pressures over 200 kb and thus come from several km from the zone of total fusion. This evidence for the intimate mixing of materials from widely separated points within the target suggests that flow regimes are intensely turbulent on a wide range of scales. Thermal equilibration

# DYNAMICAL IMPLICATIONS OF IMPACT PRODUCED ROCKS

Phinney, W. C. et al.

between cold clasts and hot melt takes only a matter of seconds once the materials are firmly in contact[13]. If enough clasts are present, the mixture equilibrates to temperatures so low that crystallization ceases leaving glass in the matrix; a higher proportion of melt typical of most of the melt rocks is sufficient to initiate crystallization, raising the melt's viscosity greatly and preventing further flow. Thus the process of mixing clasts and melt must not only be thorough but also extremely rapid.

Thermal Energy: The energy required to heat and melt target rocks now present a measurable volume derived from impact melt defines the lower limit on the thermal energy produced in cratering events. At Manicouagan, with an inferred 35-45 km transient cavity and 65 km topographic depression, the estimate is $3 \times 10^{28}$ ergs for the pre-erosional melt sheet, but not including melt in suevites and fragmental breccias which have been removed by erosion. Their inclusion would increase the estimate by a factor of two or three. A similar estimate for West Clearwater Lake[6] yielded $3 \times 10^{27}$ ergs.

Depth of Excavation: The distribution of rock types in targets and cratered debris allows limits to be placed on the depth of excavation of the larger craters. The Popagai event penetrated the 1.2 km of sediments but not completely through an inferred 5 km thick sequence of gneisses, and no clasts of granulites are reported expected if the crater penetrated more than 10 km. Considering the relative abundance of sedimentary and gneiss fragments in the breccias, a penetration depth of 2-3 km seems reasonable for the 80 km depression. For the 65 km Manicouagan structure a study of gravity and seismic data (Sweeny, J.F. in preparation) suggests a penetration depth of 3-8 km. Drilling at the 25 km Boltysh crater indicates a present depth of about 1 km. Allowing for erosion and a central uplift, the initial penetration was probably not much more than 2 km. In the lunar highlands the general lack of plutonic rock fragments in breccias and melt rocks compared to the abundance of previously existing breccias and melt rocks indicates that most craters did not penetrate more than a few km below the surface that is nearly saturated with 50-100 km craters.

(1) Grieve 1975 Bul. Geol. Soc. Am. 86, 1617-1629.
(2) Simonds 1975 Proc. Lunar Sci. Conf. 6th, 641-672.
(3) Simonds et al. 1976 Proc. Lunar Sci. Conf. 7th in press.
(4) Carstens 1975 Contrib. Mineral. Petrol. 50 145-155.
(5) El Goresy 1965 Jour. Geophys. Res. 70 3453-3456.
(6) Floran and Dence 1976 Proc. Lunar Sci. Conf. 7th in press.
(7) Dence et al. 1965 Royal Astron. Soc. Can. J. 59 13-22.
(8) Masaytis et al. 1975 The Popagai Meteorite Crater (Nauka Moscow).
(9) Engelhardt 1971 Jour. Geophys. Res. 76 5566-5575.
(10) Yurk et al. 1975 Inter. Geology Rev. 18 196-202.
(11) Hartung 1971 Jour. Geophys. Res. 76 5437-5448.
(12) Stöffler et al. 1975 Jour. Geophys. Res. 80 4062-4077.
(13) Onorato et al. 1976 Proc. Lunar Sci. Conf. 7th in press.

CRATERING MECHANISMS OBSERVED IN LABORATORY-SCALE HIGH-EXPLOSIVE EXPERIMENTS; A. J. Piekutowski, University of Dayton Research Institute, Dayton, Ohio 45469

Laboratory-scale studies of explosive crater formation and ejecta distribution were performed in cohesionless and cemented Ottawa sand (1, 2). Gram-size, spherical explosive charges were detonated in homogeneous and two-layered test beds which were carefully prepared using these media. The craters produced in these studies exhibited many of the morphological features which are present in larger scale explosive experiments, in laboratory-scale impact experiments (3), and in large impact craters (4). Features which were observed in our craters included: "normal" bowl, conical or central mound shape; flat floor; rings and terraces on wall; central mounds produced by uplift; and hummocky mounds and concentric rings in region surrounding crater. Through use of high-speed photography and specialized experimental techniques we were able to observe many of the mechanisms which produced these features.

Craters produced in homogeneous test media exhibited several different shapes which were related to the height of burst or depth of burst of the explosive and the initial density of the cratering medium. Moderately buried to deeply buried explosives always produced conical-shaped craters. This shape appeared to result when the walls of the transient cavity produced by the detonation failed and the walls assumed the angle of repose of the medium. Near-surface detonations produced bowl-shaped craters in loosely packed (relatively low shear strength) media and bowl-shaped craters with a central mound in densely-packed (relatively high shear strength) media. Experimental evidence suggested that these mounds were erosional remnants of the crater formation process and not the result of an elastic rebound or central uplift. A typical "erosional remnant" central mound is shown in the crater in Figure 1.

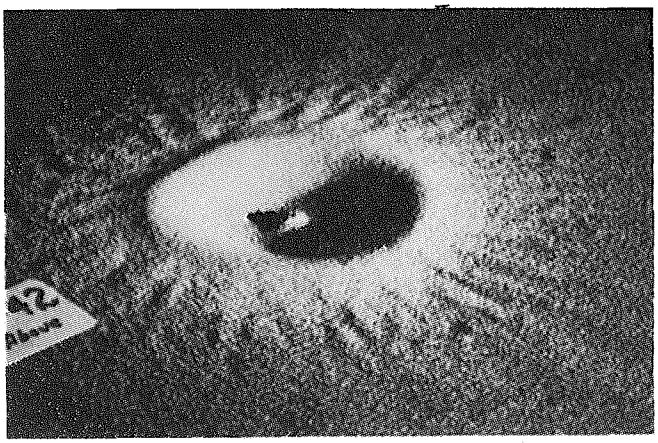

Figure 1. Bowl-shaped Crater with Central Mound Believed to be the Remnant of an Erosional Crater Formation Process.

# CRATERING MECHANISMS IN LAB-SCALE

Piekutowski, A. J.

The "normal" crater shape was altered to a flat floored shape when a discontinuity in the medium existed in the region near the bottom of the crater. For these events, the discontinuity merely consisted of a very thin layer of dyed sand which had been improperly placed in the test bed for the purpose of exhibiting displacement of material around the crater. Certain experimental evidence suggested that the thin layer also caused explosive energy to be "channeled" into the material above the layer with little coupling of this energy to the medium below the layer.

Most significant variations in apparent crater morphology occurred when the cratering medium consisted of a layer of cohesionless sand above a cemented sand layer. First indication of interaction of the lower layer with the crater formation process occurred when terraces and concentric rings appeared on the lower portion of the crater walls. Central mounds began to appear on the crater floor when the depth to the layer was within three "normal" crater depths of the preshot surface. Several different experiments which examined the formation of the central mounds showed them to be produced during the collapse of a plume of material which had been lifted from the cratered region during crater formation. Two cross-sectional views of a crater which exhibits a central mound are shown in Figure 2. When the lower layer was very near the surface (less than one-half a

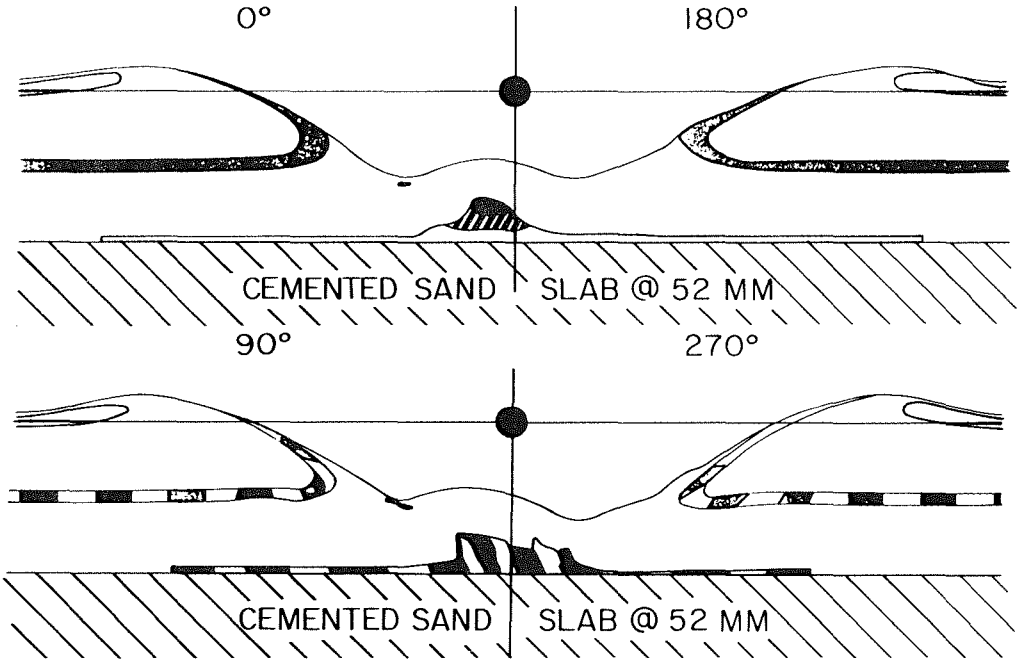


Figure 2. Cross-Sectional Views of Crater in a Simple Two-Layer Medium Showing Central Mound and Distortion and Displacement of Dyed Sand Tracer Layers.

CRATERING MECHANISMS IN LAB-SCALE

Piekutowski, A. J.

"normal" crater depth) hummocky mounds and concentric rings were formed in the region surrounding the crater, as shown in Figure 3. High-speed films of several of these experiments showed that the affected material in the region surrounding the crater had been lifted considerable distances above the preshot surface during the crater formation process.

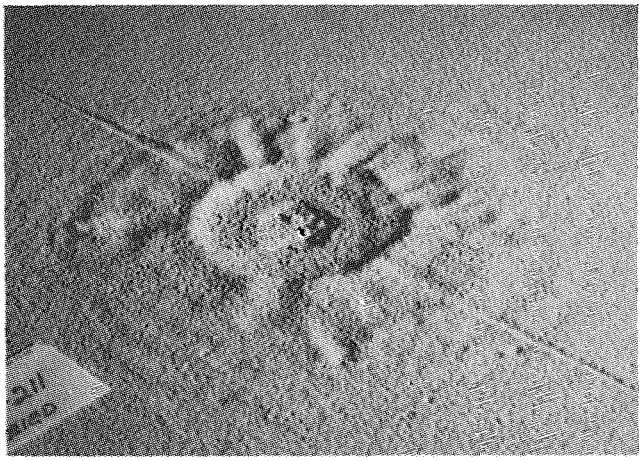

Figure 3. Hummocky Mounds and Concentric Rings Surrounding Crater Produced in Layered Media with Shallow Overburden.

References

(1) Piekutowski, A. J., Laboratory-Scale High-Explosive Cratering and Ejecta Phenomenology Studies, AFWL-TR-72-155, Air Force Weapons Laboratory, April 1974.

(2) Piekutowski, A. J., A Summary of Four Laboratory-Scale High-Explosive Cratering Parametric Studies, AFWL-TR-75-211, Air Force Weapons Laboratory, December 1975.

(3) Oberbeck, V. R., Quaide, W. L., "Estimated Thickness of a Fragment Surface Layer of Oceanus Procellarum", Journal of Geophysical Research, September 1967, Vol. 72, No. 18, pp. 4697-4704.

(4) Gault, D. E., et. al., "Some Comparisons of Impact Craters on Mercury and the Moon", Journal of Geophysical Research, June 1975, Vol. 80, No. 17, pp. 2444-2460.

EJECTA THICKNESS, RIM UPLIFT, ENERGY TYPE, AND DEPTH OF ENERGY RELEASE: R. J. Pike, U.S. Geological Survey, Menlo Park, Ca. 94025

In reconstructing the geometry of ejecta deposits surrounding impact basins and large craters on the terrestrial planets, it is essential to have some reasonable models for the internal structure of the crater rim. One useful constituent of any such model is T, thickness of the ejecta at the crater rim-crest (1). Although T is very difficult to estimate on the Moon other terrestrial planets, measurements at Meteor Crater (2) and several well-studied experimental craters (3) show that T is a constant fraction of the crater radius R ( 1 ). These and other data (4, 5, 6) also reveal that T varies systematically with h, overall height of the topographic rim-crest above precrater datum. For most experimental craters, T is about 0.5 to 0.9 of h.

It has been demonstrated (7) that the T/h proportion is highly sensitive to scaled depth-of-burst (DOB) of the charge and to whether the explosive is nuclear or chemical. The two recurved relations that resulted from these dependencies among 12 craters (7) are updated here (Figure 1) with data from 23 additional craters (8, 9, 10). Some of the 1974 findings remain unchanged. For example, explosions far too deep (e.g., Sedan, Pre-Schooner Delta) to be analogous to natural impact events coincidentally yield craters having the same T/h proportions as do the shallower bursts (e.g., Jangle U, Mixed Company 3) located within the scaled DOB range that probably furnishes the most analogous craters (-0.05 to 0.15 $m/kg^{0.33}$). Because of substantial structural differences between craters produced by shallow and deep bursts (6, 11), extrapolations of T/h or T/R to basins and large craters on the Moon and planets should be made only from shallow-burst terrestrial craters. The new data also still show that nuclear craters differ substantially from high-explosive (HE) craters with respect to the T/h:scaled DOB relation. Within the scaled DOB range 0.0 to -0.05 $m/kg^{0.33}$, the new T/h curves are mutually exclusive. Thus the choice of either an HE cratering model ($0.75 < T/h < 0.50$) or a nuclear cratering model as revised here from (7)--($0.20 < T/h < 0.0$) for extrapolation of the T/h proportion makes a crucial difference in T on extraterrestrial bodies.

The following new and revised results are evident from Figure 1 and a comparison of it with Figure 1 in (7):

First, chemical--not nuclear--explosions now appear to be the more analogous to the impacts that formed craters on Earth, the Moon, and elsewhere. The evidence is meager but indicative: The new and vastly improved drill data (2) move the point for Meteor Crater dramatically from the nuclear curve to the HE curve in Figure 1. Also, rough data (from 11, 12, and Lunar Orbiter V frame H-70) for the small lunar craters Linné and Dawes lie closer to the HE curve. The positions of these three craters in Figure 1 suggest that any subsequent calculations using T/h data should be based on the HE, not the nuclear, model.

Second, the nuclear curve for scaled bursts (in alluvium and soft rock) shallower than 0.05 $m/kg^{0.33}$ now departs radically from the preceding simple, recurved relation. The new data (Johnie Boy and corrected interpretation of Jangle S) suggest that all the rim height of shallow-burst nuclear craters

# RIM EJECTA, UPLIFT : ENERGY, BURST DEPTH

R. J. Pike

is accounted for by lateral displacement and uplift, not by deposition of ejecta.

Third, nuclear craters excavated in hard rock at large scaled values of DOB (e.g., Danny Boy, Cabriolet) depart significantly from the nuclear/alluvium curve, and may indicate yet a third--if tentative--relation. †

Fourth, There is a dearth of experimental cratering explosions in the scaled DOB range--0.00 to 0.1--that most likely may obtain for small ("simple") meteoritic-impact craters. However, scaled DOB of both lunar and terrestrial craters may vary with magnitude of the impact; lunar basins and large craters probably formed at shallower impact foci than did craters only a few km across (11). Thus, the several experiments in the -0.06 to 0.0 $m/kg^{0.33}$ range may well yield satisfactory analogs of impact basins and larger ("complex") craters (5, 13).

Fifth, central uplifts appear to form exclusively in very shallow explosion or impact events. This is consistent with the observation that central peaks occur in large but not small lunar craters plus the contention of Baldwin (11) that the larger the crater the less the scaled DOB. Highly-contrasting stratification in target materials may not be the major factor leading to formation of peaks and central uplifts (14), and conceivably neither may the material properties of the target (14). The data in Figure 1 do suggest a transition from simple to complex craters (15) with decreasing DOB, along the lower leg of the HE curve, in the progression Meteor Crater - Linné - Dawes - craters with central uplifts - Snowball crater.

Acknowledgments: Work performed under NASA Contract W13,130. Bruce Redpath, U.S. Army Corps of Engineers, kindly furnished some of the new measurements.

References: 1. MC GETCHIN, . R., SETTLE, M., and HEAD, J. W., 1973, Earth Planet. Sci. Letts., 20, 226-236. 2. RODDY, D. J., BOYCE, J. M., COLTON, G. W., and DIAL, A. L., 1975, Lunar Science VI, Houston, LSI, 680-682. 3. CARLSON, R. H., and JONES, G. D., 1965, J. Geophys. Res., 70, 1897-1910. 4. SHOEMAKER, E. M., 1960, Proc. 21st Intl. Geol. Congr., Part 18, 418-434. 5. RODDY, D. J., 1973, Defense Nuclear Agency Rept. 3151P2,2, 79-128. 6. NORDYKE, M. D., 1961, J. Geophys. Res., 66, 3439-3459. 7. PIKE, R. J., 1974, Earth Planet. Sci. Letts., 23, 265-271. 8. DAVIS, L. K., 1966, Report PNE-957, U.S. Army, Livermore. 10. CARNES, B. L., 1975, Report POR 6612 (WT-6612), U.S. Army, Vicksburg. 11. BALDWIN, R. B., 1963, The Measure of the Moon, Chicago. 12. PIKE, R. J., 1973, Sky and Telescope, 46, 364-366. 13. RODDY, D. J., 1976, Lunar Science VII, 744-746. 14. ULLRICH, G. W., 1976, Report AFWL-TR-75-88, U.S. Air Force, Kirtland AFB. 15. PIKE, R. J., 1976, Lunar Science VII, 700-702.

† No strength-related difference is evident for the HE experiments.

* POR-3008 (WT-3008), U.S. Army, Vicksburg. 9. FRANDSEN, A.D., 1970, Report

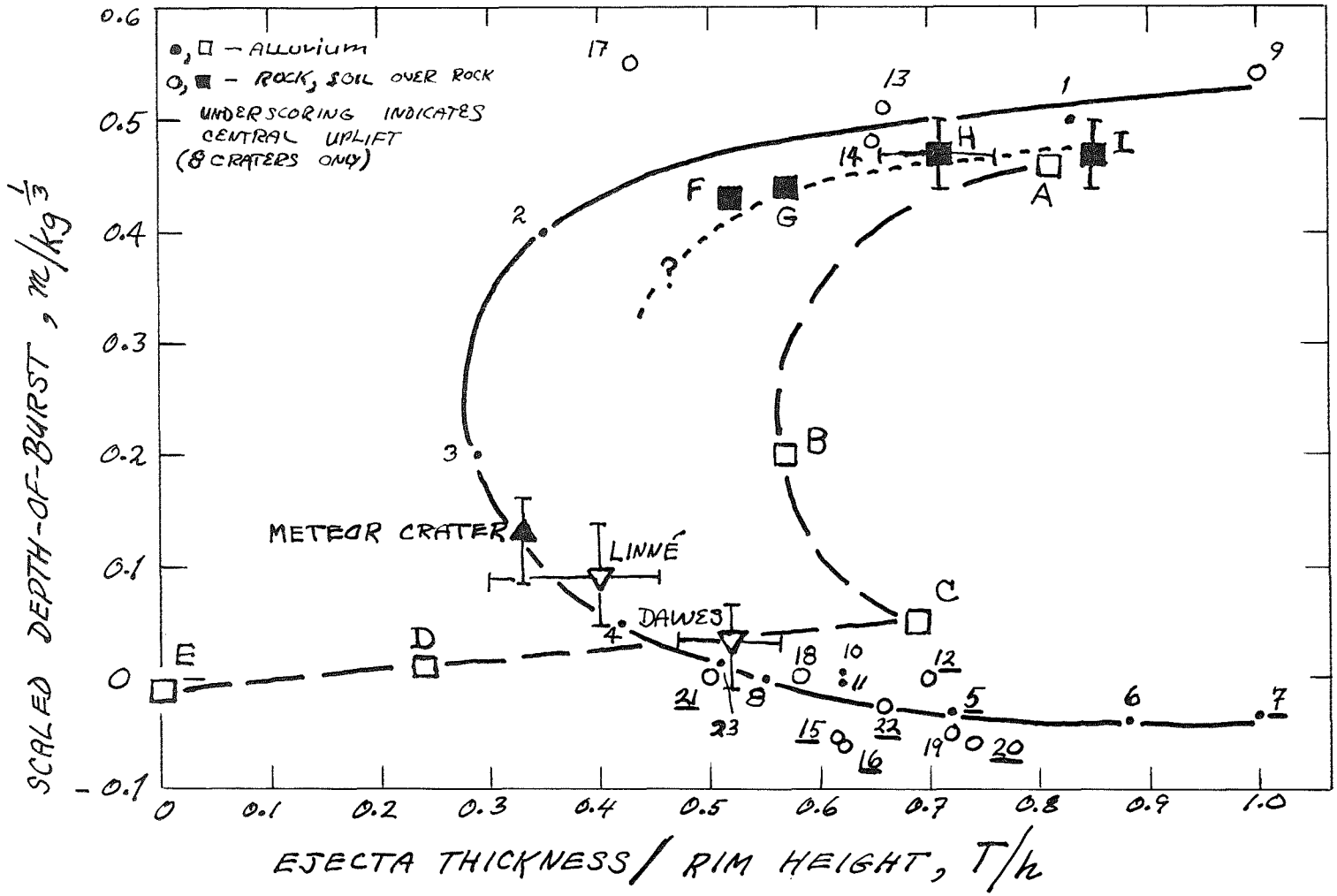


Figure 1. Key: 1-Scooter, 2-Stagecoach 3, 3-Stagecoach 2, 4-Jangle HE2, 5-Suffield 100 ton, 6-Suffield 20 ton, 7-Snowball, 8-Middle Gust 1, 9-Chariot, 10-Flat Top 2, 11-Flat Top 3, 12-Middle Gust 5, 13-Pre-Schooner II, 14-PreSchooner Delta, 15-Middle Gust 3, 16-Middle Gust 4, 17-Pre-Gondola I Bravo, 18-Flat Top 1, 19-Mine Ore, 20-Mixed Company 3, 21-Mixed Company 1, 22-Mixed Company 2, 23-Mixed Company C2, A-Sedan, B-Teapot Ess, C-Jangle U, D-Johnie Boy, E-Jangle S, F-Cabriolet, G-Danny Boy, H-1003 (Soviet), I-1004 (Soviet). Curves approximate only. Dots and circles - high explosive (HE); squares - nuclear; triangles - impact.

# CRATERING FROM LARGE EXPLOSIVE EVENTS

Robert J. Port, R & D Associates, Marina del Rey, CA 90291

The available large yield nuclear and high explosive cratering data are summarized from the major test programs conducted within the last 20 years of cratering research. The gross crater features are compared to show the major differences or similarities between crater formations at the Nevada Test Site, the Bikini and Enewetok Atolls, the Defense Research Establishment Suffield, and several smaller test sites on continental United States. Crater dimensions are related to show the critical dependence on yield, source characteristics, height or depth of burst, geology, and material property parameters. An attempt is made to show major trends and positive correlations, highlight differences and obvious anomalies, and provide a measure of the data scatter and regions of uncertainty in our understanding of the explosive cratering phenomenology.

# LUNAR WIND EJECTA TRANSPORT

D, E, Rehfuss, D, Michael, J. C, Anselmo, N. K, Kincheloe
Physics Department, San Diego State University, Ca. 92182

A cloud of vaporized material, created by high shock pressures at the moment of meteorite impact, may significantly accelerate particles ejected from the forming crater, even on a planetary surface lacking a permanent atmosphere. The vapor cloud as it expands into vacuum acts as a transient wind which can exert high dynamic pressures, This behavior is expected to be present at impact velocities exceeding 16 km $s^{-1}$ (1,2).

Oberbeck (3) and Shoemaker (4) have modeled possible ballistic trajectories for particles ejected during the formation of a lunar crater the size of Copernicus, We compare their "windless" trajectories with wind-accelerated trajectories on the basis of the characteristics of the gas cloud described by Rehfuss (1) for a basalt-against-basalt impact at 20 km $s^{-1}$. The parameters varied include ejecta particle mass, ejection velocity, particle initial position from impact center, and particle shape (sphere or cube).

## CALCULATION METHOD

If the crater radius is taken as 45,6 km and the radius of the meteorite as 0.73 km, then from Rehfuss (1) the gas cloud contains 1,1 x $10^{38}$ atoms of average atomic weight 22,6, and has these initial characteristics: density 3,0 gm $cm^{-3}$, radius 0.69 km, dynamic pressure 0.234 Mb, and expansion speed 3,95 km $s^{-1}$.

With a time delay calculated at a crater formation rate of 0,454 km $s^{-1}$, the particle is ejected into a ballistic trajectory in the range between 6 degrees at 0,17 km $s^{-1}$ and 22 degrees at 1.0 km $s^{-1}$, values suggested by Shoemaker (4) to be those largely responsible for the ejecta blanket, Once launched, the particle is subject to a gravitational force at 162 dynes/gm and to the dynamic wind pressure $P_D = \rho V^2/2$, where $\rho$ is the gas density and V is the difference between the gas expansion velocity and the instantaneous velocity of the particle. The acceleration due to the expanding gas cloud is a vector, $P_D C_D A/m$, where A is the crossectional area and m the mass of the particle. The maximum value of $P_D$ varies as $R^{-3}$, where R is the outer radius of the gas cloud. As soon as the maximum value of $P_D$ is reached at a given R, then $P_D$ will fall off as $t^{-3}$, where t is the time elapsed since impact. The drag coefficient $C_D$ is taken as a constant 2.0 for a cube and as $7/(0.2 + 5\ LOG_{10}R_e)$ for a spherical particle, where $R_e$ is the Reynolds number. The acceleration is treated as a constant over an arbitrarily short interval, iterated in time. New values of position, velocity and acceleration are found at the end of each time interval, until the particle lands.

# LUNAR WIND EJECTA TRANSPORT

Rehfuss, D. E. et al

## RESULTS

In Figure 1 are shown cases at constant ejection angle 14 degrees, ejection speed 0.52 km $s^{-1}$, and initial position $X_o$ = 0.69 km from the impact center. The windless case is compared with wind-affected trajectories of one-kilogram cubes and spheres. The range is almost doubled for the wind-accelerated cube.

In Figure 2 are presented other cases for cubes ejected at the same $X_o$ = 0.69 km, but of different masses and for three different launch velocities; the ordinate is the fraction, wind-enhanced range over the windless ballistic range. The effect is seen to be significant for cubical masses of up to a metric ton. For spherical particles, which have a drag coefficient approximately an order of magnitude lower than do cubes, the range enhancement is considerably less, although qualitatively similar curves result when plotted versus particle mass.

In Figure 3 is shown the effect of the initial horizontal position $X_o$, for cubes of 1, 10, and 100 gm and a fixed launch velocity, 0.52 km $s^{-1}$ at 14 degrees. For one gram particles the range enhancement is seen to be significant out to 10 km, about a quarter of the final crater radius.

## DISCUSSION

Lunar ejecta blankets may have spread out further from impact craters than hitherto expected, due to accelerations received from transient vaporization winds produced upon impact. As an example, we have taken the case of an impact at 20 km $s^{-1}$ involving a meteorite large enough to produce Copernicus, and have found the wind-enhanced range to be significant for ejecta particle masses up to $10^6$ gm, or for initial ejecta positions out to about a quarter of the crater radius from impact center. Such wind acceleration would be small for spherical shapes and large for cubical ejecta particles; actual ejecta fragments would be expected to exhibit an aerodynamic performance somewhere between those extreme shapes. Further parametric studies of this problem are warranted, especially those leading to quantitative estimates of the extent to which the ejecta volume could be displaced due to this transient wind transport.

This work was supported by NASA grant NSG-07026.

## REFERENCES

1. Rehfuss, D. E., 1972, J. Geophys. Res. 77, 6303-6315.
2. Zel'dovich, Ya. B., and Raizer, Yu. P., 1967, Physics of Shock Waves and High-Temperature Hydrodynamic Phenomena, vols. 1 and 2, 916 pp, English translation edited by W. D. Hayes and R. F. Probstein, Academic, New York.
3. Oberbeck, V. R., 1975, Rev. Geophys. and Space Phys. 13, 337-362.
4. Shoemaker, E. M., 1962, in Physics and Astronomy of the Moon, edited by Z. Kopal, 538 pp., Academic, New York.

LUNAR WIND EJECTA TRANSPORT

Rehfuss, D. E. et al

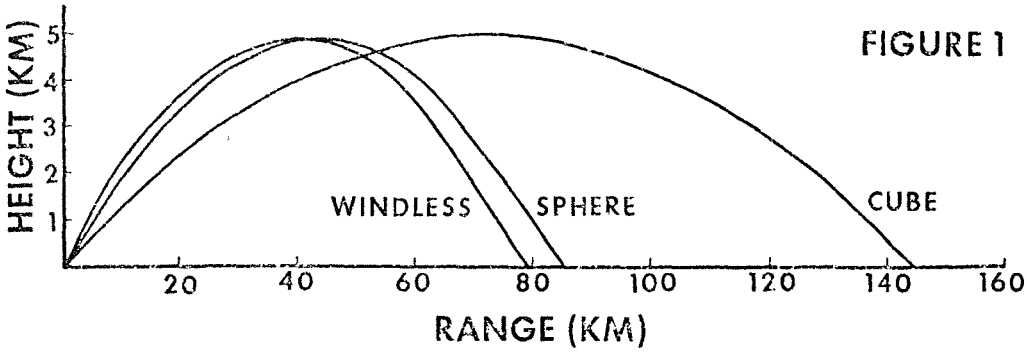


FIGURE 1

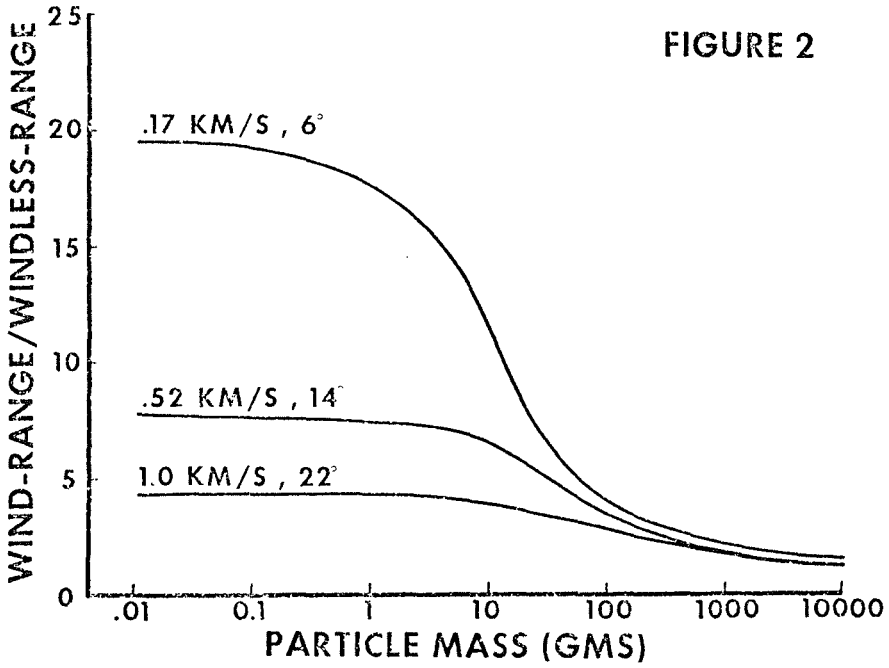


FIGURE 2

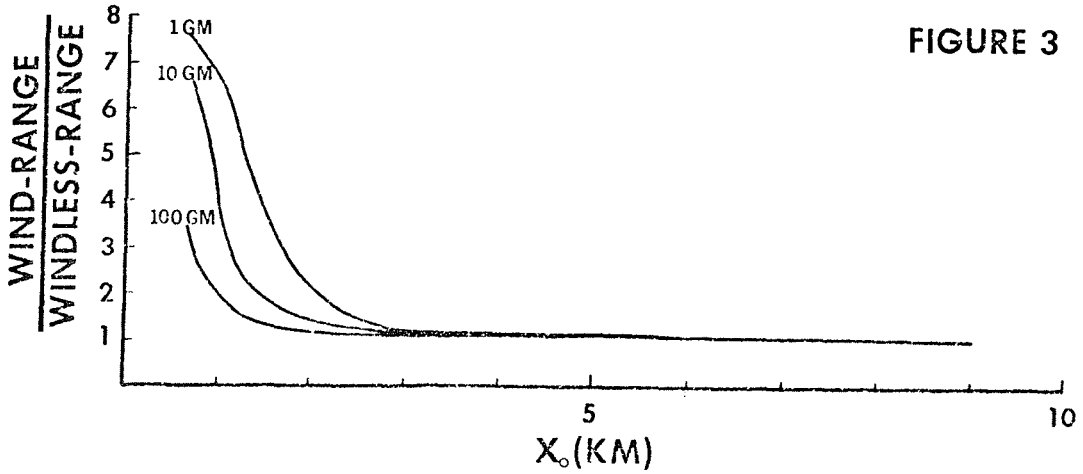


FIGURE 3

# The Steinheim Basin - a Meteorite Crater

By Winfried Reiff
Geologisches Landesamt, Baden-Wurttemberg, 7 Stuttgart 1, West Germany

Up to some 1o years ago, geologists thought that the Steinheim Basin in Southern Germany had its origin in Cryptovolcanism. During the last few years, intensive research work was done in the Steinheim Basin. 25 drillings showed the structure of the central uplift, the crater floor and the fall-back breccia. It was found that the Basin is a meteorite crater.

After the meteorite impact the Steinheim Basin had a diameter of 3 5oo m and a depth of 22o m. The depth/diameter ratio is 1:16. In the center of the shallow crater there is a central uplift of 8oo to 9oo m in diameter and 15o m in height above the crater floor. The crater is situated in well-stratified limestones and marlstone layers of the Malm. Through the impact huge blocks were thrust radially from the center of the crater and made up the rim. Today, this rim has been worn away. There is still part of these blocks forming a strip of 2oo to 4oo m which circles the inner side of the crater wall. This rock was fractured and now consists of fine to coarse grained breccia. In between there are rocks which still show their original strate;but all these rocks stand upright or are inclined in all directions and partly folded.

The rim zone shows rock that has been hardly fractured; but this 3oo m wide bell is of a shallow flexure structure studded with small faults. There is no evidence that these rocks have been uptilted or overturned, but this is quite possible that this area in the upper rim zone has been eroded or does not show any distinct exposures.

The rock of the crater floor has been disturbed. Often blocks have been uplifted and now are some 1oo m above their original bond.

# THE STEINHEIM BASIN - A METEORITE CRATER

Reiff, W.

In the central zone of the central uplift, layers of rocks of the deeper strata (Dogger and Lias) have been lifted some 250 to 320 m and are almost upright. These are mostly stratified claystones which have been shifted along the surface of their layers and which show a high degree of fracturing. It seems as if the disturbance of this megabreccia has been more intensive than that in the central uplift of the Flynn Creek Crater; roughly it corresponds to the disturbance of the central uplift of the Wells Creek Crater, which has more than twice the size of the Steinheim Basin and the Flynn Creek Crater. In the Flynn Creek Crater and the Wells Creek Crater, the rocks of the central uplift consists of dolomite. Probably, the claystones of the central uplift in the smaller Steinheim Basin account for the fact that its central uplift show a structure similar to that of the central uplift of the larger Wells Creek Crater which consists of dolomite. It seems as if the degree of deformation depends on the kind of rock and the extent and intensity of the impact.

In a depth of 200 m, the strata are no longer in an upright position but inclined at a 60° angle. Also, in a depth of 330 m, the layers have been uplifted by only 110 m. The degree of deformation decreases with the depth. For instance, in the Dogger sandstone (Aalenium), which at the time of the impact was about 400 m below the terrain surface the quartz grains show planar features. In the Triassic sandstone (Keuper), which was about 540 m below the terrain surface at the time of the impact, the quartz grains do not show any planar features. But the shock wave was strong enough to fracture them. It seems as if the striated structure of the shatter cones becomes more coarse with the greater depth and the distance between the individual strias becomes greater and, consequently, the number of strias smaller. As a reaction to the shock wave, the blocks in the central uplift moved towards the center and then in an upward direktion. There are also some blocks which were pressed downwards.

# THE STEINHEIM BASIN - A METEORITE CRATER

Reiff, W.

In the flanks of the central uplift, the upward thrust of the blocks was not as intense as in the center; it is rare that they stand upright. Almost always they show an inclination of 50 to 60°. The slopes of the central uplift are inclined at an angle of 10 to 15°, of 30° at a maximum.

The slopes of the central uplift, the crater floor and part of the thrust blocks along the wall are covered with fall-back breccia, which is up to 50 m thick. The rocks of this breccia come from the central uplift area. They consists of Lower Malm and Dogger. This breccia containes granular quartz with planar features and shatter cones.

The Steinheim Basin is a typical meteorite crater. Comparisons with other craters can be made only if they are of about the same form and size and if they originated in about the same type of rock. If just one condition differs, there are deviations of one or more typical features.

SHOCK-WAVE ATTENUATION: APPARENT VARIATION WITH CRATER DIMENSIONS.
P.B. Robertson and R.A.F. Grieve, Earth Physics Branch, Dept. of Energy, Mines and Resources, Ottawa, Ontario, K1A 0Y3, CANADA.

Petrographic observations at terrestrial craters have defined the progression of mineralogical shock deformation effects produced by increasing shock pressures (1,2). Most of these natural shock effects have been duplicated in experiments and, in some cases, pressures have been determined for their initial formation or range of development (3,4 and others). It is possible, therefore, to estimate the shock pressure experienced by shocked autochthonous bedrock samples at an impact structure from observation and measurement of their mineralogical shock effects.

Planar deformation elements produced in quartz are the most thoroughly studied low pressure effects, and develop in the approximate range of 75 to 300 kbar. Four shock levels have been identified by the development of particular crystallographic orientations of these planar features (5). These shock levels and their estimated pressures of formation are: A - planar features parallel to C $\{0001\}$ - above 75 kbar; B - parallel to $\omega$ $\{10\bar{1}3\}$ - above 100 kbar; C - $\{22\bar{4}1\}$ or $\{10\bar{1}1\}$ - above 140 kbar; D - $\pi$ $\{10\bar{1}2\}$ - above 160 kbar (6).

Using the above scheme, empirical zones of shock deformation were outlined in basement rocks beneath the simple crater, Brent (7). Also, estimates were made of the shock pressures experienced in the autochthonous rocks of the central uplift at the complex crater, Charlevoix (8). In both cases intensity of shock deformation was found to decrease outward from the point of impact according to some function of the radial distance. In an attempt to determine whether shock attenuation rates remain constant and independent of crater size and type, shock-pressure zoning studies based on planar deformation features in quartz have been carried out, enlarged, or refined for the Charlevoix (35 km), Slate Islands (15 km) and Brent (4 km) impact structures.

Comparison between Charlevoix and Slate Islands is relatively straightforward in that both are complex craters and the present radial distance of a particular sample from the centre of the respective structure is readily measurable. However, because Charlevoix is twice the size of Slate Islands, it is necessary to normalize the radial distances to a common, non-dimensional, structural parameter. This was accomplished by assuming that the structures had structurally equivalent transient cavities whose radii were estimated at 13 km and 7 km for Charlevoix and Slate Islands, respectively. Shock pressures were then correlated with the parameter, radial proportion, the ratio of sample distance from the centre of the structure to the transient cavity radius. Comparison between the two structures indicates that apparent

SHOCK-WAVE ATTENUATION

P. B. ROBERTSON

shock pressure attenuation at Slate Islands is more rapid than at the larger Charlevoix structure.

Comparisons of shock-pressure zoning between the complex craters and the simple crater, Brent, are not as straightforward. Material sampled in drill core beneath the cavity at Brent is assumed to have remained essentially in its pre-impact position, and thus distance from point of impact can be measured directly. The autochthonous rocks at Charlevoix and Slate Islands, which originally lay beneath the transient cavity, moved upward and inward during structural readjustment to form the central uplift, and so their radial distance from the point of impact position can be determined by reconstructing the transient cavity. To do this, the following assumptions must be made: (a) the transient cavity relationships determined for simple craters, $r^2=2p^2$, where r is radius and p depth (9), must hold for larger impacts; (b) the trajectories determined for the upward and inward movement to form the central peak at Gosses Bluff (10) are applicable to other structures; (c) the shape of shock contours in the basement rocks beneath the cavity are approximately hemispherical (11).

This reconstruction was carried out for Charlevoix, pressures were plotted against original radial proportion, and the results compared with those at Brent. As before, slopes of the curves at the two sites indicate much more rapid attenuation of the shock wave at the smaller site. The attenuation rate calculated at Charlevoix for pressures below 300 kbar is a function of approximately $r^6$, whereas at Brent the rate is a function of approximately $r^{12}$. (This latter high attenuation rate leads to unresolved problems concerning pressure distribution for values above 300 kbar.) In addition, to superimpose any common pressure value on the two curves requires the transient cavity at Charlevoix to be reduced in depth or increased in radius by approximately 20%. (The latter is considered less likely because of stratigraphic and structural constraints.) Either modification, or combination of the two, results in a transient cavity shallower than that described by the formula derived for simple craters (9).

We conclude that shock pressures apparently attenuate less rapidly with increasing size of impact event, possibly due to lengthened shock pulse from a larger impacting body. At this stage of the investigation, values for the actual rates cannot be determined with precision. In addition, the possibility exists that transient cavities may be shallower in impacts which result in complex craters. This suggestion finds support in the hypothesis, as determined from calculations of impact melt volumes, that crater excavation becomes less efficient with increasing crater size (12).

References

(1) Stöffler, D., Fortschr. Miner., 49, 50-113, 1972.

(2) Stöffler, D., Fortschr. Miner., 51, 256-289, 1974.

(3) Hörz, F., In Shock Metamorphism of Natural Materials, Mono, 243-254, 1968.

(4) Robertson, P.B., Jour. Geophys. Res., 80, 1903-1910, 1975.

(5) Robertson, P.B. et al., In Shock Metamorphism of Natural Materials, Mono, 433-452, 1968.

(6) Grieve, R.A.F. and Robertson, P.B., Contrib. Min. Petrol. (in press).

(7) Dence, M.R., In Shock Metamorphism of Natural Minerals, Mono, 339-362, 1968.

(8) Robertson, P.B., Bull. Geol. Soc. Am., 86, 1630-1638, 1975.

(9) Dence, M.R., Meteoritics, 8, 343-344, 1973.

(10) Milton, D.J. et al., Science, 175, 1199-1207, 1972.

(11) O'Keefe, J.D. and Ahrens, T.J., Proc. 6th Lunar Sci. Conf., 3, 2831-2844, 1975.

(12) Grieve, R.A.F. et al., This volume.

IMPACT AND EXPLOSION CRATERS: MORPHOLOGICAL AND STRUCTURAL ANALOGS. David J. Roddy, U. S. Geological Survey, Flagstaff, Arizona 86001.

Morphological and structural comparisons between impact and explosion craters demonstrate that each have one or more of the following features in common: a) bowl-shapes underlain by breccia lens, b) very shallow bowl-shapes with broad, flat floors underlain by thin breccia lenses, c) central uplifts, d) multirings, e) sub-crater floor material moved inward and upward, f) terraced walls, g) raised, outward dipping and/or lowered, inward dipping rim strata, h) zones of concentric rim deformation, i) similar scaled heights of uplift and distances to concentric zones of deformation, j) inner continuous ground cover of ejecta blankets formed by overturned flaps of inverted strata with hummocky, blocky surfaces, k) outer discontinuous ground cover of ejecta blankets formed by overturned flaps with ray extensions; l) secondary cratering and m) shock metamorphism, including shatter cones, fused alluvium, and planar features.

For example, large-scale bowl-shaped explosion craters formed by surface or shallow heights-of-burst commonly have floors underlain by saucer-shaped breccia lenses of fallback and locally disrupted country rock. Strata in the crater walls are faulted, folded, locally brecciated, and uplifted, and ejecta blankets consisting of overturned flaps of inverted stratigraphy surround the craters. This highly generalized description also applies to Meteor Crater, Arizona, a 1.2 km diameter bowl-shaped impact crater in north-central Arizona.

An analog of impact craters with central uplifts is found in the 500-ton TNT Snowball surface hemisphere explosion trial. This crater, 100 m across and 6 m deep, exhibited a well-defined central uplift on a broad flat floor. The morphology and structure of Snowball has been described as essentially identical to the Flynn Creek Crater in Tennessee, a 3.5 km diameter impact crater formed in limestone. Snowball and Flynn Creek craters were both shallow, flat-floored depressions formed in flat-lying strata. Breccia lenses and ejecta blankets of inverted strata were formed at each of the craters, and both have well-defined central uplifts with similar internal structures. The deepest horizons raised in the central uplifts of Snowball and Flynn Creek have a similar ratio of scaled vertical heights of structural uplift compared with the ratio of crater diameters, i.e., structural uplift averages approximately ten percent of the diameter. Low-angle thrust zones and high-angle faults and folds concentric to the crater walls are common in the rims of both craters. Local concentric anticlinal folding immediately adjacent to the crater walls of Snowball is equally common in the Flynn Creek crater walls. Upper plates of thrust faults in both Snowball and Flynn Creek have moved outward. Several concentric, discontinuous fracture zones around Snowball occur at equivalent scaled distances as concentric faults or folds at the Flynn Creek crater. The southeastern rim graben at the Flynn Creek crater has an equivalent scaled distance to one of the inner irregular fracture zones at Snowball. Large subsidence of this graben occurred with time at the Flynn Creek crater as it did at Snowball.

An analog of impact craters with multiring structures is found in the Prairie Flat 500 ton surface tangent sphere explosion trial. This event formed a crater, 80 m in diameter and 5 m deep, which consisted of a shallow

IMPACT AND EXPLOSION CRATERS:

Roddy, D. J.

crater with a broad, flat floor and concentric rings. Systematic comparisons with large-scale impact craters have not been completed, however, the general morphology and ring spacing bear a real similarity, despite scaling to such large sizes, to certain multiring impact structures such as the Ries Basin in Germany, 24 km across; Clearwater Lake in Canada, 32 km across; the Orientale Basin on the Moon, approximately 1000 km across; and the Caloris Basin on Mercury, over 1000 km across. The Ries Basin, for example, consists of a very shallow, broad basin with a concentric crystalline ridge exposed on the floor. This ridge forms a ring which is continuous over half-way around the crater floor and lies at an equivalent scaled distance to one of the rings in Prairie Flat.

A general physical basis permitting these comparisons rests in the studies of a number of workers (1, 2, 3, 5, 6, 8, 9, 10, to mention a few) which argue for the general applicability of shallow buried to surface-generated explosions as general analogs for certain types of impact craters and cratering processes. These studies make use of the conditions in which surface-generated explosions initiate excavation by shock compression, comminution, plastic, and brittle deformation with high stress release by rarefaction and ejection of material, i.e., conditions that more nearly approximate a hypervelocity impact event which generates a shockwave initially at the surface (1, 7, 10). Deeply buried charges on the other hand, include the above processes but depend strongly on excavation by "upward" directed shock waves, gas acceleration, and spallation (4, 11), conditions initially quite unlike an impact event. To date, applications of explosion crater analogs to impact cratering have been most useful in: a) comparing general impact and explosion crater morphologies to determine if a specific crater in question was formed by a shockwave process, i.e., if it has an impact origin; b) predicting general sequences of cratering events for large-scale impact craters; c) predicting the styles of subsurface deformation at impact craters, and d) "suggesting" certain impact structures have been formed by lower-density impacting bodies.

It should be emphasized, however, that although morphological and structural explosion analogs are a useful tool in studying impact cratering processes, one must exercise considerable care in application of the data. Consideration must be given in such analog comparison of physical processes to a number of factors such as; energy coupling and momentum transfer as a function of time, similitude conditions, energy scaling, material-strength scaling, gravity effects, different types of impacting bodies, layering and the strength-related problems in the target and projectile, and presence of an atmosphere, to mention a few. Of these areas, impact velocity, energy coupling, strength of materials, and gravity play dominant roles.

(1) Baldwin, R. B. (1949) The face of the Moon. Univ. of Chicago Press, 230 p.

Baldwin, R. B. (1963) The measure of the Moon. Univ. of Chicago Press, 488 p.

(2) Gault, D. E., W. L. Quaide, and V. R. Oberbeck (1968) Impact cratering mechanics and structures. Proc. 1st Conf., NASA, Goddard Space Flight Center, April 14-16, 1966. Mono Book Corp., Baltimore, p. 87-100.

(3) Johnson, S. W., J. A. Smith, E. G. Franklin, L. K. Moraski, and D. J. Teal (1969) Gravity and Atmospheric Pressure Effects on Crater Formation in Sand. J. Geophys. Res., v. 74, n. 20, p. 4838-4850.

(4) Knox, J. B. (1969) Nuclear Excavation: Theory and Applications. Nuclear Applications and Technology, v. 7, n. 3, p. 189-231.

(5) Milton, D. J. and D. J. Roddy (1972) Displacements within impact craters. Proceedings, Internatl. Geological Congress, Twenty-fourth Session. Section 15 (Planetology), p. 119-124.

(6) Moore, H. J., R. W. MacCormack, and D. E. Gault (1963) Fluid impact craters and hypervelocity--high-velocity impact experiments in metals and rocks, in Proceedings of the Sixth Symposium on Hypervelocity Impact, Cleveland, Ohio, April 30, May 1, 2, 1962: Cleveland, Firestone Tire & Rubber Co., v. 2, pt. 2, p. 367-399.

(7) Nordyke, M. D. (1961) On Cratering. A brief history, analysis and theory of cratering. Lawrence Radiation Laboratory, UCRL 6578, 72 p.

(8) Oberbeck, V. R. (1971) Laboratory Simulation of Impact Cratering with High Explosives. J. Geophys. Res., 76, n. 23, p. 5732.

(9) Roddy, D. J. (1968) The Flynn Creek Crater, Tennessee, in French, B. M., Short, N. M., eds. Shock Metamorphism of Natural Materials. Proc. 1st Conf., NASA, Goddard Space Flight Center, April 14-16, 1966, Mono Book Corp., Baltimore, p. 291-322.

Roddy, D. J. (1973) Geologic Studies of the Middle Gust and Mixed Company Craters, in Proceedings of the Mixed Company/Middle Gust Results Meeting 13-15 March 1973, Vol. II, Defense Nuclear Agency, DNA 3151P2, p. 79-124.

(10) Shoemaker, E. M. (1960) Penetration mechanics of high velocity meteorites illustrated by Meteor Crater, Arizona. Internat. Geol. Cong., 21st, Copenhagen, Rept. 18, p. 418-434.

(11) Terhune, R. W., T. F. Stubbs, and J. T. Cherry (1970) Nuclear cratering on a digital computer. Proc. of Symposium on Engineering with Nuclear Explosives, Las Vegas, Nevada, Jan. 14-16, 1970.

THE FLYNN CREEK CRATER: STRUCTURAL DEFORMATION AND CRATERING PROCESSES. David J. Roddy, U. S. Geological Survey, Flagstaff, AZ 86001.

Approximately 360 million years ago a large, flat-floored crater, 3.6 km in diameter and over 200m deep, was formed in what is now north central Tennessee. The impacting body delivered a minimum of $10^{25}$ ergs while violently fragmenting over 2.0 cubic km of flat-lying Middle and Upper Paleozoic limestone and dolomite. Total brecciation and mixing of rock units to a depth of about 0.2 km were completed in seconds with over 1.5 cubic km of rock ejected during the event. Within the crater a thin breccia lens of limestone and dolomite, averaging 40m in thickness, remained as fallback and locally disrupted country rock. Fragments in this lens lie in chaotic orientations in a carbonate powder matrix and range in size from a fraction of a millimeter up to blocks 100m across. Drill core data now indicate that the limestone and dolomite beds immediately below the base of the breccia lens are highly faulted and folded with deformation rapidly decreasing downward until the rocks are nearly flat-lying and relatively undisturbed at depths of about 100m beneath the breccia lens.

During the excavation phase, a massive central uplift over 1.0 km across and 120m high formed in the middle of the crater. This dynamic structural uplift consists of steeply-dipping, faulted, folded, and brecciated Middle Ordovician limestone and dolomite which have been raised as much as 350m above their normal stratigraphic positions. Shatter cones are common in the dense dolomites from the deeper units.

During the later stages of excavation, flat-lying Middle and Upper Ordovician limestone and dolomite in the rim were moved outward during compression and abruptly uplifted a minimum of 10 to 50m. Structural deformation in the rim yielded tightly folded, doubly plunging anticlines and synclines that have fold axes either radial or parallel to the crater walls. Locally, folds concentric to the walls have produced structural shortening as large as 35 percent caused by radial compression. During the final stages of cratering normal, reverse, and thrust faulting remained a common mode of structural failure. At some time during the last phase of excavating, or somewhat later, parts of the rim experienced a minor downdropping to the extent that the entire rim dips into the crater. The downdropping of a few meters in the inner rim appears to be a material readjustment related to the large inward and upward movements forming the central uplift. In these areas the rim strata immediately adjacent to the walls also commonly exhibit a monoclinal fold dipping into the crater, the result of the initial compression.

In the southern and eastern rims, a major thrust block, over a kilometer in length, was forced out from the crater during the excavation phase and uplifted strata over 50m. The thrust block partly overrides a very large tilted graben that later downdropped about 100m and moved towards the crater. Breccia overlying this graben was ejected during the early stages of excavation and remains today in the downdropped section as part of the ejecta blanket that once surrounded the entire crater.

Erosion began to modify the crater immediately after its formation, washing part of the debris back into the crater and lowering the regional

THE FLYNN CREEK CRATER:

Roddy, David J.

surface on the order of a few meters. A thin deposit of marine sedimentary breccia overlain by a thin marine dolomite of early Late Devonian age form the first crater deposits. Deposition remained continuous during this time until the crater was filled by the black muds of the early Late Devonian Chattanooga Sea.

Flynn Creek is now known to be one of a class of structures which have flat-floors and central uplifts. Decaterville, Gosses Bluff, Manicouagan, Sierra Madera, and Steinheim, to mention a few, each have certain structural similarities with Flynn Creek. Theoretical calculations by (1) indicate that central uplifts can be formed by surface events. Certain field studies and experimental explosion crater data suggest flat-floored impact craters with central uplifts may be formed by low density impacting bodies, a process which needs further examination (2).

(1) Ullrich, W. G., 1976, The Mechanics of Central Peak Formation in Shock Wave Cratering Events, AFWL-TR-75-88, 138 pp.

(2) Roddy, D. J., 1968, The Flynn Creek Crater, Tennessee, in Shock Metamorphism of Natural Materials, French & Short, eds., Mono Book Corp., Baltimore, Md., p. 291-322.

Roddy, D. J., 1976, High-Explosive Cratering Analogs for Bowl-Shaped, Central Uplift, and Multiring Impact Craters, Proc. Lunar Sci. Conf. 7th, in press.

Model of the Flynn Creek crater, constructed from the structure contour map, showing the crater shortly before deposition of the Chattanooga Shale in early Late Devonian time. The large hills near the outer parts of the crater are underlain by megabreccia blocks derived from the crater walls. The dotted line indicates the position of the top of the crater wall in areas where large volumes of ejecta have been washed back into the crater, modifying the original crater shape. No vertical exaggeration. Lighting is from south. (1)

Structure contour map of Flynn Creek Crater drawn on the base of the Chattanooga Shale showing topography just before deposition of shale. (1)

# THE FLYNN CREEK CRATER:

Roddy, David J.

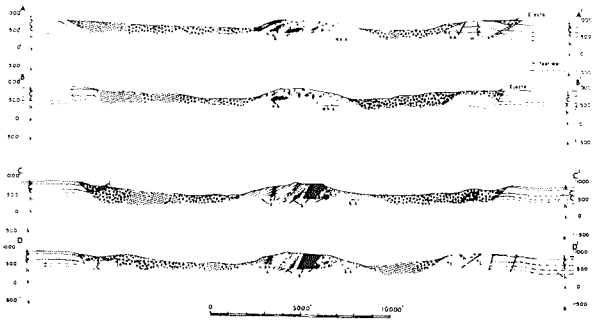

Generalized geologic cross-sections of the Flynn Creek crater, showing the structure shortly before deposition of the Chattanooga Shale in early Late Devonian time.

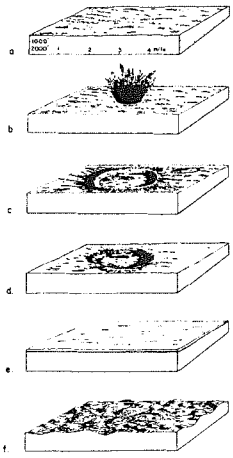

Diagrammatic sequence of events during formation and subsequent history of the Flynn Creek crater. (a) The Flynn Creek area, shortly before formation of the crater, about 360 million years ago, was apparently a rolling lowland or coastal plain exposing rocks of Leipers (Upper Ordovician) age. (b) Formation of the Flynn Creek crater by a comet impact about 360 million years ago, as interpreted by the writer. The area may have been inundated by the first shallow waters of the Chattanooga Sea. (c) The final crater, immediately after formation, was 3.6 km in diameter and about 150 m in depth; it contained a central hill that stood about 120 m above the crater floor. Rocks in the central hill were uplifted as much as 350 m from their original position; brecciated Knox dolomite contains shatter cones. An ejecta blanket surrounded the crater and overlay the highly deformed strata in the crater rim. The large rim thrust blocks and rim faulting and folding occurred when the crater was formed. (d) A period of erosion followed formation of the crater; many small valleys were formed on the crater rim. The ejecta blanket was removed, much of the ejecta being washed back into the crater. Subaqueous erosion and marine deposition of bedded breccias and bedded dolomite occurred in the crater during early Late Devonian time, in the first shallow waters of the Chattanooga Sea. (e) The Chattanooga Sea filled the crater with black muds in early Late Devonian time; the Flynn Creek area remained under water through at least Early Mississippian time, when the Fort Payne sediments were deposited. (f) Uplift and erosion during Quaternary (and probably Tertiary) time has produced a highly dissected region of steep-sided hills and valleys with an average relief of 150 m. The structure of the Flynn Creek crater is now well-exposed along the valley floors and walls. (1)

CRATER-RELATED GROUND MOTIONS AND IMPLICATIONS FOR CRATER SCALING, by F. M. Sauer, Physics Int., and H. F. Cooper, R & D Associates

The physical parameters that affect crater formation, (e.g., energy and momentum coupled to the ground, geologic properties, etc.) also affect the neighboring close-in ground motions. A variation in these parameters that lead to larger (or smaller) craters also likely lead to larger (or smaller) ground motions. This simple notion motivated a search for a characteristic length that is common to crater-forming process and the subsequent ground motion phenomena. The low-frequency, near-surface ground motion data from a large number of cratering explosions in a variety of media suggest that the cube root of the crater volume $V^{1/3}$ is such a characteristic length. In particular, for more or less uniform media, the free surface peak transient particle displacement data are reasonably correlated by

$$\underset{\sim}{d}/V^{1/3}=K(V^{1/3}/R)^3$$

where $\underset{\sim}{d}$ is the peak transient displacement, V is the apparent crater volume, R is the range from the explosion, and K is a parameter which depends on the height-of-burst of the source. Thus, the use of $V^{1/3}$ as a characteristic length integrates the effects of source parameters and the geologic material properties in such a way that the near-surface particle displacement for various geologies can be correlated independently of source parameters and material properties.

Given such a correspondence, it seems reasonable that information on cratering phenomena might be inferred from a study of the ground motions near a cratering burst. In particular, analysis of the temporal variations of the ground motions may provide insight into the time scale for crater formation. For example, the time to peak particle displacement data from high explosive and nuclear experiments in Pacific Coral vary proportionally to $V^{1/6}$. Also the ground motion data from high explosive experiments in playa demonstrate that the time of peak displacement scales as $W^{1/6}$ where W is explosive yield. This observation suggests that times important to the crater-forming processes scale as $V^{1/6}$ or $W^{1/6}$.

If particle displacements scale as $V^{1/3}$ and the characteristic times scale $V^{1/6}$, then peak particle velocities would be expected to scale as $V^{1/6}$. This suggestion is consistent with observations on scaling the initial velocities of ejecta from high explosive experiments. Also, measurements of the time

CRATER SCALING

F. M. Sauer and H. F. Cooper

of impact crater formation observed in the laboratory are consistent with this hypothesis.

# A CENTRIFUGE CRATERING EXPERIMENT:

R. M. Schmidt
Boeing Aerospace Co., Seattle, WA 98124

A centrifuge was used to perform explosive cratering tests under the influence of gravitational accelerations up to 500G's. The preliminary test matrix of 12 shots, primarily designed to demonstrate the feasibility of such experiments, provided data which suggests that increased gravitational acceleration may offer a means for understanding large scale crater formation. This relevance was the primary objective of the experiment and led to the tentative formulation of a gravity yield scaling law.

Relationships determining crater volume in terms of several key variables were sought in the form of suitable non-dimensional parameters. Such a parameter for volume is $V(\rho/W)$. This parameter must be expressible as a function of independent variables which include a term containing a product of the acceleration due to gravity and the charge mass or the yield energy. The form of the grouping can be chosen to include variables thought to be important. As shown by Chabai[1], a cube root scaling law results from non-dimensionalizing charge mass in terms of density and a characteristic length. Following Chabai[1,2] an appropriate non-dimensional grouping which contains gravity and yield is $(g/U^2)(W/\delta)^{1/3}$ (see footnote 3 for definition of symbols). Other choices which may be more useful when comparing different explosive sources such as H.E. and nuclear include $(g/U^{8/3})(E/\delta)^{1/3}$ or $ga/Q$. In the present discussions all the data are compared on the basis of equivalent mass of TNT. The parameters U and $\delta$ define the explosive (in its active state). These have not been dealt with in detail, but are regarded as essentially constant among shots since only H.E. data are considered. The appropriate form then leads to the scaling $gW^{1/3}$ = constant, inferred by Hess and Nordyke[4] in discussing the dynamic similarity requirement for terrestrial and lunar craters, based upon throwout mass trajectories.

Crater volume is also found to be influenced by the depth of burial, so an additional non-dimensional parameter is defined to characterize this: $d(\rho/W)^{1/3}$. A three-space plot of volume as a function of gravity-normalized yield and depth of burial is shown in Fig. 1, which is constructed from the following data sets.

| CHARGE (equivalent TNT) | GRAVITY | GEOLOGY | REFERENCE |
|---|---|---|---|
| 256 lbs-100 KT | 1 | Desert Alluvium | Chabai[1] |
| 10 grams | 25-65 | Wet Sand | Viktorov & Stepenov[5] |
| 1 gram | .2-2.5 | Dry Sand | Johnson[6] et. al. |
| .2-.6 grams | 1-500 | Clay | present work |

CENTRIFUGE EXPERIMENT

Schmidt, R. M.

Fig. 2 is a cross-section of the surface at constant $(g/U^2)(W/\delta)^{1/3}$, showing good correlation of the small charge high gravitational acceleration data with the 256# desert shots. The agreement is better than the scatter band on the field data.

The parametric representation appears useful and the quality of the initial fit (in which material is represented only by its density) is very promising. The next step is to include large scale nuclear and more small scale (1G) laboratory results such as the Dayton[7] sand data. In addition to crater volume, aspect ratio must be considered. Again the analogy is valid in that increased gravity increases aspect ratio and a similar representation for aspect ratio in terms of $(g/U^2)(W/\delta)^{1/3}$ and $d(\rho/W)^{1/3}$ can be generated. The non-dimensional analysis should be extended to include the characteristics of different explosives, as well as additional pertinent medium material properties.

The conclusion is that centrifuge testing provides a unique cratering experiment and preliminary results indicate a definite correspondence between high gravity and large yields suggesting the existence of a "gravity-yield" scaling law.

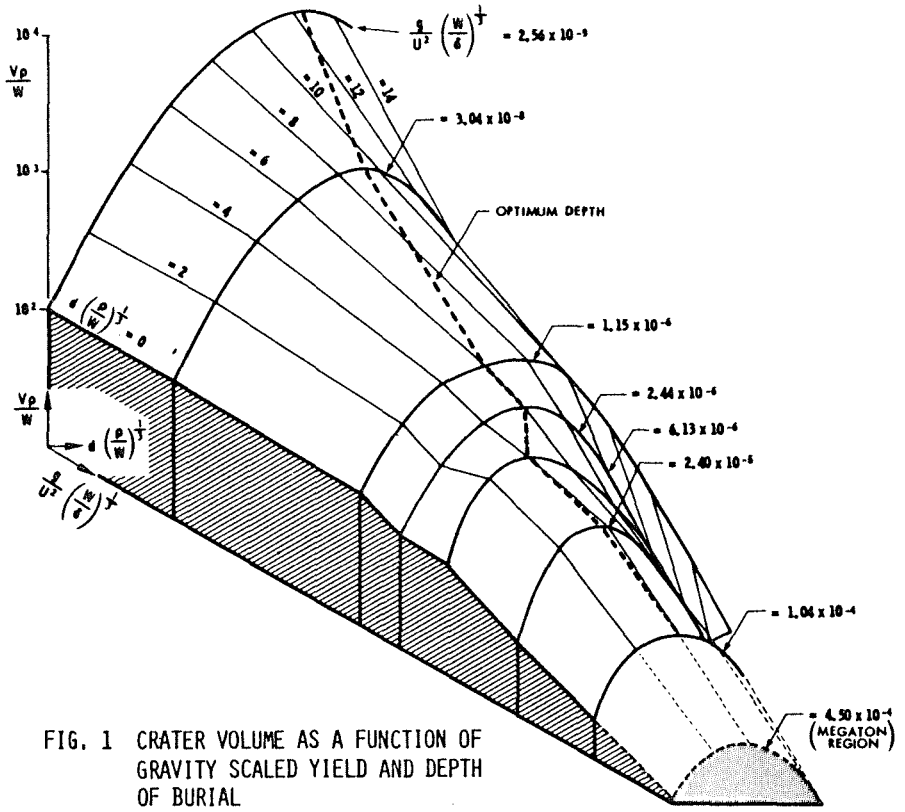


FIG. 1 CRATER VOLUME AS A FUNCTION OF GRAVITY SCALED YIELD AND DEPTH OF BURIAL

CENTRIFUGE EXPERIMENT

Schmidt, R. M.

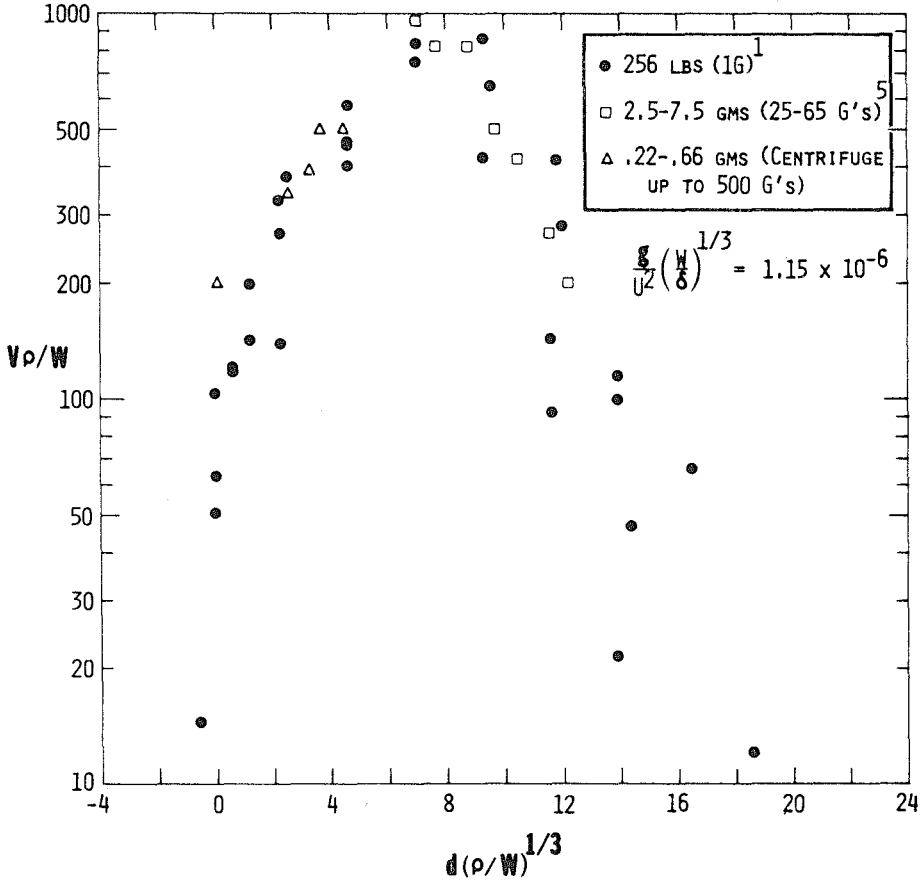


FIG. 2 GRAVITY PARAMETER SCALING FOR DEPTH OF BURIAL EFFECT ON CRATER VOLUME OVER $10^6$ RANGE ON YIELD

REFERENCES

(1) Chabai,A.J.,J.Geophys.Res.,Vol.70,No.20,5075-5098,1965.
(2) Chabai,A.J.,Proceed. of Symp. on Nuclear Craters and Ejection. Aerospace Report #TR-1001(S2855-40)-4, Nov. 1967.
(3) Footnote:
V = apparent crater volume W = charge mass
ρ = medium density E = charge energy
g = acceleration of gravity U = Chapman-Jouguet particle velocity
d = depth of burial
a = charge radius δ = Chapman-Jouguet density
Q = charge energy per unit mass
(4) Hess,W.N. and M.D. Nordyke,J.Geophys.Res.,Vol.66,No.10, 3405-3431,1961.
(5) Viktorov,V.V. and R.D.Stepenov,Inzh.Sb.,28,87-96,1960, (translation Sandia Report SCL-T-392, 1961).
(6) Johnson,S.W.,et.al.,J.Geophys.Res.,Vol.74,No.20,4838,1969.
(7) Piekutowski,A.J.,Four Laboratory-Scale High-Explosive Parametric Sensitivity Studies, AFWL-TR-75-211, 1975.

THE RESPONSE OF ROCKS TO LARGE DEFORMATION STRESSES, R. N. Schock, University of California, Lawrence Livermore Laboratory, Livermore, CA 94550

When a body impacts a rock surface, its energy is either converted to heat or does work on the rock. This work may be in the form of elastic deformation and dissipated as an acoustic wave, or as permanent compaction, fracture, or other inelastic processes. The relative roles of these processes are dependent on the physical characteristics of the rock and determine the effect of the impact (i.e. form of the crater and ejecta). Essential to the prediction of the effect of the impact is knowledge of the nature of the relation between stress and mechanical response. Such predictions can be either of the crater form when the impacting conditions are known, or of the impacting conditions when the crater form is known.

Laboratory studies of the deformation of rock at low to intermediate strain rates have been useful in formulating constitutive relations which govern the dynamic response of rocks to large-amplitude stress pulses. As part of these studies, experiments have been designed to study three-dimensional stress-strain relations along a variety of loading and unloading paths. Materials studied have ranged from those exhibiting brittle fracture to ductile flow, those with and without porosity, and with varying degrees of fluid content. Stress states have ranged from compressive to tensile, and strains to 0.20 have been studied. Maximum compressive stresses attained were 3.5 GPa. A number of observations based on these studies are useful in simplifying the complex behavior of rocks.

Most polycrystalline solids which fail by brittle fracture are very weak in tension in comparison to their compressive strength. Failure strengths often differ by factors of ten or more because when the stresses are compressive, cracks close and friction across crack surfaces reduces their influence. Thus, failure envelopes for these materials are strongly dependent on confining pressure. With increasing shear stress, cracks in the unfailed material which are oriented parallel to the direction of maximum compressive stress can grow because the tensile strength of the solid at the crack tip is exceeded, even though the macroscopic stresses may all be compressive. The result is progressive increase in strain in the direction normal to the maximum compressive stress (as oriented cracks open and grow). In turn this results in an increasing void volume (porosity) with increasing mean stress. It is observed that both the onset of this dilatant behavior and ultimate failure in compression are described by curves in shear stress - mean stress space which are independent of loading path, under the general condition of equal minimum and intermediate principal stresses. This implies that shear strain is a unique function of shear stress and mean pressure. This hypothesis has been verified for several brittle rocks and strain predicted. In the dilatant region (between the onset of dilatancy and failure), dilatant strain is given by

# INELASTIC ROCK DEFORMATION

Schock, R. N.

$$\varepsilon_d = \exp\left[\frac{\delta P}{x(\tau)} - A(\tau)\right],$$

where x and A are explicit functions of the shear stress $\tau$ and are dependent on the rock, and P is mean stress.

Dilatancy has been shown to be characteristically associated with failure in tension as well as failure in compression. Tensile stress-states become important on release after dynamic loading.

In dynamic plane-wave loading, yielding (decrease in rigidity) with a subsequent decrease in stress rate will result from dilatant behavior. Available shock-wave data indicate that the onset and the amount of dilatant strain is dependent on strain rate, as is failure stress. Microcracking and dilatant behavior in brittle rocks are part of the process of failure which results eventually in complete loss of rigidity and the observed strain-rate dependence of failure envelopes is a direct result of the strain-rate dependence of micro-crack propagation.

Many polycrystalline solids undergo a transition from brittle to ductile behavior with increasing pressure; thus a maximum value of shear stress is not achieved at a fixed strain. This increase in plasticity results from increasing friction along crack surfaces as cracks close, combined with the tendency of solids to flow or creep under pressure. The observation that dilatancy decreases and vanishes as ductile failure becomes predominant is evidence that cracks no longer play a significant role in failure. However, with increasing strain rate, ductility is decreased and the brittle to ductile transition pressure is increased.

Porosity considerably alters the behavior of rocks. With abundant porosity, failure now occurs by pore failure, and compaction takes place. The onset of this compaction appears to be dependent primarily on the mean stress, although the subsequent amount of compaction is strongly dependent on the associated shear stress. Dynamic results indicate that pore collapse is strain rate dependent.

These observations point to the development of simplified constitutive models which can be used to predict the response of rock to impact loading by identifying the important parameters which determine that response.

# CRATER EVOLUTIONARY TRACKS

Gerald Schubert and Richard E. Lingenfelter
Department of Geophysics and Space Physics
University of California
Los Angeles, California 90024

and

Richard Terrile
Division of Geological and Planetary Sciences
California Institute of Technology
Pasadena, California 91125

We show that a description of crater morphology based on rim height/depth (h/d) and depth/diameter (d/D) ratios provides a quantitative method of assessing the relative importance of competing crater modification processes. Different classes of modification processes produce distinctive evolutionary tracks on a h/d vs. d/D diagram. We have calculated such tracks for three general classes of crater modification: those processes which add material to the crater, e.g. aqueous and aeolian sedimentation, volcanic ash, and lava flooding; those which redistribute material within the crater vicinity, e.g., slumping, viscous relaxation and meteoritic bombardment; and those which remove material from the crater vicinity, e.g. aeolian and aqueous erosion and permafrost withdrawal.

New data on both Martian and lunar craters are also presented. High resolution ground-based radar altimetry[1] together with Mariner 9 imagery allows a determination of Martian crater profiles. The radar scans cover a latitude range of $-13.9^{\circ}$ to $-18.0^{\circ}$ with a surface resolution of 8 km E-W by 80 km N-S and an altitude resolution of about 100 m. Correlation of imagery and radar altimetry removes ambiguities in the interpretation of the radar data. Lunar crater rim heights, depths and diameters were obtained from Lunar Topographic Orthophotomaps with 100 m contours based on Apollo metric photography. The only

CRATER EVOLUTIONARY TRACKS

Schubert, G. et al.

published[2] tabulations of lunar crater rim height were derived from earth-based telescopic observations and have much poorer altitude resolution. Ratios of h/d and d/D for terrestrial craters are based on data from several sources[2,3].

We have compared these ratios for craters on the Earth, Moon and Mars with theoretical evolutionary tracks for models of these general classes of crater modification. Lunar and terrestrial craters occupy similar regions of the h/d vs. d/D diagram, whereas Martian craters lie distinctly apart. This implies that Martian craters fall on a different evolutionary track from terrestrial or lunar craters. The evolution of the lunar and terrestrial craters can be modelled by a combination of filling and slumping processes. Martian crater evolution, however, cannot be understood on the basis of these two classes of crater modification alone. Instead, a process which removes material from the crater rims such as aeolian erosion, must have been the principal form of modification and evolutionary tracks based on such a model coupled with weak aeolian deposition within the crater can indeed fit the Martian h/d vs. d/D data.

This study of crater evolutionary tracks on a h/d vs. d/D diagram demonstrates the importance of quantitative data on crater rim heights to understanding crater morphology and crater modification histories.

References

1. Downs, G.S., Goldstein, R.M., Green, R.R., Morris, G. A. and Reichley, P.E., 1973, Icarus 18, 8.

2. Baldwin, R.B., 1963, The Measure of the Moon (Univ. of Chicago), 442.

3. Nordyke, M.D., 1961, editor Proceedings of the Geophysical Laboratory - Lawrence Radiation Laboratory Cratering Symposium (Univ. of California, Lawrence Radiation Lab. Report UCRL-6438).

A DYNAMIC CRATER EJECTA MODEL, W.R. Seebaugh, Science Applications, Inc., McLean, Va. 22101.

The model developed for generating the ejecta environment for a nuclear burst is delineated schematically in Figure 1. The inputs to the model are the following:

(1) Theoretical velocity distribution for continuous hydrodynamic material emerging from the nuclear crater
(2) Empirical models for ejecta mass, fragment size distribution, and maximum fragment size
(3) Experimental observations of fragment velocity for high-explosive (HE) shots
(4) Vortex flow model (VORDUM), Reference 3, for the fireball and afterwinds which affect aerodynamic drag
(5) Compressible flow aerodynamic drag model.

Items (1) through (3) above define the crater source. Ejecta fragments produced by this source are transported through the flowfield defined by the VORDUM program [Item (4) above] using the aerodynamic drag model for ejected crater material [Item (5) above]. The source model and the trajectory calculation form the complete ejecta model as shown in Figure 1. The method of analysis is applicable to the modeling of both the ground deposition of crater ejecta and the airborne ejecta cloud. The deposition results are obtained in the form of the ejecta mass per unit impacting the ground plane at a particular range of interest, the associated number of ejecta fragments, and the distributions of mass and number of fragments as functions of fragment diameter. The cumulative mass and number of fragments impacting per unit area, the fragment size class (minimum and maximum frequent diameters), and the minimum and maximum values of the impact time, velocity, angle, momentum, and kinetic energy are also obtained as functions of range from the burst point. The ejecta environment model may also be used to obtain predictions for the early-time airborne ejecta environment, which is termed the ejecta cloud. During the VORDUM trajectory calculations (Figure 1), trajectory parameters in the form of range and altitude versus time are recorded for each trajectory. This information is combined with the crater source description to give the ejecta cloud mass and number densities. The ejecta cloud outlines and the density contours within the cloud are obtained from the spatial plots of fragment mass and number densities.

The ejecta source is defined by the velocity distribution, minimum and maximum velocities, mass, fragment size distribution, and the maximum fragment size associated with the ejected crater material. The most important assumptions in the analytical ejecta model are related to the ejecta source. In a preliminary investigation (References 1 and 2) results of theoretical cratering calculations and experimental observations were combined to give a complete source model for simultaneous ejection of all crater material at zero time after burst. The parameters for this simplified source model are listed in Table 1. The ejecta mass is dispersed over a range of ejection angles with the distribution centered at $45^{o}$. This distribution is applicable to surface bursts.

The simplified ejecta source model is oriented toward the long-range

# A DYNAMIC CRATER EJECTA MODEL

W.R. Seebaugh

ejecta problem. The effects of simultaneous ejection of all fragments at zero time can be shown to be small within the framework of the VORDUM flowfield model (Reference 3); however, at high overpressures, the assumption of simultaneous ejection of all fragments at the burst point leads to substantial errors in fragment impact ranges when it is recognized that many fragments may originate as far from the burst point as 80 percent of the apparent crater radius. The experimental ejecta origin description of Reference 4 is modeled effectively by the dust source model employed in the DICE code (Reference 5). This model simulates the development of the crater as described by the same hydrocode cratering calculations that form the basis for the simplified ejecta source model described above. The distributions of ejection velocity and mass flux through the ground surface from the DICE source model, modified to ensure consistency with the source model parameters given in Table 1, have been incorporated into the ejecta source model as an option for high overpressure environment calculations.

## REFERENCES

1. Seebaugh, W.R., "Private Communication," Science Applications, Inc., April 1974.
2. Seebaugh, W.R., "Studies of the Nuclear Crater Ejecta Environment," Science Applications, Inc., SAI-75-507-WA, DNA 3640F, June 1975.
3. Shannon, J.A., "Private Communication," Science Applications, Inc., July 1972.
4. Davis, L.K. and Carnes, B.L., "Operation Mine Shaft: Cratering Effects of a 100-Ton TNT Detonation on Granite," U.S. Army Engineer Waterways Experiment Station, MS-2151, February 1972.
5. Rosenblatt, M. and Eggum, G.E., "Private Communication," California Research and Technology, May 1975.

# A DYNAMIC CRATER EJECTA MODEL

W.R. Seebaugh

Figure 1. Ejecta Environment Analysis

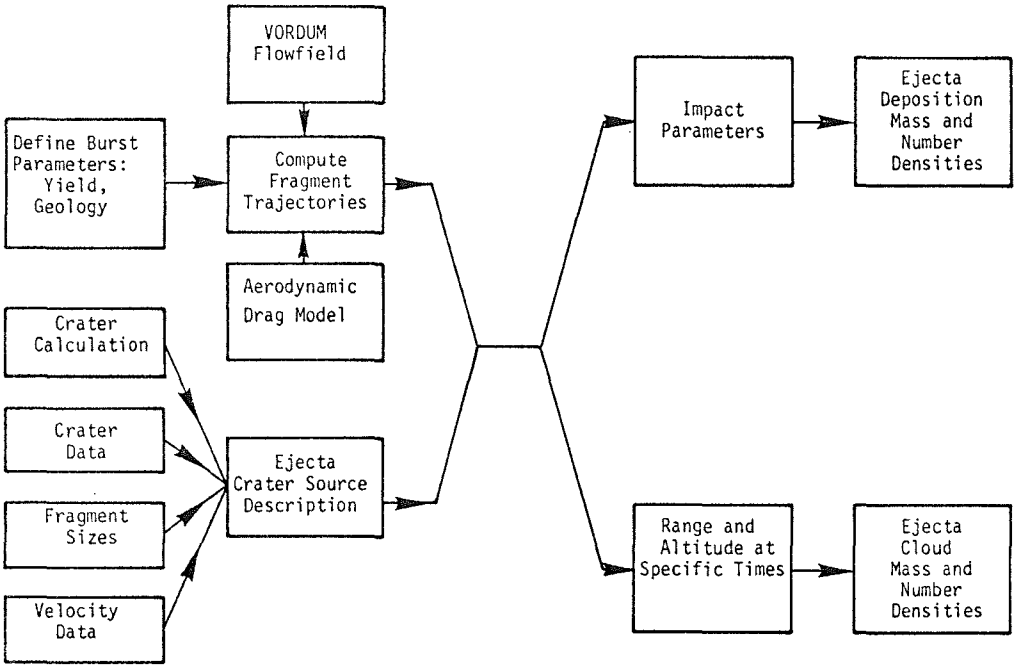


Table 1. Parameters for Simplified Source Model

| PARAMETERS | EJECTA ENVIRONMENT MODEL | BASIS |
|---|---|---|
| Source Velocity Function | $\frac{\delta M}{\delta V} = M_e \frac{V_{min,\,z}}{\sin\theta} V^{-2}$ | Hydrocode Cratering Calculations |
| Minimum Ejection Velocity | | Hydrocode Cratering Calculations |
| Vertical Component | $V_{min,\,z} = 21$ | |
| Total Velocity | $V_{min} = (V_{min,\,z})/\sin\theta$ | |
| Ejecta Mass | $M_e = 1.44\,W^{0.9}$ | Experimental Data |
| Fragment Size Distribution | $\frac{\delta M}{\delta a} = \frac{0.5\,M_e}{\sqrt{a_m}} a^{-0.5}$ | Experimental Data |
| Maximum Fragment Mass | $m_m = 6.6\times10^{5}\,M_e^{0.8}$ | Experimental Data |
| Maximum Fragment Diameter | $a_m = \left(\frac{6\,m_m}{\pi\rho}\right)^{1/3}$ | |
| Maximum Ejection Velocity | | Experimental Data |
| Size Dependent Maximum | $V_{max} = 200\,\frac{a_m}{a}$ | |
| Absolute Maximum | $V_{max} = 3000$ | |

Units: M (Mt), V (ft/sec), m (kg), a (m), $\rho$ (kg/m$^3$)

# RIES DEEP DRILLING: FALLBACK BRECCIA PROFILE AND STRUCTURE OF THE CRATER BASEMENT

D. Stöffler, Institute of Mineralogy, University of Münster, D-4400 Münster, Germany

A drill core of 1206 m depth was obtained in the Ries crater 3.8 km west of the presumable center of the structure (1,2). Based on the composition and texture of the rocks the core may be subdivided into the following units from top to bottom: a) 0-331 m upper Miocene post-impact lake sediments and reworked suevite breccia, b) 331-602 m, suevite breccia with intercalations of shattered crystalline rocks, mainly in the core sections 390-435 m and 505 to 602 m, c) 602-1206 m, fractured and brecciated crystalline rocks dissected by numerous, small, dike- or vein-like fine-grained polymict breccias. We have studied the petrographic composition, texture and grain size characteristics of the whole suevite profile (40 samples within 180 m of suevite) and the dike-like polymict breccias of the lower core section (22 samples).

Results. The grain size distribution of the breccias was measured in the size range from -4.75 Ø (26.9 mm) to +3.5 Ø (0.088 mm) with the Zeiss particle size analyzer using photographs of macroscopic and microscopic sections. The volume frequency distribution is usually bimodal for all samples with a main maximum above 8 mm and a second maximum between 2 and 4 mm. Statistical parameters obtained from cumulative frequency distributions show a general decrease of the mean grain size with increasing depth but skewness and kurtosis remain rather constant trough the whole profile.

The modal composition of the fragment population of the breccias was measured macroscopically in the 8 to 28 mm size range, and microscopically in the 1 to 0.06 mm fraction. The fragmental material of the suevite comprises mainly gneisses, granites, amphibolites, minerals (quartz, feldspar, biotite, amphibole) and recrystallized melt particles. The relative proportions of the crystalline rocks are variable and show no clear systematic trend with depth. However the abundance of melt particles (maximum: ∿ 8 vol.% of the total rock) decreases with increasing depth. At about 525 m the melt fraction drops to a rather low value of about 1 vol.% of the total rock. This leads to a subdivision of the suevite into a top layer which is melt-rich (330-525 m) and a bottom layer which is melt-poor. The melt content in this suevite profile is distinctly lower than that of the fallout suevite occurrences outside the crater rim where the average melt volume ist about 15 %. The average composition of the whole fallback suevite in the 8-28 mm size range is the following:
melt products (28 %), gneisses (42 %), amphibolites (14,5 %), granitic rocks (12,5 %), sedimentary rocks (0.2 %).

Ries deep drilling

Stöffler, D.

This population is in strong contrast to the frequency distribution of crystalline rock masses ejected beyond the crater rim and exposed at the present surface (3). According to (3), 82 % of these rocks are granitic, 13,5 % are gneisses.

The fragment population of the suevite in the microscopic size fraction reveals the following characteristics: The proportion of rock-fragments increases with increasing depth whereas the proportion of melt particles decreases. The ratio quartz: feldspars varies between 0.6 and 2.0. The ratio shocked quartz (quartz with planar elements) to total quartz is mostly between 0.2 and 0.5, but drops to less than 0.1 in the glass-poor suevite below 525 m. The ratio mafic minerals:quartz:feldspars in the suevite is different from all ejected crystalline rocks and could be explained by an admixture of quartz from the sequence of sedimentary rocks (sandstones).

The mineral fragment population of the dike-like breccias below 602 m is distinctly different from the suevite. The content of mafics is extremely low. The dikes above 1065 m have a low proportion of shocked quartz and quartz:feldspar ratios similar to the suevite; in the dikes below 1065 m no shocked quartz was found, the quartz:feldspar ratio is higher than 2, and the abundance of fragments of sedimentary rocks is much less than above 1065 m.

In all breccias samples the highly vesiculated melt products are recrystallized and replaced by montmorillonite and analcite. In addition the top layer of suevite contains clinoptilolite, erionite, phillipsite and chabasite, whereas below 434 m only analcite and montmorillonite was found. No zeolites were detected in the dike-breccias except for analcite at 1015 m; instead anhydrite is quite common.

Discussion. A comparison of the reconstructed pre-impact stratigraphy (4) with pre-impact stratigraphy of the drill core leads to the conclusion that at the drilling point up to about 825 m of rocks ( ∿ 575 m of sedimentary rocks and ∿ 250 m of crystalline rocks) have been removed by the crater excavation if post-impact-uplifting of the crater basement is excluded. The observed differences between the types of crystalline rocks found in the ejecta (3) and those of the fallback suevite indicate that at least the coarse fraction, that is the major part of the volume of the suevite is derived from zones of the crystalline basement which reach deeper than 250 m. The stages of shock metamorphism observed in the suevite (unshocked to molten or vaporized rocks) require that a layer of crystalline basement rocks which must be thicker than 250 m - at least in the central part of the crater - was affected by the corresponding shock zones of radially decreasing pressure and temperature and by the excavation process.

Ries deep drilling

Stöffler, D.

In conclusion the presently high position of the crystalline basement in the central part of the crater which according to the seismic and magnetic obervations (5, 6) is probably in the same level than at the drill core location might be due to post-impact uplifting.

The question whether the whole layer of fallback material producing the observed negative magnetic anomalies (6) is completely composed of suevite as found in the drill core cannot be answered yet. The existence of coherent masses of impact melt rock in the unknown central part of the crater is favored for three reasons:

a) the total volume of melt calculated from modal analyses of suevite assuming a total volume of suevite of about 10 $km^3$ (provided that the whole fallback layer is suevite) amounts to only $\sim$ 0.1 $km^3$. For the size of the Ries crater this seems extremely low. It would be only about 0.05 % of the total displaced mass.

b) The occurence of small coherent masses of impact melt ejected to the eastern rim of the crater near Polsingen and Amerbach.

c) The distribution pattern of impact melt rock and fallback suevite at the Rochechouart crater near Limoges, France, which can be considered as a deeply eroded analogue of the Ries crater (7, 8).

References. (1) Bayerisches Geologisches Landesamt (ed.), 1974, Die Forschungsbohrung Nördlingen 1973, Geologica Bavarica 72, p. 1-98 (2) Stöffler, D., 1975 Meteoritics (abstract) 10, p. 495-497 (3) Graup, G., 1975, Doctoral thesis, University of Tübingen, Germany (4) Schmidt-Kaler, H., 1969, Geologica Bavarica 61, p. 38-40 (5) Angenheister, G., and Pohl, J., 1969, Geologica Bavarica 61, p. 304-326 (6) Pohl, J., and Angenheister, G. 1969, Geologica Bavarica 61, p. 327-336 (7) Lambert, P., 1976, Earth Planet. Sci. Letters, in press (8) Kraut, F., and Becker, J., 1975, Meteoritics (abstract) 10, p. 430-431.

CHAOTIC FORMATION ON THE MOON James M. S. Sun, National Central University, Chung-li, Taiwan 320, Republic of China

Since acquiring a solid crust, the moon had been bombarded by mirad of exogenous projectiles, namely, meteorites, asteroids, and comets. Penetration into the lunar crust and cratering explosion of the projectiles, and secondary cratering had transformed the top veneer of the hard lunar crust into fragmental chaotic formation all over the moon. The chaotic formation is a rudimentary interbedded formation of ejecta, fallback, fine-grained base surge, and swarms of discrete rock blocks (rock missiles). It is compcsed of local and exotic lunar materials, and some exogenous additives. The rock fragments, either occurring in breccia or as discrete blocks, indicate the presence of an original hard rock lunar crust. After repeated cratering, and on account of the large range of the lunar ejecta, profuse admixing of the lunar surface materials became evident. Local variation of the major mineralogical composition of the chaotic formation is small.

Cratering during the terminal cataclysm ($4 \times 10^9$ to $3.5 \times 10^9$ yrs) occurred not on hard rock lunar crust, but on the soft chaotic formation. The shape of the lunar craters formed in the chaotic formation are comparable to that of experimental craters formed in alluvium and other soft rocks on earth. Such cratering during the terminal cataclysm caused further mixing of the chaotic formation. Although rock fragments of anorthosite or basalt may be identified, their transportation history is difficult to decipher. Because of increasing frequency of small craters, the mixing of the materials is more thorough toward the top of the chaotic formation. Toward the bottom of the chaotic formation, large rock blocks prevail, whereas fine-grained materials prevail toward the lunar surface. The chaotic formation is underlain by a zone of rupture and plastic deformation of the lunar crust.

Previously, the chaotic formation was estimated to be about 4 km thick in the vicinity of Copernicus (1). This was estimated according to the shape of Copernicus in comparison with the shape of experimental craters on earth. The shape of an explosion crater may be expressed by a ratio of apparent crater diameter, $2R_a$, and depth, $D_a$, or by a ratio of diameter ($2R_{al}$)

CHAOTIC FORMATION ON THE MOON

Sun, James M. S.

measured from apparent crater lip crest, and the depth from apparent crater lip crest to bottom of the crater ($D_{al}$).

The ratio $2R_{al}/D_{al}$ and $2R_a/D_a$ are comparable. Through the courtesy of R. J. Pike (2), the data of diameter and depth of some 202 lunar craters were made available for this study. Radius/depth of such craters, and that of experimental craters may vary from 2 to 4, due to variation of depth of burst (Fig. 1). When the diameter of a large lunar crater exceeds about 20 km, the radius/depth ratio begin to increase abovl 4. As a rule, the large lunar craters are broad, shallow, and have central peaks. This is caused by the effect of the boundary between the chaotic formation and its underlying zone of rupture and plastic deformation. The data show that the depth of such large craters vary from about 2.42 km to 5.37 km. This is the varying thickness of the chaotic formation all over the moon. Lunar seismic data indicate a soft rock layer of about 1 km thick, gradually grading into a zone of rupture and plastic deformation (3).

REFERENCES

(1) Sun, James M. S., Cometary impact origin of Copernicus, J. Geophys. Res., 73, 2721-2728, 1968.

(2) Pike, Richard J., Depth/Diameter relatilns of fresh lunar craters: Revision from spacecraft data, Geophys. R. Letters, 1, 291-294, 1974.

(3) Burnett, D. S., Lunar science: The Apollo legacy, Rev. Geophys. Space Phys., 13, 13-34, 1975.

CHAOTIC FORMATION ON THE MOON

Sun, James M. S.

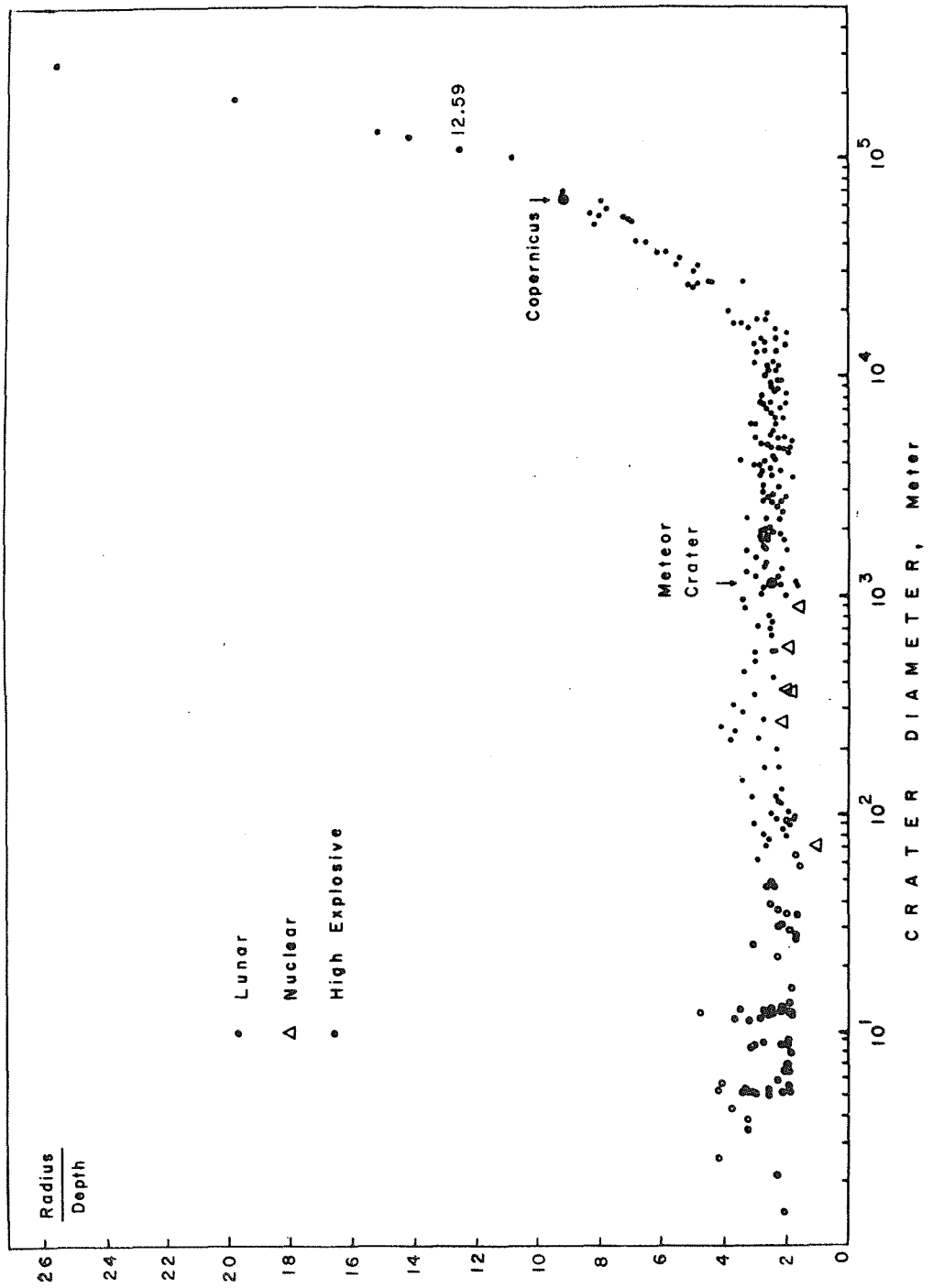


FIG. 1.

MATERIAL STRENGTH DEGRADATION EFFECT ON CRATERING DYNAMICS: R. P. Swift, Physics International Co., San Leandro, CA. 94577

An assessment of the effect of shock-induced degradation of material strength on crater formation is made by comparing two crater computations for a 5-MT nuclear surface burst over layered rock. Both computations were performed with ELK, a two-dimensional, coupled Euler-Lagrange finite difference code.

In the first calculation, denoted as ELK 76, the rock material was assumed to have the same failure surface characteristics after shock-wave passage as the original competent rock. A characteristic of the strength models used was a cohesive strength (i.e., yield strength at zero confining pressure) that was about 0.5 to 0.7 of the high-pressure von Mises limit. It was postulated that the cohesive strengths in the ELK 76 calculation were too high to represent the true characteristics of the material in and near the crater region following shock passage, and as a consequence, crater growth was retarded.

In the second calculation, denoted as ELK 76-DEG, the failure strength model was modified to allow the cohesive strength and pressure dependent portion of the failure surface to be reduced as a function of peak mean stress that the material experiences during the passage of the outgoing shock wave. This modification mainly affected the low-pressure portion of the material failure surfaces where the material resides during most of the crater formation time. The von Mises limits remained unchanged. The cohesive strength of the material experiencing peak shock pressures of a 100 bars or more above their seismic limit were reduced to approximately 2 bars. Cohesive strengths for material experiencing weaker peak shock pressures are reduced less, so that material near the elastic transition ranges essentially had no change in its failure model. Aside from this alteration to the failure surface model, the material models and all other calculational aspects for both computations were the same.

A comparison of the results from the two computations show the following features:

- The reduction in material strength behind the shock wave causes a drop in distortional energy in the ELK 76-DEG Lagrange grid as compared to the ELK 76 Lagrange grid which is first noticeable after 100 msec. This difference in distortional energy continues to increase until about 300 msec where, thereafter, it remains constant at about 9.5

percent of the total distortional energy. Forty percent of this energy change occurs in the zones adjacent to the crater boundary with the rest spread throughout the active part of the grid, decreasing with increasing distance from the crater.

- The above loss in distortional energy is offset by gains in kinetic energy and dilatational energy with a ratio of about 3:2 in favor of kinetic energy. The major increase in kinetic energy is confined to the near crater region, the gain in dilatational energy appears uniformly distributed throughout the near and far crater field.

- The dynamic growth of the crater remains essentially unchanged prior to 100 msec. Thereafter, the ELK 76-DEG crater grows at a higher rate with corresponding longer formation times for the crater depth and radius than those observed for ELK 76.

- The reduced strength effect leads to an increase in the maximum depth of the computed crater from 56 meters to 69.8 meters and an increase in the final crater radius from 65 meters to about 115 meters. This results in an increase in radius to depth ratio of 1.42 and an increase in volume of 3.3 for ELK 76-DEG over those computed for ELK 76.

- The influence of the enhanced crater growth is reflected in the displacement response beyond the immediate crater region in a manner compatible with the distribution of the change in kinetic energy. This influence down along the axis of symmetry extends only to a little beyond twice the crater depth, while near the surface the influence is noticeable out to about five crater radii.

The above results show that crater shape and formation time are strongly dependent on material strength, with larger R/D, larger volume, and longer formation time associated with a reduction in strength. The increase in volume and formation time are a consequence of the gain in kinetic energy at the expense of distortional energy, and the increase in R/D is attributed to the eventual distribution of this kinetic energy to the crater side, near-surface and lip regions.

Thus, while the material strength is indicated to be a significant parameter in crater formation, the complex nature of the ELK 76 computational configuration, that is, the multilayering and the complicated material models, detracts from any conclusive inference of what the results would be for a greater

reduction in material strength or even treating the shocked condition crater region as a hydrodynamic media. This uncertainty concerning the influence of post-shock material behavior on cratering dynamics suggests an area in need of further study. One important aspect of such a study should include determining and modeling material behavior in states of stress and deformation that are representative of those occurring in the crater region for surface or near-surface explosions. Furthermore, investigative cratering computations should first be conducted for single layer homogeneous media in order to assess the influence of material strength or other material properties without the coupled effects of multiple layers. After an understanding of material property effects are ascertained, multiple layering should then be addressed.

Acknowledgement

This work was performed with the support of the Defense Nuclear Agency under Contract DNA 001-76-C-0123 with Captain J. Stockton as the Contracting Officer Representative.

ON FRACTURE MECHANISM OF ROCKS BY EXPLOSION. Tsvetkov V.M., I.A.Sisov, N.M.Syrnikov, O.J.Schmidt Institute of Physics of the Earth, USSR Acad. Sci. Moscow, USSR.

Fracture is known to be such a type of rock fracture where a great number of cracks is formed in the volume deformed. The range of practical problems associated with the rock fracture by explosion is wide, however the fracture process itself has now been studied insufficiently. Below we discuss the results of model laboratory investigations and calculations which give an idea of fracture mechanism of brittle rocks fractured by explosion.

Rosin is chosen as a model experimental medium. The explosion of spherical charges were performed in the rosin blocks. The rosin transparency provides using the optical methods to record the front of compressional wave and the front of fracture. The compressional wave front has been recorded as a narrow dark line on the photographs due to the short-term change of the medium refraction coefficient; the fracture front having been determind by the irreversible loss of the rosin transparency as a result of forming a great number of cracks. The optical technique was described in [I]. The displacement velocity of the compressional wave was measured by the electromagnetic sensors. The numerous experiments displayed the high stability of the compressional wave front and, of particular importance, the fracture front. The latter shows one to note the distribution not separate cracks but the front of a great number of cracks. Time curve locuses are shown on fig.1.

The condition of medium fracture at different distances differs appreciably. In the zone which is in immediate contact with the explosion cavity ($R < 2a_o$), where $a_o$-the charge radius, the medium following the compressional wave front remains transparent for some time. In this zone the stresses exceed $10^4 kg/sm^2$ and the rosin deforms plastically without crack formation. At a distance of $2a_o < R < 4a_o$ the fracture takes place directly at the wave front, and finally, beginning with the distance $4a_o$ the fracture front lags the compressional wave front. Then the fracture front moves with decreasing velocity and ceases its movement at a distance of $25a_o$. The velocity of compressional wave front doubles the velocity of sound in nearest zone and at a distance of $R \simeq 4a_o$ drops to the value equal to velocity of sound. The decreasing of maximum displacement velocities in the medium can be represented by $V \sim a_o/R$ with $R > 8.5a_o$ The latter relation is typical for elastic wave propagation. This phenomenon warrants the assumption of elastic rosin behavious in the compressional wave up to the fracture moment.

The displacement velocity curves recorded in the process

ON FRACTURE MECHANISM OF ROCKS BY EXPLOSION.

Tsvetkov V.M. et al.

of experiments allow to calculate the compressional wave parameters by the elastic potential at the moment immediately proceeding the medium fracture.In this fasion the stresses $\sigma_r$ and $\sigma_\varphi$ (fig.2),the density,the deformations $\varepsilon_r$ and $\varepsilon_\varphi$ ,the strain rates $\dot{\varepsilon}_r$ and $\dot{\varepsilon}_\varphi$ and also various value combinations specified were calculated.The calculation data obtained give the possibility to represent medium fracture at various distances.In the zone nearest to the center ($R < 9a_0$),where the stresses $\sigma_r$ and $\sigma_\varphi$ are known to be compressional,the shear fracture is realized The value $\tau = |\sigma_r - \sigma_\varphi|$ as a function of $P = -(\sigma_r + 2\sigma_\varphi)/3$ and $\tau$ as a function of $\sigma_\varphi/\sigma_r$ in accordance with fracture criteria suggested in [2,3] provide satisfactory correlation for the experiments of different charges.In the far zone ($R > 9a_0$) the stress $\sigma_\varphi$ becomes extensive and the velocity of fracture front appears to be less than Rauleigh wave which is common knowledge to be the limited one of extensive crack propagation.In this zone the fragments of the fracture medium are expanded in the radial direction.Here the fracture occurs by means of forming radial grid cracks.It should be noted that the volume of the latter fracture zone exceeds I0 times the volume of the shear fracture zone.The analysis of experimental and calculation data showed that the medium fracture at the fracture front is not final.Following the fracture front especially in the vicinity of the nearest zone there takes place additional fracture.

References.

I. Lukishov B.G.,Rodionov V.N.,Sisov I.A.,Tsvetkov V.M.(I975) Model research on the crushing effect of explosions."Peacful nuclear explosions IV",Int.atom.energy agency.Vienna.

2. Cherry J.T.,Larson D.B.,Rapp E.T.(I968) A unique description of the failure of a brittle material.Int.J.Rock Mech.Min.Sci. 5,55.

3. Stavrogin A.N.(I969)The study of limiting states and deformation of rocks.Izvestia AN SSSR,Ser.Physics of the Earth,No.I2

ON FRACTURE MECHANISM OF ROCKS BY EXPLOSION.

Tsvetkov V.M. et al.

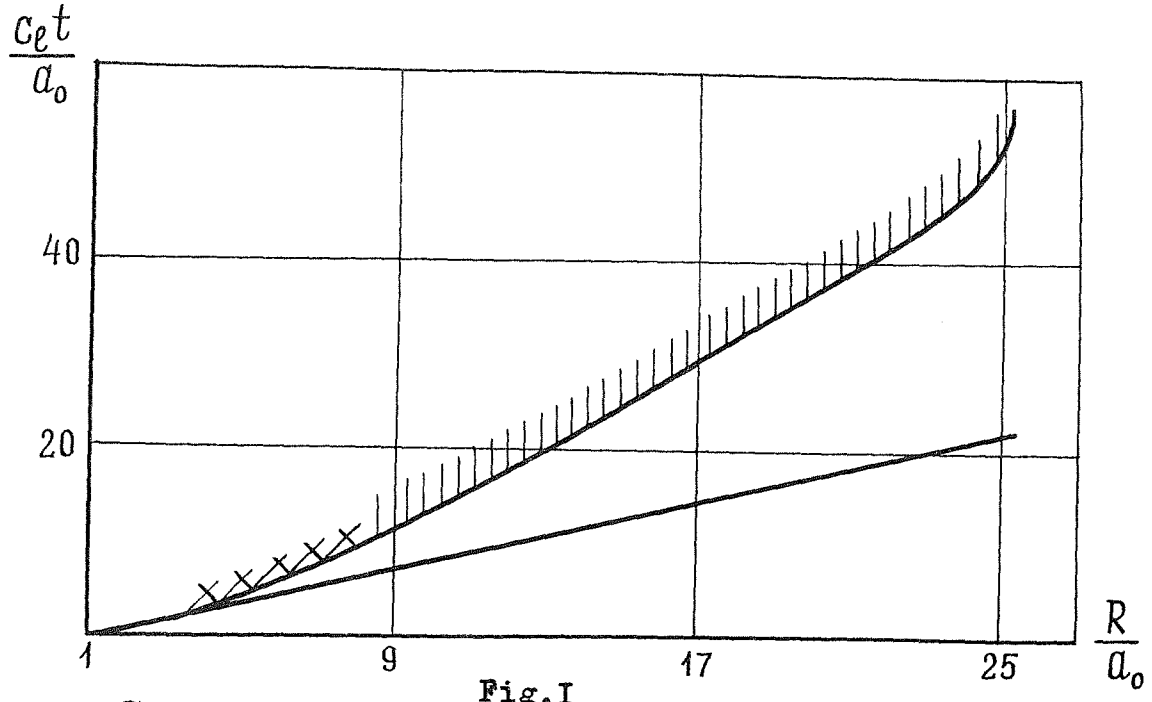


Fig.I

$C_\ell$ -the velocity of longitudinal waves (for rosin $C_\ell = 2.37 \cdot 10^3$ m/s)

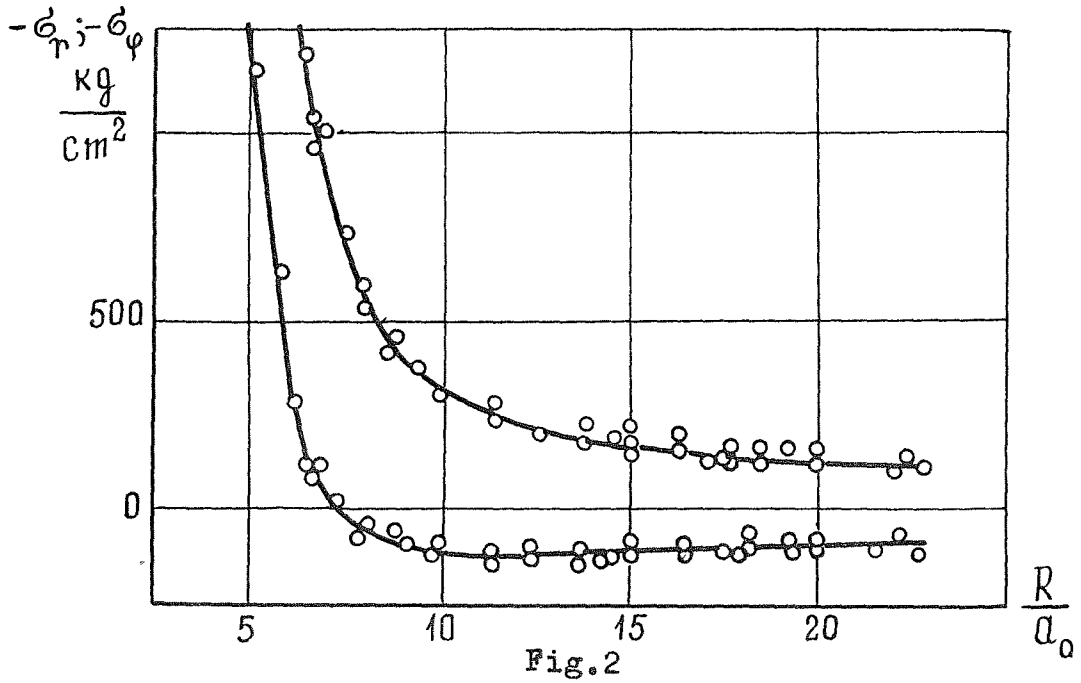


Fig.2

NUMERICAL SIMULATIONS OF A 20-TON TNT DETONATION ON THE EARTH'S SURFACE AND IMPLICATIONS CONCERNING THE MECHANICS OF CENTRAL PEAK FORMATION, G. W. Ullrich, Air Force Weapons Laboratory, Kirtland AFB, NM 87117; Gene Simmons, Dept of Earth and Planetary Sci, Mass Inst of Tech, Cambridge, Mass 02139, and D. J. Roddy, US Geological Survey, 601 E. Cedar, Flagstaff, AZ 86001

Central peaks are common features observed in craters on the Earth, the Moon, Mars, and Mercury. Since the peaks do not occur in all craters, they should be useful in providing strong constraints on both planetary evolution and numerical cratering simulations. Unfortunately, because the mechanics of central peak formation has been poorly understood, little use of those constraints has yet been made.

Observations of the occurrence and characteristics of central peaks and hypotheses concerning the mechanics of central peak formation provide an important background to this work. Observations of the structure of central uplifts and their occurrence in craters indicate that similar relations apply to both hypervelocity impact events and explosive detonations (1). The material in the central peak is displaced upward (1), probably inward (2), and shatter cones are frequently found (3) indicating that maximum stresses were on the order of, but above, the Hugoniot elastic limit of the material. Porous material tends to inhibit the formation of central peaks. The postulated mechanisms may be broadly divided into (A) effects related to stress waves and (B) rapid gravitational adjustments (4). Stress-wave mechanisms include material rebound, reflection of stress-waves at material discontinuities, shear-wave focusing, and complex stress-wave interactions near a free-surface. Gravitational hypotheses emphasize the failure of transient crater walls by sliding along deep slip surfaces.

High explosive cratering experiments provide excellent opportunities to examine the causes of central peak formation through numerical simulation because (A) the preshot material properties of the medium are extensively tested, (B) the test conditions are known, and (C) strong constraints on the numerical results are provided both by dynamic ground-motion measurements and by careful documentation of the structure of the crater and the central peak. A surface-tangent, 20-ton TNT event, designated Mixed Company II was a particularly useful experiment because the central mound was large compared to the size of the crater. This large size indicated that central peak mechanisms were particularly effective in this test event and reduced resolution problems associated with numerical calculations.

Therefore, in order to verify the numerical-simulation technique and to determine the material-response model, the Mixed Company II experiment was numerically simulated. We used three mathematical models of the physical processes assumed to be important. The first was based on numerical simulation of a high-explosive detonation to provide a surface boundary-stress condition. The ground response to 24 msec was simulated by a computer code

CENTRAL PEAK MECHANICS

Ullrich, G. W., et. al.

that modeled two-dimensional, axisymmetric problems of continuum mechanics with elastic-plastic material models. By 24 msec, material in the crater was moving ballistically; the final model was a ballistic extrapolation of the velocity conditions at 24 msec. Comparisons between measured dynamic data and velocity-time histories from the numerical simulation agreed in waveform and maximum velocities. The model crater was formed by 620 msec and a fallback phase of the problem was beginning. The radius and slope of the model true-crater wall, defined by the motionless material without extreme shear deformation, was consistent with the true crater profile. An extreme shear zone, with horizontal grid lines extending into an overturned flap, was calculated near the range of the observed southern crater wall and within the asymmetry of the apparent crater. The bottom radius of a central-peak region was comparable to the deepest point of the true crater located at a range of 2.6 meters. Within that radius an upward velocity of 4 m/sec was calculated in a location where an observed displacement would be obtained ballistically if the velocity was 8 m/sec. This difference is minimal when compared to the maximum downward velocity of nearly 130 m/sec that was calculated for that location.

The results of the Mixed Company II simulation were in sufficient agreement with observations to warrant a series of calculations to determine important influences on the numerical results. In that series, 12 additional numerical simulations were completed in which the models of compaction, layering, strength, and plastic-flow were varied. The most prominent result was that reducing the volumetric recovery from maximum compression from 90% to 70% eliminated the calculated upward-motion below the crater. A second significant influence on the Mixed Company II simulation was found to be the volumetric dilatancy associated with the Mohr-Coulomb yield condition. When this dilatancy was not included, significantly different motions, that were inconsistent with the Mixed Company II crater, were calculated. The numerical results also indicated that upward velocities for points on the axis of symmetry were first obtained where strength effects were important, and the model of test-site layering in the Mixed Company numerical simulation only slightly influenced the upward velocities below the crater. The inclusion of a lower, "fluid" layer modified the calculated response in a manner consistent with a deep "transient" cavity that would later collapse with the resulting central splash.

A mechanical model of central peak formation was developed with the results of the numerical calculations as a guide. Material rebound in the region where strength is important was emphasized in the model. Central peaks would be inhibited by material compaction unless a lower layer responded as a fluid. The mechanical model includes enhancement of the central peak primarily by material bulking but also by reflections of stress waves and the effect of the main shear wave. Gravitational adjustments contribute and may dominate when a lower layer responds as a "fluid." This model was

CENTRAL PEAK MECHANICS

Ullrich, G. W., et. al.

found to be consistent with both the observed occurrences and structural relations at sites of high-explosive detonations and hyper-velocity impact events. The conclusions were that the mechanical model is generally applicable to central peak formation, the occurrence of a central peak in a crater is primarily dependent on material properties of the medium, and the calculational code used for the numerical simulations can serve as a tool to investigate those material properties.

References: (1) D. J. Roddy (1968), Shock Metamorphism of Natural Materials, ed French and Short, 291-322. (2) D. J. Milton, et. al. (1972), Science, 184, 1199-1207. (3) R. S. Dietz (1968), Shock Metamorphism of Natural Materials, pg 267-284. (4) M. R. Dence, (1968), Shock Metamorphism of Natural Materials, pg 169-184.

CRATERS FROM SURFACE EXPLOSIONS AND ENERGY DEPENDENCE, A RETROSPECTIVE VIEW, L. J. Vortman, Sandia Laboratories, Albuquerque, NM 87115

The results of a 1968[1] determination of the energy dependence of the dimensions of craters from HE and nuclear explosions at or very near the surface of the earth are reexamined with the addition of data from terrestrial and lunar impact craters. The energy dependence has the form

$$R_a = C_1 W^{n1} \quad (1)$$

$$D_a = C_2 W^{n2} \quad (2)$$

$$V_a = C_3 W^{n3} \quad (3)$$

where $R_a$, $D_a$, and $V_a$ are radius, depth, and volume of the apparent crater and W represents the energy of the explosion. The principal findings of the earlier work were that $n_1 \neq n_2$ and that for some of the data sets of craters from high explosive $n_3$ was greater than 1. The retrospective view is that the results are credible and can be explained by known or postulated mechanisms, supported in some cases by published work of others.

The $n_3$ greater than 1 was brought about not by larger charges producing more crater volume per unit energy, but by smaller charges producing relatively smaller craters. There are two mechanisms which bring this about. First, since most materials contain cracks or planes of zero or near-zero shear and tensile strength, the volume moved by a large explosion encompasses many such planes and strength of the material is of relatively little importance. As energy decreases and fewer crack planes are encountered strength of the material becomes important and per unit of energy less material is removed. Second, stress pulses have durations and rise times which decrease with decreases in energy, probably by close to the cube root of energy. At some point in the decreased energy the strain resistance of the medium becomes rate dependent and a higher stress is required to overcome the strain resistance. That higher stress exists at a smaller radial distance, and the true crater volume is smaller. Assuming fallback is unchanged the apparent crater would be smaller and values of $n_3$ greater than 1, an explainable observation over the energy range for which they were reported.

Observed values of $n_1 \neq n_2$ differ from most dimensional analyses[2] and crater formulae[3] treatments of energy dependence of apparent crater radius and depth were $n_1$ and $n_2$ are usually considered equal. The inequality simply means that the apparent crater is changing shape as energy is increased. Ratios of $R_a/D_a$ were determined for the HE and nuclear craters of Reference 1 and for 5 terrestrial and 9 lunar craters for which energy was reported by Baldwin.[4] The ratios were plotted versus energy and energy dependence $(n_1 - n_2)$ determined by regression analysis. Except for certain of the high explosive crater data for which the number of events is small there is an increase in $R_a/D_a$ of about a factor of 15 over an energy range of $10^{18}$. Each data set shows a characteristic value of $n_1 - n_2$ and those for most of the sets can be explained in terms of crater dimension modifying phenomena. The most significant modifying phenomenon is ejecta fallback. Let it be assumed for different sized surface explosions that particles at geometrically similar positions will have the same initial velocity and trajectory

angles, then particles so located on unequal explosions will have the same trajectory and range. As the energy and crater radius increase more of the ejecta fails to clear the crater edge, falls back into the crater and decreases the crater depth and volume. There would be differences between explosion and impact craters because initial velocity fields would be different, but the data sample is small and the observed discontinuity in $R_a/D_a$ for the two types of energy sources is not significant in view of the large variance.

There is also a discontinuity between terrestrial and lunar impact craters as would be expected where the lower gravitational acceleration and lack of atmosphere would increase trajectory for lunar craters with consequently less fallback, deeper depth, and smaller $R_a/D_a$. Again the number of craters in each set is small, and the variance too large for the discontinuity to be conclusive.

The lunar data fall into two distinct sets with a discontinuity in both $R_a/D_a$ and $n_1 - n_2$ at about the point where Gault et al[5] found a discontinuity which was attributed to slump terraces and perhaps central peaks. Although the number of craters included in this work is too small to provide a definite conclusion, it is observed that the discontinuity in $R_a/D_a$ and $n_1 - n_2$ results from a discontinuity in depth rather than diameter. Slumping would increase apparent crater diameter. The apparent diameters used here were based on Baldwin's observation[4] that apparent crater diameter is 0.83 times rim diameter. Slumping effect would not change the dimension unless it extended beyond the top of the rim and increased the rim diameter. There is evidence[6] that central peaks are of shock origin, and horizontal transport of slumped material as far as would be necessary to reduce crater depth for the largest lunar craters does not seem credible. Head's[7] postulated fragmental megaregolith on the moon surface is more plausible and consistent with the shock origin of the central peak.

The nuclear surface bursts have greater $n_1 - n_2$ than impact craters or HE craters in playa. This is consistent with the mechanisms described by Ganong and Roberts[8] who found that reflected air shocks and afterwinds shortened or reversed the trajectory of particles in certain size ranges resulting in more fallback and shallower craters. High explosive craters in silt exhibit large $n_1 - n_2$ because of the effect of a shallow water table which reduced the crater depth more drastically as the explosion energy increased. Here the effect is similar to that of layered media and the lunar fragmented megaregolith.

Dimensional analyses and cratering formulae approaches to the energy dependence of crater dimensions will continue to be inadequate until recognition is made of the observation that $n_1 \neq n_2$, until the true crater is treated as the fundamental one, and until the modifying phenomena are properly introduced to relate the apparent crater dimensions to energy.

CRATERS FROM SURFACE EXPLOSIONS

Vortman, L. J.

1. Vortman, L. J., Craters from Surface Explosions and Scaling Laws, J. Geophys. Res., 73(14), 4621-4636, 1968.
2. Chabai, A. J., On Scaling Dimensions of Craters Produced by Buried Explosives, J. Geophys. Res., 70(20), 5075-5098, 1965.
3. White, J. W., An Empirically Derived Cratering Formula, J. Geophys. Res., 78(35), 8623-8633, 1973.
4. Baldwin, R. B., The Measure of the Moon, University of Chicago Press, Chicago, IL, 1963.
5. Gault, D. E., J. E. Guest, J. B. Murray, D. Dzurisin, and M. C. Malin, Some Comparisons of Impact Craters on Mercury and the Moon, J. Geophys. Res., 80(17), 2444-2460, 1975.
6. Ullrich, G. W., The Mechanics of Central Peak Formation in Shock Wave Cratering Events, Rep. AFWL-TR-75-88, Air Force Weapons Laboratory, Kirtland Air Force Base, NM, 1976.
7. Head, J. W., Significance of Substrate Characteristics in Determining Morphology and Morphometry of Lunar Craters, Abstracts of 7th Lunar Science Conference, 1976.
8. Ganong, G. P., and W. A. Roberts, The Effect of the Nuclear Environment on Crater Ejecta Trajectories for Surface Bursts, Rep. AFWL-TR-68-125, Air Force Weapons Laboratory, Kirtland Air Force Base, NM, 1968.

# DYNAMIC EJECTA PARAMETERS FROM HIGH EXPLOSIVE DETONATIONS

John Wisotski, University of Denver, Denver Research Institute, Denver, Colorado 80210

Dynamic ejecta, photographed during the detonation of 1/2,- 20- and 100-ton TNT spheres in the MIDDLE GUST Series, were analyzed to give impact and escape parameters. The TNT spheres were detonated at height-of-burst (HOB) of 0, 1 and 2 charge radii. The HOB = 2 data are excluded from this abstract. There were two test sites (wet and dry). The wet site geological profile was composed of an alluvial soil overburden approximately 9 feet thick overlaying approximately 14 feet of weathered fractured clay shale; this in turn overlies a more competent clay shale bedrock. The ground watertable was at a depth of approximately 4 feet. Five of the six 1/2-ton events (5 thru 9) covered by this abstract were detonated in a specially prepared test pit at the wet site at three different depths -4, -9 and -16 feet. The depths were obtained by the removal of some of the overburden. The water was prevented from seeping into the pit by sheet piles placed at the perimeter of the pit. Event 3a was detonated in the natural wet-site geology with no overburden removed. The profile at the dry site comprises an average of 28 feet of weathered fractured clay shale overlying a more competent, relatively impervious clay shale. The craters formed at the wet site in the natural geology were two to three times the size formed at the dry site in its natural geology.

The largest ejecta impacting any regions of interest were tracked back toward the fireball and crater debris. Approximately one hundred of these large particles were tracked for each event. The position-time data obtained from the ejecta trajectories were adjusted for camera tilt. The ejecta trajectory planes were rotated until the ejecta drag coefficients corresponded with their Reynolds number values. The Reynolds numbers were generally so large, because of the ejecta sizes and velocities, that they indicated ejecta drag coefficients which approached zero, i.e., the in-flight particles were very near ballistic.

Least-squares curve fits to the impact velocity, time, angle and weight data versus impact distance were made for each event. Parametric values obtained from these curve fits at specific scaled $(w_1/w_2)^{1/3}$ distances were compared between events having: (a) dissimilar charge configuration and similar geologies and equal charge weights; (b) similar charge configurations and equal charge weights, and dissimilar geologies; and (c) similar charge configurations and geologies, and unequal charge weights (scaling). Parametric data over impact distances of 200 to 400 feet for the 1/2-ton events, and scaled distances of 684 to 1368 feet for the 20-ton events and scaled distances of 1170 to 2340 were used in these comparisons. Summary type data at these impact distances are presented in the table.

Under comparison (a) impact velocities and times were nearly the same but impact angles were shown to be greater for half-buried than for tangent configurations. The weight of the largest ejecta impacting any region of interest was found to be higher for tangent charge configuration over half-buried when the surface overburden was alluvial. When the surface overburden was weathered-fractured clay-shale obtained by the removal of the original alluvial surface material, the half-buried configuration produced larger

ejecta than the tangent configuration.

Comparison (b) indicated that dynamic ejecta from the wet geologies had higher impact velocities, longer times of flight, greater impact angles and higher weights than the dynamic ejecta produced by similar charge configurations at the dry site.

It was found under comparison (c) that the impact velocities and times of the dynamic ejecta appeared to scale by $(w_1/w_2)^{1/6}$.

Since the trajectories were near ballistic outside the fireball, the maximum range any ejecta would have travelled (neglecting drag forces) is:

$$S_{max} = (V_E^2 \text{ Sin } 2\ \theta_E)/g$$

where: $V_E$ = escape velocity, $\theta_E$ = escape angle and g = acceleration due to gravity.

It can be assumed since the trajectories are near ballistic for the greatest portion of the trajectory path, impact velocity ($V_I$) and impact angle ($\theta_I$) would be nearly equal to their escape counterparts, i.e., $V_E \simeq V_I$ and $\theta_E \simeq \theta_I$.

Assume $S_2 = (w_2/w_1)^{1/3} S_1$, where $w_1$ and $w_2$ are the TNT charge weights.

$$S_1 = (V_1^2 \text{ Sin } 2\ \theta_1)/g \text{ and } S_2 = (V_2^2 \text{ Sin } 2\ \theta_2)/g, \text{ and } \theta_1 = \theta_2.$$

Then: $(w_2/w_1)^{1/3}\ V_1^2 = V_2^2$ therefore: $V_2/V_1 = (w_2/w_1)^{1/6}$

Since the geology for Calibration Event 5 and 6 compare fairly well on a scaled basis to the geology for the main events, i.e., watertable position one foot from the surface, comparisons of impact, velocity and impact time were made to Events III and I, respectively.

| Events 1 and 6 $(w_1/w_6)^{1/6} = 1.85$ | | | | Events III and 5 $(w_{III}/w_5)^{1/6} = 2.42$ | | | |
|---|---|---|---|---|---|---|---|
| Ratio | $S_1$ | $S_2$ | $S_3$ | Ratio | $S_1$ | $S_2$ | $S_3$ |
| $V_1/V_6$ | 1.92 | 1.92 | 1.89 | $V_{III}/V_5$ | 2.54 | 2.52 | 2.56 |
| $t_1/t_6$ | 2.00 | 2.04 | 2.18 | $t_{III}/t_5$ | 2.57 | 2.59 | 2.50 |

The above tabulation show good agreement of the ratios of velocity and time to the charge weight ratios to the 1/6 power. The differences are mainly due to the slightly lower (4 to 5 degrees) angle values for the 1/2 ton detonations which are indicative of slightly lower velocities and slightly lower times. These lower values would increase the ratios as indicated.

Impact Velocities, Angles, Times and Weights Versus Distances ($S_n$) of 200, 300, and 400 Feet for a 1/2-Ton Charge; Scaled Distances of 684, 1026, 1368 Feet for a 20-Ton Charge; and 1170, 1755 and 2340 Feet for a 100-Ton Charge.

| Event | Weight (tons) | Charge Conf. | Site | Velocity (ft/sec) | | | Time (sec) | | | Angle (degrees) | | | Weight (Pounds) | | |
|---|---|---|---|---|---|---|---|---|---|---|---|---|---|---|---|
| | | | | $S_1$ | $S_2$ | $S_3$ | $S_1$ | $S_2$ | $S_3$ | $S_1$ | $S_2$ | $S_3$ | $S_1$ | $S_2$ | $S_3$ |
| MGI | 20 | ½-Buried | Wet | 159 | 204 | 240 | 7.8 | 10.4 | 12.4 | 58.5 | 62.0 | 64.5 | 1300 | 1000 | 810 |
| MGV | 20 | ½-Buried | Dry | 154 | 200 | 237 | 6.8 | 8.2 | 9.5 | 51.5 | 49.5 | 49.5 | 830 | 890 | 930 |
| MGIII | 100 | Tangent | Wet | 208 | 267 | 322 | 9.5 | 11.9 | 13.5 | 55.5 | 58.5 | 59.0 | 3600 | 2100 | 1300 |
| MGIV | 100 | Tangent | Dry | 206 | 263 | 311 | 8.1 | 9.4 | 10.0 | 48.5 | 47.0 | 44.0 | 500 | 490 | 480 |
| MG3a* | 1/2 | ½-Buried | Wet | 90 | 115 | - | 4.1 | 4.3 | - | 58.5 | 52.0 | - | 34 | 15 | - |
| MG5 | 1/2 | Tangent | -4Ft | 82 | 106 | 126 | 3.7 | 4.6 | 5.4 | 49.5 | 52.5 | 54.0 | 71 | 45 | 29 |
| MG6 | 1/2 | ½-Buried | -4Ft | 83 | 106 | 127 | 3.9 | 5.1 | 5.7 | 54.5 | 59.0 | 59.5 | 31 | 22 | 16 |
| MG7 | 1/2 | Tangent | -9Ft | 83 | 107 | 133 | 3.5 | 4.4 | 5.3 | 48.5 | 52.5 | 57.0 | 21 | 23 | 26 |
| MG8 | 1/2 | ½-Buried | -9Ft | 88 | 111 | 128 | 4.3 | 5.4 | 6.0 | 59.5 | 61.0 | 60.0 | 71 | 35 | 16 |
| MG9 | 1/2 | ½-Buried | -16Ft | 90 | 116 | 140 | 4.2 | 5.2 | 6.0 | 58.5 | 61.0 | 64.0 | 82 | 46 | 24 |

*Events 3a, and 5 thru 9, wet site.

A MODEL FOR TRANSPORT AND DEPOSITION FROM BASE SURGE OF VOLCANIC ORIGIN Kenneth H. Wohletz, Geoscience Group, Univ. of California, Los Alamos Scientific Laboratory, Los Alamos, NM 87545, and Michael F. Sheridan, Dept. of Geology, Arizona State Univ., Tempe, AZ 85281

Base surge has been shown to accompany a wide variety of pyroclastic volcanic eruptions and to have a similar phenomenology to that produced by underground thermonuclear and chemical explosions and high energy impacts (1,2,3). The surge is generated either during initial explosive phases of eruption where volatiles under one to several kilobars of pressure exolve and blast out of a near-surface magma body or when magma encounters abundant ground or surface water explosively flashing it to steam.

This paper results from studies of base-surge deposits in the Bishop Tuff, CA, and in the tephra at Ubehebe Crater, CA, Peridot Mesa, AZ, Coronado Mesa, AZ, and Crater Elegante, Sonora, Mexico. These five localities represent areas of at least five types of volcanic eruptions producing base surge: a large ash flow, a maar, a diatreme, a tuff ring associated with a rhyolite dome, and a collapse-maar eruption respectively. Over 70 stratigraphic sections measured at varying distances from the vents were input for a Markov analysis of transitions in bed-form structures in base-surge deposits.

Tephra in surge deposits is composed of beds that average 1 to 10 cm in thickness, are continuous in nature, and show three principal bedding structures. These structures are massive beds, planar beds showing inverse grading, and sandwave beds that include features such as cross and ripple laminations, dunes, and antidunes. Markov analysis shows that sections are characterized by a dominance of: 1) sandwave to massive transitions; 2) planar to massive to sandwave transitions; or 3) planar to massive transitions. Maps correlating sections of similar character demonstrate that surge deposits follow a typical lateral variation in character away from the vent. Sandwave to massive bedding transitions predominate in sections nearest the vent (sandwave facies), planar to massive to sandwave transitions at an intermediate distance (massive facies), and planar to massive transitions in sections furthest from the vent (planar facies). Figure 1 shows the distribution of facies around Ubehebe Crater. This lateral variation in character of surge deposits is also shown by composite stratigraphic sections generated for three distance intervals away from the vent. Figure 2, an example taken from Coronado Mesa, demonstrates this relationship of composite sections. Furthermore, Markov analysis shows a low probability of transition from planar beds to sandwave beds without a massive bed between the two, suggesting that massive beds are likely to be the result of transport and deposition in an energy environment intermediate to those that produce planar and sandwave beds.

The lateral variation of surge deposits away from vents is compatible with a fluidization-deflation model of transport and deposition. The model is as follows. (I) A base-surge cloud is erupted being greatly inflated with entrapped gas due to the eruption's phreatomagmatic nature, volatile content, bulk subsidence, or any combination of the three. The cloud

travels horizontally away from the vent due to gravity flow and the horizontal component of velocity of the fluidized particles within the cloud. (II) Near the vent, void space within the cloud is dominantly in a range greater than 90% resulting in viscous flow (4). During viscous flow, saltation of grains occurs forming beds of dominantly sandwave structure (5). (III) As the cloud continues to move away from the vent, gas escapes, the cloud deflates, and void space decreases so that it is dominately in the range of 60% to 90%. At this point, viscous forces and inertial forces in the cloud interact and massive beds interfingering with sandwave and planar beds are deposited. (IV) Still further from the vent the cloud deflates to the point where inertial flow dominates and void space is generally less than 60% (4). Here grain collisions set up shear planes along which grains of different sizes seek their respective zone of lowest shear energy and inversely graded planar beds result (4). Figure 3 illustrates the model.

Complications of the model are: 1) the superposition of many surges of differing sizes and energies that commonly exist around volcanic vents; 2) topographic and meteorologic effects upon the surge cloud; and 3) the effect of residence time needed for particles of differing sizes and densities to establish the energy regimes required for formation of bedding structures.

## REFERENCES

(1) Moore, J. G., 1967, Bull. Volcanol., v. 30, p. 337-363.
(2) Fisher, R. V., and Waters, A. C., 1970, Am. Jour. Sci., v. 268, p. 157-180.
(3) Waters, A. C., and Fisher, R. V., 1971, Jour. Geophys. Res., v. 76, p. 5596-5614.
(4) Bagnold, R. A., 1954, Proc. Royal Soc. London, v. 225, p. 49-63.
(5) _____, 1954, the Physics of windblown sand and dessert dunes: Methuen and Co., London, 265 p.

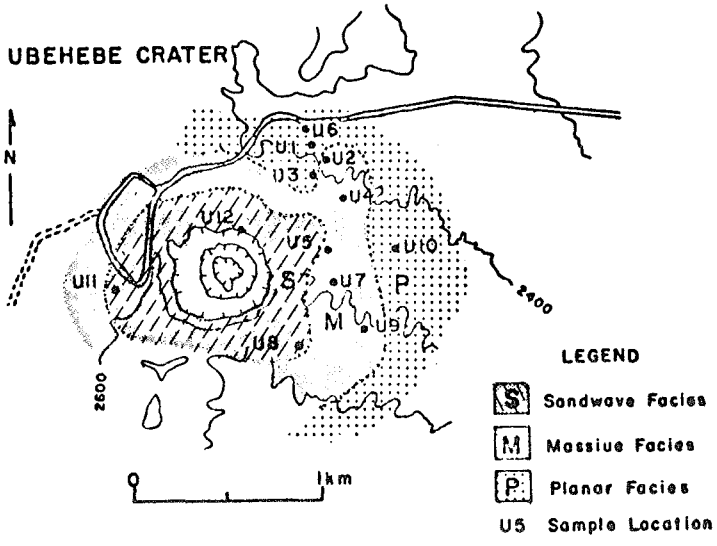


Fig. 1 A map showing the distribution of base-surge facies around Ubehebe Crater, CA.

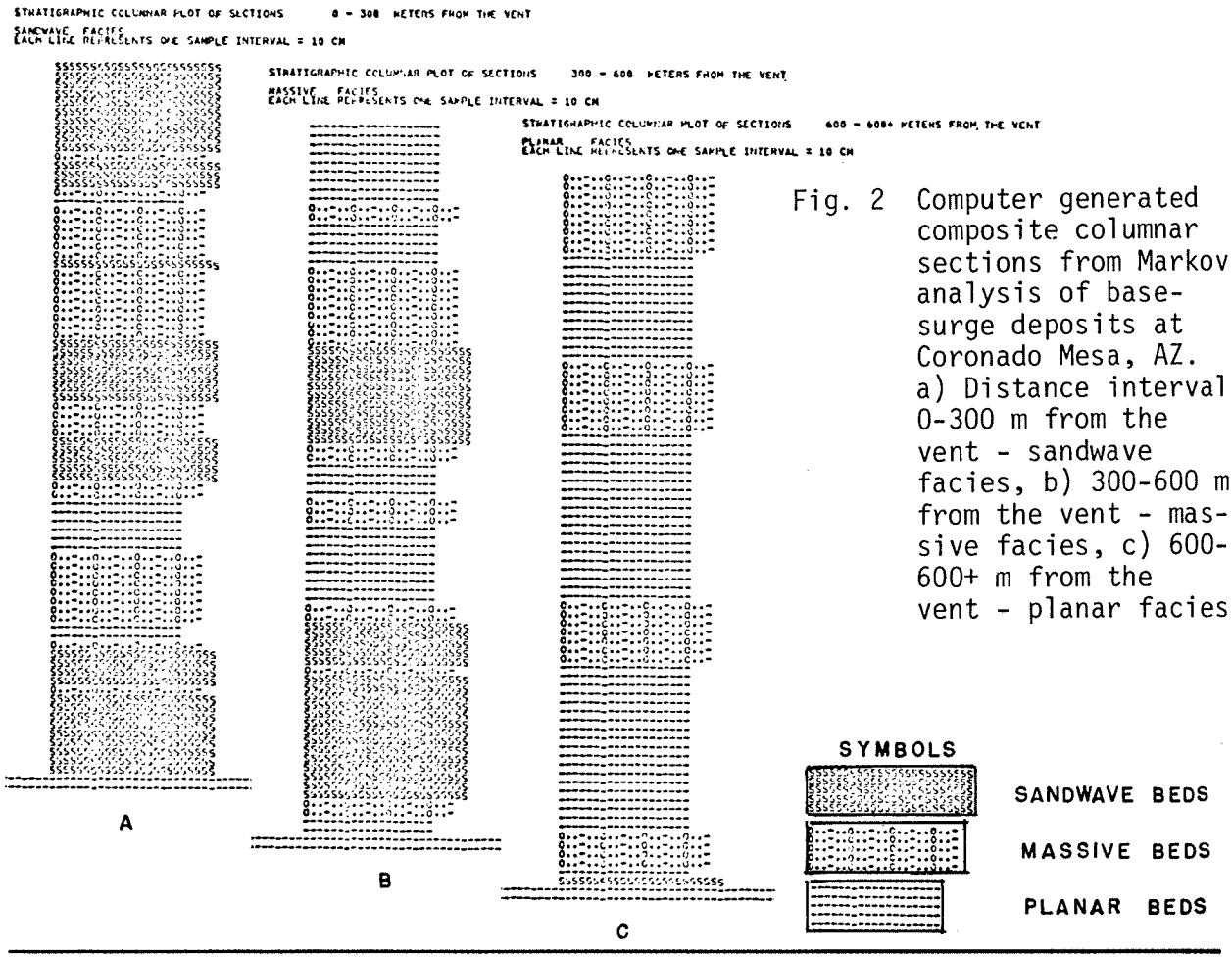


Fig. 2 Computer generated composite columnar sections from Markov analysis of base-surge deposits at Coronado Mesa, AZ. a) Distance interval 0-300 m from the vent - sandwave facies, b) 300-600 m from the vent - massive facies, c) 600-600+ m from the vent - planar facies.

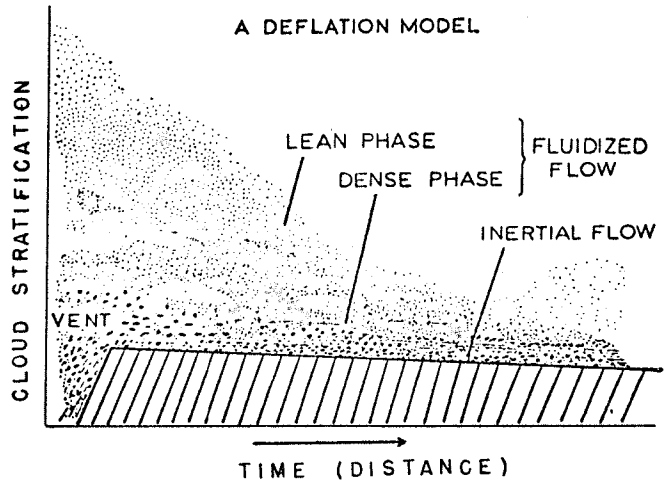


Fig. 3 A time integrated diagram showing the transport and depositional regimes within a base-surge cloud at increasing times (distances) after (from) the eruption. For lean phase fluidized flow void space is greater than 90%, dense phase is 60% to 90%, and for inertial flow void space is less than 60%.

# A STRATIGRAPHIC MODEL FOR BESSEL CRATER

R.A. Young, Dept. Geol. Sciences, SUNY, Geneseo, N.Y. 14454.

Layering in the walls of Bessel Crater (Fig. 1,2), combined with photogeologic and remote sensing information for southern Mare Serenitatis, allows construction of a reasonable model for some of the important parameters required for comparison of terrestrial and planetary cratering mechanics.

Evidence from flooded craters, the Apollo Lunar Sounder, crater size-frequency distributions, the color of Bessel ejecta, infrared reflectance spectroscopy, and regional photogeology has been summarized by Young (1) in support of a shallow "dark mantle" layer buried less than 300m beneath the younger brownish-gray lavas in central Mare Serenitatis.

The diameter of Bessel (∿15 km) lies within the transition interval cited by Pike (2) as a region in which crater parameters cannot always be accurately predicted by mathematical relationships. This fact, combined with the unique stratigraphic setting near Bessel, may limit the application of measurements at this site to other lunar regions.

More recent information from the Apollo Lunar Sounder Experiment and 15 MHz radar (3,4) indicates a major regional subsurface boundary at 900 to 1200m overlain by 12 to 20 thinner layers. Direct evidence for the near-surface layers is visible in the wall of Bessel. Its wide, relatively shallow floor is at a depth below the original surface (∿1100m) which closely coincides with the postulated major disconformity (3,4).

An interpretation of the photogeology seen in Figure 2, in combination with all of the information cited above, is the basis for Figure 1 and Table 1.

The following assumptions were made to construct the model: 1) The dark stripes circling the crater wall come from a layer cropping out near the top of the most prominent dark band ∿420m below the west rim. A minor amount of dark material from the rim is moving down the slope and may represent the same layer capping the inverted stratigraphy on the rim crest. 2) Because this dark layer only appears to crop out once at depth in the upper half of the crater wall, it must lie at the base of or below the section which is assumed to be inverted near the rim; otherwise the dark layer would be repeated <u>within</u> the overturned rim flap. Because of the location of the dark layer and its inferred composition, it is assumed to be the horizon along which the crater rim strata were peeled back and overturned. 3) The prominent layer (E) nearest the surface in the low sun elevation view (vertical distance ∿150m down from rim) is unlikely to be part of the overturned stratigraphic section due to its relatively undisturbed appearance around the inner wall for a distance of at least 10 km. This layer may have been near the original surface, covered with <10m of regolith.

# BESSEL CRATER

R.A. Young

4) There are at least 6 detectable layers between the dark mantle and the original surface over a vertical distance of 270m.

References

(1) Young, R.A. (1976) Evidence for a Shallow Regional Subsurface Discontinuity in Southern Mare Serenitatis. In Lunar Science VII, p. 959-961. The Lunar Science Inst.

(2) Pike, R.J. (1976) Simple to Complex Impact Craters: The Transition on the Moon. In Lunar Science VII, p. 700-702. The Lunar Science Inst.

(3) May, T.W. et al. (1976) Subsurface Layering in Maria Serenitatis and Crisium: Apollo Lunar Sounder Results. In Lunar Science VII, p. 540-542. The Lunar Science Inst.

(4) Brown, W.E. Jr. et al. (1976) Lunar Subsurface Structure in the Sulpicius Gallus Region, In Lunar Science VII, p. 97-98. The Lunar Science Inst.

Table 1: Average or Estimated Values for Dimensions of Bessel Crater from LTO Map 42D2 and Orbital Photography.

| | |
|---|---|
| Elevation of original surface | 4700m |
| Diameter | 15.3km |
| Rim height above original surface (ave. 5350m elev.) | 650m |
| Rim height west wall (layers visible) | 450m |
| Interior relief using ave. rim height | 1750m |
| Floor elevation | 3600m |
| Original thickness of strata above dark mantle, west wall (estimated) | 350m |
| Thickness of overturned flap at rim (west wall) | 180m |
| Uplift of west rim (estimated) | 380m |
| Dip of upturned rim strata (assumed) | 10° |

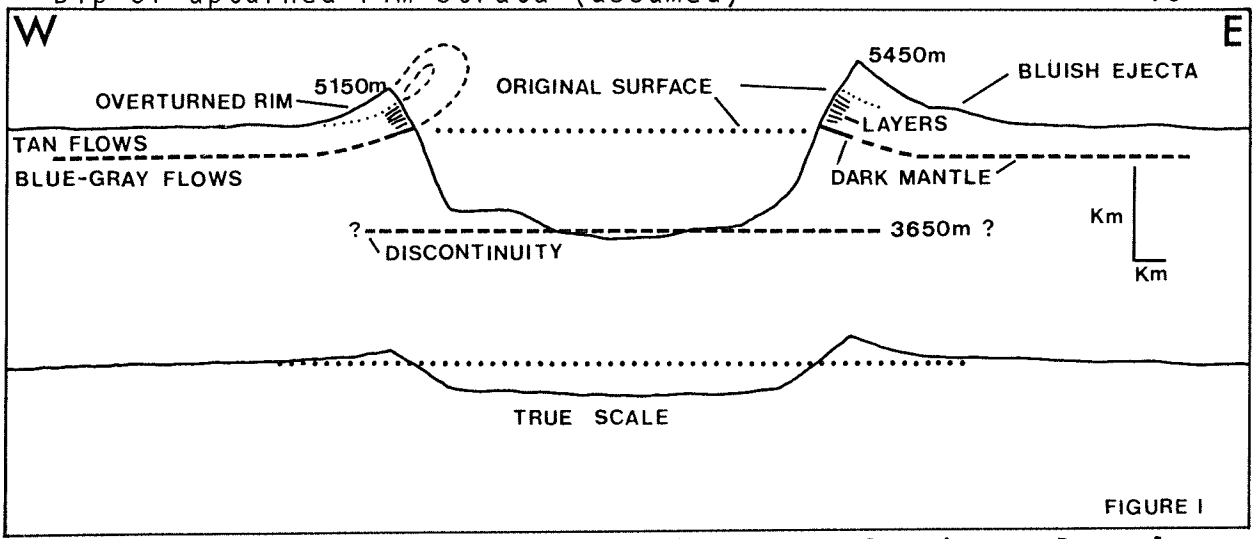


FIGURE 1: Profiles and Interpretative Cross Sections, Bessel.
FIGURE 2: Pans AS15-9330(26°), AS17-2345(3°) of Bessel dodged for max. detail. A,B,C, Same points. D, Dark mantle. E, Upper surface layer. F, Sharp tone changes due to mosaic and dodging.

BESSEL CRATER

R. A. Young

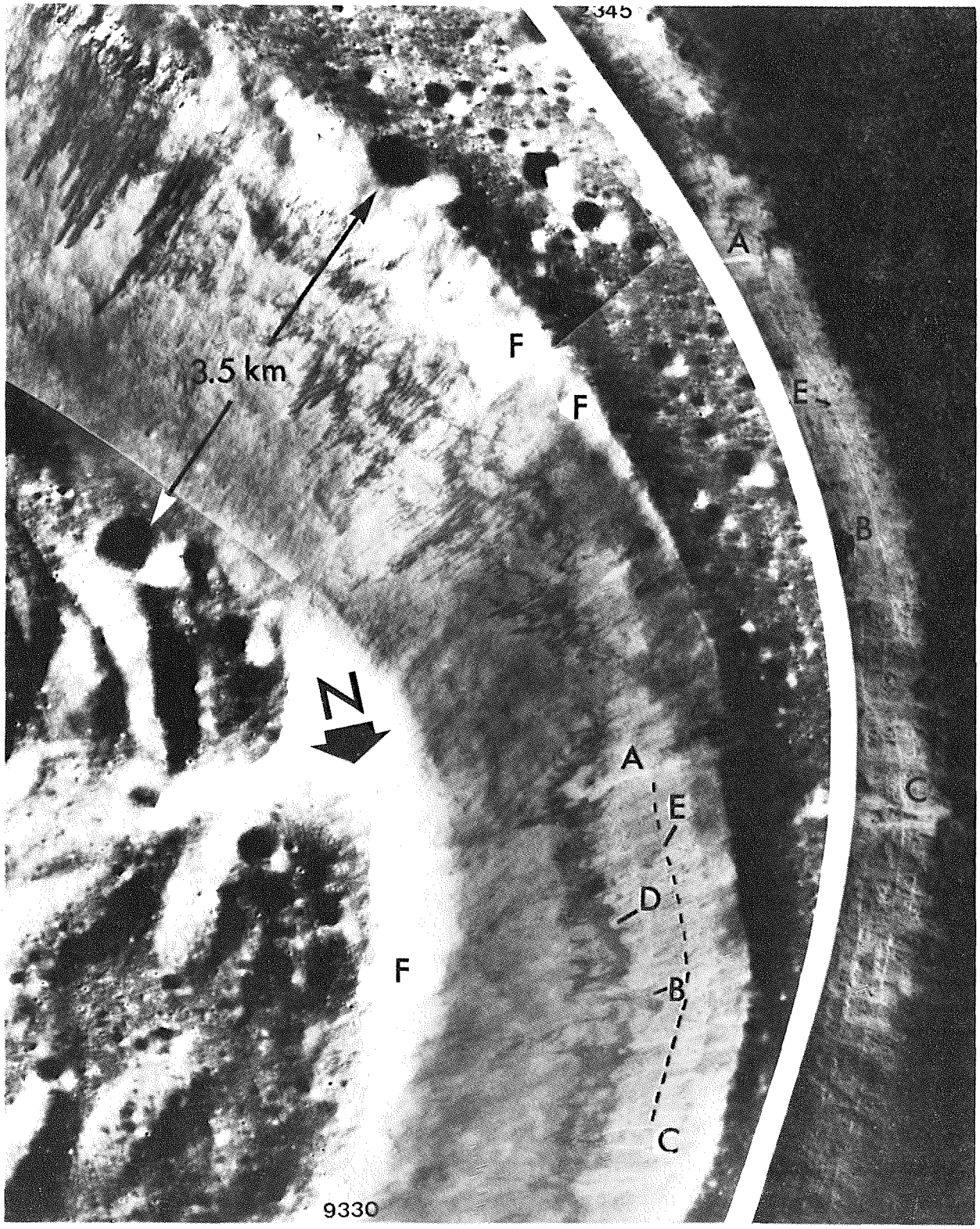

# SUBJECT INDEX*



*Pagination refers to first page of paper in which subject is cited.

# TOPIC INDEX

(Paper to be identified by first author)

## TOPIC I
## EXPERIMENTAL STUDIES



## TOPIC II
## PLANETARY IMPACT CRATERING



## TOPIC III
## THEORETICAL CALCULATIONS



## TOPIC IV
## SCALING



## TOPIC V
## TERRESTRIAL IMPACT CRATERING

## TOPIC VI
## MATERIAL PROPERTIES AND SHOCK EFFECTS



## TOPIC VII
## EJECTA

# AUTHOR INDEX*



---

*Pagination refers to first page of paper in which author is cited.

National Aeronautics and
Space Administration

**Lyndon B. Johnson Space Center**
Houston, Texas 77058